

The image features two complex, interconnected wireframe structures. The top structure is composed of white lines on a black background, while the bottom structure is composed of orange lines. Both structures are made of numerous interconnected triangles and polygons, creating a dense, mesh-like appearance. Two thin white lines connect the top and bottom structures, passing behind the central text. The overall composition is symmetrical and visually striking due to the contrast between the colored lines and the black background.

Producing and Constraining Self-Interacting Hidden Sector Dark Matter

LAURENT VANDERHEYDEN
PHD THESIS



FACULTÉ
DES SCIENCES



UNIVERSITÉ LIBRE DE BRUXELLES

Producing and Constraining Self-Interacting Hidden Sector Dark Matter

Thesis presented by Laurent VANDERHEYDEN

in fulfilment of the requirements of the PhD Degree in Physics ("Docteur en Sciences Physiques")
Academic year 2020-2021

Supervisor : Professor Thomas HAMBYE
Service de Physique Théorique

Thesis jury :

Laura LOPEZ-HONOREZ (Université libre de Bruxelles)
Riccardo ARGURIO (Université libre de Bruxelles)
Michele REDI (INFN, Florence)
Kai SCHMIDT-HOBERG (DESY, Hamburg)
Thomas HAMBYE (Université libre de Bruxelles)



Abstract




incompatibilities between numerical simulations, theoretical predictions and cosmological observations at small and large scales suggest that the Dark Matter (DM) could strongly self-interact. It has been shown that introducing a light mediator would greatly help in accounting for large DM self-interactions. This mediator can allow portal interactions between the "hidden sector" containing the DM and the mediator and the "visible sector" containing the ordinary SM particles we know. However, more and more of the parameter space is excluded due to strong tensions between cosmological and astrophysical observations, on the one hand, and the fact that there is, until now, still no hint of DM in particle physics experiments, on the other hand.

In this thesis, we start by reviewing all constraints applying on self-interacting DM with a light mediator considering well-known Higgs portal and Kinetic Mixing portal models as concrete examples. Then, we elaborate on the Sommerfeld effect, and we study its many implications on self-interacting DM models with light mediator. Next, we investigate how to account for the DM relic abundance in such portal models which present a generic structure with three populations (Standard Model, DM and mediator particles) connected to each other through three interactions resulting from two coupling strengths. It appears that this can be done through five different dynamical ways which give rise to nine regimes among which four are new. Those new production regimes are relevant for a situation where the hidden sector particles are not thermally connected to the visible vector particles.

We further study the possibility of a thermally disconnected Hidden Sector and establish the general allowed parameter space for DM thermal candidates in the hidden-to-visible temperature ratio versus DM mass plane. We show that, in this framework, simple portal models such as the two we consider can alleviate tensions at small scale while offering suitable DM candidates. Other minimal self-interacting DM with light mediator frameworks which consistently fulfil all constraints are also proposed and explored.

KEYWORDS: Dark matter, hidden sector, self-interactions, light mediator, production mechanism, portal.

Résumé

es incompatibilités entre les simulations numériques, les prédictions théoriques et les observations cosmologiques à courtes et larges échelles suggèrent que la Matière Noire (MN) auto-interagit fortement. Il a été démontré qu'introduire un médiateur léger peut permettre de rendre compte de telles auto-interactions pour la MN. Un tel médiateur permet, de plus, des interactions "portails" entre le "secteur caché" (contenant la MN et le médiateur léger) et le "secteur visible" (contenant les particules que l'on connaît déjà, c'est-à-dire du Modèle Standard). Toutefois, l'espace des paramètres se voit de plus en plus exclu aux vues d'une tension entre, d'une part, les observations cosmologiques et astrophysiques et, d'autre part, le fait que l'on ait à ce jour toujours pas mis en évidence des traces de MN dans aucune expérience de physique des particules.

Nous commençons par détailler toutes les contraintes qui s'appliquent aux modèles pour lesquels la MN auto-interagit au moyen d'un médiateur léger. Pour cela, nous considérons les deux exemples de modèles connus du portail de Higgs et du portail de mélange cinétique. Nous discutons ensuite l'effet Sommerfeld et étudions ses nombreuses implications sur de tels modèles. Nous poursuivons en établissant comment rendre compte de la densité relique de MN observée aujourd'hui dans l'Univers dans de tels modèles, c'est-à-dire dans des modèles qui présentent une structure générique composée de trois populations de particules (le Modèle Standard, la MN et le médiateur) connectées les unes aux autres au travers de trois interactions résultantes de deux couplages fondamentaux entre particules. Il apparaît que cela peut être fait selon cinq manières dynamiques différentes qui donnent lieu à neuf régimes de production de la MN dont quatre sont nouveaux. Ces nouveaux régimes de production sont pertinents pour la situation où les particules du secteur caché ne sont pas en équilibre thermique avec les particules du secteur visible.

Nous étudions ensuite plus en détail la possibilité d'un secteur caché qui n'est pas thermiquement connecté au secteur visible, en déterminant en particulier l'espace des paramètres autorisé pour des candidats de MN thermaux en termes du ratio des températures des deux secteurs et de la masse de la MN. Nous montrons ensuite que si les deux secteurs ne sont pas thermalement connectés, les deux modèles simples de portails que nous considérons permettent de diminuer les tensions à courtes échelles tout en offrant des candidats de MN viables. Enfin, nous proposons et explorons d'autres modèles minimaux de MN auto-interagissante qui satisfont aux nombreuses contraintes de manière consistante.

MOTS-CLÉS: Matière noire, secteur caché, auto-interactions, médiateur léger, mécanisme de production, portail.

Acknowledgements

Au travers de ces quelques lignes, je souhaiterais remercier chaque personne qui aura directement ou indirectement contribué à ce travail, en commençant, bien sur, par mon promoteur Thomas Hambye. Durant ces cinq dernières années, il m'aura énormément appris, tant d'un point de vue professionnel que personnel. Depuis le premier jour, il a pris son rôle à coeur en m'enseignant tout ce qu'il pouvait, en me guidant dans ce monde qui m'était alors totalement inconnu, sans jamais s'impatienter. Il m'a fait découvrir le monde de la recherche, ses obligations, ses opportunités, ses voyages et les incroyables rencontres qui y sont liées. Grâce à lui, j'ai le sentiment d'avoir vécu mes années de thèse à fond et n'ai aucun regret. I also warmly thank Laura Lopez-Honorez, Riccardo Argurio, Michele Redi and Kai Schmidt-Hoberg, the members of my jury for agreeing to read my manuscript and for the useful remarks and comments they have made during the private defense.

Je tiens également à remercier l'ensemble des membres du Service de Physique Théorique qui m'a accueilli durant toute la durée de mon mémoire de fin d'étude et de mon doctorat. Je pense notamment à Michel Tytgat avec qui j'ai eu le plaisir de collaborer plusieurs fois, à Petr Tyniakov grâce à qui j'ai pu participer à l'encadrement du cours de relativité restreinte, à Laura Lopez-Honorez pour avoir apporté tant de bonne humeur et de dynamisme au quotidien et enfin à Jean-Marie Frère qui aura contribué à mon apprentissage. Je n'oublie évidemment pas Isabelle Renders et Sarah Bouzerda qui m'ont aidées à maintes reprises au sujet de tâches administratives qui m'étaient parfois obscures. I thank everybody I met during my thesis in the group: Iason, Aritra, Deanna, Marco, Mikhail, Xunjie, Quentin, Sam, Baptiste, Raghuveer, Yoann, Mikaël, Daniele, Julian and many more. Let thank also Camillo, Chaïma, Rupert, Matteo and Jérôme, my collaborators, which all helped me to be the physicist I became.

Durant ma thèse et mes années passées à l'ULB, j'ai eu la chance de rencontrer et côtoyer bon nombre de personnes qui ont permis de transformer un quotidien parfois répétitif en des instants inoubliables. Je pense à toutes ces VUB et interminables pauses cafés passées avec notamment Martin, Adrien, Béa, Pawel, Louis, Daniel, Romain, Colin, Quentin, Je retiendrai tout particulièrement Bilal, Antoine, Jérôme et Tanguy sans qui ces années à l'ULB n'auraient jamais pu être aussi extraordinaires. Je ne compte plus les heures passées aux salles d'étude, salles de repos, cafés, restaurants, billards à discuter de tout et de rien, à divaguer mais surtout à nous soutenir les uns les autres. Leur amitié durant mes études et ensuite durant ma thèse restera inoubliable.

Ma passion pour la physique est née bien avant d'entrer à l'université, grâce notamment à ma rencontre avec Salahdin, lorsque nous avions dix ans environ. Nous nous sommes tout de suite parfaitement entendus et n'avons jamais cessé depuis de parler de physique et de sciences en général. Bien que nos chemins se soient quelques peu éloignés, il a toujours su éveiller ma curiosité et entretenir ma passion pour la physique, pour ça et pour notre longue amitié, je lui serai éternellement reconnaissant.

Sans aucun doute, ma famille a joué un rôle primordial dans l'accomplissement de cette thèse. Que ce soit Bruno, Isabelle, Catherine, Papa ou Maman, vous avez tous toujours cru en moi. Jamais vous n'avez douté et ce même lorsque j'ai pu traverser des moments plus difficiles. Tantôt tour à tour, tantôt à l'unissons, vous avez tous su me remotiver et me montrer comment grandir, comment passer au-dessus des épreuves. Vous avez et êtes toujours des exemples pour moi, c'est donc pour moi une immense fierté de pouvoir enfin vous présenter ma thèse, mon travail. Le "petit" ne l'est peut-être plus tant que ça finalement ...

Enfin, je finirai ces lignes en remerciant ma compagne (et presque épouse!) Élise qui, sans le moindre doute, m'aura été et m'est toujours d'un grand soutien. Depuis notre rencontre, tu es derrière moi, me motives, me forces à me dépasser et ce comme nul autre n'a pu le faire. Tout en suivant ton propre chemin, en menant de longues et passionnantes études, tu as su m'épauler en y mettant du coeur et de l'énergie. Il est certain que sans toi à mes côtés, je ne serais jamais arrivé là où j'en suis aujourd'hui. Grâce à toi, j'ai également rencontré ta famille, Alain, Evelyne et Christophe qui eux aussi m'auront soutenu et motivé, notamment en s'intéressant à ma thèse malgré le sujet plus qu'abstrait mais aussi en suivant mon parcours de près et en me conseillant. Pour ça, encore merci.

Contents

Abstract	iii
Résumé	v
Acknowledgements	vii
Introduction	1
 I The Self-Interacting Dark Matter with light mediator problematic	 7
1 SIDM with a light mediator: a highly constrained scenario	9
1.1 Gravitational evidences for DM	9
1.1.1 Velocities in galaxy clusters	9
1.1.2 Rotation curves	11
1.1.3 Bullet cluster	12
1.1.4 Cosmic Microwave Background	14
Hydrogen recombination	14
Optical depth and photons decoupling	18
CMB anisotropies	20
Relic density	22
1.2 Dark Matter relic density	25
1.2.1 The Boltzmann equation	25
1.2.2 Freeze-out case	28
1.2.3 Freeze-in case	29
1.3 Small scale structure	32
1.3.1 Too-big-to-fail	32
1.3.2 Core-vs-cusp	32
1.3.3 Diversity	34
1.3.4 DM hidden sector and portals	34
Benchmark model A: Higgs portal DM model	36
Benchmark model B: Kinetic Mixing portal DM model	37
1.3.5 Dark matter self-interaction cross section	41

1.4	Cosmic microwave background	43
1.4.1	CMB constraint on DM annihilation rate	43
1.4.2	CMB constraints on mediator decay	45
1.4.3	CMB constraint on N_{eff}	46
1.5	Big bang nucleosynthesis	47
1.5.1	Production of light nuclei	48
1.5.2	Photodisintegration BBN constraints	51
1.5.3	BBN constraints from modification of the Hubble constant and entropy injection	51
1.6	Supernovae 1987a	52
1.7	Direct detection	54
1.8	Indirect detection	60
1.9	Production at colliders	62
1.10	A global picture	63
2	The Sommerfeld effect	65
2.1	Self-scattering case	66
2.1.1	The dimensionless Schrödinger equation	66
2.1.2	Relic density requirement for a freeze-out	70
2.1.3	Dark Matter self-interactions	71
2.1.4	Smaller annihilation cross section	76
2.2	Effect of the Sommerfeld effect on DM annihilations	77
2.2.1	The Sommerfeld factor	79
2.2.2	s-wave annihilation	80
2.2.3	p-wave annihilation	82
II	DM production and Hidden Sector	87
3	Dark Matter production mechanisms	89
3.1	The three sectors and their connections	89
3.2	Phase diagram of dark matter production	90
3.2.1	Set of Boltzmann equation	94
3.2.2	Freeze-in: regimes Ia and Ib	101
3.2.3	Sequential freeze-in: regime II	105
3.2.4	Reannihilation: regimes IIIa and IIIb	107
3.2.5	Secluded freeze-out: regimes IVa and IVb	111
3.2.6	Freeze-out: regimes Va and Vb	112
3.3	Specificity of the vector portal model	114
3.3.1	Thermal effects	114
3.3.2	Freeze-in regimes	118

3.3.3	Sequential freeze-in regime	119
3.3.4	Reannihilation regimes	119
3.3.5	Secluded freeze-out regimes	119
3.3.6	Freeze-out regimes	120
3.4	Specificity of the scalar portal model	120
3.4.1	The broken phase	121
3.4.2	The semi-broken phase	122
3.4.3	The symmetric phase	123
4	Thermally disconnected HS	127
4.1	Theoretical constraints	128
4.1.1	Relativistic decoupling floor	128
4.1.2	Unitarity wall	130
4.1.3	Thermalised Hidden Sector requirement	134
4.1.4	Thermal DM mass range	137
4.2	Observational constraints	140
4.2.1	N_{eff}	140
4.2.2	Free-streaming constraints	144
4.3	The 2D domain	146
4.4	Explicit models in the 2D domain	147
4.4.1	Scenario 1 : t-channel	148
4.4.2	Scenario 2: s-channel	149
4.4.3	The role of the heavy mediator	150
III	Self-Interacting Dark Matter ways-out	155
5	SIDM in a colder Hidden Sector	157
5.1	Hidden sector temperature	157
5.2	Portal strength to the visible sector	161
5.3	Constraints	163
5.3.1	CMB	163
	DM annihilation rate	163
	Mediator decay	164
	N_{eff}	165
5.3.2	BBN	166
5.3.3	Direct detection	167
5.3.4	Indirect detection	168
5.4	Summary plot	168
5.4.1	Kinetic mixing portal	168
5.4.2	Higgs portal	169

5.5	What if no portal at all?	171
6	Additional minimal solutions for SIDM	173
6.1	Subleading DM annihilation into light mediators	173
6.1.1	CMB	177
6.1.2	BBN	177
6.1.3	Direct detection	178
6.1.4	Indirect detection	179
6.1.5	Detailed results	179
6.2	The p-wave option	181
6.2.1	CMB	182
6.2.2	BBN	183
6.2.3	Direct detection	184
6.2.4	Indirect detection	184
6.2.5	Results	184
6.3	Stable mediator option	185
6.3.1	Non-overclosure	189
6.3.2	CMB	189
6.3.3	BBN	189
6.3.4	Direct detection	189
6.3.5	Indirect detection	189
6.4	The neutrino option	190
6.5	The asymmetric dark matter option	191
	Summary and outlooks	193
IV	Appendices	197
A	Cross sections	199
A.1	Higgs portal	199
A.2	Kinetic mixing	200
B	Thermal effects	203
C	Instantaneous freeze-out approximation	209
C.1	The thermally connected HS case	209
C.2	The thermally disconnected HS case	210
C.3	Further the instantaneous freeze-out approximation	211
	Bibliography	213

List of Figures

1.1	Velocity of stars in NGC 6503 as a function of their distance to the centre	11
1.2	Illustration of the offset between interacting and non-interacting matter after a cluster collision	12
1.3	Representation of the Bullet cluster	13
1.4	Last scattering surface	15
1.5	Fraction of free electrons in the Universe as a function of the redshift	18
1.6	Flux of photons going through an electron gas	19
1.7	Visibility function as a function of the redshift	20
1.8	CMB temperature anisotropies spectrum	23
1.9	Energy density content of the Universe	24
1.10	Representation of an open/flat/closed Universe	24
1.11	DM yield time evolution in a freeze-out scenario	29
1.12	DM relic abundance as a function of the cross section	30
1.13	DM yield time evolution in a freeze-in scenario	31
1.14	Circular velocity of satellite galaxies as a function of their distance to the galactic centre	33
1.15	Rotation curve of DDO 154 and core versus cusp galaxy profile . . .	34
1.16	Couplings between the DM and the mediator (left), and between the mediator and the visible sector (right) in the symmetric phase	36
1.17	Couplings between the DM, the mediator and the visible sector in the broken phase	38
1.18	Couplings between the DM, the mediator and the visible sector for a massless dark photon	39
1.19	Couplings between the DM, the mediator and the visible sector for a massive dark photon	40
1.20	Self interaction constraints for a Dirac DM and a vector or a scalar mediator	42
1.21	CMB upper bound on the s-wave annihilation rate into light mediators cross section	44
1.22	Upper bound on the amount of mediator particles there would be today if there were no decay	46

1.23	Upper bound on the amount of mediator particles there would be today if there was no decay from the N_{eff} constraint	48
1.24	Time evolution of abundances of light nuclei produced during BBN .	50
1.25	Upper bound on the amount of mediator particle there would be today if there was no decay from the BBN constraint	52
1.26	Constraints from observation of SN1987A for the vector portal model and the scalar portal model	53
1.27	Upper bound on the DM-nucleon collision spin-independent cross section for a contact interaction from Xenon1T	55
1.28	Feynman diagrams of DM elastic scattering on nucleus.	57
1.29	Comparison of DM scattering on nucleon differential rate between short and long range interactions	58
1.30	Direct detection constraints for an interaction mediated by a light mediator	60
1.31	Indirect detection constraints on the DM annihilation cross section .	61
1.32	Illustration of tensions between all observations on SIDM with light mediator	64
2.1	Illustration of the Sommerfeld effect for a two-to-two process	65
2.2	Feynman diagram of DM annihilation	71
2.3	Contour of the DM-to-med coupling in the DM versus mediator mass plane	72
2.4	Ladder diagram of a DM self-scattering process in the scalar portal model	72
2.5	Ladder diagrams of a DM self-scattering process in the vector portal model for the attractive and the repulsive contributions	73
2.6	Contour of the self-scattering cross section divided by the DM mass for the scalar and vector portal models	73
2.7	Contour of the self-scattering cross section divided by the DM mass for the scalar and vector portal models for a subdominant DM component	78
2.8	Sommerfeld factor for s-wave annihilation	81
2.9	Sommerfeld factor for p-wave annihilation	83
2.10	Sommerfeld factor times the velocity squared for p-wave annihilation	84
2.11	DM annihilation cross section with and without the Sommerfeld factor as a function of the DM mass for annihilation in the Milky way and in dwarf galaxies	86
3.1	The three sectors and their three connections for the vector and scalar portal models	90

3.2	The three sectors and their two connections for the kinetic mixing portal model	90
3.3	Feynman diagram of DM annihilation into SM fermions	91
3.4	Feynman diagram of DM annihilation into light bosons	92
3.5	Feynman diagram of dominant processes connecting the SM and mediator baths	93
3.6	Vector and scalar portal models global phase space	94
3.7	Schematic representation of all 9 possible DM production regimes in the three sectors three connectors scenario	95
3.8	Couplings required for thermalisation as a function of the DM mass .	98
3.9	Phase space of portal models subdivided by the three thermalisation lines	99
3.10	Dominant processes in the phase space of portal models subdivided by the three thermalisation lines	100
3.11	Qualitative representation of the parameter space of a three sectors three connectors scenario for the regime Ia and Ib	102
3.12	Couplings as a function of the DM mass fixed by the relic density in regime Ia and Ib	104
3.13	Qualitative representation of the parameter space of a three sectors three connectors scenario for the regime II	106
3.14	Couplings as a function of the DM mass fixed by the relic density in regime II	108
3.15	Qualitative representation of the parameter space of a three sectors three connectors scenario for the regime IIIb	110
3.16	Qualitative representation of the parameter space of a three sectors three connectors scenario for the regimes Va and Vb	113
3.17	Couplings as a function of the DM mass fixed by the relic density in regimes Va and Vb	114
3.18	The imaginary part of the dark photon propagator in a medium . . .	115
3.19	Comparison of the evolution of the dark photon and DM abundances, with and without thermal effects on dark photon production	117
3.20	Vector portal model global phase space including thermal effects . .	118
3.21	Couplings as a function of the DM mass fixed by the relic density in regime II including thermal effects	120
3.22	Couplings between the DM, the mediator and the visible sector in the fully broken phase	121
3.23	Couplings as a function of the DM mass fixed by the relic density in the broken phase	122
3.24	Couplings between the DM, the mediator and the visible sector in the broken hidden sector phase	123

3.25	Couplings as a function of the DM mass fixed by the relic density in the semi-broken phase	124
3.26	Couplings between the DM to the mediator and the mediator to the visible sector in the symmetric phase	124
3.27	Values of the DM-to-SM connector to account for the observed DM relic abundance in the symmetric phase in the regime II (green). . . .	125
4.1	Contour of the normalised DM relic abundance in the temperature ratio versus DM mass plane for a relativistic decoupling	130
4.2	Contour of the normalised DM relic abundance in the temperature ratio versus DM mass plane for a non-relativistic decoupling	135
4.3	Schematic behaviour of interaction rates	136
4.4	Contour of the normalised DM annihilation cross section in the temperature ratio versus DM mass plane for a non-relativistic decoupling	138
4.5	Theoretical constraints from the relativistic floor, the unitarity wall and the thermalisation condition on the temperature ratio versus DM mass plane	139
4.6	N_{eff} exclusion area together with the relativistic floor, unitarity wall and thermalisation condition	142
4.7	Free-streaming exclusion area together with the N_{eff} ceiling, the relativistic floor, unitarity wall and thermalisation condition	145
4.8	Domain of thermal DM candidates	146
4.9	Parameter space for DM freeze-out driven by DM annihilating into two dark photons in the t-channel	149
4.10	Parameter space for DM freeze-out driven by DM annihilating into two Dirac fermions in the s-channel mediated by a scalar	151
4.11	Allowed parameter space for a relativistic decoupling in the s-channel	153
5.1	Feynman diagram of DM annihilating into bosons	158
5.2	Temperature ratio as a function of the DM mass for thermally disconnected DM portal models	160
5.3	Contour of the SM-to-med coupling for thermally disconnected DM portal models	162
5.4	Contour of the DM annihilation cross section at CMB for thermally disconnected DM portal models	164
5.5	Summary plot for thermally disconnected vector portal model	170
5.6	Summary plot for thermally disconnected scalar portal model	172
6.1	Summary plot for the subleading DM annihilation scenario - vector portal model	175
6.2	Summary plot for the subleading DM annihilation scenario - scalar portal model	176

6.3	Summary plot for the p-wave scenario	182
6.4	Evolution of relevant annihilation rates in the stable mediator scenario	188
B.1	The imaginary part of the dark photon propagator in a medium . . .	203
B.2	Dispersion relations for transversal and longitudinal modes in the relativistic regime	206
B.3	Time evolution of the dark photon yield with all production contri- butions	208


List of Tables

1.1	Upper bound on the light mediator lifetime from CMB and BBN constraints	49
1.2	Upper bounds on the mixing parameter for four DM masses, based on the correspondence with WIMP exclusion limits	59
5.1	Upper bound on the light mediator lifetime from N_{eff} at CMB for several values of the hidden-to-visible temperature ratio at DM decoupling	166
5.2	Upper bound on the light mediator lifetime from photodisintegration and Hubble constant/entropy injection during BBN for several values of the hidden-to-visible temperature ratio at DM decoupling .	167
6.1	Examples of parameters values which satisfy the various constraints for the vector and the scalar models of the subleading DM scenario .	179
6.2	Summary of how tensions are alleviated in the subleading annihilation option	180
6.3	Examples of parameter values which satisfy the various constraints for a model with two light scalars for the p-wave option	185
6.4	Summary of how tensions are alleviated in the p-wave option	186

List of Abbreviations

BBN	Big Bang Nucleosynthesis
CDM	Cold Dark Matter
CMB	Cosmic Microwave Background
DG	Dwarf Galaxy
DM	Dark Matter
FLRW	Fridemann - Lemaître Robertson Walker
FI	Freeze-In
FO	Freeze-Out
FS	Free-Streaming
HP	Higgs Portal
HS	Hidden Sector
IR	Infrared
KM	Kinetic Mixing
LHC	Large Hadron Collider
MW	Milky Way
MR	Matter-Radiation
NFW	Navarro-Frenk-White
NR	Non-Relativistic
QCD	Quantum ChromoDynamics
SIDM	Self Interacting Dark Matter
SM	Standard Model
VEV	Vacuum Expectation Value
VS	Visible Sector

Introduction

o understand its environment is one of the oldest quests of humanity. In particular, the observations of the sky have been the matter of mystery and questions since the "dawn of time". It has been observed in particular since a very long time that globally, that is to say for large angular scales, the sky looks similar in all directions: the distribution of astrophysical objects looks almost the same. Since then, more and more refined observations did not stop to confirm this isotropy of the Universe. If, to the isotropy, one adds the Copernican principle which says that there is no privileged place in the Universe, one gets the cosmological principle. Hence, the statement that the observable Universe is homogeneous and isotropic at large scale is by today the fundamental principle in cosmology. Furthermore, it has been observed since very long too that the Universe develops more complex structures at small scales: The Earth belongs to our solar system which itself belongs to our galaxy, the Milky Way. In the Universe, many other spiral galaxies, like ours, exist and many of them have already been studied in detail.

Those numerous observations have brought more questions than answers concerning the composition of the Universe. Indeed, Newton's law of gravitation has failed to explain several phenomena observed at various scales from the galactic scale (galaxy rotation curves) to galactic cluster scale (mass distribution in the Bullet cluster, distribution of galaxies) all the way to cosmological scales (Cosmic Microwave Background anisotropies). There are two general ways of solving these issues: either Newton's law is wrong at the relevant scales, or observations are missing "something". The first idea is not favoured because in practice it is very hard to modify Newton's law at these several scales in a consistent way that could account for all these observations at the same time. However, the second idea has been largely investigated this past century and people first named this missing piece of the Universe "Dark Matter" (DM) as J. Oort [1], F. Zwicky [2] and V. Rubin [3] did. Later, it became clear that from cosmological scale observations one also needs "dark energy" on top of DM. According to observations, 26% and 69% of the energy content of the Universe should be due to DM and to dark energy, respectively. Only 5% would then be due to the presence of the ordinary matter we know, as made of protons, neutrons, electrons in stars, and in galactic and inter-galactic gas.

So far, only the gravitational effects that DM induces could be seen, as these effects are necessary to explain the various observations above. However, the microscopic nature of DM "as a particle" is still not established and there are many different possibilities of particle physics realisations. Alternatively, it is not fully ruled out that DM could be made of primordial black holes, massive compact halo objects, To establish what DM is made of is one of the most fundamental research topics in theoretical and experimental physics of the last decades even if the existence and characteristics of this new kind of matter intrigue physicists since almost a hundred years. Of course, as long as we will not establish what DM is made of, we will have no absolute proof for the existence of the DM. However, an extremely impressive series of experiments and a long series of theoretical consistency arguments do constrain already in many ways the properties of the DM particle, if it is made of a new particle. They establish in particular that these particles must be dark (i.e. feebly coupled to the photon) otherwise we would see it, stable (i.e. a lifetime larger than the age of the Universe) otherwise it would not be present today, be highly non-relativistic today and do not interact much with ordinary matter.

In the following, we will assume that the DM is made of a new particle, which is by far the most plausible of all possibilities. The mass of the DM particle is still very poorly constrained. It could go all the way from a tiny fraction of eV to the Planck scale ($\sim 10^{19}$ GeV). However, its interactions are more constrained. For example, DM candidates which have electroweak interactions are already excluded or highly constrained [4]–[17] by many particle physics experiments (direct detection, indirect detection, colliders). These numerous constraints are such that the standard Weakly Interacting Massive Particle (or WIMP) scenario which used to be the main possibility for explaining the DM relic density becomes more and more disfavoured. Hence, the lack of proof of the existence of DM in particle physics experiments tends to suggest that it could be neutral under all SM gauge groups, in other words, it is a singlet of the $SU(3)_c \times SU(2)_L \times U(1)_Y$ SM fundamental interactions. Pushing this principle to its limit, DM particles would be insensitive to all SM particles except through gravity and would form a separate sector evolving on its own. One can then distinguish the "Visible Sector" (VS) made of all SM particles and the "Hidden Sector" (HS) made of DM particles and possibly other particles. Indeed, without any additional symmetry, there is nothing which forbids the DM to have other interactions, typically new gauge interactions in the new sector, the HS. Hence, the HS could be much more complex than if it was just composed of DM particles and could be ruled by new interactions and/or new gauge symmetries. All particles of the VS would be a singlet of all HS gauge groups as all HS particles are singlets of all SM gauge groups such that the only already established interaction that would couple the two sectors is gravity.

If there is no additional connection other than gravity between the VS and the HS, this would be the end of the story as to see the DM particles through gravity is presumably almost impossible. Alternatively, the existence of a portal between the two sectors, i.e. a new renormalisable (or not) interaction which couples to a singlet combination of the particles of the two sectors at the same time, is perfectly possible. Hence, in such scenarios, DM particles are connected to the VS thanks to this additional interaction, the portal, and thus one can hope that through this portal one could constrain and/or detect DM particles. A DM candidate living in a HS and talking to the VS through a portal can be seen as an extension, a generalisation [18]–[35] of the traditional WIMP scenario, as we will see below. The idea of a DM candidate being part of a HS and coupling to the VS through a portal has already been suggested long ago in scenarios of the "mirror DM" type in which the HS is a copy of the VS. There are, in these specific mirror DM frameworks, many different ways to account for the DM relic abundance, see [36]–[40] for more details.

The idea of a new HS is not relevant only for the DM issue, it is a much broader concept which can be relevant for many other purposes. One can cite the Minimal Supersymmetric Standard Model (MSSM) in which a HS is often used for the purpose of breaking supersymmetry, [41]–[44]. More generally, HS also exists in string theories by constructions, see top-down string constructions [45]. On top of the supersymmetric models, one also needs or encounters HS in particle physics models aiming to solve other issues than DM, such as the hierarchy problem, composite Higgs models, see for example [46]–[49].

Another major argument favouring the whole concept of a HS arises when looking at the Universe at small scale. Indeed, the DM hypothesis was introduced in order to explain different phenomena at large scale. However, there also exist inconsistencies observed at small scales (i.e. at galactic scales) which can be solved if the DM undergoes large self-interactions [50]–[83]. A theory of a strongly interacting DM is difficult to build if substantially connected to the VS. Indeed, such strong self-interactions between DM particles could have many imprints on different experiments such as direct detection experiments or could have an impact on astrophysical observations (e.g. supernovae). As a direct consequence, the very simple idea of a relatively strongly interacting HS evolving on its own and feebly coupled to the VS emerges naturally from all possible observations and it seems absolutely necessary to properly investigate this possibility.

All the above brings a series of new questions concerning in particular the portal, "How strongly connected to the VS, the DM can be?", and on the structure of the HS itself, "How strongly self-interacting the HS has to be?". Those two fundamental

questions, albeit not new, are still unclear now. These are the main questions we will ask in this thesis together with the question of knowing how we can account for the observed DM relic density in frameworks based on a HS. Thus, this thesis is all about the dynamics of such models. The aim is really to be able to establish the simple and minimal models of DM connected to the VS through a portal which could answer these questions or, at least, clarify the situation.

The first two chapters, "**Part I**", are essentially introductory. To start this study, in **Chapter 1** we first present all relevant evidences favouring the hypothesis of DM as well as arguments pointing out the possibly self-interacting behaviour of this DM. We will also see how such scenarios are constrained in many ways explaining the physical principles these constraints are based on. To discuss this in a concrete way, we will consider two well-known HS portal models. One is based on a Higgs portal and one on a kinetic mixing portal. These models contain a light mediator in the HS, which is fully relevant for both the DM relic density and the DM self-interactions issues, as we will see. **Chapter 2** will be dedicated to the analysis of the Sommerfeld effect, which is a physical phenomenon highly relevant for all these constraints especially for having large enough self-interactions thanks to the presence of the light mediator. The next two chapters, "**Part II**", concern essentially the DM relic density issue in HS frameworks. In **Chapter 3** we will see both qualitatively and quantitatively how this needed HS can be produced and along which dynamical production mechanisms. We investigate the full allowed parameter space of a generic thermal DM candidate living within a HS in **Chapter 4**. In the last two chapters, "**Part III**", we come back to the self-interactions issue proposing ways to fulfil all constraints discussed in Part I. In **Chapter 5**, we propose a solution which is based on chapter 4: a HS which thermalises within itself, but not with the VS thermal bath. The last chapter, **Chapter 6** will allow us to explore other minimal solutions which are also perfectly compatible with the idea of a HS. Finally, we draw our conclusions.

Before going deeper in the subject of this work, we give here the list of preprints and published articles, sorted by chronological order, on which this thesis is based:

- T. Hambye, M. H. G. Tytgat, J. Vandecasteele, and **L. Vanderheyden**, "Dark matter direct detection is testing freeze-in", *Physical Review D*, vol. 98, no. 7, p. 75017, 2018.
DOI : 10.1103/PhysRevD.98.075017 - arXiv: 1807.05022.
- T. Hambye, M. H. G. Tytgat, J. Vandecasteele, and **L. Vanderheyden**, "Dark matter from dark photons: a taxonomy of dark matter production", *Physical Review D*, vol. 100, no. 9, p. 95018, 2019.
DOI : 10.1103/PhysRevD.100.095018 - arXiv: 1908.09864.

- T. Hambye and **L. Vanderheyden**, "Minimal self-interacting dark matter models with light mediator", *Journal of Cosmology and Astroparticle Physics*, vol. 05, 001, 2020.
DOI : 10.1088/1475-7516/2020/05/001 - arXiv : 1912.11708.
- M. Lucca, T. Hambye and **L. Vanderheyden**, "Dark matter as a heavy thermal hot relic", *Physics Letters B*, vol. 807, p. 135553
DOI : 10.1016/j.physletb.2020.135553 - arXiv : 2003.04936
- R. Coy, T. Hambye, M. H. G. Tytgat, and **L. Vanderheyden**, "The domain of thermal dark matter candidates"
DOI : [Submitted in PRD] - arXiv: 2105.01263.
- **L. Vanderheyden**, "Dark matter from dark photons", [Contribution to the 2021 EW session of the 55th Rencontres de Moriond]
DOI : / - arXiv: 2105.07039.

There is another published article that we did not discuss in this thesis as it concerns a work did during my master thesis and is not directly related to HS nor to self-interacting DM scenarios. However, one can learn more about neutrino line produced by DM annihilation in:


- C. El Aisati, C. Garcia-Cely, T. Hambye, and **L. Vanderheyden**, "Prospects for discovering a neutrino line induced by dark matter annihilation", *Journal of Cosmology and Astroparticle Physics*, vol. 10, 021, 2017.
DOI : 10.1088/1475-7516/2017/10/021 - arXiv : 1706.06600

Part I

The Self-Interacting Dark Matter with light mediator problematic

Chapter 1

SIDM with a light mediator: a highly constrained scenario

 In this first introductory chapter, we will review the main constraints applying on self-interacting DM scenarios (SIDM) starting with historical evidences which brought the whole idea of DM and of SIDM. The following discussion is based on already well-established works as well as on personal contributions which have been published [84], [85].

1.1 Gravitational evidences for DM

In the first half of the twentieth century, two physicists pointed out that we could have missed a large proportion of the gravitational mass of the observable Universe. The Dutch Jan Oort and the Swiss Fritz Zwicky studied the velocity of extra-galactic objects and found inconsistencies with Newton's law of gravity. While the first one studied the motion of stars in galaxies and the second the motion of galaxies in the Coma cluster¹, they both used the Doppler shift to determine the velocity of these luminous objects.

1.1.1 Velocities in galaxy clusters

The rotation velocity of galaxies in such clusters is not arbitrary. Starting from Newton's law and Virial's theorem, one gets that the time average of the kinetic energy of all particles in a system (the particles are galaxies in the study of Zwicky) is equal to the opposite of the time average of the potential energy of the same particles,

$$\left\langle \sum_i m_i |\vec{v}_i|^2 \right\rangle = - \left\langle \sum_i \vec{r}_i \cdot \vec{F}_i \right\rangle, \quad (1.1)$$

¹A cluster is a group of galaxies bounded by gravity.

where the brackets “ $\langle \rangle$ ” indicate a time average quantity, $m_i, \vec{r}_i, \vec{v}_i$ are the mass, the position and the velocity of the particle (galaxy) i and \vec{F}_i is the total force applying on the particle i . As the observable Universe is homogeneous and isotropic at large scale, such as galaxy cluster scales, and as the distribution of these galaxies in the cluster was presenting a global spherical symmetry, Fritz Zwicky could apply Eq. 1.1 to the gravitational force (i.e. $\vec{F}_i = G \sum_j m_i m_j \vec{r}_{ij} / |\vec{r}_{ij}|^3$)² and easily conclude that velocity of those galaxies within the Coma cluster were inversely proportional to the square root of their distance to the gravitational centre of the cluster. He got,

$$|\vec{v}_i| \propto \frac{1}{\sqrt{|\vec{r}_i|}}. \quad (1.2)$$

He compared velocities obtained by Doppler shift and those obtained with the help of Virial’s theorem and found that velocities did not match at all. Even though his measures were not very accurate, he could qualitatively show that the velocity of galaxies was not decreasing with the distance to the centre of the cluster. He observed that galaxies sitting in the periphery of the cluster were moving with velocity up to three times the one predicted by Newton’s law. He could not figure out how this matter could move so fast without being ejected from the galaxy. Indeed, these observed velocities are much bigger than the predicted ones. If we believe in the theory of Gravitation and if there is nothing we are missing, with such velocities, stars should have been ejected of galaxies since a long time ago! We have then two solutions: either there is a physical phenomenon, totally unknown, which we are missing, or gravitation’s law have to be modified at these relevant scales but unchanged at larger scale (where predictions match with observations). On the one hand, changing gravitation’s law at several scales in a consistent way that could account for all observations at the same time is a very challenging option. Until now, this was not successful and there is no clue for this being actually possible. On the other hand, one can easily imagine that, for the first option, if there were more massive objects inside the virtual sphere of radius r_\star ³, the gravitational attraction would be much stronger and this could simply explain why stars are not ejected outside galaxies. Thus, Zwicky understood that a simple way for his observations to match with the predicted velocities was to assume that there was additional gravitational mass within the cluster. He named this missing mass *Dunkle Materie* (Dark Matter or DM) [2] as it was invisible, see also [1]. It was one of the very first time, the idea of DM was introduced. Since Oort and Zwicky many scientists worked on this topic and performed the same measurement on many more objects with more and

²Where we define $\vec{r}_{ij} \equiv \vec{r}_i - \vec{r}_j$ and where the gravitational constant is $G = 6.674 \times 10^{-11} \text{ m}^3 \text{ kg}^{-1} \text{ s}^{-2}$.

³ r_\star being the distance to the cluster centre of a chosen galaxy which appears to move fast.

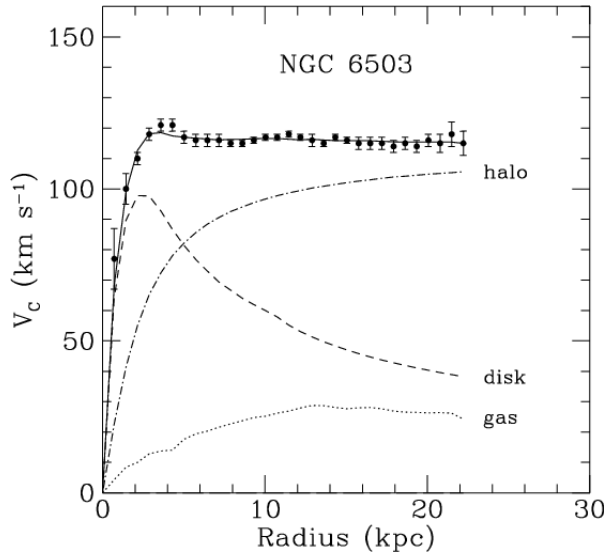


FIGURE 1.1: Velocity of stars in NGC 6503 as a function of their distance to the centre, see [86]. The dots show data points extracted from observations while the lines indicate what should be expected for a galaxy made of a gas (dotted), a disk of matter (dashed) or a halo of DM (dot-dashed).

more precision. This leads us to the very first quantitative evidence for DM, galaxy rotation curves.

1.1.2 Rotation curves

Vera Rubin [3], an American physicist, was the first to perform a precise analysis of galaxy rotation curves and could quantify for the first time the discrepancies. Her measurements of the mass-to-luminosity ratio show that there is about five times more mass than expected from visible matter. As an example, Figure 1.1 shows measured velocities (dots) of stars in NGC 6503 (taken from [86]), predicted velocities for visible matter, gas and a halo of DM are respectively shown in dashed, dotted and dot-dashed. One can see that, for this galaxy, introducing a halo of additional matter interacting only through gravity would explain the observed curve. At the time of those first quantitative measurements, this was only an example, for now, many more galaxies have been studied in great details and most of them are suggesting additional invisible matter (see e.g. [87], [88] and papers therein).

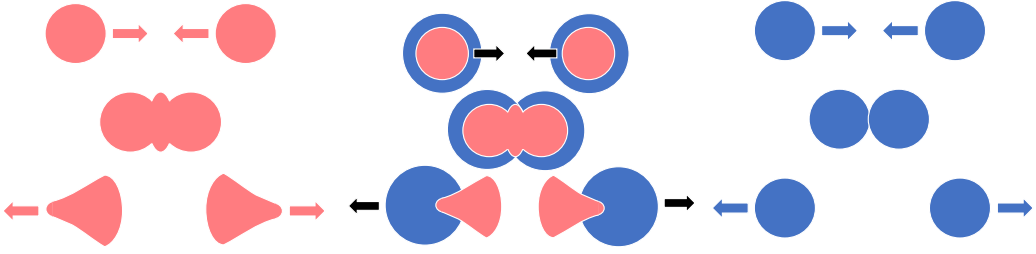


FIGURE 1.2: Illustration of the offset between interacting (red) and non-interacting (blue) matter after a cluster collision.

1.1.3 Bullet cluster

The introduction of DM from the rotation curves argument may seem a little bit artificial or even unconvincing, albeit chronologically the first one, but this argument is far to be the only one. A little bit less than twenty years ago, the space telescope Chandra has observed vestiges of galaxy collisions in the Bullet cluster. Again, observations pointed out existence of additional invisible matter interacting only through gravity. In order to understand how such observations led to this conclusion, let us first resume how objects made of visible matter collide. Imagine two spheres of matter which are attracted to each other because of gravity, if these spheres are made of interacting matter, they can interact and there will be many impacts during collision between constituents. After the collision, shapes will be highly modified due to these impacts, this is represented in red in Figure 1.2. If these spheres interact only through gravity (as it is supposedly the case for DM or stars), there will be no contact interaction and spheres will only go through each other without actually "seeing" the other one. Shapes will remain spherical after the collision since the gravitational interaction is much feebler than all other interactions⁴ (see blue in Figure 1.2).

If both visible and invisible matter are present, even if the centre of mass of both kind of matters remains unaffected after the collision, one should expect a shift between distributions of visible and invisible matter after the collision. In other word, if one is able to determine the centre of mass of the entire system (= visible and invisible matter), one should see that it is aligned with the centre of mass of stars and not with the centre of mass of the supposedly dominant component of the cluster, the gases. This is exactly what the space telescope Chandra observed in 2005 [89], [90], see Figure 1.3.

⁴The strength of the electromagnetic force between two protons is $\sim \mathcal{O}(10^{36})$ stronger than the strength of the gravitational force at the same distance.

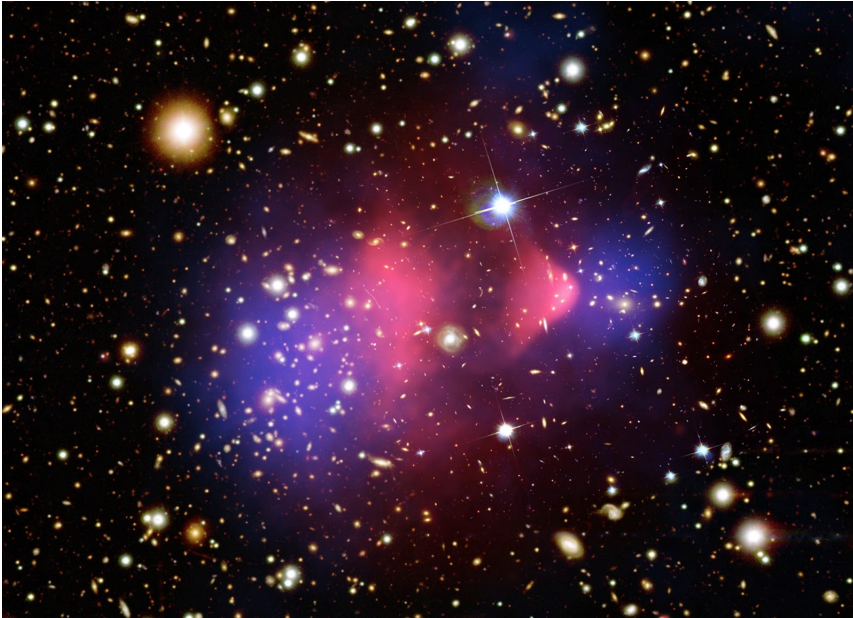


FIGURE 1.3: Representation of the Bullet cluster. The pink area shows X-ray emission from visible matter while the blue area shows a reconstruction of the total mass from measurements of gravitational lensing. Credit: X-ray: NASA/CXC/CfA/ M.Markevitch et al.

Figure 1.3 shows reconstructed data measured by the Chandra telescope. It represents a collision of galaxies in the Bullet cluster. Galaxies are made of stars and gas, but as distances between stars are huge, they never interact with each other and the stars distributions remain the same after the collision. However, the gases were playing the role of the interacting matter in Figure 1.2 and the gas distribution was modified due to the collision tending to remain closer to the centre of the all system, according to Chandra measurements. Thanks to the gravitational lensing, the collaboration was able to measure the offset between the centre of mass of the luminous matter and the centre of gravity of the whole matter distribution. Indeed, the gravitational lensing techniques use a light property which is known since Einstein's theory of general relativity. In this framework, it is not only the mass energy which interacts with gravity but the whole energy content of an objects. Thus, even a light beam (made of massless particles, the photons) would be bended when passing close to massive objects. This bending intensity will be directly related to the mass of the gravitational source around which the light beam is travelling. One very powerful application of this effect is that if there is a luminous source behind (with respect to us) a massive (visible or invisible) object, one can determine the

mass of this object by measuring the bending intensity of the light coming from behind the massive object. It is thanks to this technique that the distribution of invisible matter has been determined and that the offset between luminous matter and non-luminous matter in the Bullet cluster has been resolved.

Moreover, it has also been shown that this very same offset cannot be explained by a modification of the theory of gravity [90] such that the favoured conclusion of the Chandra collaboration results were the existence of DM.

1.1.4 Cosmic Microwave Background

We will now review the whole physics behind the Cosmic Microwave Background or CMB and we will see how its measurement today gives an additional strong hint for the existence of DM.

Hydrogen recombination

During the early Universe epoch, the temperature was so high that atoms could not stay bounded for long. Every time an electron (e^-) and a proton (p^+) interact together to form a bound state, a hydrogen atom (H), the very high kinetic energy of the bound state was high enough to make it unstable and break it. The Universe was then mostly composed of charged particles (electrons and protons⁵) and photons (γ) always interacting strongly with the medium. But, as we learned from the Universe expansion, the temperature eventually dropped below the hydrogen ionisation temperature. The corresponding process (see Eq. 1.3) frozen out and photons decoupled from the thermal bath (finally composed of neutral particles), evolving freely. The Universe became transparent. This is known as the recombination. This last emission happened when Universe's temperature was about the hydrogen ionisation energy, $E_I^H = 13.6$ eV, or actually $\simeq 0.3$ eV because at the time there were already many more photons than electrons and protons so that the dissociation process stopped later than 13.6 eV.

$$e^- + p^+ \leftrightarrow H + \gamma \quad (1.3)$$

Photons which decoupled from the early Universe were then able to pursue their travel following the direction and the distribution they had just after their last scattering process. They compose the so called CMB and can be detected today. The last scattering surface is the "picture" of the actual measurement of the temperature of those photons. Figure 1.4 shows the CMB temperature distribution measured today

⁵There were also light nuclei like we will see in the section dedicated to BBN, see Section 1.5. However, this has a negligible impact in this context.

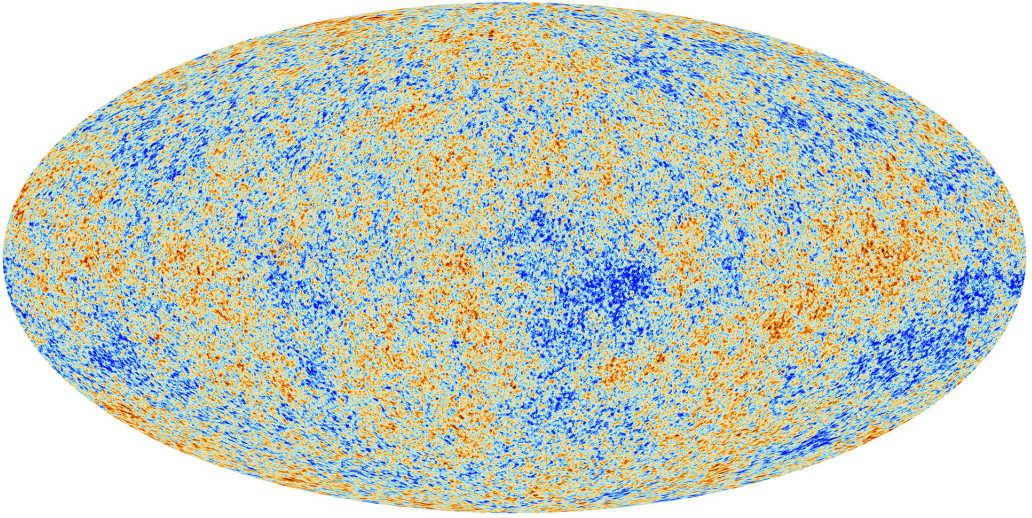


FIGURE 1.4: Last scattering surface seen by the Planck collaboration.
Taken from [91]

by the Planck collaboration (picture taken from [91]).

In order to understand this picture, let us review the physics behind it. Making the hypothesis that the recombination was dominated by the hydrogen, Eq. 1.3. At very high temperature, when $T \gg E_I^H$, all particles involved were in chemical equilibrium, and we had then the following relation between chemical potentials: $\mu_e + \mu_p = \mu_H + \mu_\gamma$, with μ_x the chemical potential of the x species. If these quantities can take many different values in general, the photons chemical potential is always zero due to the non-conservation of the photon number⁶. When the temperature reached the hydrogen ionisation energy, $T \simeq E_I^H$, the freeze-out of this process happened. At this moment, since all massive particles involved in the process (e , p and H) had their mass being larger than the temperature ($m_H \simeq m_p \gg m_e \gg T \simeq 0.3$ eV), they all were non-relativistic and were following a Maxwell-Boltzmann distribution. The photons, as massless particles, are of course relativistic and follow the Bose-Einstein distribution, we write

⁶Looking at the following process: $e^- + \gamma \leftrightarrow e^- + \gamma + \gamma$. We have then $\mu_e + \mu_\gamma = \mu_e + 2\mu_\gamma$ which implies that $\mu_\gamma = 0$.

$$n_x = g_x \left(\frac{m_x T}{2\pi} \right)^{3/2} e^{-\frac{m_x - \mu_x}{T}}, \quad \text{for } x = e^-, p^+, H, \quad (1.4)$$

$$n_\gamma = g_\gamma \frac{\zeta(3)}{\pi^2} T^3, \quad (1.5)$$

where $\zeta(3) \simeq 1.202$ and with m_x and g_x the mass and the degrees of freedom of the x species respectively. Moreover, since we have $E_I^H \equiv m_H - m_p - m_e$ and $m_p \simeq m_H$, one can write Saha's equation,

$$\left(\frac{n_e n_p}{n_H} \right)_{eq} \simeq \eta \left(\frac{m_e T}{2\pi} \right)^{3/2} e^{-E_I^H/T}, \quad (1.6)$$

where the "eq" subscript refers to quantities taken at equilibrium and where the baryon-to-photon ratio is given by $\eta \equiv \frac{n_B}{n_\gamma}$ in terms of the baryonic number which is approximately given by $n_B \simeq n_p + n_H$ since there were almost no other baryon at this time.

We can look at the degree of ionisation of the bath by comparing the amount of (free) protons and hydrogen atoms (bounded protons) evolving in the bath: $X \equiv \frac{n_p}{n_p + n_H}$. This number can be related to the baryon-to-photon ratio, we have: $X \simeq \frac{1}{\eta} \frac{n_p}{n_\gamma}$. Assuming the photons kinetic equilibrium and adding the neutrality requirement⁷ (i.e. $n_e = n_p$), we finally get,

$$\frac{X_{eq}^2}{1 - X_{eq}} = \frac{\sqrt{\pi}}{4\sqrt{2}\eta\zeta(3)} \left(\frac{m_e}{T} \right)^{3/2} e^{-E_I^H/T}. \quad (1.7)$$

In order to describe the photons decoupling, one can use a tool that we will develop in more details in Chapter 3, known as Boltzmann equation (Eq. 1.33) for electrons, protons and hydrogen atoms. In substance, the Boltzmann equation expresses the time evolution of the number density of a given species. It takes into account interactions the species could have and the dilution factor due to the expansion of the Universe. One has,

⁷The Universe appears to be globally neutral today and thus, by charge conservation, was always globally neutral.

$$\frac{dn_e}{dt} + 3Hn_e = n_e^{eq} n_p^{eq} \langle \sigma v \rangle_{ep \rightarrow H\gamma} \left(\frac{n_H n_\gamma}{n_H^{eq} n_\gamma^{eq}} - \frac{n_e n_p}{n_e^{eq} n_p^{eq}} \right), \quad (1.8)$$

$$\frac{dn_p}{dt} + 3Hn_p = n_e^{eq} n_p^{eq} \langle \sigma v \rangle_{ep \rightarrow H\gamma} \left(\frac{n_H n_\gamma}{n_H^{eq} n_\gamma^{eq}} - \frac{n_e n_p}{n_e^{eq} n_p^{eq}} \right), \quad (1.9)$$

$$\frac{dn_H}{dt} + 3Hn_H = n_H^{eq} n_\gamma^{eq} \langle \sigma v \rangle_{ep \rightarrow H\gamma} \left(\frac{n_e n_p}{n_e^{eq} n_p^{eq}} - \frac{n_H n_\gamma}{n_H^{eq} n_\gamma^{eq}} \right), \quad (1.10)$$

where $\frac{d}{dt}$ refers to the time total derivative while $H \equiv \frac{1}{a} \frac{da}{dt}$, the Hubble parameter, is the total expansion rate of the Universe with a the scale factor. From Eqs. 1.8-1.10, neutrality, photons kinetic equilibrium and matter conservation⁸, we have

$$\frac{dX}{dt} = \langle \sigma v \rangle_{ep \rightarrow H\gamma} \left(n_b \frac{X_{eq}^2}{1 - X_{eq}} (1 - X) - X^2 n_b \right). \quad (1.11)$$

The cosmological redshift z , which is defined as the ratio of the observed wavelength and the emitted wavelength $1 + z \equiv \lambda_0 / \lambda$, is often used as a measure of the time. Indeed, because of the expansion of the Universe, objects are moving away to each other. Moreover, thanks to the Hubble law, we also know that more objects are far away from us, more they are moving away quickly. Thus, if one can measure the velocity at which an object is moving away from us, one is able to determine how far it is and thus one is able to determine the age of the image we are seeing. This is again due to the expansion of the Universe. More an object is far more it is old. At the end of the day, the redshift can be related to the age of the Universe (i.e. the time) and one can finally write the time evolution equation (in terms of the redshift) of the degree of ionisation X of the thermal bath in the early Universe

$$\frac{dX}{dz} = C_r \frac{a}{H} [n_b A(z) X^2 - B(z) (1 - X)], \quad (1.12)$$

where we have used the fact that the recombination is the most efficient for a de-excitement from the 2s to the 1s atomic level at a rate of $\Gamma_{2s} \simeq 8 \text{ Hz}$ [92],

⁸The baryonic density Liouville operator has to be null: $dn_b/dt + 3Hn_b = 0$ since there is no source of baryonic matter at this stage.

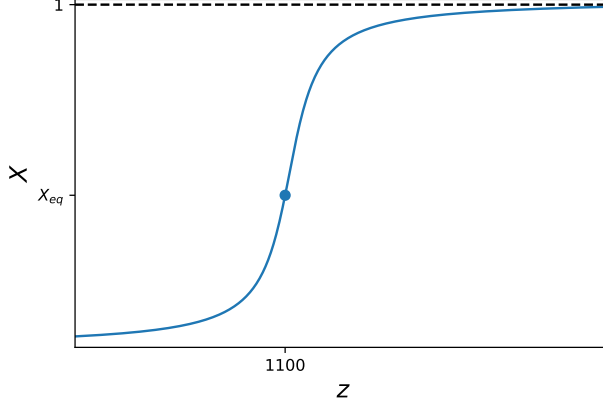


FIGURE 1.5: Fraction of free electrons in the Universe as a function of the redshift.

$$C_r(z) \equiv \frac{\Gamma_\alpha + \Gamma_{2s}}{\Gamma_\alpha + \Gamma_{2s} + B(z)e^{E_I^H/T(z)}}, \quad (1.13)$$

$$A(z) \equiv \langle \sigma v \rangle_{2s} \simeq 9.78 \frac{\alpha^2}{m_e^2} \sqrt{\frac{E_I^H}{T(z)}} \log \left(\frac{E_I^H}{T(z)} \right), \quad (1.14)$$

$$B(z) \equiv \frac{X_{eq}^2}{1 - X_{eq}} A(z) n_b(z), \quad (1.15)$$

with $\alpha \simeq 1/137$ is the fine structure constant and $m_e = 511$ keV. The correcting factor C_r takes into account the possibility of de-excitements from the $2p$ to the $1s$ atomic level and of Lyman α emissions ($\Gamma_\alpha = \frac{9(E_I^H)^2 H}{2(1-X_{eq})n_b}$).

The results of a numerical integration of Eq. 1.12 are shown in Figure 1.5 where we highlighted when $X = X_{eq}$ which is around $z \simeq 1100$. This instant will be taken as the time of recombination: $z_{rec} \simeq 1100$ since it is the time when the fraction of ionised protons drops below its equilibrium value.

Optical depth and photons decoupling

Photons propagation in the early Universe thermal bath is highly related to the number of free electrons, due to the Thomson diffusion: $e^- + \gamma \rightarrow e^- + \gamma$. Above, we have seen that the number of free electrons as a function of the redshift is given by the number of free protons which is related to the fraction number X through the

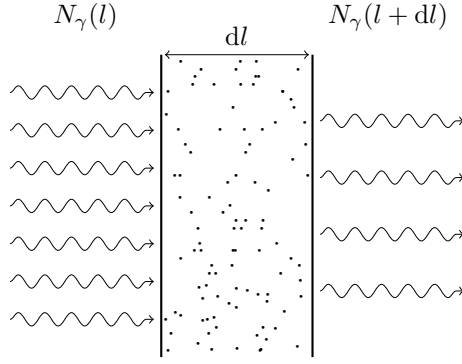


FIGURE 1.6: Flux of photons going through an electron gas of width dl .

baryon-to-photon ratio and the photon number: $n_e(z) = X(z)\eta(z)n_\gamma(z)$.

Let us consider the following picture: a photon flux going through an electron gas, see Figure 1.6. With a good approximation, the number of photons which were unaffected by the electron gas $N_\gamma(l + dl)$ is given by the number of photons before $N_\gamma(l)$ minus the number of photons which have been scattered by the electrons in the gas,

$$N_\gamma(l + dl) = N_\gamma(l) - \sigma_{Thom.} N_\gamma(l) n_e(z) dl, \quad (1.16)$$

where the Thomson diffusion cross section is given by $\sigma_{Thom.} = 8\pi\alpha^2/3m_e^2 \simeq 6.65 \times 10^{-25} \text{ cm}^2$ and where l refers to the depth of the gas. From Eq. 1.16, one gets the evolution equation for the photon number:

$$\frac{dN_\gamma}{dl} = -n_e(z) N_\gamma(l) \sigma_{Thom.} \quad (1.17)$$

which can be converted into a differential equation on N_γ as a function of the redshift z thanks to the relationship between the depth and the redshift ($dz = -Hdl/a$),

$$\frac{dN_\gamma}{dz} = \frac{n_e(z) \sigma_{Thom.}}{(1+z)H(z)} N_\gamma(z). \quad (1.18)$$

This equation can be easily solved and gives,

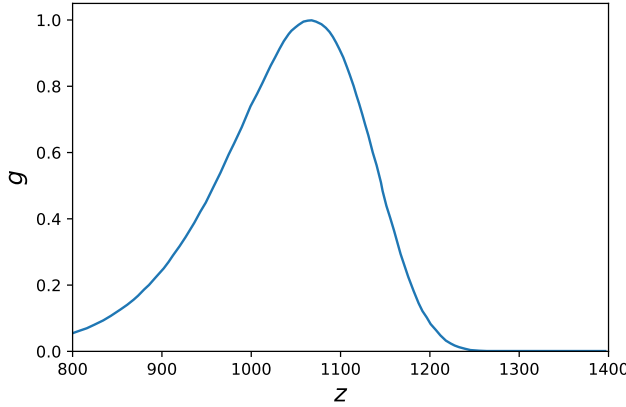


FIGURE 1.7: Visibility function as a function of the redshift.

$$N_\gamma(z) = N_\gamma^0 e^{-\tau(z)}, \quad (1.19)$$

$$\tau(z) = \int_0^z \frac{n_e(x) \sigma_{Thom.}}{(1+x)H(x)} dx. \quad (1.20)$$

The decreasing exponential in Eq. 1.19 represents the probability for a photon to not scatter between $z = 0$ and z . Now, we can define the visibility function $g(z)$ as the probability density for a photon from the CMB to scatter one last time at $z \pm dz$,

$$g(z) \equiv e^{-\tau(z)} \frac{d\tau}{dz}. \quad (1.21)$$

The thickness of the visibility function gives the thickness of the last scattering surface while the position of its maximum gives the moment where it is most probable for a photon to decouple. Both of those characteristics, the last scattering surface thickness and the redshift at recombination, will be observables and will provide strong constraints as we will see in the following.

CMB anisotropies

Eqs. 1.12 and 1.21 give a description of the decoupling and, thus, on how the last scattering surface was formed. Photons emitted from this last scattering surface, known as the CMB as already said above, have a specific spectrum which is measured today by the Planck collaboration. This spectrum gives many crucial information about the Universe from recombination until today. As a simple example, it gives the Earth motion with respect to the CMB. Indeed, there is a Doppler effect

affecting the perception of the CMB on Earth because of its motion such that the speed of Earth in CMB's frame can be extracted from the dipolar term. Taking the Earth motion to be small relatively to the speed of light, this effect is simply given in terms of the Earth velocity v_{\oplus} , the average temperature T_0 and the polar angle θ , by:

$$T \simeq T_0 \left(1 + \frac{v_{\oplus}}{c} \cos \theta + \mathcal{O} \left(\frac{v_{\oplus}^2}{c^2} \right) \right). \quad (1.22)$$

The measurement of the dipolar term gives $\delta T_{dip} = (3.346 \pm 0.017) \times 10^{-3} \cos \theta$ K, in Kelvin. We have then, $v_{\oplus} \simeq 368$ km/s⁹ into the direction $(l, b) = (263.85^\circ, 48.25^\circ)$ where l , the galactic longitude, is the angle between the line of sight and our galaxy plane and b , the galactic latitude, is the azimuthal angle around our galaxy rotation axis, see [93] for more details.

After subtracting the dipolar term, tiny anisotropies were found and are the part of the CMB spectrum we are interested in. These anisotropies are really small as they are of the order of $\sqrt{\langle (\delta T/T_0)^2 \rangle} \simeq 1.1 \times 10^{-5}$ where we defined,

$$\delta T(\theta, \phi) = T(\theta, \phi) - T_0, \quad (1.23)$$

$$T_0 \equiv \frac{1}{4\pi} \int \int T(\theta, \phi) \sin \theta d\theta d\phi, \quad (1.24)$$

with $\theta \in [0; 2\pi]$ and $\phi \in [0; \pi]$ which are the polar and the azimuthal angles respectively (in spherical coordinates). The actual average CMB temperature is known, $T_0 \simeq 2.725 \pm 0.001$ K.

To understand these very small fluctuations, let us develop the CMB angular power spectrum. Taking $\vec{n} \in S^2$ such that $|\vec{n}|^2 = 1$, we can decompose the temperature contrast on the spherical harmonics basis, Y_n^l ,

$$\frac{\delta T}{T_0}(\vec{n}) = \sum_{l=0}^{\infty} \sum_{m=-l}^l A_{lm} Y_n^l(\vec{n}), \quad (1.25)$$

⁹Note that in Eq. 1.22 we explicitly used the light velocity $c \equiv 299792.458$ km/s such that we express the Earth velocity in km/s. However, if not explicitly said, for the rest of this thesis we will fix $c = 1$ such that the velocities given in the following will be expressed in units of c .

where the $A_{lm} \equiv \int d\Omega_{\vec{n}} \frac{\delta T}{T_0}(\vec{n}) Y_{lm}^*(\vec{n})$ are the coefficient associated to the Fourier transform. A very useful statistical tool is given by the two-points correlation function associated to the measured temperature of the CMB. This function encodes how the measured value of the temperature in two different directions \vec{n}_1 and \vec{n}_2 are correlated. This indicates if the temperature distribution is purely random or if there is some correlations even if small. Under the statistical isotropic hypothesis, the two-points correlation function, $C(\vec{n}_1, \vec{n}_2)$, depends only on one parameter, the relative direction: $\mu \equiv \vec{n}_1 \cdot \vec{n}_2$. It can thus be developed on the Legendre polynomial basis, P_l ,

$$C(\mu) = \left\langle \frac{\delta T}{T_0}(\vec{n}_1) \frac{\delta T}{T_0}(\vec{n}_2) \right\rangle \quad (1.26)$$

$$= \sum_{l=0}^{\infty} \frac{2l+1}{4\pi} C_l P_l(\mu). \quad (1.27)$$

Then, one can relate the C_l coefficients to the coefficient of the Fourier transform which form the so-called angular spectrum of temperature anisotropies,

$$\langle A_{l'm'}^* A_{lm} \rangle = C_l \delta_{ll'} \delta_{mm'}. \quad (1.28)$$

Figure 1.8 shows the CMB anisotropies angular power spectrum and its very characteristic shape. One can distinguish clearly a first pic at $l \simeq 200$ and that the curve starts to flatten at $l \gtrsim 1000$.

Relic density

The position and the height of the pics visible in Figure 1.8 depend on the proportion of each ingredient present in the early Universe (baryon, dark matter, dark energy, radiation). Observations of CMB anisotropies indicate that 26% (see Figure 1.9) of the energy content of the Universe has to be in the form of a sector which interacts mostly through gravitational interactions with the rest of the Universe, but which is not ordinary matter as baryons for example, see [94]. This requirement represents the strongest evidence for the introduction of DM. It also is the first theoretical constraint every DM model will inevitably have to satisfy and it gives in practice two constraints. First, the DM energy density ρ_{DM} constitutes 26% of the total energy density today. This means that the sum of energy densities of all relic particles should represent 26% of the whole energy content of the Universe. Thus, all those relic particles should constitute what we call DM. Second, if a model is composed of a more complex structure (i.e. other particles on top of the DM one), the energy density of any of those new particles $\sum_i \rho_i$ has to be negligible today compared to

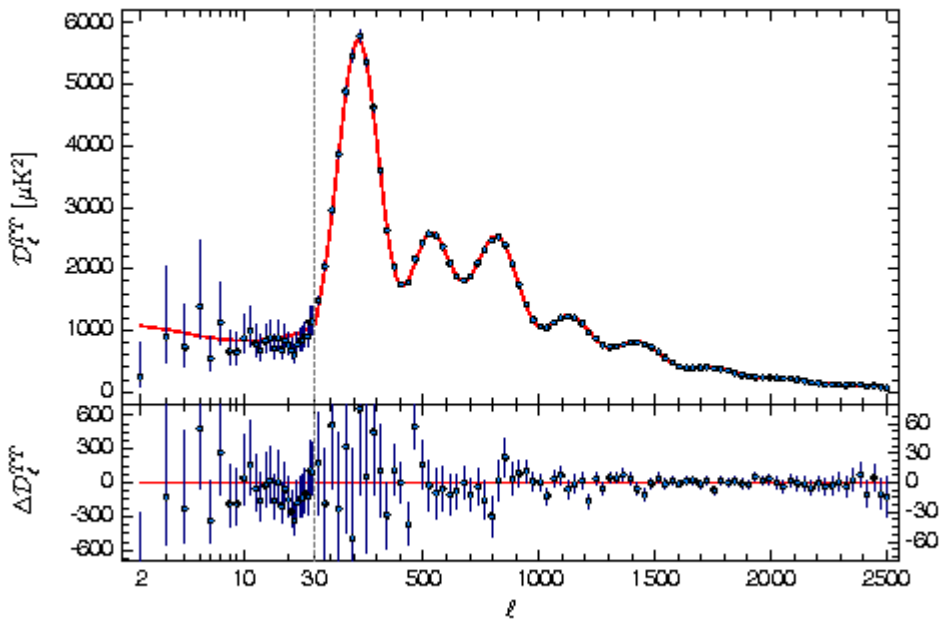


FIGURE 1.8: CMB temperature anisotropies spectrum, with $D_l \equiv l(l+1)C_l/2\pi$.

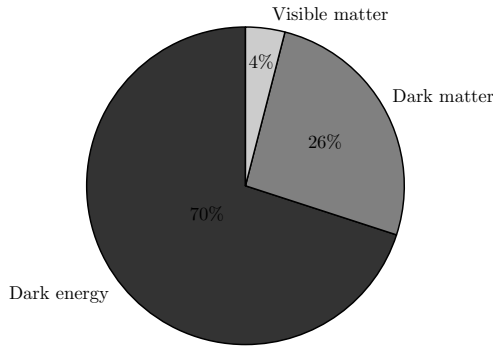


FIGURE 1.9: Pie chart of the energy density content of the Universe that measurements of the CMB anisotropies pointed out.

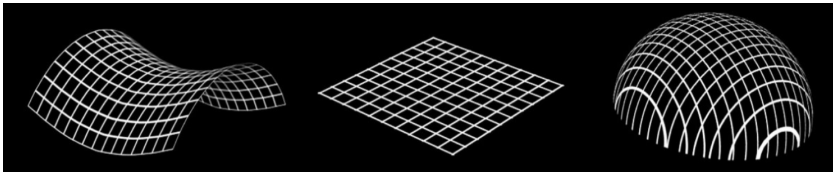


FIGURE 1.10: Two dimensional representation of an open/flat/-closed Universe from left to right. CMB anisotropies strongly suggest a flat Universe.

the DM one (see Figure 1.10), otherwise, it would be part of the DM.

For the rest of this thesis, we will consider cases where there is only one species which constitutes the DM. Other additional particles i will also be considered, but not as part of the DM. We have,

$$\Omega_{DM} = 0.2645 \pm 0.0050, \quad (1.29)$$

$$\sum_i \Omega_i \ll \Omega_{DM}. \quad (1.30)$$

If the first constraint is generically dubbed as the relic density constraint (as it refers to the energy density of DM particles today), the second one is referred as the overclosure constraint. This comes from the fact that if this last constraint is not satisfied, i.e. if $\sum_i \Omega_i \gtrsim \Omega_{DM}$, the universe would contain too much energy coming from the additional particles i and would overclose ($\Omega_{tot} > 1$). The total energy density today would be bigger than the one expected from standard cosmology which would indicate a closed Universe while it is known to be flat. Indeed, the CMB anisotropies measurements also indicate a flat Universe, see [94].

1.2 Dark Matter relic density

More concretely, in order to get more intuition on how the first constraint plays a role in a given model, let us consider two simple different production mechanisms (they will be detailed later on) as examples. But before proceeding to that we need to develop a coherent and well-established mathematical framework in which one can compute the evolution of a particle number density as a function of time.

1.2.1 The Boltzmann equation

The Λ CDM cosmological model describes an evolving Universe with a "beginning" (the Big Bang) followed by an inflation era. After this period of inflation, the Universe was constituted of a considerably hot and dense plasma. There was no bound state of particles at this stage since the Universe was too hot to allow such state to be stable as bound states would be right away disintegrated by plasma particles with kinetic energy larger than the bound state binding energy. Thus, there were only free elementary particles. One can show that, in the simplest picture one can think of, if 26% of the energy content of the Universe today is indeed made of DM, the DM should have been already there in the early Universe.

It would be very useful to be able to describe the DM production/depletion mechanism during the whole thermal history of the Universe. Then we would be able to quantify and to track the amount of DM from the early Universe epoch until now. In order to do so, we are going to consider the early Universe as a succession of thermal baths in which most of the particles are in thermal equilibrium. This hypothesis is well justified as the very high temperature favours thermalisation. Thus, it makes sense to use an equilibrium description for the early Universe. To describe accurately the evolution of a species in the thermal bath, one has to solve the Boltzmann equation which describes the microscopic evolution of the particle phase space distribution function. The Boltzmann equation, $\hat{L}[f] = \hat{C}[f]$, is built from two operators. On the left-hand side, we have the relativistic Liouville operator, \hat{L} , which describes the global variation of the particle phase space distribution function:

$$\hat{L} = p^\alpha \frac{\partial}{\partial x^\alpha} - \Gamma_{\beta\gamma}^\alpha p^\beta p^\gamma \frac{\partial}{\partial p^\alpha}, \quad (1.31)$$

where x and p are the position and momentum four vectors respectively and where $\Gamma_{\beta\gamma}^\alpha$ are the entries of the Christoffel symbols:

$$\Gamma_{\beta\gamma}^{\alpha} = \frac{1}{2} g^{\alpha\delta} \left(\frac{\partial}{\partial x^{\gamma}} g_{\delta\beta} + \frac{\partial}{\partial x^{\beta}} g_{\gamma\delta} - \frac{\partial}{\partial x^{\delta}} g_{\beta\gamma} \right), \quad (1.32)$$

with g the metric tensor.

On the right-hand side of the Boltzmann equation, we have the relativistic collision term, $\hat{\mathcal{C}}$, which in general is non-zero thanks to the interactions between particles in the bath. This operator can be very complicated, but under some well motivated assumptions, there is a way to rewrite the Boltzmann equation in a simpler form. Indeed, in the Friedmann-Lemaître-Robertson-Walker (FLRW) framework, the phase space distribution function is isotropic and homogeneous in the spatial directions. One can then integrate both sides of the Boltzmann equation $\hat{L}[f] = \hat{\mathcal{C}}[f]$ over all possible momenta (i.e. over the whole phase space). The new Boltzmann equation obtained in this way will express the evolution of the number density instead of the phase space distribution function. Moreover, assuming CP invariance and considering Maxwell-Boltzmann distributions for all species in kinetic equilibrium, one can write this evolution equation for a given species χ under the following form:

$$\frac{dn_{\chi}}{dt} + 3Hn_{\chi} = -\langle\sigma v\rangle_{\bar{\chi}\chi\rightarrow XX} \left[n_{\chi}^2 - (n_{\chi}^{eq})^2 \right], \quad (1.33)$$

where $\langle\sigma v\rangle_{\bar{\chi}\chi\rightarrow XX}$ is the χ 's thermally average annihilation cross section into some finale particles X ,

$$\langle\sigma v\rangle_{\bar{\chi}\chi\rightarrow XX} \equiv \frac{\int \sigma v \, dn_{\chi}^{eq} \, dn_{\bar{\chi}}^{eq}}{\int dn_{\chi}^{eq} \, dn_{\bar{\chi}}^{eq}}, \quad (1.34)$$

with n_{χ}^{eq} the number density of χ at equilibrium and where the Hubble parameter can be expressed in terms of the total energy density of the Universe ρ and the Planck mass M_{pl} :

$$H(t) = \sqrt{\frac{8\pi}{3M_{pl}^2} \rho(t)}. \quad (1.35)$$

The interpretation of this equation is in fact simple. The $\langle\sigma v\rangle_{\bar{\chi}\chi\rightarrow XX} n_{\chi}^2$ term counts the number of annihilation of χ 's per unit of time per unit of volume, whereas the $\langle\sigma v\rangle_{\bar{\chi}\chi\rightarrow XX} (n_{\chi}^{eq})^2$ term counts the number of production process of χ 's per unit of time per unit of volume. Equivalently, as the entropy s evolves in the same way

as the number density when there is no interaction changing its number, one can introduce the *Yield*, a comoving quantity $Y \equiv n/s$ and $x \equiv m_\chi/T$ as well as the relationship between temperature T and time t during the radiation dominated era. This leads to,

$$\frac{dY}{dx} = -\frac{\langle\sigma v\rangle_{\bar{\chi}\chi\rightarrow XX^S}}{xH} \left[Y_\chi^2 - (Y_\chi^{eq})^2 \right], \quad (1.36)$$

where Y_χ^{eq} is the yield of χ taken at equilibrium. If there is more than one annihilation or production channel, the equation on the yield gets one additional contribution for each new channel. Eq. 1.33 will be our Boltzmann equation prototype that we will use and adapt to portal models in the following, see Chapter 2.

Note that the total energy density is dominated by the contribution of relativistic particles such that one can write,

$$\rho = \sum_{i=rel} \frac{\pi^2}{30} g_i T_i^4 = \frac{\pi^2}{30} g_* T^4, \quad (1.37)$$

where we defined the effective number of degrees of freedom taking the difference between Bose-Einstein and Fermi-Dirac statistics into account

$$g_* \equiv \sum_{i=rel} g_i^B \left(\frac{T_i}{T} \right)^4 + \frac{7}{8} \sum_{i=rel} g_i^F \left(\frac{T_i}{T} \right)^4. \quad (1.38)$$

These useful way to condensate the expression of the energy density can also be applied to the entropy density which is also dominated by its relativistic components. We have,

$$s = \sum_{i=rel} \frac{2\pi^2}{45} g_i T_i^3 = \frac{2\pi^2}{45} g_*^S T^3, \quad (1.39)$$

where this time we have,

$$g_*^S \equiv \sum_{i=rel} g_i^B \left(\frac{T_i}{T} \right)^3 + \frac{7}{8} \sum_{i=rel} g_i^F \left(\frac{T_i}{T} \right)^3. \quad (1.40)$$

1.2.2 Freeze-out case

If one assumes DM to be in thermal equilibrium with the SM in the early Universe, one should have a mechanism which could deplete the large amount of DM it implies. Since DM is actually matter, it will eventually dominate over radiation during the Universe's expansion. One would then require a very small amount of DM just after having decoupled from SM compared to thermal particles, otherwise one would get $\Omega_{\text{DM}} \gg 0.26$. In the light of the mathematical framework we have just developed, one possibility would be to use a Boltzmann suppression which arises naturally for thermal particles once the temperature drops below their mass. Indeed, on the one hand, as long as the DM is relativistic, its number density goes like $\sim T^3$ such that its yield is constant with time. On the other hand, once the particle becomes non-relativistic, its number density fall exponentially $\sim (mT)^{3/2} e^{-m/T}$ and its yield with it. This mechanism is the so-called freeze-out (FO) mechanism where a particle (here the DM) is in thermal equilibrium with at least one other lighter species (say X). Because of the expansion of the Universe, the Universe's temperature decreases with time and will eventually drops below the DM mass. Then, as long as the DM is in thermal equilibrium, its number density will fall very quickly and, at some point, will become so suppressed that it will not be high enough anymore to satisfy the thermalisation condition. That is to say that the DM changing number reaction ($X \leftrightarrow \text{DM}$) will stop to occur and the DM number density will freeze-out.

We will see in the third Chapter (see Section 3.2) more specifically that the DM yield can be written, in the instantaneous freeze-out approximation (see also Appendix C), in terms of the annihilation cross section which is responsible for the FO mechanism. But this yield can also be easily related to the energy density and then to the DM relic abundance. We have for a s-wave annihilation process,

$$\Omega_{\text{DM}} h^2 \simeq 8.77 \times 10^{-11} \times \left(\frac{m_{\text{DM}}}{T_{\text{dec}}} \right) \times \left(\frac{\text{GeV}^{-2}}{\langle \sigma v \rangle_{T=T_{\text{dec}}}} \right) \times \left(\frac{\sqrt{g_{\star}^{\text{eff}}(T_{\text{dec}})}}{g_{\star}^S(T_{\text{dec}})} \right), \quad (1.41)$$

with T_{dec} the temperature of DM decoupling. This constraint fixes the value of the annihilation cross section at decoupling in terms of the DM mass and the decoupling temperature, T_{dec} ,

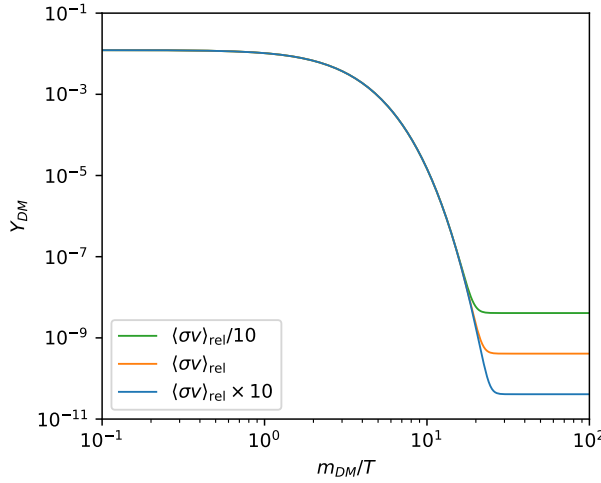


FIGURE 1.11: Example of DM yield evolution as a function of the inverse temperature for three cross sections in a freeze-out scenario. The value of $\langle\sigma v\rangle_{\text{rel}}$ has been set by Eq. 1.42.

$$\langle\sigma v\rangle_{T=T_{\text{dec}}} \simeq 7.38 \times 10^{-10} \text{GeV}^{-2} \times \left(\frac{m_{\text{DM}}}{T_{\text{dec}}}\right) \times \left(\frac{0.1188}{\Omega_{\text{DM}} h^2}\right) \times \left(\frac{\sqrt{g_{\star}^{\text{eff}}(T_{\text{dec}})}}{g_{\star}^S(T_{\text{dec}})}\right). \quad (1.42)$$

The $m_{\text{DM}}/T_{\text{dec}}$ ratio is roughly constant¹⁰ and lies around $m_{\text{DM}}/T_{\text{dec}} \simeq 23$. This implies that the DM annihilation cross section responsible for the FO process should be, at the time of decoupling, of the order of $\langle\sigma v\rangle \sim 10^{-9} \text{GeV}^{-2}$ and this whatever the DM mass and the model specificities. Figure 1.11 shows the evolution of the DM yield as a function of $x \equiv m_{\text{DM}}/T$ for three different values of the annihilation cross sections. One sees that the more the annihilation cross section is strong the longer the DM stays at equilibrium the more its number density is depleted as explained above.

1.2.3 Freeze-in case

Another simple way to have a small amount of DM at decoupling compared to thermal particles would be to have DM to be out of equilibrium. In this way, if the other particle X which couples to DM is in kinetic equilibrium, it will slowly produce DM particles. However, when the temperature reaches the DM mass scale, as the X 's

¹⁰It depends on the inputs of the problem only through a logarithm, see Appendix C.

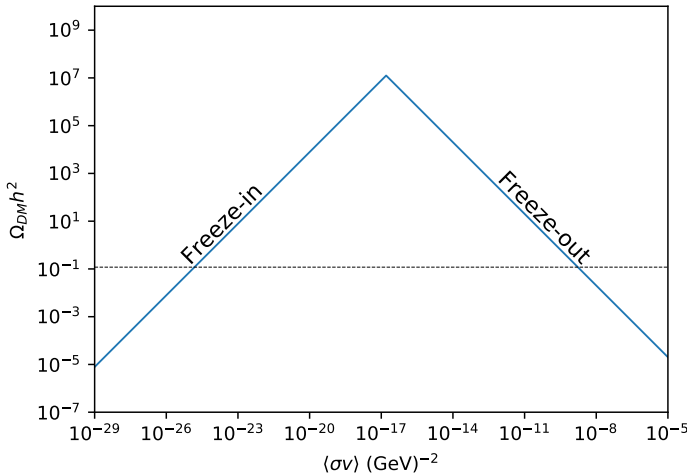


FIGURE 1.12: The freeze-out and freeze-in are two extremes of a same process. One with strong interactions, the freeze-out and the other with feeble interactions, the freeze-in.

are lighter, they will not have enough kinetic energy to produce DM particles and the process stops. The DM number density freezes. This is the so-called freeze-in (FI) mechanism and is the other extreme (and simplest) way to account for the DM relic abundance. Here, the suppression does not come from a Boltzmann suppression as in the FO mechanism, but from the fact that in this case, the relic density is proportional to the production cross section which we assume to be driven by tiny couplings. Figure 1.12 shows the DM relic abundance as a function of the annihilation/production cross section in the instantaneous freeze-out and freeze-in cases. It shows that the FO and the FI mechanisms are two faces of a same phenomenon in which the DM abundance is set by the value of the annihilation/production cross section. The two production mechanisms merge when the cross section starts to be large enough for the DM to thermalise with its partner, it is the top of the "volcano" diagram shown in Figure 1.12.

We will also see in the following (see Section 3.2.2) that the DM yield can be written, in the instantaneous freeze-in approximation, in terms of the production cross section which is responsible for the FI mechanism. Again, this yield can be related to the energy density and then to the DM relic abundance. We have for a s-wave annihilation process,

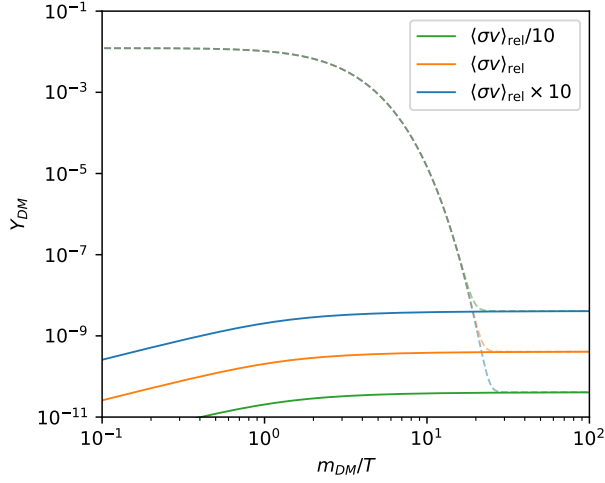


FIGURE 1.13: Example of DM yield evolution as a function of the inverse temperature for three cross sections in a freeze-in scenario. We used $m_{\text{DM}} = 1 \text{ GeV}$.

$$\Omega_{\text{DM}} h^2 \simeq 7.85 \times 10^{26} \times \left(\frac{m_{\text{DM}}}{\text{GeV}} \right)^2 \times \left(\frac{\langle \sigma v \rangle_{T=m_{\text{DM}}}}{\text{GeV}^{-2}} \right) \times \left(\frac{1}{g_{\star}^S(m_{\text{DM}}) \sqrt{g_{\star}^{\text{eff}}(m_{\text{DM}})}} \right). \quad (1.43)$$

This constraint fixes the value of the production cross section at decoupling in terms of the DM mass,

$$\begin{aligned} \langle \sigma v \rangle_{T=m_{\text{DM}}} &\simeq 1.51 \times 10^{-28} \text{GeV}^{-2} \times \left(\frac{\text{GeV}}{m_{\text{DM}}} \right)^2 \times \left(\frac{\Omega_{\text{DM}} h^2}{0.1188} \right) \\ &\times \left(g_{\star}^S(m_{\text{DM}}) \sqrt{g_{\star}^{\text{eff}}(m_{\text{DM}})} \right). \end{aligned} \quad (1.44)$$

From this last expression, we can see that, in contrary with the FO case, in the FI case, the required value for the DM production cross section depends on the DM mass. Figure 1.13 shows (for $m_{\text{DM}} = 1 \text{ GeV}$) the same as Figure 1.11, but for a freeze-in scenario. One sees from this figure that the stronger the production cross section, the more DM can be created before the process stops, as expected.

These two simplified examples which are the FO and the FI mechanisms show how, given a production mechanism, the relic abundance requirement constrains

explicitly a model (i.e. the cross section). When the simplified version is not precise enough and one has to solve the Boltzmann equation, it is solved numerically.

1.3 Small scale structure

In section 1.1, we have seen that there are many different hints for DM at large scale in the Universe. In the current section, we will see that there are also hints for DM at small scale, cosmologically speaking. Let us review the most important ones.

1.3.1 Too-big-to-fail

The *Too-big-to-fail* problem comes from the solution of an older problem of Λ CDM: the *missing satellites* problem. This last refers to the fact that Λ CDM simulations predict a significant bigger number of satellite galaxies for Milky-Way like galaxies [50]–[52] than what is actually observed [53], [54]. A favoured solution to this problem argues that those satellite galaxies had their stars stripped from them during tidal interactions. Thus, if most stars have disappeared, this could explain why we are not seeing more dwarf galaxies. They are there but simply empty of visible matter.

On the other hand, Λ CDM simulations predict relatively massive satellite galaxies and it appears that it is very unlikely that such galaxies have no visible stars [55]–[58]. This failure in the solution of the *missing satellites* problem is what is called the *too-big-to-fail* problem.

Figure 1.14 shows the measured rotation velocity of actual satellite galaxies as a function of their distance to the galactic centre [56]. Even if we agree on the fact that most of the satellite galaxies have lost their stars, we should still be able to observe the heaviest ones. Since high rotation velocities indicate massive galaxies, we can see on this figure that we do not observe such massive dwarf galaxies as we should.

1.3.2 Core-vs-cusp

Λ CDM simulations show that the DM energy density profile should slope as $1/r^3$ in the outer region of the DM halos while it should slope as $1/r$ closer to the centre [59]–[61], in the inner part. This cuspy profile has been parametrised in several ways. As a concrete example, we give the Navarro-Frenk-White (NFW) profile,

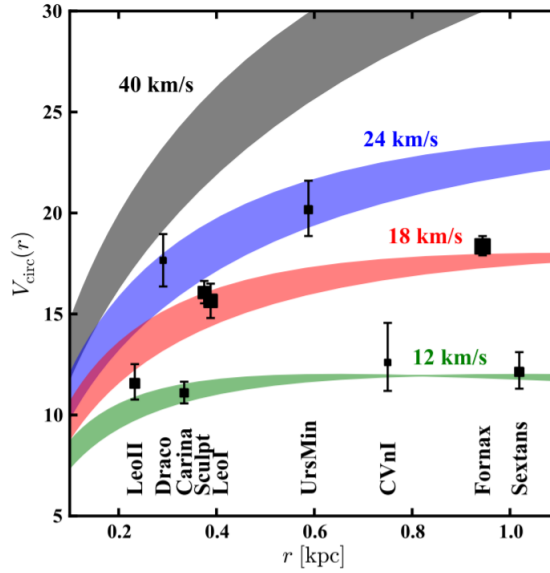


FIGURE 1.14: Circular velocity of satellite galaxies as a function of their distance to the galactic centre, taken from [56]. One can also distinguish rotation curves corresponding to the specified maximal velocity.

$$\rho_{NFW}(r) = \rho_0 \times \frac{1}{\frac{r}{r_s} \left(1 + \frac{r}{r_s}\right)^2}, \quad (1.45)$$

with ρ_0 some energy density normalisation and r_s the value of the critical radius for which the behaviour of the profile changes.

The problem arises once we compare this expected cuspy behaviour to observations. The outer regime behaviour agrees pretty well with it, but the inner part seems, according to observations of many halos, to flatten. Indeed, experiments show a core profile in the inner region of halos [62]–[64]. Figure 1.15 shows discrepancies between simulations and observations (taken from [65], see also [66], [67]). This *core-vs-cusp* problem is a major issue of modern cosmology and has been studied extensively in the literature [68]–[79].

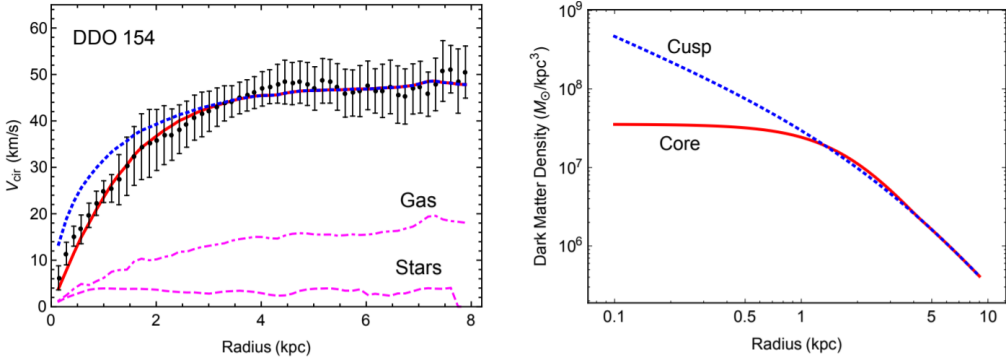


FIGURE 1.15: Left: Data points show the measured rotation curve of DDO 154 [80]. On the same figure, one can see expectation from a cuspy (blue) or a core (red) profile for DM. Right: The cuspy and core profiles associated to both fits. [65]

1.3.3 Diversity

There is a last discrepancy between Λ CDM simulations and observations we would like to highlight. Looking again at the DM energy density profile in the inner region of halos of similar size and mass, observations pointed out many different behaviours [81], [82]. While simulations give a small scatter in density profile for halos of similar size and mass [61], [83]. This variety in the slope of the DM energy density profile is known as the diversity problem.

1.3.4 DM hidden sector and portals

The relic density issue above as well as the possible constraints from small scale structure have important implications on the DM particle model. Depending on the type and the strength of the interaction one assumes between the DM and the SM, one could constrain the DM mass, its coupling to SM particles as well as coupling to new particles that could exist. On top of these constraints, as we will see, there exist many additional constraints on the DM particle model coming from cosmology, astrophysics and particle physics experiments which suggest a feeble connection between the DM and SM particles. For this reason, in the following, we will consider a particular structure of DM models in which the DM particle is a singlet of all SM gauge groups. Additionally, there is no reason for the DM to have no interaction at all, actually we will see later in this chapter that small scale structure tensions could be alleviated if the DM particle self-interacts. Thus, one necessarily needs a new interaction which would allow the DM to self-interact. We will then consider DM models in which the DM self-interactions would be due to the introduction of a new light particle which would also be a singlet of $SU(3)_c \times SU(2)_L \times U(1)_Y$ and

a singlet of all gauge groups which could arise in the HS. Thus, the DM particles together with the new light particles form a new self-interacting sector, independent of the one formed by SM particles (called visible sector or VS) which we will refer to as the hidden sector (HS). Moreover, the new particle will directly couple to one or more SM particles in addition to its coupling to the DM such that one has an indirect connection between the DM and the SM. These type of model in which the DM evolves on its own in a HS and couples to the VS through an additional degree of freedom is usually referred as portal models.

It exists different types of portal models. Indeed, the only requirement is that a particle which is a singlet of all gauge groups of the theory (VS and HS) directly couples to a combination of DM fields and independently to a combination of SM fields which are both singlet of all possible gauge groups. There are three combination of SM fields which are singlet of all possible gauge groups such that $d < 4$ ¹¹: $\bar{L}H$, $H^\dagger H$ and $F_Y^{\mu\nu}$ where L is the lepton doublet, H the Brout-Englert-Higgs scalar doublet and $F_Y^{\mu\nu}$ the strength field tensor associated to the hypercharge gauge boson. The first operator, $\bar{L}H$, can only couple to a fermion ψ if one imposes the final operator to have a dimension $d \leq 4$. This portal, that one could write $\bar{L}H\psi$, is called the "neutrino portal" and will not be further studied in this thesis. The second operator, $H^\dagger H$, can couple to either a single real scalar or to a neutral combination of a complex scalar Φ . The portal, $H^\dagger H\Phi$, $H^\dagger H\Phi^2$ or $H^\dagger H\Phi^\dagger\Phi$, is called the "Higgs scalar portal". Finally, the third operator, $F_Y^{\mu\nu}$, can only couple to another strength tensor field $F'_{\mu\nu}$ of a new gauge boson for example. This last portal, $F_Y^{\mu\nu}F'_{\mu\nu}$, is called the "kinetic mixing portal".

Assuming a Dirac fermion DM χ , the singlet combination of the DM fields is simply given by $\bar{\chi}\chi$ such that one ends up with only two possibilities for the portal (excluding the neutrino portal):

$$\bullet \quad H^\dagger H\Phi \quad \& \quad H^\dagger H\Phi^2 \quad \& \quad \bar{\chi}\chi\Phi, \quad (1.46)$$

$$\bullet \quad F_Y^{\mu\nu}F'_{\mu\nu} \quad \& \quad i\bar{\chi}\gamma^\mu \left(\partial_\mu - ie'A'_\mu \right) \chi, \quad (1.47)$$

where in the last line, e' and A' are the gauge charge and the gauge field associated to a new $U(1)'$ symmetry and with $F'_{\mu\nu} \equiv \partial_\mu A'_\nu - \partial_\nu A'_\mu$. Note that we have joined the trilinear and the quadrilinear terms for the scalar option as if one of the two terms is theoretically allowed, the other is as well. We thus apply the principle saying that "everything which is not forbidden exists".

¹¹The dimension d of the operator made of SM fields has to be smaller than 4 if one wants a renormalisable interaction.

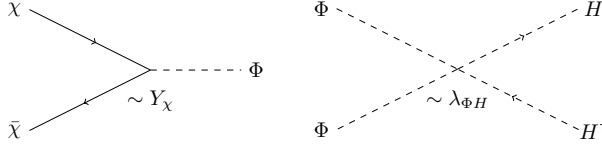


FIGURE 1.16: Couplings between the DM and the mediator, and between the mediator and the visible sector in the symmetric phase (i.e. no vacuum expectation value).

In order to illustrate the constraints mentioned above, in the following, we will then consider both possibilities of DM portal models given in Eqs. 1.46 and 1.47 as they are generic and very well motivated models. Indeed, this type of model is well motivated in the context of scenarios where one assumes that DM undergoes self-interactions usually named Self-Interacting DM (SIDM), see Chapter 2.

Benchmark model A: Higgs portal DM model

As a representative of a DM model with a Higgs portal, we take the Higgs scalar Portal (HP) where the DM is a singlet fermion χ and where the mediator role is played by a new real scalar field Φ . The Lagrangian of this model is given by,

$$\mathcal{L} = \mathcal{L}_{SM} + i\bar{\chi}\not{D}\chi - m_{DM}\bar{\chi}\chi + Y_{\chi}\Phi\bar{\chi}\chi - \mu_{\Phi}^2\Phi^2 + \lambda_{\Phi}\Phi^4 - \mu_H^2H^{\dagger}H + \lambda_H\left(H^{\dagger}H\right)^2 + \lambda_3\Phi H^{\dagger}H + \lambda_{\Phi H}\Phi^2H^{\dagger}H, \quad (1.48)$$

where the key interactions are the Yukawa interaction ruled by the Y_{χ} , the Higgs portal interaction ruled by $\lambda_{\Phi H}$ and the scalar potential interactions (involving the purely non-derivative scalar interactions). Note that in Eq. 1.48, we have explicitly written the scalar potential already included in the SM as we will need it in the following. From the expression of this Lagrangian, one can see that the connection between the hidden and the visible sectors goes through the last term and the Higgs portal parameter, $\lambda_{\Phi H}$. The two new couplings are represented in Figure 1.16 and connect the DM to the mediator and the mediator to the visible sector.

Moreover, if the new field Φ acquires a non-zero vacuum expectation value (VEV), a mixing occurs between the two real scalars of the theory, \tilde{h} and $\tilde{\phi}$. The original fields can be expanded around their respective VEV (v_H and v_{Φ}):

$$H = \begin{pmatrix} h^+ \\ \frac{v_H + \tilde{h} + ig}{\sqrt{2}} \end{pmatrix} \quad \text{and} \quad \Phi = \frac{v_\Phi + \tilde{\phi}}{\sqrt{2}}, \quad (1.49)$$

where λ_3 has been absorbed in the definition of v_Φ . Due to this mixing, the real scalars \tilde{h} and $\tilde{\phi}$ are not mass eigenstates and a transformation is needed to diagonalise the mass matrix given by

$$M_{\Phi H}^2 = \begin{pmatrix} 2\lambda_H v_H^2 & \lambda_{\Phi H} v_H v_\Phi \\ \lambda_{\Phi H} v_H v_\Phi & 2\lambda_\Phi v_\Phi^2 \end{pmatrix}. \quad (1.50)$$

The diagonalisation of this matrix can be done with an usual rotation,

$$\begin{pmatrix} h \\ \phi \end{pmatrix} = \begin{pmatrix} \cos \theta & -\sin \theta \\ \sin \theta & \cos \theta \end{pmatrix} \begin{pmatrix} \tilde{h} \\ \tilde{\phi} \end{pmatrix}, \quad (1.51)$$

where the mixing angle θ has to be given by

$$\tan(2\theta) = \frac{\lambda_{\Phi H} v_H v_\Phi}{\lambda_\Phi v_\Phi^2 - \lambda_H v_H^2}. \quad (1.52)$$

We show in Figure 1.17 the various couplings of this theory in terms of mass eigenstate fields in the case of a small mixing angle. We will see later in this chapter (see Sections 1.4 to 1.9) that small mixing angles are strongly required for this kind of model. Depending on the mass and VEV hierarchy, one can distinguish different cases. In the following, we will generally consider the fully broken cases: $m_{\text{med}} < m_{\text{DM}} < v_H < v_\Phi$. We will see in the following that the DM abundance is generally set at a temperature close to its mass $T \lesssim m_{\text{DM}}$. Then, in the case where the DM mass is smaller than the two VEV's of the theory ($m_{\text{med}} < m_{\text{DM}} < v_H < v_\Phi$), the DM abundance will be set while the symmetries of the theory are broken ($T < v_H < v_\Phi$). Therefore, the hierarchy we are focusing on is such that the VS and the HS symmetries are broken when the DM is produced/depleted. We will discuss in Section 3.4 other possible hierarchies and their implications.

Benchmark model B: Kinetic Mixing portal DM model

As a representative of a model based on a vector portal, we use the Kinetic Mixing portal (KM) where the DM is again a fermion denoted as χ but the mediator is the

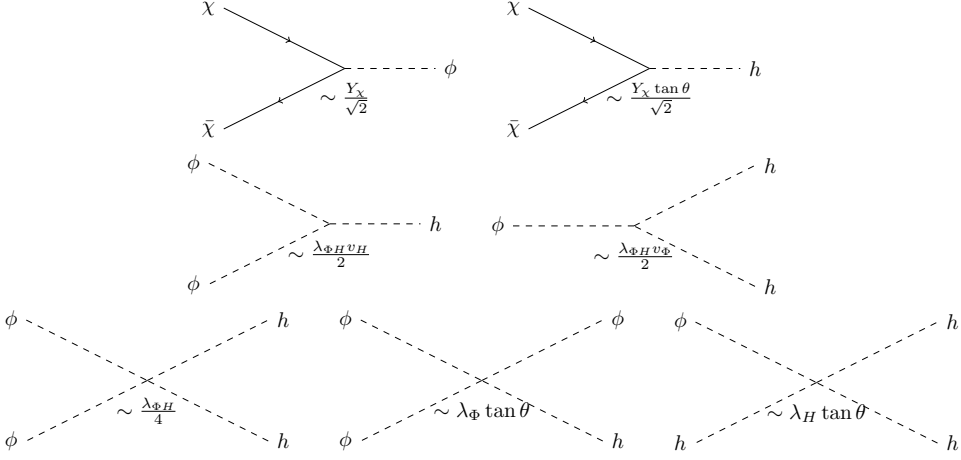


FIGURE 1.17: Couplings (at leading order for a small mixing angle) between the DM, the mediator and the visible sector in the broken phase.

gauge field B'_μ of a new $U(1)'$ gauge symmetry. Such a new gauge symmetry is well motivated both experimentally and theoretically [95]–[97]. In this framework, the DM field is charged under this new symmetry which makes it naturally stable [98]–[102].

The Lagrangian of this model is given by,

$$\mathcal{L} = \mathcal{L}_{SM} + i\bar{\chi}\not{D}\chi - m_{DM}\bar{\chi}\chi - \frac{1}{4}\tilde{B}'^{\mu\nu}\tilde{B}'_{\mu\nu} - \frac{\hat{e}}{2}\tilde{B}^{\mu\nu}\tilde{B}'_{\mu\nu} + \frac{1}{2}m_{\gamma'}^2\tilde{B}'^\mu\tilde{B}'_\mu + \dots, \quad (1.53)$$

where the dots refer to what would be needed for giving a mass to the new mediator and the DM covariant derivative is $D_\mu = \partial_\mu + ie'\tilde{B}'_\mu$, where \tilde{B}'_μ and e' are the $U(1)'$ gauge field and coupling respectively. Such a mass for the new gauge boson could arise through the Stückelberg [103] or through the Brout-Englert-Higgs mechanism [104], [105]. In this model, the connection between the mediator and the visible sector goes through a kinetic mixing term (ruled by the kinetic mixing parameter \hat{e}) such that fields appearing in the Lagrangian are not propagation eigenstate fields. One must perform first a non-orthogonal transformation in order to have canonical kinetic terms. For a small mixing parameter (as it will be required later, see Sections 1.4 to 1.9), this transformations at leading order in \hat{e} is simply,

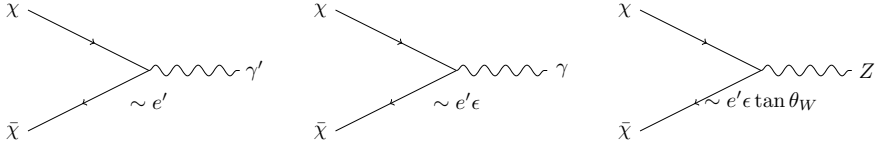


FIGURE 1.18: Couplings (at leading order for a small mixing parameter) between the DM, the mediator and the visible sector for a massless dark photon.

$$\begin{pmatrix} B'^{\mu} \\ B^{\mu} \end{pmatrix} = \begin{pmatrix} 1 & \hat{\epsilon} \\ 0 & 1 \end{pmatrix} \begin{pmatrix} \tilde{B}'^{\mu} \\ \tilde{B}^{\mu} \end{pmatrix}. \quad (1.54)$$

After this transformation on the fields, we get for the relevant terms in the Lagrangian (still at the leading order in the mixing parameter),

$$\mathcal{L} \supset -\frac{1}{4}B'^{\mu\nu}B'_{\mu\nu} + \frac{1}{2}m_{\gamma'}^2 B'^{\mu}B'_{\mu} - \hat{\epsilon} m_{\gamma'}^2 B^{\mu}B'_{\mu} - e' \bar{\chi} \gamma^{\mu} \chi (B'_{\mu} - \hat{\epsilon} B_{\mu}). \quad (1.55)$$

From here, one has to consider the massless and massive mediator cases separately as the continuous limit $m_{\gamma'} \rightarrow 0$ is not trivial and will be discussed later (see Section 3.3). In the massless case, since fields are directly mass eigenstates, after having perform the Weinberg rotation,

$$\begin{pmatrix} B^{\mu} \\ W^{3\mu} \end{pmatrix} = \begin{pmatrix} \cos \theta_W & -\sin \theta_W \\ \sin \theta_W & \cos \theta_W \end{pmatrix} \begin{pmatrix} A^{\mu} \\ Z^{\mu} \end{pmatrix}, \quad (1.56)$$

one can identify B'^{μ} , A^{μ} and Z^{μ} as the dark photon, the photon and the Z boson respectively. Couplings between relevant particles are then shown in Figure 1.18 where we have defined $\epsilon \equiv \hat{\epsilon} \cos \theta_W$. The final Lagrangian in the massless dark photon case is given by,

$$\mathcal{L} \supset -\frac{1}{4}B'^{\mu\nu}B'_{\mu\nu} - e' \bar{\chi} \gamma^{\mu} \chi B'_{\mu} + e' \epsilon \bar{\chi} \gamma^{\mu} \chi (A_{\mu} - \tan \theta_W Z_{\mu}). \quad (1.57)$$

In the massive case, fields are not mass eigenstates after having performed the Weinberg rotation,

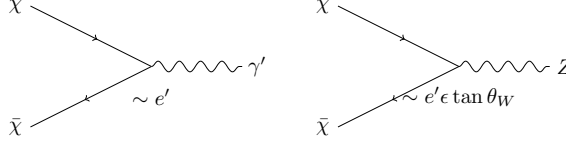


FIGURE 1.19: Couplings (at leading order for a small mixing parameter) between the DM, the mediator and the visible sector for a massive dark photon.

$$\begin{pmatrix} B^\mu \\ W^{3\mu} \end{pmatrix} = \begin{pmatrix} \cos \theta_W & -\sin \theta_W \\ \sin \theta_W & \cos \theta_W \end{pmatrix} \begin{pmatrix} A_0^\mu \\ Z_0^\mu \end{pmatrix}. \quad (1.58)$$

One needs a further orthogonal diagonalisation of the mass term which, at leading order in ϵ , is

$$\begin{pmatrix} B'^\mu \\ A_0^\mu \end{pmatrix} = \begin{pmatrix} 1 & \epsilon \\ -\epsilon & 1 \end{pmatrix} \begin{pmatrix} A'^\mu \\ A^\mu \end{pmatrix}. \quad (1.59)$$

Such that the final Lagrangian in the massive dark photon case is given by,

$$\begin{aligned} \mathcal{L} \supset & -\frac{1}{4}F'^{\mu\nu}F'_{\mu\nu} - e'\bar{\chi}\gamma^\mu\chi A'_\mu - e'\epsilon \tan \theta_W \bar{\chi}\gamma^\mu\chi Z_\mu + \frac{1}{2}m_{\gamma'}^2 A'^\mu A'_\mu \\ & + \epsilon \tan \theta_W m_{\gamma'}^2 A'^\mu Z_\mu, \end{aligned} \quad (1.60)$$

with $F'^{\mu\nu}$ is the strength field tensor associated to the dark photon A'^μ and where the last term is not diagonal, but it will introduce a mass splitting between A'^μ and Z_0^μ of order $\mathcal{O}(\epsilon^2)$ and will then be neglected as our whole computation was already done at leading order in ϵ . Then one can identify A'^μ , A^μ and Z_0^μ to the dark photon¹², the photon and the Z boson, respectively. Two major consequences of this diagonalisation are that the DM field does not couple to the photon but only to the Z boson and that the dark photon is distinguishable from the SM photon as one can read from the third term of Eq. 1.60. The latter consequence will have a strong impact on the DM production mechanisms as we will see in Chapter 3. Couplings between different relevant particles can be seen in Figure 1.19.

¹²In the massive case, the new vector boson is sometimes called Z' instead of γ' (dark photon) as it is closer to "be" a Z than a γ as it is massive. However, in this thesis, we will keep the name "dark photon" whatever its mass is.

The treatment of the limit $m_{\gamma'} \rightarrow 0$ may seem discontinuous and leading to incoherences. Indeed, in the massive case, one distinguishes the dark photon propagation and mass eigenstate basis, while for $m_{\gamma'} \rightarrow 0$, the two fields are degenerate, and the distinction between the basis disappears. The proper way to treat this limit starting from a massive dark photon goes through the incorporation of thermal effects which can be important in some cases. This has been studied at length in the context of dark photon production, in particular in stars [106]–[111]. As this problem is relevant for our work but not central, we only summarise the salient points in a dedicated section (see Section 3.3 and Appendix B for more details on some technical issues) and we refer to [106]–[111] for a more detailed explanation of the effects.

1.3.5 Dark matter self-interaction cross section

In Subsections 1.3.1 and 1.3.2, we discussed the *Too-big-to-fail* and the *Core-vs-cusp* problems. Both problems arise when comparing results of small-scale structure simulations of galaxy formations which were performed with collisionless DM to observations of these structures. However, simulations also show that if the new form of matter, the DM, self-interacts relatively strongly, these problems could be alleviated. In practice, simulations show that this requires a self-interaction cross section divided by the DM mass lying within the range $0.1 \text{ cm}^2/\text{g} \lesssim \sigma_T/m_{\text{DM}} \lesssim 10 \text{ cm}^2/\text{g}$ [112]–[115]. Moreover, observations of galaxy or cluster mergers can also provide an upper bound on the self-interaction cross section. Indeed, the lack of a visible offset between stars and DM tells us that the number of self-interactions cannot be as large as we want such that this quantity is bounded above. Concretely, the Bullet cluster gives $\sigma_T/m_{\text{DM}} < 1.25 \text{ cm}^2/\text{g}$ at 68% CL [116]–[118] while the most recent observations of cluster mergers lead to $\sigma_T/m_{\text{DM}} < 0.47 \text{ cm}^2/\text{g}$ at 95% CL [119] (or even smaller with $\sigma_T/m_{\text{DM}} < 0.3 \text{ cm}^2/\text{g}$ in [120]). We will finally keep in mind that, if a model allows self-interactions, we must have that

$$0.10 \text{ cm}^2/\text{g} < \sigma_T/m_{\text{DM}} < 0.47 \text{ cm}^2/\text{g}. \quad (1.61)$$

Rewriting this constraint in particle physics units for a DM mass of the same order of the electroweak scale, one gets $\sigma_T \sim 10^5 \left(\frac{m_{\text{DM}}}{100 \text{ GeV}}\right) \text{ GeV}^{-2}$. This order of magnitude is considerably larger than the value of the annihilation (or production) cross section considered in standard freeze-out (or respectively freeze-in) scenarios. Indeed, one can verify that typically, the cross section is 14 and 29 order of magnitudes smaller in a FO and FI scenario respectively, see Figure 1.12. To account for this large difference between both type of cross sections (annihilation/production and self-interaction), one possibility turns out to assume the light mediator to be much lighter than the DM particle. This hierarchy between the two masses would

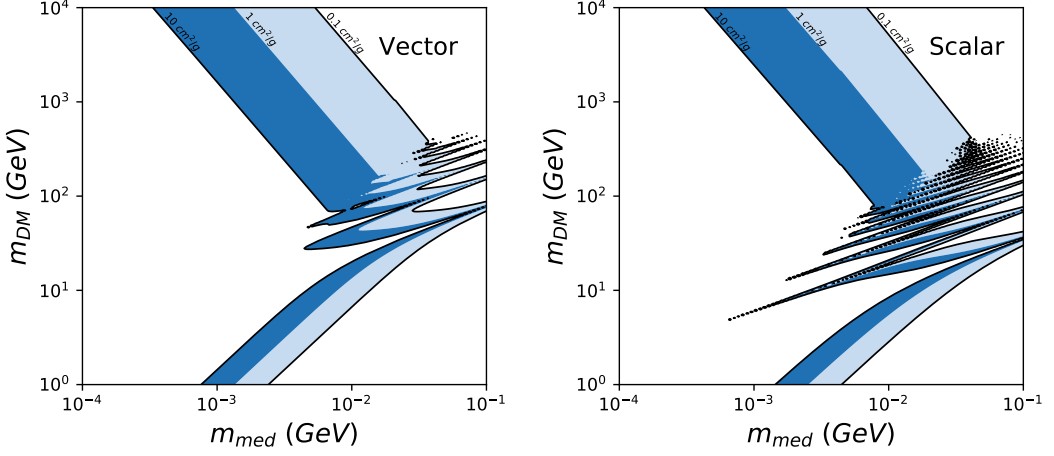


FIGURE 1.20: Self interaction constraints for a Dirac DM and a vector (Left) or a scalar (Right) mediator. See text for more details.

boost the t-channel mediator exchange (i.e. the self-interaction) with respect to the annihilation cross section. Indeed, in this case, the so-called Sommerfeld effect (see Chapter 2) will play a major role by increasing the self-interaction cross section at tree level by several order of magnitudes.

This potential necessity of a large self-interaction consequently motivates models with light mediators, in particular the two portal benchmark models considered above (see Subsection 1.3.4) and taking $m_{\text{med}} \ll m_{\text{DM}}$. More concretely and as we will see in Chapter 2, one needs $v_{\text{DM}}/2 \ll \alpha_{\text{med}}^{13}$ and $m_{\text{med}} \ll \alpha_{\text{med}} m_{\text{DM}}$ [121]. Under those conditions, the model enters the highly resonant regime and the Sommerfeld effect enhances drastically the self-interaction cross section. This is shown in Figure 1.20 where we have highlighted areas, in the mediator mass - DM mass plane, where $0.10 \text{ cm}^2/\text{g} < \sigma_T/m_{\text{DM}} < 10 \text{ cm}^2/\text{g}$. We fixed the coupling (e' or y_ϕ) between the mediator and the DM imposing that it leads to the observed relic density (see Eq. 1.29), assuming a standard freeze-out. From this figure, one can conclude that the allowed parameter space is globally the same in both cases even if the two models have two important differences which will be further detailed in Chapter 2. First, the DM annihilation cross section is either s- or p-wave (in the vector or scalar portal model respectively). Second, in the vector mediator case, the self-interaction has an attractive and a repulsive contribution while there is only an attractive contribution in the scalar mediator case. This explain why the Sommerfeld enhancement resonances appears to be smoothed. Despite these relevant

¹³ $\alpha_{\text{med}} = \alpha' \equiv e'^2/4\pi$ in the vector portal and $\alpha_{\text{med}} = \alpha_\phi \equiv y_\phi^2/4\pi$ in the scalar portal model.

differences, the final allowed part of the parameter space is barely the same for both models.

In the following, we will consider constraints which apply on these two self-interacting benchmark models. This will allow us to show that these constraints are very strong in most cases and thus will be the basis of Chapters 5 and 6 which are precisely devoted to the study of the various ways out. Most of these constraints, as we will see, are coming from the fact that the light mediator will be typically present in large numbers at relatively late time. That is to say that there are extra degrees of freedom in the thermal bath at late time and then potential additional production of SM particles¹⁴. This bounds, that we will see, typically apply when the number of light mediators is large prior to the decay, which is mostly the case when it decouples relativistically because in this case, it decouples when not Boltzmann suppressed. But a relativistic decoupling for the light mediator is generic of light mediator models because it will typically decouple at the same time than DM: $T \sim m_{\text{DM}} > m_{\text{med}}$.

1.4 Cosmic microwave background

We have already discussed on how the measurements of the CMB anisotropies brought a tremendous evidence for DM. But the CMB also brings his own set of constraints on SIDM with light mediator. In this section, we will review how portal models can be constrained by the CMB.

1.4.1 CMB constraint on DM annihilation rate

If DM annihilates into electromagnetically charged particles (or directly into photons) during the recombination (around redshift $z_{\text{rec}} \simeq 1100$), it would inject energy into the thermal bath. The plasma composition (made of a mix of photons, electrons and baryons) could be perturbed. Indeed, because of this new energy source, a consistent proportion of neutral hydrogen could be ionised. This would increase the proportion of unbound electrons in the bath. CMB photons would thus be more scattered which would thicken the last scattering surface. Therefore, correlations in the temperature perturbation spectrum would be attenuated. Depending on the quantitative impact on the spectrum, this attenuation could be seen in the temperature angular power spectrum (Figure 1.8).

In practice, for a given model, this has strong consequences. If DM particles annihilate into electromagnetically charged particles (or directly into photons), the

¹⁴Through the decay or annihilation of the new degrees of freedom.

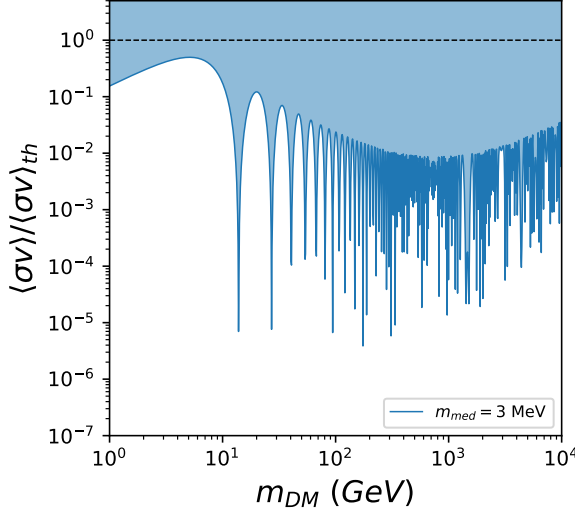


FIGURE 1.21: CMB upper bound on the s-wave annihilation rate into light mediators cross section, normalised to the thermal value. The dashed horizontal line corresponds to a cross section with the thermal value.

DM annihilation cross section is bounded from above by the CMB. If DM particles annihilate into neutral particles which can produce photons or charged particles, this bound obviously applies as well. In models such as benchmark portal models of Eqs. 1.48 and 1.53, the DM annihilates into a pair of light mediators and, thanks to the portal interaction, the light mediator particles decay into SM particles. Except if the annihilation into a pair of neutrinos (i.e. to not producing electromagnetic materials) is the only available channel, the constraint on the annihilation cross section at the time of recombination (i.e. at redshift $z \sim 1100$) is then

$$\langle\sigma v\rangle_{rec} \lesssim N_{\chi} \cdot 4 \times 10^{-25} \text{ cm}^3\text{s}^{-1} \left(\frac{f_{eff}}{0.1}\right)^{-1} \left(\frac{m_{\chi}}{100 \text{ GeV}}\right), \quad (1.62)$$

where f_{eff} is related to the fraction of the released energy ending up in photons or electrons, with $f_{eff} \gtrsim 0.1$ for any SM final states except neutrinos (see e.g. [122]), and where $N_{\chi} = 1, 2$ for Majorana and Dirac dark matter respectively.

The bound given in Eq. 1.62 has many implications which have been analysed at length in [123], [124]. In particular, Eq. 1.62 can be fully relevant when considering a specific model and fixing the coupling between the light mediator and the DM from to the constraint on the DM abundance today and assuming a secluded freeze-out

(i.e. $\chi\bar{\chi} \rightarrow XX$, with X the light mediator). On the one hand, in the case of the scalar portal, even if the light mediator decays into SM charged particles, since the DM annihilation process is p-wave (i.e. $\sim v^2$, with v the DM relative velocity), the annihilation at recombination will be suppressed ($v_{rec} \ll 1$). This constraint will then be automatically satisfied in the framework of the scalar portal model. On the other hand, in the case of the vector portal, the DM annihilation process is s-wave (i.e. $\sim v^0$). Thus, the upper bound given by Eq. 1.62 is strong enough to exclude most of the parameter space. Indeed, as we will see in Chapter 2, the Sommerfeld effect largely enhance the annihilation process at this time (see Figure 1 of [123]). This is due to the fact that DM particle at recombination time are highly non-relativistic ($v \lesssim 10^{-7}$) with respect to the annihilation time where $v \lesssim 1/4$. In Figure 1.21, we show constraints obtained in the vector portal case for a 3 MeV mediator mass. We have plotted the annihilation cross section at recombination divided by the one at freeze-out. The large number of resonances are characteristics of the Sommerfeld effect as we will see in Chapter 2. Every point localised in the blue shaded area is excluded. One then sees that, in order to not disturb too much the CMB spectrum, one requires a much smaller value of the annihilation cross section at recombination than at freeze-out. For the whole parameter space to be totally excluded (or not) relies on the possibility for the mediator to be lighter than two electrons ($m_{med} < 2m_e$). In this case, the light particle will essentially decay into neutrinos and will no longer affect the CMB, see Ref. [123] for a detailed discussion.

1.4.2 CMB constraints on mediator decay

We have seen in the previous subsection that CMB can provide an upper bound on the DM annihilation cross section as soon as the decay products can inject photons in the thermal bath. This means that if the light mediator is also present in a large proportion in the bath, its decay rate into SM particles (except neutrinos) could also be constrained in the same way (the decay rate and thus the lifetime will play an important role in this bound). If the light mediator is not much heavier than two electrons, it can decay only to e^\pm , neutrinos and photons. If, among these particles, the mediator decays mainly to electromagnetic channels (e^+e^- or $\gamma\gamma$) and if it is still present in the thermal bath at the time of recombination (i.e. $\tau_{med} \gtrsim 10^{12}$ sec), the energy the mediator will inject would change significantly the CMB anisotropy spectrum. This would have been already observed unless the light mediator has a short enough or a very long lifetime or if its abundance is low enough that the changes on the CMB anisotropy structure are smaller than experimental uncertainties. It is standard to illustrate this type of constraint in the $\tau_{med} - \frac{\Omega_{med}}{\Omega_{DM}}$ plane where $\frac{\Omega_{med}}{\Omega_{DM}}$ expresses the light mediator abundance (it would have today if it was not decaying) divided by the DM abundance today. Figure 1.22 gives then the upper

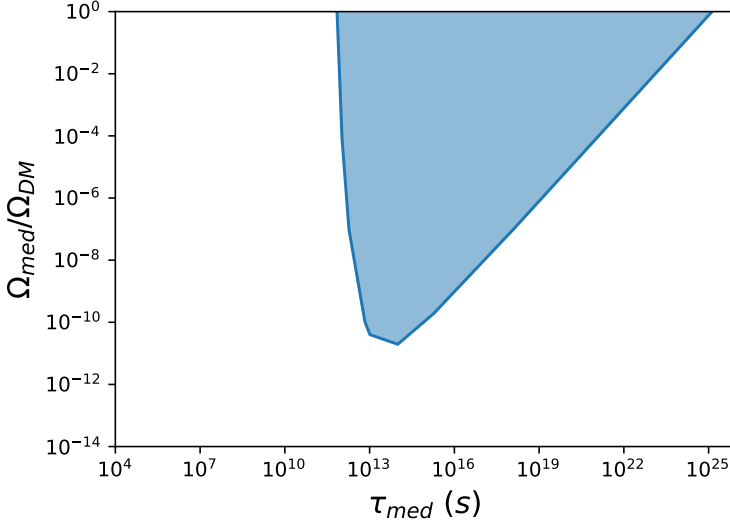


FIGURE 1.22: Upper bound on the amount of mediator particle there would be today if there were no decay [125] (see also [126]).

bound on this ratio as a function of the mediator lifetime.

For a lifetime larger than the age of the Universe today and $m_{\text{med}} < 2m_e$ (i.e. not producing electron-positron pairs), there are additional constraints coming from X-ray observation, which in a conservative way require [127]–[129],

$$\tau_{\text{med}} \gtrsim 10^{28} \text{ sec} \times \Omega_{\text{med}} h^2 / 0.12, \quad (1.63)$$

and which apply basically to any scenario as soon as the mediator decay produces SM particles (apart from neutrinos).

1.4.3 CMB constraint on N_{eff}

The precise measurement of the CMB anisotropies does not provide constraints only on the DM abundance today or on the number of electromagnetic materials a model can inject, but also on the Hubble rate at recombination. Since any modification of the Hubble rate is highly related to the number of relativistic degrees of freedom contained in the thermal bath, CMB also provides a stringent constraint on this quantity at the time of recombination. The number of relativistic degrees of freedom is generally expressed in terms of the effective number of neutrinos, N_{eff} . The most recent constraint on the minimum of effective neutrinos, given by the Planck satellite, is $2.66 < N_{\text{eff}} < 3.33$ at 2σ level [94]. It is straightforward

to translate these bounds into constraints on the light mediator lifetime and abundance at the time of neutrino decoupling. Indeed, light mediator particles which decay after neutrino decoupling reheat the photons but not the neutrinos. Thus, a particle decaying after neutrino decoupling, i.e. when $T < T_{\text{dec}}^\nu \simeq 1 \text{ MeV}$ (equivalently $t > t_{\text{dec}}^\nu \simeq 7 \text{ sec}$), will change the amount of relativistic particles and change the value of N_{eff} at this epoch. This constraint is thus only relevant if the decoupling time of the new light particle (t_{dec}) is bigger than the neutrino decoupling time (t_{dec}^ν). t_{dec} can be written in terms of the light mediator lifetime (τ_{med}) and the Lorentz boost factor ($B_{\mathcal{L}}(T_{\text{dec}})$): $t_{\text{dec}} = B_{\mathcal{L}}(T_{\text{dec}})\tau_{\text{med}}$. With $B_{\mathcal{L}}(T_{\text{dec}} < m_{\text{med}}) \simeq 1$ and $B_{\mathcal{L}}(T_{\text{dec}} > m_{\text{med}}) \simeq T_{\text{dec}}/m_{\text{med}}$ in a good approximation. We will not review more this effect since a detailed study of it has already been performed in Ref. [130]. In this reference, the authors have chosen to constrain the mediator number density divided by the photon number density at the time of decoupling $(n_{\text{med}}/n_\gamma)|_{T_{\text{dec}}}$, assuming a chemical decoupling of the light mediator from the thermal bath at $T_{\text{dec}} = 10 \text{ GeV}$. Thanks to the following conversion formula, it is easy to translate this bound into a bound on $\Omega_{\text{med}}/\Omega_{\text{DM}}$ (same ratio than previously).

$$\Omega_{\text{med}} h^2 \leq 8 \times 10^4 \left(\frac{g_*^{\text{eff}}(T_{\text{dec}})}{g_*^S(T_{\text{dec}})} \right) \left(\frac{m_{\text{med}}}{\text{MeV}} \right) \left(\frac{n_{\text{med}}(T'_{\text{dec}})}{n_\gamma(T_{\text{dec}})} \right) \left(\frac{T'_{\text{dec}}}{T_{\text{dec}}} \right)^3, \quad (1.64)$$

We show in Figure 1.23 the upper bound on $\Omega_{\text{med}}/\Omega_{\text{DM}}$ as a function of the mediator lifetime for $m_{\text{med}} = 60 \text{ MeV}$ (taken from [130]). This constraint is fully relevant for a particle decaying while still relativistic. Indeed, using Eq. 1.64 one can find from Ref. [130] that the light mediator number density given by its relativistic decoupling is perfectly compatible with these constraints if its lifetime is small enough. We give in Table 1.1, for both scalar and vector portal models and for various values of m_{med} , the upper bound on the light mediator lifetime.

All these lifetimes have been obtained from Ref. [130] assuming here too that $T_{\text{dec}} = 10 \text{ GeV}$. For another decoupling temperature, the bound will be moderately affected by a factor of the relativistic degrees of freedom contributing to the entropy, $g_*^S(10 \text{ GeV})/g_*^S(T_{\text{dec}})$ due to decoupling of relativistic species between both temperatures.

1.5 Big bang nucleosynthesis

New light degrees of freedom does not affect only the thermal history of the Universe at recombination, but may also easily affect the *Big Bang Nucleosynthesis* (BBN) process. In this section, after a brief explanation of what occurs during the BBN, we

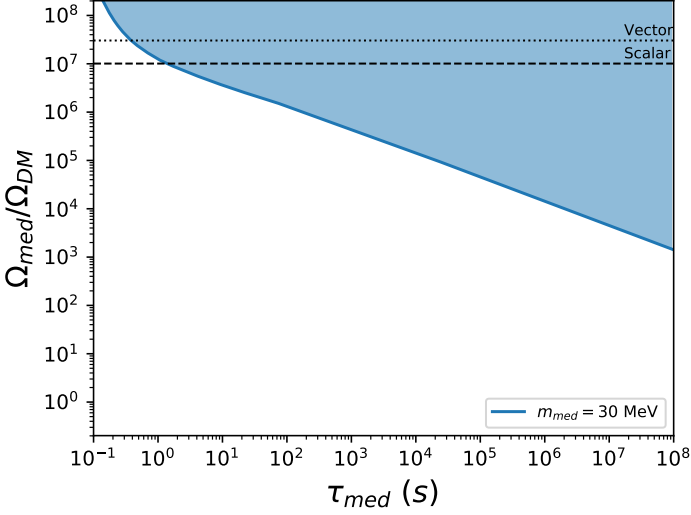


FIGURE 1.23: Upper bound on the amount of mediator particle there would be today if there was no decay [130] from the N_{eff} constraint. The dotted (dashed) line shows the value of Ω_{med}/Ω_{DM} one would expect from a relativistic decoupling of a non-decaying vector (resp. scalar) particle.

will review the two main ways for additional relativistic degrees of freedom to affect the BBN process. First, we will discuss the photodisintegration of light nuclei during and after the BBN process from decay of the light particle. Then we will see how the modification of light nuclei relative abundances from modification of the Hubble constant and entropy injection by the light mediator can constrain portal models.

1.5.1 Production of light nuclei

The BBN refers to the epoch, during the early Universe, when the light nuclei were formed. Let us recap the few steps which led to the formation of the lightest nuclei ${}^4\text{He}^{++}$, ${}^3\text{He}^{++}$, ${}^7\text{Li}^{+++}$ and ${}^2\text{H}^{+}$.

At high temperature, there was no free proton nor free neutron in the thermal bath. The Universe was exclusively made of elementary particles like quarks, electrons, But, due to the expansion of the Universe, its temperature continued to

$m_{\gamma'} \text{ (MeV)}$	0.01	0.03	0.1	0.3	1	3	10	30	100	300
N_{eff}	$10^{6.3}$	$10^{5.3}$	$10^{4.3}$	$10^{3.3}$	$10^{2.2}$	$10^{1.1}$	$10^{0.1}$	$10^{-0.4}$	$10^{-0.7}$	$10^{-0.9}$
Photodis./Entropy inj.	$10^{5.9}$	$10^{4.9}$	$10^{3.9}$	$10^{3.1}$	$10^{2.4}$	$10^{2.0}$	$10^{1.0}$	$10^{0.0}$	$10^{-0.4}$	$10^{-0.5}$
$m_\phi \text{ (MeV)}$	0.01	0.03	0.1	0.3	1	3	10	30	100	300
N_{eff}	$10^{7.3}$	$10^{6.3}$	$10^{5.3}$	$10^{4.3}$	$10^{3.2}$	$10^{2.1}$	$10^{1.1}$	$10^{0.1}$	$10^{-0.5}$	$10^{-0.7}$
Photodis./Entropy inj.	$10^{6.8}$	$10^{5.9}$	$10^{4.8}$	$10^{3.9}$	$10^{3.0}$	$10^{2.4}$	$10^{2.0}$	$10^{1.0}$	$10^{-0.1}$	$10^{-0.4}$

TABLE 1.1: Upper bound on the light mediator lifetime (in seconds) from N_{eff} , photodisintegration and Hubble constant/entropy injection constraints, assuming a relativistic decoupling of the light mediator for the vector portal model (top) and the scalar portal model (bottom). A value of $T'/T = 1$ has been assumed at DM freeze-out time.

cool down such that, at some point, it became cold enough for the QCD¹⁵ phase transition to occur, when $T \sim 1 \text{ GeV}$, at which point protons and neutrons were formed by the fusion of quarks. Even if the neutron particle is unstable and decays into proton, electron and anti-neutrino, the bath was sufficiently hot to ensure the reverse process to occur as fast as the direct process. That is to say that the neutron decay was in thermal equilibrium with the bath: $\Gamma_{n \rightarrow p+e+\bar{\nu}_e} \gg H$.

Thus, as long as the neutron decay and the conversion process (i.e. $n + e^+ \rightarrow p^+ + \bar{\nu}_e$) were in thermal equilibrium with the rest of the bath, the number of neutrons was equal to the number of protons in the bath, $n_n = n_p$. However, this equilibrium did not last for ever and protons started to be dominant. This happened when $T \lesssim \Delta m \equiv m_n - m_p$ where the number of neutrons started to decrease: $n_n \propto e^{-\Delta m/T}$. Later on, when the inverse decay stopped to be as efficient as the decay, the number of neutrons followed an usual decay law: $n_n \propto e^{-(t-t_{\text{dec}})/\tau_n}$ with t_{dec} the decay time and τ_n the neutron lifetime. The most favourable (energetically speaking) configuration for neutron to survive was to bind with protons and form deuterium. It was the beginning of a small chain of reactions which produced the lightest stable nucleus.

$$^1H^+ + ^1H^+ \rightarrow ^2He^{2+} \rightarrow ^2H^+ + e^+ + \nu_e \quad (1.65)$$

$$^2H^+ + ^1H^+ \rightarrow ^3He^{2+} + \gamma \quad (1.66)$$

$$^3He^{2+} + ^3He^{2+} \rightarrow ^6Be^{4+} \rightarrow ^4He^{2+} + ^1H^+ + ^1H^+ \quad (1.67)$$

¹⁵The Quantum Chromodynamics (QCD) is the theory of strong interactions. It describes how quarks and gluons interact and how they may form hadrons such as protons, neutrons, pions, kaons, ...

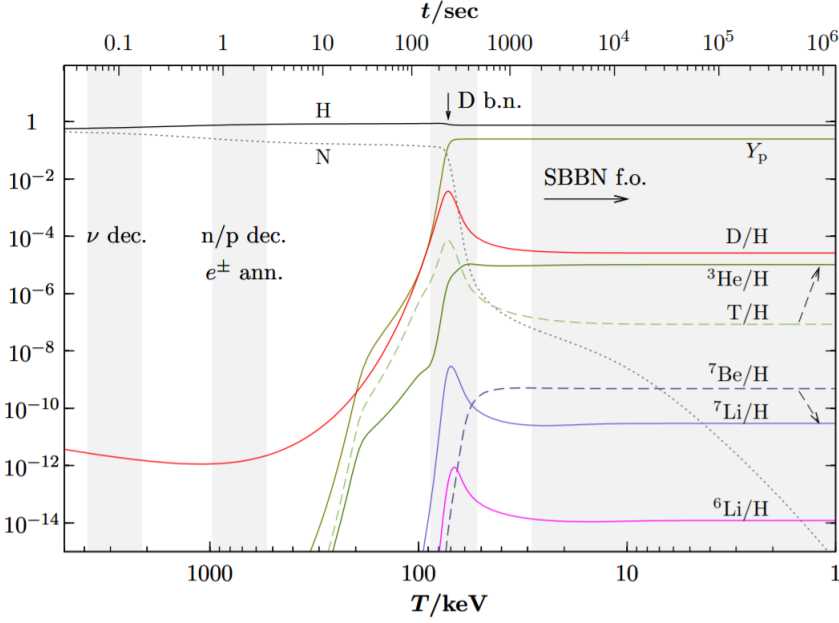


FIGURE 1.24: Evolution of abundance of light nuclei produced during BBN with respect to time and temperature, taken from [131].

Theoretically, this chain could have continued and form heavier nuclei since the temperature was still high enough to allow more fusions but, in practice it stopped. Indeed, the formation of ${}^4\text{He}^{2+}$ occurs very late because it has to wait for the deuterium to be first produced (this is called the "deuterium bottleneck"). The deuterium formation occurs also very late due to the fact that its binding energy is very small and that during a long time there were still too many photons with enough energy to dissociate the deuterium.¹⁶ Moreover, the fusion of two ${}^4\text{He}^{2+}$ or of a ${}^4\text{He}^{2+}$ and a proton would produce a nucleus with an atomic mass of 8 or 5 respectively and there is no such such nucleus. However, there is a small fraction of the ${}^3\text{He}^{2+}$ population which has been able to react with some ${}^4\text{He}^{2+}$ to produce a small proportion of ${}^7\text{Li}^{3+}$.

Figure 1.24 gives the light nuclei relative abundances with respect to time (as the temperature of the Universe decreases with time) [131]. One can see that the BBN started while the Universe had $T \sim 0.2$ MeV and stopped when the temperature reached a few keV. Afterwards, the relative abundance of light nuclei was fixed and

¹⁶The photons average kinetic energy was smaller than the deuterium binding energy, but there were so many photons with respect to deuterium than even the small proportion of photons with enough energy to dissociate the deuterium was large: $n_\gamma/n_B \sim 10^{10}$.

these relative abundances provide strong constraints on any new physics modifying the thermal bath at these energies.

1.5.2 Photodisintegration BBN constraints

If, by decaying, the light mediator produces eventually photons (either directly or indirectly from decay products), these photons could potentially dissociate the light nuclei formed during BBN. This would then change the relative abundances of light nuclei today which are known today with a good accuracy for some of them (see e.g. [132], [133]) such that constraints can be stringent as we will see.

This effect of photodisintegration will be particularly relevant if the light mediator decays into e^+e^- or $\gamma\gamma$ directly and also if these particles are energetic enough to dissociate light elements 2H , 3H and 4He . The minimum energy to dissociate these elements are $E_\gamma^{^2H} = 2.22$ MeV, $E_\gamma^{^3H} = 6.92$ MeV and $E_\gamma^{^4He} = 28.3$ MeV respectively. These thresholds imply that if the mass of the decaying particle lies below the lowest of the three (i.e. if $m_{\text{med}} < 4.4$ MeV) there is no constraint coming from photodisintegration. Moreover, due to the deuterium bottleneck that we have seen in the previous subsection, the light nuclei predominantly form only when $t \geq 180$ sec. Constraints are then much weaker for shorter lifetime or actually even up to $\sim 10^{3.5}$ sec.

1.5.3 BBN constraints from modification of the Hubble constant and entropy injection

Like in the case of CMB constraints, as long as the mediator has not decayed it modifies the Hubble constant. While when it eventually decays, it will inject entropy into the thermal bath. Both the Hubble constant modification and the entropy injection modify the relation between time and temperature, which can lead to significant modification of the light nuclei abundances when integrating the Boltzmann equations for the abundances of the nuclei. Since observations are able to precisely determine relative abundances of some of the light nuclei, it is then possible to constrain the light mediator number density prior to decay or, equivalently, the abundance it would have today if it was not decaying, as a function of its lifetime.

As for the previous constraint, this one is also relevant only if a sizeable fraction of the light mediator decays while the light elements are already dominantly formed. That is to say when $t > t_{\text{BBN}} \simeq 180$ sec, or equivalently when $T < T_{\text{BBN}} \simeq 0.07$ MeV. Which means that this constraint applies only if $t_{\text{dec}} = B_{\mathcal{L}}(T_{\text{dec}})\tau_{\text{med}} \gtrsim t_{\text{BBN}}$ where $B_{\mathcal{L}}(T_{\text{dec}}) \simeq T(t_{\text{dec}})/m_{\text{med}}$ is the approximate relativistic Lorentz boost

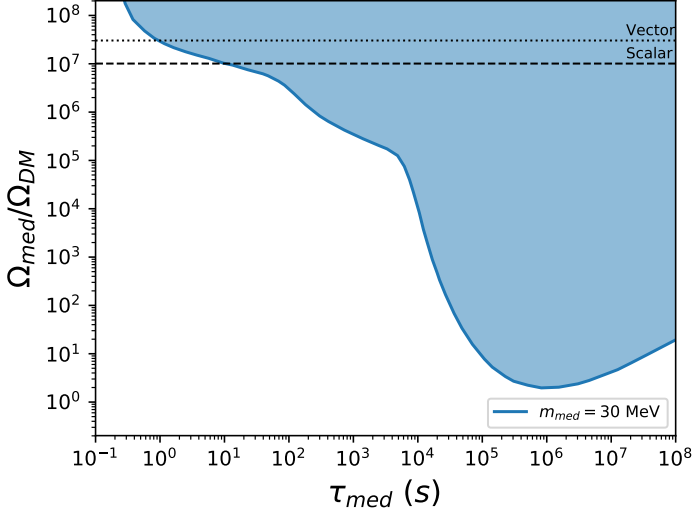


FIGURE 1.25: Upper bound on the amount of mediator particle there would be today if there was no decay [130] from the BBN constraint. The dotted (dashed) line shows the value of Ω_{med}/Ω_{DM} one would expect from a relativistic decoupling of a non-decaying vector (resp. scalar) particle.

factor which applies when $m_{med} \lesssim T^{BBN}$.

Similarly to the N_{eff} bound, we used in Table 1.1 the results taken from [130], to give the upper bounds on the light mediator lifetime that the Hubble constant/entropy injection constraints, together with the previous constraint, require. Results in this table are given assuming that the light mediator decouples relativistically at $T_{dec} = 10$ GeV. Looking at all constraints given in Table 1.1, one can conclude that, when the decaying particle decouples while still relativistic, the Hubble constraint and the entropy injection constraints turn out to be always more stringent than the constraint coming from the photodisintegration. We present in Figure 1.25 all constraints given by the BBN [130] in the plane $\tau_{med} - \frac{\Omega_{med}}{\Omega_{DM}}$ for $m_{med} = 30$ MeV.

1.6 Supernovae 1987a

Astrophysical observations are also considerably helpful in the quest to constrain DM portal models. Indeed, DM models with MeV-scale mediator can be probed by observations of supernovae collapse, but these bounds are model-dependant.

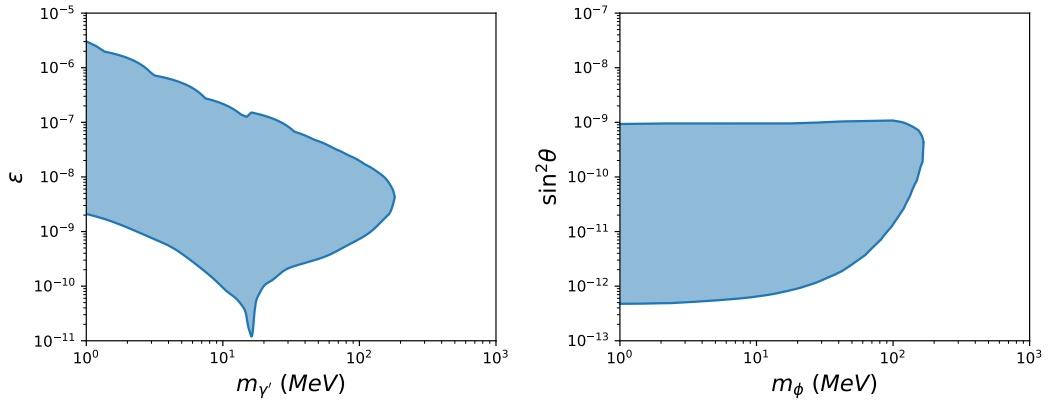


FIGURE 1.26: Constraints from observation of SN1987A for the vector portal model (left) (see e.g. [134]–[137]) and the scalar portal model (right) (see e.g. [137]–[144])

Inside supernovae, in particular for the SN1987A supernovae observed in 1987, proton-proton and proton-neutron scattering occur very often and can produce photons in the final state. In the kinetic-mixing portal model, those photons have a non-zero probability to oscillate into dark photons (i.e. the light mediator in this model). This effect can have a strong impact on the supernovae luminosity, on its internal dynamics or on the observable gamma ray flux. The one of these effects which will be dominant depends on where the oscillation mostly happen and where the dark photons mostly decay: in the core of the supernovae, between the core and the external surface or outside the object already travelling toward us. Observations of SN1987A can constrain the strength of the mixing parameter and the mediator mass since they are parameters ruling the conversion and the decay rates. It is then convenient to present bounds from supernovae in the $m_{\gamma'} - \epsilon$ plane for this portal model, see left panel of Figure 1.26. This figure can be summarised by requiring that $\epsilon \notin [10^{-10}, 10^{-6}]$ [134]–[137].

For the case of the scalar portal, the new light mediator could also be produced during the supernovae explosion and could contribute to its energy loss. The observable neutrino pulse which is emitted during the collapse of the core would thus be shortened. This kind of constraint has been used to reduce the viable parameter space of axions and axion-like particles for which the production in supernovae is dominated by radiative production off nucleons. Right panel of Figure 1.26 shows this constraint in the $m_\phi - \sin^2 \theta$ plane and can be summarised by imposing $\lambda_{\phi H} \times (v_\phi / \text{GeV}) \notin [3 \times 10^{-5}, 2 \times 10^{-3}]$ [137]–[144].

However, note that physics of supernovae is subject to systematic uncertainties

and such constraints (for both the vector and the scalar portal models) are generally considered as less robust than those based on cosmological production and decay of light mediator that we have seen in previous sections.

1.7 Direct detection

Aside from Cosmology and Astrophysics, if the DM is made of new particles, it should be possible to constrain a DM model from the particle physics perspective. There are many different particle physics experiments trying to constrain DM models, but most of them can be organised in three categories: direct detection, indirect detection and collider experiments. Let us start by developing the first category. Direct detection experiments try to constrain DM models by looking at heavy nucleus in ordinary matter which could be hit by some extra-terrestrial particles. In this case, the nucleus will move backward and emit an electromagnetic signal which will propagate in the material and is proportional to the strength of the collision. The energy recoil is then measured and, comparing it to what is expected from the known background, it is possible to provide an upper bound on the scattering cross section of DM on the chosen nucleus (or on nucleon).

It is usual for direct detection experiments to report their results in the plane: elastic collision cross section on nucleon ($\sigma_{\text{DM},n}$) and DM mass (m_{DM}). The considered cross section can be nucleus spin-dependent or spin-independent, but we choose to focus on the spin-independent cross section case as it provides the strongest constraint. Experimental constraints on the DM-nucleon spin-independent cross section are generally given assuming a contact interaction. It means that collaborations usually assume a short-range interaction between DM and the nucleon mediated by a heavy mediator. This assumption has as the consequence that the cross section can be taken as independent of the nucleus recoil energy (E_R):

$$\sigma_{\text{DM},n} \sim \frac{1}{(t - m_{\text{med}}^2)^2} = \frac{1}{(2m_N E_R + m_{\text{med}}^2)^2} \simeq \frac{1}{m_{\text{med}}^4}. \quad (1.68)$$

The contact interaction approximation holds when $m_{\text{med}} > \sqrt{2m_N E_R} \sim \mathcal{O}(40 \text{ MeV})$. Where we have used the typical value of the measured recoil energy which applies for the most sensitive current experiment, Xenon1T, which uses xenon material with $E_R \gtrsim 5 \text{ keV}$ and $m_{^{131}_{54}\text{Xe}} \simeq 123 \text{ GeV}$. We show in Figure 1.27 the latest results of the Xenon1T collaboration which follow a 1 tonne \times year exposure, considering this contact interaction assumption [145]. We can see on this figure that, for a 30 GeV DM mass, it goes down to $7 \times 10^{-47} \text{ cm}^2$.

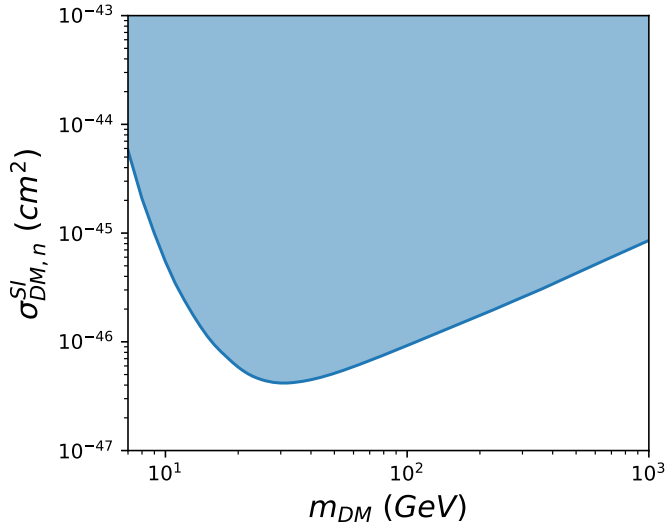


FIGURE 1.27: Upper bound on the DM-nucleon collision spin-independent cross section for a contact interaction from Xenon1T [145].

In this work, we are more interested in the long range interaction scenario (i.e. light mediator) where the cross section goes like $\sigma_{DM,n} \propto 1/(m_N E_R)^2$ for $m_{\text{med}} < \mathcal{O}(40 \text{ MeV})$ as we can see from Eq. 1.68. Then, the upper bound from Figure 1.27 cannot be directly applied to the light mediator case and need to be recast since, surprisingly, direct detection experiments like Xenon1T did not do an analysis devoted to the light mediator assumption. This is what we did and, even if this chapter is mostly introductory, we will here already present this original part. In fact, since the experimental recoil energy is typically of the order of a few keV, one understands that the scattering cross section is highly boosted in the light mediator case with respect to the heavy mediator case. To this end, we start from the differential rate of collisions (the number of events per second per unit of recoil energy)

$$\frac{dR}{dE_R} = N_T n_{DM} \int \frac{d\sigma}{dE_R} v f_{\oplus}(\vec{v}) d^3v, \quad (1.69)$$

with N_T the number of target nucleus, n_{DM} the local number density of DM and $f_{\oplus}(\vec{v})$ its velocity distribution in the Earth frame, which we take to be Maxwellian with r.m.s¹⁷ velocity $\sigma_v = 270 \text{ km/s}$ in the Galactic reference frame. The integration is made on $v \in [v_{\min}, c]$ where $v_{\min} = \sqrt{m_N E_R / 2\mu_{\chi N}^2}$ with $\mu_{\chi N}$ the DM-N reduced

¹⁷Root mean velocity: $\sigma_v \equiv \sqrt{\langle v^2 \rangle}$.

mass and c the speed of light. The DM-nucleus differential cross section given as a function of the recoil energy can be written as [146]

$$\frac{d\sigma}{dE_R} = \frac{m_N}{2\mu_{\chi p}^2} \frac{1}{v^2} \sigma_{\chi p}(E_R) Z^2 F^2(q r_A), \quad (1.70)$$

$$\frac{d\sigma}{dE_R} = \frac{m_N}{2\mu_{\chi n}^2} \frac{1}{v^2} \sigma_{\chi n}(E_R) A^2 F^2(q r_A). \quad (1.71)$$

Where $\mu_{\chi p}$ (resp. $\mu_{\chi n}$) is the DM-proton (resp. DM-nucleon) reduced mass and Z (resp. A) the nucleus atomic number (resp. the nucleus mass number). The $F(q r_A)$ is the nucleus form factor, which for concreteness we take from [146], [147]. The first of the two cross sections above is used if the mediator couples only to the proton, like in the kinetic mixing portal model where the interaction goes through the electromagnetic charge. The second is used when the mediator also couple to the neutrons. Like in the scalar portal model where the interaction goes through the Higgs coupling, the DM couples then in the same way to the proton and to the neutron (modulo small isospin breaking effects). For concreteness, these elastic collision cross sections of Figure 1.28 are given by,

$$\sigma_{\chi p}(E_R) = \frac{16\pi\mu_{\chi p}^2\alpha^2\kappa'^2}{\left(2m_N E_R + m_{\gamma'}^2\right)^2}, \quad (1.72)$$

$$\sigma_{\chi n}(E_R) = \frac{\mu_{\chi n}^2 y_{hnn}^2 \kappa_\phi^2}{\pi \left(2m_N E_R + m_\phi^2\right)^2}, \quad (1.73)$$

with α the QED fine structure constant and $y_{hnn} \simeq 1.2 \times 10^{-3}$ the h -nucleon-nucleon coupling constant [142]. Note that in Eqs. 1.72 and 1.73, we have introduced the DM-to-SM coupling which is, as we will see in Chapter 3, a combination of the SM-to-med and DM-to-med couplings: $\kappa' \equiv \epsilon\sqrt{\alpha'}/\alpha$ in the vector portal model and $\kappa_\phi \equiv Y_\chi \sin(2\theta)/2$ in the scalar portal model. When the mediator is lighter than the threshold given above (i.e. $m_{\text{med}} < 40$ MeV), direct detection constraints depend only on two parameters: the DM mass (m_{DM}) and the coupling between the DM and the SM (κ' and κ_ϕ). It is then natural to represent these constraints in the plane $m_{\text{DM}} - \kappa$.

In order to convert constraints on $m_{\text{DM}} - \sigma_{\text{DM},n}$ for a contact interaction into constraints on $m_{\text{DM}} - \kappa$ for a long range interaction, we will have to look a little bit closer to the shape of the differential rate. Indeed, for a same DM mass, the shape of the differential rate in the light mediator case can behave differently than

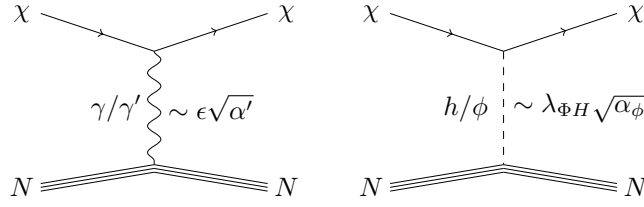


FIGURE 1.28: Feynman diagrams of DM elastic scattering on nucleus for the vector (left) and scalar (right) portal model.

in the heavy mediator case. Thus, the limit on the coupling strength for one value of the DM mass in the light mediator case, m_{DM} , cannot be obtained directly from the limit in the heavy case. Instead, one must look for the value of the DM mass in the heavy case, $m_{\text{DM}}^{\text{heavy}}$, for which the differential rate matches the best the differential rate obtained in the light mediator case for the DM mass considered, i.e. m_{DM} . This must be done within the range of the energy recoil where the differential rate is the highest as given by the efficiency form factor. The measured differential rates fall rapidly at low and high recoil energies and this regardless of the type of interactions. These experimental features allow to convert every couple $(m_{\text{DM}}^{\text{heavy}}, \sigma_{\text{DM},n})$ from Figure 1.27 onto a new couple (m_{DM}, κ) . In practice, to get a proxy for the observable differential rate,

$$\left(\frac{dR}{dE_R}\right)_{\text{exp}} = \epsilon(E_R) \frac{dR}{dE_R}, \quad (1.74)$$

where $\epsilon(E_R)$ is the detector efficiency from Figure 1 in [145] and with dR/dE_R given by Eq. 1.68. The differential cross section which appears in the expression of the differential rate for a short range interaction is the same as given in Eq. 1.73 but with a constant cross section. For every couple $(m_{\text{DM}}^{\text{heavy}}, \sigma_{\text{DM},n})$ along the upper bound line in Figure 1.27, we then determine the couple (m_{DM}, κ) that would have a similar observable differential rate $(dR_{\text{DM}}/dE_R)_{\text{exp}}$. Concretely, we consider the couple (m_{DM}, κ) that minimizes the quadratic distance between the two rates

$$\Delta_{\text{DR}}^2 = \frac{1}{R_{\text{exp}}^2} \int dE \epsilon(E)^2 \left(\left(\frac{dR}{dE}\right) - \left(\frac{dR_{\text{DM}}}{dE}\right) \right)^2, \quad (1.75)$$

where R_{exp} is the total measurable rate from Eq. 1.74 and dR_{DM}/dE_R is the differential rate corresponding to a candidate with a light mediator.

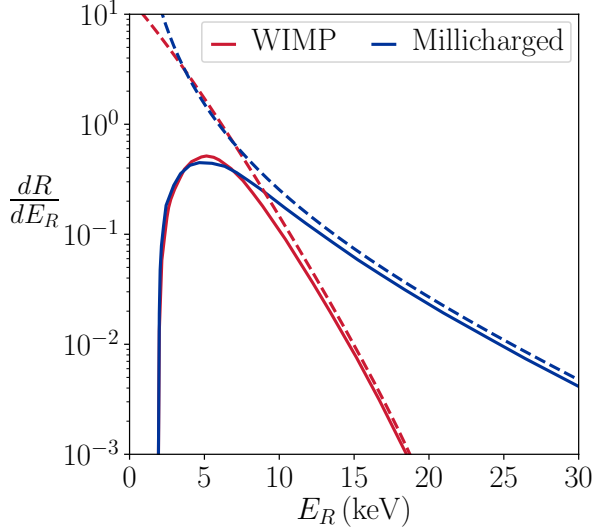


FIGURE 1.29: Red solid: differential rate for a $(m_{\text{DM}}, \sigma_{\text{DM},n}) = (15 \text{ GeV}, 10^{-46} \text{ cm}^2)$. Blue solid: best fit for a DM candidate with long range interactions with $(m_\chi, \kappa) = (70 \text{ GeV}, 3.1 \times 10^{-11})$. The error is $\Delta_{\text{DR}} \approx 25\%$. The dashed curves are for the same candidates, but not taking into account Xenon1T efficiency. Taken from [84].

In Figure 1.29 is shown an example of this recasting procedure according to our criteria (Eq. 1.75). Starting from the couple $(m_{\text{DM}}^{\text{heavy}}, \sigma_{\text{DM},n}) = (15 \text{ GeV}, 10^{-46} \text{ cm}^2)$ from the Xenon1T upper bound (see Figure 1.27), we have computed the theoretical (dashed red) and observable (solid red) differential rates. The latter is obtained from the former by multiplying by the experimental efficiency curve. Taking the kinetic mixing model (i.e. Eqs 1.70 and 1.72) for example, our procedure of Eq. 1.75 tells us that the candidate $(m_\chi, \kappa) = (70 \text{ GeV}, 3.1 \times 10^{-11})$ produces a differential rate which minimizes Δ_{DR} . Thus, we show also on Figure 1.29 the theoretical (dashed blue) and observable (solid blue) differential rates. At this point, we must emphasise that both differential rates (from heavy and light mediator cases) match mostly at low recoil energies $E_R < 10 \text{ keV}$ which correspond to higher expected number of events. In the example we are showing in Figure 1.29 [84], the error is $\Delta_{\text{DR}} \simeq 25\%$ while the error on the total number of event (see Eq. 1.76 below) is $\Delta_{\text{TR}} \simeq 20\%$.

Defining the error on the total number of event N_{DM} as,

m_{DM} (GeV)	$\kappa' (10^{-11})$	$\kappa_\phi (10^{-9})$	$m_{\text{DM}}^{\text{heavy}}$ (GeV)	$\sigma_{\text{DM},n} (\text{cm}^2)$	Δ_{DR}	Δ_{TR}
15	3.0	1.0	10	5.6×10^{-46}	16%	15%
70	3.1	1.0	15	1.1×10^{-46}	23%	22%
200	5.2	1.8	20	5.9×10^{-47}	22%	13%
500	8.2	2.8	22	5.3×10^{-47}	26%	3%

TABLE 1.2: Upper bounds on the mixing parameter κ (2nd and 3rd columns) for four DM masses (1st column), based on the correspondence with WIMP exclusion limits (4th and 5th columns). The last two column give respectively the error on the differential rate Δ_{DR} and total rate Δ_{TR} .

$$\Delta_{\text{TR}} = \frac{N_{\text{DM}} - N_{\text{DM}}^{\text{heavy}}}{N_{\text{DM}}^{\text{heavy}}}, \quad (1.76)$$

where $N_{\text{DM}}^{\text{heavy}}$ is the total number of event obtained in the heavy mediator case. One can then compare the two errors Δ_{DR} and Δ_{TR} . As an illustration, we give in Table 1.2 several DM candidates from the heavy mediator case and the one it corresponds to in the light mediator case. With the error on the total rate Δ_{TR} and the error on the differential rate Δ_{DR} . We emphasise that the errors on the total rate are positive, meaning that the total number of events is always larger for the χ particle than for the corresponding DM particle with a massive mediator. Reducing the error on the total number of events would thus require decreasing the parameter κ . In that sense, we deem our constraints on κ to be conservative.

We show in Figure 1.30, the bound from Figure 1.27 adapted for a light mediator scenario following our procedure we have just explained. From this figure, we can conclude that the direct detection constraint requires $\kappa_\phi \lesssim 10^{-9}$ and $\kappa' \lesssim 3 \times 10^{-11}$ for a Higgs portal and a kinetic mixing portal respectively. This applies as soon as the light mediator below is lighter than $m_{\text{med}} \ll 40$ MeV and the DM is heavier than $m_{\text{DM}} \gtrsim \text{GeV}$, which is usually the case while considering self-interactions constraints. To consider a value of $m_{\text{med}} \sim 100$ MeV hardly relaxes this bound. The very tiny values of the coupling, that direct detection can probe, show that this type of experiments is an extremely powerful tool to constrain light mediator scenarios. For comparison, in the heavy mediator scenario, with the mediator mass of order of the electroweak scale, direct detection experiments are able to probe coupling down to typically 10^{-1} or 10^{-2} . Let us finally mention that in [84], we have shown that these bounds on the DM-to-SM coupling in the light mediator scenario allow to constrain FI scenario as the one described in Subsection 3.2.2. This will not be more detailed in this thesis, see [84] for more details.

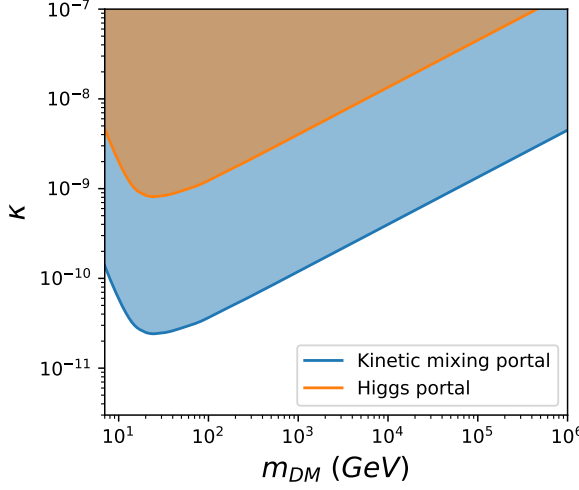


FIGURE 1.30: Direct detection constraints for an interaction mediated by a light mediator (i.e. $m_{\text{med}} \lesssim 30$ MeV). The blue (orange) solid line is the current constraints from Xenon 1T experiment [145] from [84].

1.8 Indirect detection

We have already insisted on the key role of the mediator in order to constrain DM portal models (for CMB, BBN and particularly for direct detection as we just discussed), especially if the mediator is much lighter than the DM. This mass hierarchy turns out to play an important role for indirect detection experiments too. That is to say for intensity of the flux of particles that could result from DM annihilation or decay happening today in the Milky Way or beyond, see Section 2.2. A mediator much lighter than the DM particle will boost the DM annihilation today into lighter particles (SM or not) via the Sommerfeld effect. This effect is known for being crucial in indirect detection experiments for s-wave annihilation. It will considerably enhance indirect detection rates, as a result of the small dark matter particle velocity today. On the other hand, for a p-wave annihilation, indirect detection signals are usually not studied because considered as hopeless as they are suppressed by 2 powers of the velocity v (instead of 0 power for the s-wave annihilation). Nevertheless, in presence of an extremely strong mass hierarchy between the DM and the light mediator, the Sommerfeld effect can compensate for this suppression, a property which has been hardly considered (see [148] for an example of non self-interacting model). The Sommerfeld enhancement factor, which multiplies the annihilation cross section at tree level, goes like $1/v^3$ for p-wave annihilation, giving an overall $1/v$. This gives, in both s-wave and p-wave cases, an overall $1/v$

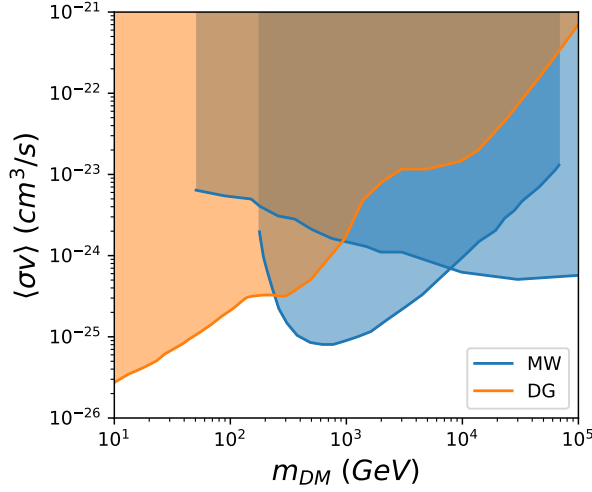


FIGURE 1.31: Indirect detection constraints on the DM annihilation cross section into a e^+/e^- pair. Blue solid lines show current constraints for annihilation in the Milky Way and have been taken from Fermi-LAT, H.E.S.S and Antares experiments [149]–[153]. Orange solid line shows current constraints for annihilation in dwarf galaxies, taken from Fermi-LAT and MAGIC experiments [154]. All these constraints assume a NFW profile.

dependence. This arises in the same way as for the Sommerfeld boost enhancing the cross section at the CMB time. The difference comes from the fact that at recombination the velocity is so small that the scaling in v does not go anymore in $1/v$ as it is the case today but scales as v^0 and v for s-wave and p-wave respectively [123]. Thus, for p-wave annihilations, the CMB constraint is clearly worse than for s-wave annihilations, but for indirect detection, this is not the case. This relevant property will be further studied below in Chapter 2.

We present in Figure 1.31 the current experimental upper bounds on the annihilation cross section today. The distinction between annihilation of DM in the Milky Way (MW) galactic centre and in dwarf galaxies (DG) comes from the fact that indirect detection observations both look at a flux of particles coming from the MW or DG, but that the DM velocity is not expected to be the same in both environments. In the Milky Way, $v_{DM}^{MW} \simeq 2 \times 10^{-3}$ while in dwarf galaxies, $v_{DM}^{DG} \simeq 1 \times 10^{-5}$.

1.9 Production at colliders

Last but not least, instead of detecting directly or indirectly DM particles, one can think to produce DM particles directly in collider experiments. In practice, since it is unlikely to detect a particle which supposedly interacts feebly with the SM, collider experiments are looking for signals with missing energy or with a lack of SM particles where more were expected if there was no interaction with DM. For example, in the light scalar mediator case, the Higgs portal interaction, Eq. 1.48, induces an invisible decay channel for the Higgs boson, $H \rightarrow \phi\phi$. The Higgs decay rates into SM particles are well known theoretically and the corresponding lifetime and branching ratios are now measured with a good accuracy. It is then possible to constrain the Higgs invisible decay width with collider experiments. The current LHC bound is obtained combining two constraints given by CMS and ATLAS collaboration at LHC¹⁸. The first comes from the fact that expected SM decay products are missing while looking at Higgs decay events. This gives an upper bound on the branching ratio of the Higgs invisible decay channel: $\text{BR}(h \rightarrow \text{inv.}) < 0.19$ (95% C.L.) [155]. This upper bound can be easily translated into an upper bound on the invisible decay width: $\Gamma_{\text{inv}} < 0.96$ MeV. The second constraint comes from the observed Higgs production rate and impose an upper bound on the ratio of experimental and theoretical Higgs production rates: $\mu \equiv [\sigma_h \text{BR}(h \rightarrow \text{SM})]_{\text{exp}} / [\sigma_h \text{BR}(h \rightarrow \text{SM})]_{\text{SM}} < 0.89$ (95% C.L.) [156] where σ_h gives the Higgs production cross section. Again, this last bound is translated into $\Gamma_{\text{inv}} < 0.50$ MeV. This value has to be compared to the decay width induced by the scalar portal interaction:

$$\Gamma_{H \rightarrow \phi\phi} \simeq 0.50 \left(\frac{\lambda_{\phi H}}{0.01} \right)^2 \text{ MeV.} \quad (1.77)$$

If the decay into two light mediator particles is the only invisible decay channel, this bound can be converted into an upper bound on the portal strength parameter: $\lambda_{\phi H} < 0.01$.

It is also possible to constrain the scalar portal scenario by looking for meson decays involving the light mediator in the final state (see e.g. Figure 3 of [157]). As a summary, this constraint requires that $\sin \theta < 3 \times 10^{-4}$ for a mediator mass smaller than $m_\phi \leq 100$ MeV, but does not constrain the model for heavier mediator masses.

For the kinetic mixing portal, there are many constraints applying on the mixing parameter ϵ , but all of them are relevant for rather large kinetic mixing value. As an example, the LHCb detector is looking for dark photon decays ($\gamma' \rightarrow \mu^+ \mu^-$) which

¹⁸Large Hadron Collider.

could have been produced in proton-proton collisions with a centre-of-mass energy of 13 TeV. This experiment is able to exclude kinetic mixing of order $\epsilon \sim 10^{-5}, 10^{-4}$ for dark photon masses of about $m_{\gamma'} \sim 200, 300$ MeV [158]. Other constraints can be found in e.g. [95], [159]–[162].

1.10 A global picture

Finally, we conclude this long introducing chapter by collecting all the above information to emphasise how self-interacting DM models are constrained in many ways. Indeed, throughout this chapter, we have seen that there are three kinds of constraints applying on DM models (illustrated in Figure 1.32):

- Particle physics experiments dominantly constrain the strength of the interaction between DM and SM particles. They require a small interaction strength since no DM candidate has been discovered for now;
- Small scale structures probe the strength of the interaction between DM and the mediator, i.e. the HS interactions. Problems at small scale can be alleviated if the DM self-interaction cross section is strong enough;
- Cosmological and astrophysical observations test, above all, the interaction between the mediator and SM particles. They exclude a range of mediator lifetime or, for example, small couplings unless if very tiny.

All in all, small scale structures constraints together with cosmological and astrophysical observations suggest that DM should couple significantly to some SM particles while particle physics experiments forbid it. This tension seems inevitable and seems very difficult to alleviate in minimal DM models. This was one of the starting points of this thesis. In the following chapters, we will see how these many constraints can be partially or totally evaded and what is the price to pay for that in terms of assumptions to be made, extra particles to assume, etc

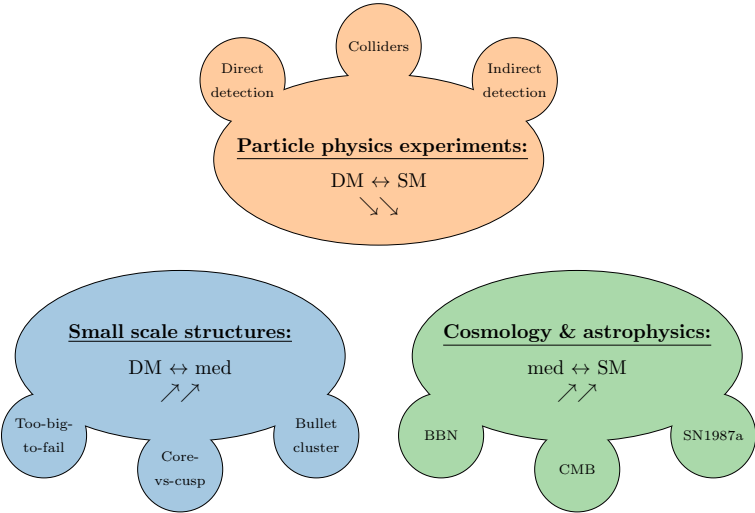


FIGURE 1.32: Illustration of tensions between all observations on SIDM with light mediator.

Chapter 2

The Sommerfeld effect

During an interaction between two non-relativistic particles, if they are close enough to each other¹, some non-perturbative effects can be significant. The Sommerfeld effect describes how two particles, if they couple to an additional lighter particle, can exchange this particle many times before that the proper interaction takes place [163] as depicted in Figure 2.1. The exchange of those particles can be determined from the non-relativistic potential holding between the incident particles. This potential can be either attractive or repulsive depending on the types and natures of the interactions and the involved particles.

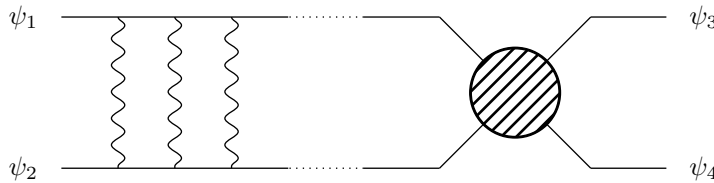


FIGURE 2.1: Illustration of the Sommerfeld effect for a two-to-two process.

This Sommerfeld effect has an important impact for DM in many different contexts as DM freeze-out, DM self-interaction and DM indirect detection, where all of those situations involve non-relativistic scattering of two DM particles. This will have a major impact on all subsequent chapters. Results discussed in this second chapter are partially new and unpublished while others have been detailed in [85].

¹To be define quantitatively below.

2.1 Self-scattering case

2.1.1 The dimensionless Schrödinger equation

Non-relativistic scattering of two DM particles can be determined from the Schrödinger equation which describes how a wave function (associated to the motion of particle) is modified by the action of an external potential well. Thus, this equation naturally encodes the Sommerfeld enhancement such that one must solve the Schrödinger equation for the reduced DM two-particle system. Moreover, we have learned from scattering theory that the differential cross section can be related to the out-coming wave function. Indeed, if the out-coming particles are of the same nature of the incoming particles (i.e. a simple self-scattering), one can write the out-coming wave function $\psi(\vec{r})$ as the incoming wave (which is simply a spherical wave) plus a perturbation:

$$\lim_{r \rightarrow \infty} \psi(\vec{r}) \simeq e^{i\vec{k} \cdot \vec{r}} + f(\theta) \frac{e^{ikr}}{r}, \quad (2.1)$$

where \vec{r} is the position vector of both particles relatively, \vec{k} the relative impulsions vector and $f(\theta)$ is a function of the azimuthal angle of the scattering in spherical coordinates. The f function could be very complicated in general, but assuming an isotropic, short-ranged and elastic scattering, it can be expressed using the Legendre polynomial basis:

$$f(\theta) = \sum_{l=0}^{\infty} (2l+1) f_l(k) P_l(\cos \theta), \quad (2.2)$$

with f_l the partial wave scattering amplitudes for l the angular momentum quantum number of the incoming wave and P_l the Legendre polynomials. It is usual to use the phase shift parametrisation of the partial wave scattering amplitudes for each wave: $f_l(k) = e^{i\delta_l(k)} / k \sin \delta_l(k)$ such that the differential cross section can be written in terms of the phase shifts. Indeed, one can show that the differential cross section can be related to this $f(\theta)$ function by

$$\frac{d\sigma}{d\Omega} = |f(\theta)|^2. \quad (2.3)$$

We then finally have for the differential cross section,

$$\frac{d\sigma}{d\Omega} = \frac{4\pi}{k^2} \sum_{l=0}^{\infty} (2l+1) \sin^2 \delta_l(k). \quad (2.4)$$

From this last expression, we understand that one must solve the Schrödinger equation for the reduced (incoming) two-particle system if one wants the full self-scattering cross section with the Sommerfeld enhancement taken into account. Indeed, since the Schrödinger equation describes the evolution of the reduced two-particle wave function, solving it gives the wave function which, as we just saw, can be related to the differential cross section through the phase shift δ_l . Then, one has, in principle, to integrate the differential cross section to get the total self-interacting cross section:

$$\sigma = \int \frac{d\sigma}{d\Omega} d\Omega. \quad (2.5)$$

However, this cross section develops a divergence for the light mediator case known as the forward-scattering divergence. This divergence comes from the fact that at very small relative velocities, that is to say when angle between the trajectories of both incoming particles tends to zero, $\cos \theta \rightarrow 1$, the trajectories remain unchanged after the interaction. To regulate this divergence, assuming classical distinguishability between incoming particles², one can instead consider the transfer cross section which is obtained from the differential cross section, but weighted by the fractional longitudinal momentum transfer:

$$\sigma_T = \int (1 - \cos \theta) \frac{d\sigma}{d\Omega} d\Omega. \quad (2.6)$$

The Schrödinger equation describing the evolution of the reduced two-particle wave function for particles of mass m_ψ and impulsion \vec{k} in a potential V is given by,

$$\frac{1}{m_\psi} \nabla^2 \psi_k - V(r) \psi_k = -\frac{k^2}{m_\psi} \psi_k, \quad (2.7)$$

where r is the radial coordinate in spherical coordinates and ∇ is the gradient operator. Note the missing factor of two wherever the mass appears compared to the Schrödinger equation of a lonely free particle. This is due to the fact that we are considering the two-particle system wave function and thus its mass is the reduced mass which corresponds to $\frac{1}{2}m_\psi$. To this equation we impose as boundary

²This assumption will be always valid for what is our concern since we consider only DM Dirac fermion, see [121], [164] for more details.

conditions that the waves produced by the perturbation at $r = 0$ are out-going: $\lim_{r \rightarrow \infty} \psi_k(r) \sim e^{ikx} + f(\theta) \frac{e^{ikr}}{r}$. Where we assumed that the incoming wave is going along the x-axis and where $f = f(\theta)$ can be written as in Eq. 2.2. In other words, before entering inside the zone of influence of the potential, the incoming wave is a plane wave (as it should) which is modified only when close to the perturbation at $r = 0$. Later, far from the perturbation, the out-going wave is the original plane wave plus a spherical wave due to the central potential as required by Eq. 2.1. Assuming a spherical symmetry for the potential, the wave function can be developed on the spherical harmonic basis [165],

$$\psi_k(r, \theta, \phi) = \sum_{l=0}^{\infty} \sum_{m=-l}^l R_{k,l}(r) Y_l^m(\theta, \phi). \quad (2.8)$$

Imposing invariance under rotation for the wave function, 2.7 becomes,

$$\frac{1}{m_\psi r^2} \frac{\partial}{\partial r} \left(r^2 \frac{\partial R_{k,l}}{\partial r} \right) - \frac{l(l+1)}{m_\psi r^2} - V(r) R_{k,l} = -\frac{k^2}{m_\psi} R_{k,l}, \quad (2.9)$$

$$R_{k,l}(r \rightarrow \infty) \rightarrow \frac{1}{r} \sin \left(kr - \frac{l\pi}{2} + \delta_l(r) \right), \quad (2.10)$$

where the second equation which normalises the function $R_{k,l}$ stems from the fact that the wave function oscillates and goes to zero very far from the potential. The phase shift δ_l is there to regularise the wave function such that it does not diverge when $r \rightarrow 0$. Equation 2.9 can be written as,

$$\left(\frac{1}{r^2} \frac{\partial^2}{\partial r^2} + \frac{2}{r} \frac{\partial}{\partial r} - \frac{l(l+1)}{r^2} - m_\psi V(r) + k^2 \right) R_{k,l} = 0, \quad (2.11)$$

In the simplest scenario where the mediator particle responsible for the self-scattering is a boson and considering a Dirac fermion as interacting particles, the potential interaction can be represented by a Yukawa potential at leading order. It is the case for the scalar portal model and the vector portal model developed in Eqs. 1.48 and 1.53 respectively. As just said, in those scenarios the potential is the ordinary Yukawa potential:

$$V_\phi(r) = -\frac{\alpha_\phi}{r} e^{-m_\phi r}, \quad (2.12)$$

$$V_{\gamma'}(r) = \pm \frac{\alpha'}{r} e^{-m_{\gamma'} r}. \quad (2.13)$$

The minus signs indicate an attractive potential while the plus sign indicates a repulsive one. The scalar potential can be only attractive as it allows only particle/antiparticle scatterings while the vector potential also allows particle/particle and antiparticle/antiparticle scatterings such that the potential in this case can also be repulsive. One can now use the explicit form of the potential into Eq. 2.11 and define a dimensionless function and a dimensionless variable as suggested in [121]:

$$\chi_l \equiv r R_{k,l}, \quad (2.14)$$

$$x \equiv \alpha_{\text{med}} m_\psi r, \quad (2.15)$$

where α_{med} can be either α_ϕ in the scalar portal model or α' in the vector portal model. Eq. 2.11 becomes,

$$\left(\frac{d^2}{dx^2} + \frac{v^2}{4\alpha_{\text{med}}^2} - \frac{l(l+1)}{x^2} \pm \frac{1}{x} e^{-x m_{\text{med}}/\alpha_{\text{med}} m_\psi} \right) \chi_l(x) = 0. \quad (2.16)$$

Here, we would like to emphasise the fact that Eq. 2.16 depends only on three dimensionless parameters: l , $v/2\alpha_{\text{med}}$ and $\alpha_{\text{med}} m_\psi/m_{\text{med}}$. As already mentioned above, l is the angular momentum quantum number and indicates in which configuration the incoming wave is. The two other parameters can also be studied, but first let us define for clarity,

$$a \equiv \frac{v}{2\alpha_{\text{med}}}, \quad (2.17)$$

$$b \equiv \frac{\alpha_{\text{med}} m_\psi}{m_{\text{med}}}. \quad (2.18)$$

The first parameter, a , regulates the strength of the bound of the incoming particles. Indeed, the larger the relative velocity is, the more it is difficult for the incoming particles to interact with each other as they have "less time" to interact. Moreover, the smaller the coupling is, the less sensitive to the potential well the particles are. In other words, on the one hand, a large value of the a parameter indicates for each of the two incoming particles a small sensitivity to the other particle presence such that the Sommerfeld enhancement will be small. On the other hand, a small value means a strong Sommerfeld effect.

The second parameter, b , regulates the mass hierarchy between the incoming particles and the exchanged one and more precisely the sensitivity to this hierarchy. Larger the mass hierarchy is, easier it is for the incoming particles to produce the mediator a large number of time as represented in Figure 2.1. Note that b is

not exactly the mass ratio, but contains the DM-to-med coupling. This weights the DM mass by α_{med} such that it is in practice the product $\alpha_{\text{med}} m_{\text{DM}}$ which has to be compared with the mediator mass m_{med} . This can be understood as following: the larger the DM-to-med coupling is, the less heavy the DM need to be compared to the mediator in order to be sensitive to the potential well. Indeed, if the mediator is much lighter than the DM, but the DM-to-med coupling is approximately zero, no Sommerfeld effect can enhance the cross section. Thus, this parameter indicates how strongly coupled to the potential well the incoming particles are.

In terms of these dimensionless parameters, the Schrödinger equation for a two-particle system which interacts through a Yukawa potential can be written,

$$\left(\frac{d^2}{dx^2} + a^2 - \frac{l(l+1)}{x^2} \pm \frac{1}{x} e^{-x/b} \right) \chi_l(x) = 0. \quad (2.19)$$

2.1.2 Relic density requirement for a freeze-out

Before applying what we just have seen to the portal models we consider, let us use the relic density constraint in a freeze-out scenario (see Eq. 1.41) to fix the DM-to-med coupling α'/α_ϕ . To do so, one needs to compute the thermally averaged cross section as given in Eq. 1.34. Albeit this expression could be in general very complicated, the square of the Møller velocity³ v of the incoming particles is small at DM decoupling $v_{\text{dec}}^2/c^2 \simeq 0.24^2 \ll 1$ such that one can expand the annihilation cross section in power of v^2 , see [166], [167] and references therein. One has,

$$\langle \sigma v \rangle \simeq \langle \sigma v \rangle_s + \langle \sigma v \rangle_p v^2 + \langle \sigma v \rangle_d v^4 + \dots, \quad (2.20)$$

where s, p, d stand for s-wave, p-wave and d-wave respectively which corresponds to an angular momentum quantum number of $l = 0, 1, 2$ respectively⁴.

The thermally averaged DM annihilation in the scalar and vector portal models as depicted in Figure 2.2 are given by

³The Møller velocity is defined in terms of the velocity of the two incoming particles \vec{v}_1 and \vec{v}_2 by $v \equiv \sqrt{|\vec{v}_1 - \vec{v}_2|^2 - |\vec{v}_1 \times \vec{v}_2|^2}$. It can be simplified to $v = 2\sqrt{1 - 4m_{\text{DM}}^2/s}$ with s the Mandelstam variable for pair annihilation.

⁴The wave naming follows the nomenclature of atomic physics.

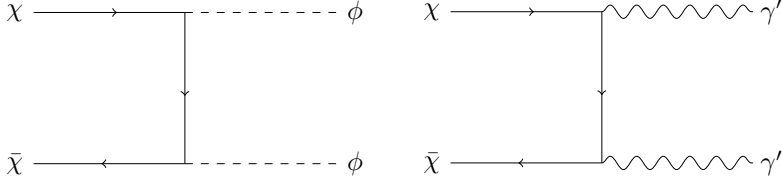


FIGURE 2.2: Feynman diagram corresponding to the DM annihilation process responsible for the freeze-out mechanism for the Higgs portal model (left) and the kinetic mixing portal model (right).

$$\langle \sigma v \rangle_{\bar{\chi}\chi \rightarrow \phi\phi} = \frac{3v^2}{4} \frac{\pi \alpha_\phi^2}{m_{\text{DM}}^2} \sqrt{1 - \frac{m_{\phi^2}}{m_{\text{DM}}^2}}, \quad (2.21)$$

$$\langle \sigma v \rangle_{\bar{\chi}\chi \rightarrow \gamma'\gamma'} = \frac{\pi \alpha'^2}{m_{\text{DM}}^2} \sqrt{1 - \frac{m_{\gamma'^2}}{m_{\text{DM}}^2}}, \quad (2.22)$$

at leading order in v^2 and at tree level. Note that, as we will see in Section 2.2, Sommerfeld enhancement is totally negligible for DM annihilation at decoupling such that we neglected it while computing the DM relic density. Plugging Eqs 2.21 and 2.22 into the expression of the DM relic density in terms of the DM annihilation cross section (Eq. 1.41), one is then able to fix the DM-to-med coupling as a function of the two left couplings: the DM and mediator masses (the velocity being fixed at DM decoupling as mentioned above). Figure 2.3 gives contours of the DM-to-med coupling in the DM versus mediator mass plane for both benchmark models we consider.

2.1.3 Dark Matter self-interactions

Now that we have seen how to compute the DM self-interactions and that we have fixed the DM-to-med coupling in Figure 2.3, we are able to actually constrain the DM versus mediator mass plane by the small scale structure constraint of Section 1.3 for both the scalar and the vector portal models presented in Chapter 1 and studied in the rest of this thesis.

We saw above in Eq. 2.12 that in the scalar portal model, there is only an attractive contribution to self-interactions from the Yukawa potential such that only one of the two Schrödinger equations of Eq. 2.19 has to be solved (process depicted in Figure 2.4)⁵.

⁵The equation corresponding to the attractive case is the one with a plus sign in Eq. 2.19 as the potential comes with a minus sign in the Schrödinger equation.

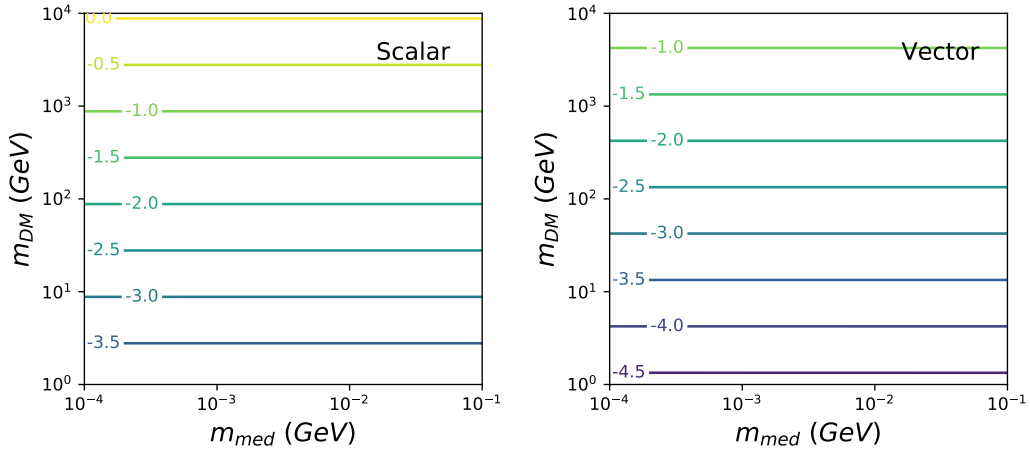


FIGURE 2.3: Contour of $\log(\alpha_{\text{med}})$ fixed by the relic density constraint in the DM versus mediator mass plane for the scalar (left) and vector (right) portal models.

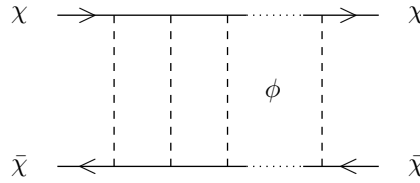


FIGURE 2.4: Ladder diagram of a DM self-scattering process in the scalar portal model.

However, in the vector portal model, DM self-interactions get both attractive and repulsive contributions from the Yukawa potential such that both Schrödinger equations of Eq. 2.19 have to be solved (processes depicted in Figure 2.5).

Following the numerical resolution method of [121]⁶ one can thus solve Eq. 2.19 in the DM versus mediator mass plane as those are the only free parameters. Indeed, the DM-to-med coupling is fixed by the relic density and the DM relative velocity which is pointed out by simulations to alleviate tensions at small scales is approximately fixed to $v \simeq 3 \times 10^{-5}$ [99], [101], [168]–[171].

⁶One can also use the analytical formulas given in [121] as very good proxy of the solutions of the Schrödinger equation.

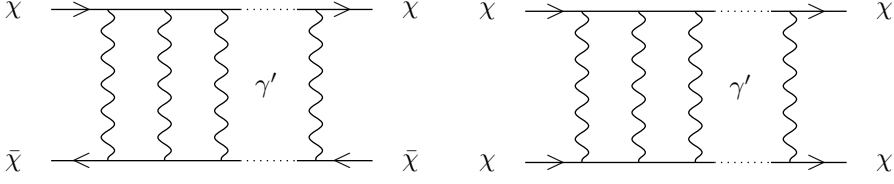


FIGURE 2.5: Ladder diagrams of a DM self-scattering process in the vector portal model for the attractive (left) and the repulsive (right) contributions.

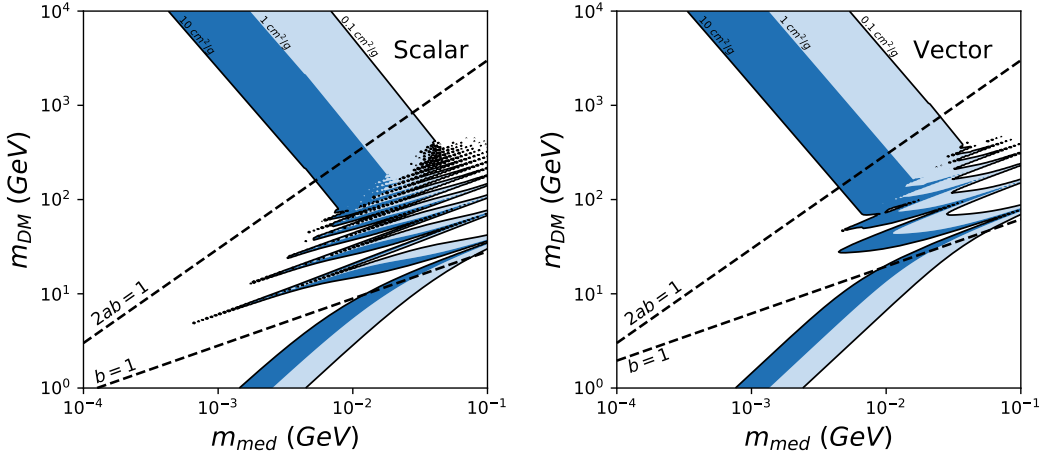


FIGURE 2.6: Contour of the self-scattering cross section divided by the DM mass for the scalar (left) and vector (right) portal models. The DM-to-med coupling has been fixed requiring that the self-interacting particle constitute 100% of the DM today.

Figure 2.6 shows then in this plane where the self-scattering transfer cross section satisfy the small scale structure constraints, i.e. where $0.1 \text{ cm}^2/\text{g} \leq \sigma_T/m_{\text{DM}} \leq 10 \text{ cm}^2/\text{g}$ (see Section 1.3 on small scale structure constraints). These results have been obtained using the tools developed in [121] for DM candidate, that is to say fixing the DM-to-med coupling by the relic density constraint as explained in the previous subsection. Left panel of Figure 2.6 presents the self-interacting cross section corresponding to the diagram shown in Figure 2.4 taking the Sommerfeld enhancement into account for the scalar portal model. While the right panel of the very same Figure shows results for the vector portal model that is to say from both attractive and repulsive contributions in this case, see Figure 2.5.

From left and right panels of Figure 2.6, one can distinguish three regimes delimited by the values of a and b defined above in Eqs. 2.17 and 2.18. This is why

the two lines defined by $2ab = 1$ and $b = 1$ are shown (dashed lines on Figure 2.6). These lines arise for similar values of the DM and mediator particles masses in both plots of Figure 2.6. Because the annihilation cross sections responsible for the DM freeze-out are similar (see Eqs. 2.21 and 2.22). Indeed, the major difference comes in the factor of $3v^2/4$ in the scalar case which does not appear in the vector case (p-wave annihilation versus s-wave). This only brings a global moderate numerical factor once fixing the DM-to-med coupling from the DM relic abundance constraint. As a result, the required coupling is bigger in the scalar case than in the vector case for a chosen set of masses as this extra factor is smaller than unity at DM decoupling: $3v_{\text{dec}}^2/4 \simeq 0.043$. A larger DM-to-med coupling is then needed to compensate this additional suppression factor in the cross section. This explains why the $b = 1$ line is a little bit closer to the top for the vector case compared to the scalar one. Let us now discuss these regimes one by one. Starting from the bottom of left and right panels of Figure 2.6, both the DM-to-med coupling and the DM mass are small such that $b < 1$ ⁷. In such a case, the exponential term of Eq. 2.19 coming from the Yukawa potential is suppressed with respect to the other terms so its impact is small. Thus, for both attractive and repulsive cases, one enters into the so-called *Born* regime in which the Born approximation holds. In this regime, one can compute the self-scattering without considering the full ladder diagram, that is to say without taking any Sommerfeld enhancement into account. Indeed, this regime corresponds to a feeble Yukawa potential and a weak mass hierarchy as $\alpha_{\text{med}} m_{\text{DM}} < m_{\text{med}}$. Solving Eq. 2.19 and plugging its solution for χ_l in Eq. 2.4, one gets a cross section which is the same for both the attractive and the repulsive potentials [168],

$$\sigma_T^{\text{Born}} = \frac{2\pi}{a^2 m_{\text{med}}^2} \frac{1}{(2ab)^2} \left(\log(1 + (2ab)^2) - \frac{(2ab)^2}{1 + (2ab)^2} \right). \quad (2.23)$$

In this regime, one does not expect any specific features as there is no enhancement of the cross section. The self-scattering cross section divided by the DM mass increases only with $b = \alpha_{\text{med}} m_{\text{DM}} / m_{\text{med}}$. On the one hand, for a fixed mediator mass, one expects the self-scattering cross section divided by the DM mass to increase with the DM mass. On the other hand, for a fixed DM mass one expects this quantity to increase if the mediator mass decreases. These behaviours can be seen in both panels of Figure 2.6 in the region $b < 1$, below the $b = 1$ dashed line.

The intermediate regime for which $b > 1$ and $2ab \ll 1$ shows up when all terms in Eq. 2.19 have comparable impact and no effect can be neglected. However,

⁷We recap that the DM-to-med coupling is fixed by the relic density constraint such that the DM-to-med coupling increases with the DM mass.

solving Eq. 2.19 in this case is not easy. One can nevertheless solve a proxy of this equation using the Hulthén potential instead of the Yukawa potential:

$$V^{\text{Hulthén}}(x) = \pm a\eta \frac{m_{\text{med}}^2}{m_{\text{DM}}} \frac{e^{-\eta x/b}}{1 - e^{-\eta x/b}}, \quad (2.24)$$

where η is a numerical factor used to fit the Yukawa solution, $\eta \simeq 1.6$ [121], [172] and the minus or plus signs stand for the attractive and repulsive potential respectively. In that case, Eq. 2.19 can be solved analytically for the $l = 0$ contribution which dominates in this regime. We have [121],

$$\sigma_T^{\text{Hulthén}} = \frac{16\pi}{m_{\text{med}}^2} \frac{1}{(2ab)^2} \sin^2 \left(\arg \left(\frac{i\Gamma(i2ab/\eta)}{\Gamma(\lambda_+)\Gamma(\lambda_-)} \right) \right), \quad (2.25)$$

where Γ is the Euler function and the parameters λ_{\pm} are given by,

$$\lambda_{\pm} = \begin{cases} 1 + \frac{iab}{\eta} \pm \sqrt{\frac{a}{\eta} - \left(\frac{ab}{\eta}\right)^2} & \text{(attractive potential),} \\ 1 + \frac{iab}{\eta} \pm i\sqrt{\frac{a}{\eta} + \left(\frac{ab}{\eta}\right)^2} & \text{(repulsive potential).} \end{cases} \quad (2.26)$$

It can be shown that these analytical results give a good approximation of the exact numerical results, see [121], [173]. In this regime, the self-interacting cross section depends periodically and strongly on the values of the parameters a and b . This is due to the fact that this regime for the attractive case displays quantum resonances especially in the attractive scalar case, but also in the attractive vector case in a less significant way. The addition of the repulsive component for the vector case explains why the resonances are smoothed in the right panel of Figure 2.6. Moreover, as we already mentioned above, the DM-to-med coupling is sizeably larger in the scalar case than in the vector one due to the extra numerical factor in the DM annihilation cross section at freeze-out. Thus, if for a given set of DM and mediator masses, the coupling is larger in the scalar case, one expects a stronger self-interaction cross section as well as a wider resonant regime (i.e. more resonances) in the scalar model. This specific difference in the two models can be seen comparing left and right panels of Figure 2.6 and more specifically the number of resonances which is bigger in the scalar case as expected.

Finally, the last regime is defined for $2ab > 1$, i.e. for $m_{\text{DM}}v > m_{\text{med}}$ and describes the so-called classical regime. The behaviour of the self-scattering cross section divided by the DM mass is here much simpler than in the resonant regime.

Indeed, in the classical regime, the mediator is much much lighter than the DM such that the Yukawa potential can be associated to a Coulombian-like potential as a proxy. Thus, in the limit $2ab \gg 1$, the self-scattering rate reduces to the case we obtained in the classical regime of a particle propagating in a classical Coulombian potential. This results in an analytic solution for the transfer cross section (see [121], [168], [174], [175]) which for the attractive potential case is

$$\sigma_T^{\text{Classical}} = \begin{cases} \frac{4\pi}{a^2 m_{\text{med}}^2} \frac{1}{(2ab)^2} \log(1 + 2a^2 b) & 10 \leq 2a^2 b, \\ \frac{8\pi}{a^2 m_{\text{med}}^2} \frac{1}{(2ab)^2} (1 + 1.5(2a^2 b)^{-1.65})^{-1} & 10^{-3} \leq 2a^2 b \leq 10, \\ \frac{\pi}{m_{\text{med}}^2} \left(1 - \log(2a^2 b) + \frac{1}{2 \log(2a^2 b)}\right)^2 & 2a^2 b \leq 10^{-3}, \end{cases} \quad (2.27)$$

while for the repulsive potential case it is instead

$$\sigma_T^{\text{Classical}} = \begin{cases} \frac{2\pi}{a^2 m_{\text{med}}^2} \frac{1}{(2ab)^2} \log(1 + a^2 (2ab)^2) & 1 \leq 2a^2 b, \\ \frac{\pi}{m_{\text{med}}^2} (\log(1/a^2 b) - \log \log(1/a^2 b))^2 & 2a^2 b \leq 1. \end{cases} \quad (2.28)$$

For a fixed DM mass we recover a behaviour similar to the one obtained in the Born regime: the self-scattering cross section divided by the DM mass increases if the mediator mass decreases but slower than in the Born regime (i.e. the interaction is less sensitive to the mediator mass). Moreover, for a fixed mediator mass, the self-scattering cross section divided by the DM mass decreases if the DM mass increases. This is because at high DM mass there is only one relevant scale, the DM mass. Thus the self-scattering cross section has no other choice to go like $\sigma_T \sim 1/m_{\text{DM}}^2$ such that it decreases with the DM mass. This can be seen also from the fact that the self-interacting cross section divided by the DM mass does not depend on the mass ratio $m_{\text{DM}}/m_{\text{med}}$ in this regime. In other words, the mediator is so light that in practice it is massless and the solution of the Schrödinger equation cannot depend on this ratio like in the case of a coulombian potential. Once again, this behaviour can be seen in both panels of Figure 2.6 for the scalar and the vector portal models.

2.1.4 Smaller annihilation cross section

Until now, one has assumed that the interaction at the origin of the self-interactions is also the one leading to the observed relic density through the FO mechanism. However, this does not have to be necessarily the case. One could instead consider smaller DM-to-med couplings leading to a smaller DM annihilation cross section at FO. This interaction alone would then lead to a larger DM relic density than the one

observed today and needs an additional annihilation process to take care of the FO mechanism. In this case, one expects the self-interactions to decrease too since the DM-to-med coupling decreases. Then, the dimensionless parameter b (resp. a) will decrease (resp. increase) while the combination $2ab$ will remain unchanged. Thus looking at the DM versus mediator mass plane, even if the $2ab = 1$ line does not move, the $b = 1$ line will go up and this will shrink the resonant regime. However, we found that, in such a case, small scale structure constraints can still be satisfied for a wide range of the parameter space even for an annihilation cross section suppressed by a factor of one million. Figure 2.7 shows what the DM versus mediator mass plane looks like if one considers a smaller annihilation cross section at freeze-out than the one required by the DM relic abundance constraint in a standard scenario. By standard we mean a scenario where the HS is in thermal equilibrium with the VS and in which the DM undergoes an usual freeze-out. In Figure 2.7 for both the scalar (left) and vector (right) portal models, we fixed the DM-to-med coupling requiring that the annihilation process alone would give a DM relic density Ω_{DM} larger by a factor of 10^2 , 10^4 and 10^6 for top, middle and bottom respectively.

This shows how easy it is to satisfy the small scale structure constraints (see Section 1.3) even if the DM annihilation cross section is much smaller than the one usually expected, that is to say if $\langle\sigma v\rangle_{\text{dec}} \ll 2.2 \times 10^{-9} \text{ GeV}^{-2}$. We will make a great use of this results in the following when we will study minimal ways out for self-interacting DM models with light mediators, see Chapters 5 and 6.

2.2 Effect of the Sommerfeld effect on DM annihilations

In the previous section we were focused on how to take into account the Sommerfeld effect for a self-scattering process in which the particle responsible for the self-scattering is the same as the one responsible for the Sommerfeld effect. However, the Sommerfeld effect can also be very relevant for all scattering processes, particularly for DM annihilations. Indeed, before the proper interaction (here the annihilation), the DM incoming particles may interact in the exact same way they do in self-interactions. The computation of the impact of the Sommerfeld enhancement in the case of an annihilation is a little bit different than for purely self-interacting processes. One has to distinguish two processes: the annihilation itself and the Sommerfeld effect which takes into account the self-interactions which may occur before the annihilation. Ideally, one should then solve the full Schrödinger equation which would take the Yukawa potential (responsible for the self-interaction) and the final annihilation process into account all together, but this is rather complicated as the former is a non-perturbative effect and the latter can only be computed in a perturbative theory. However one may assume that these two processes are independent

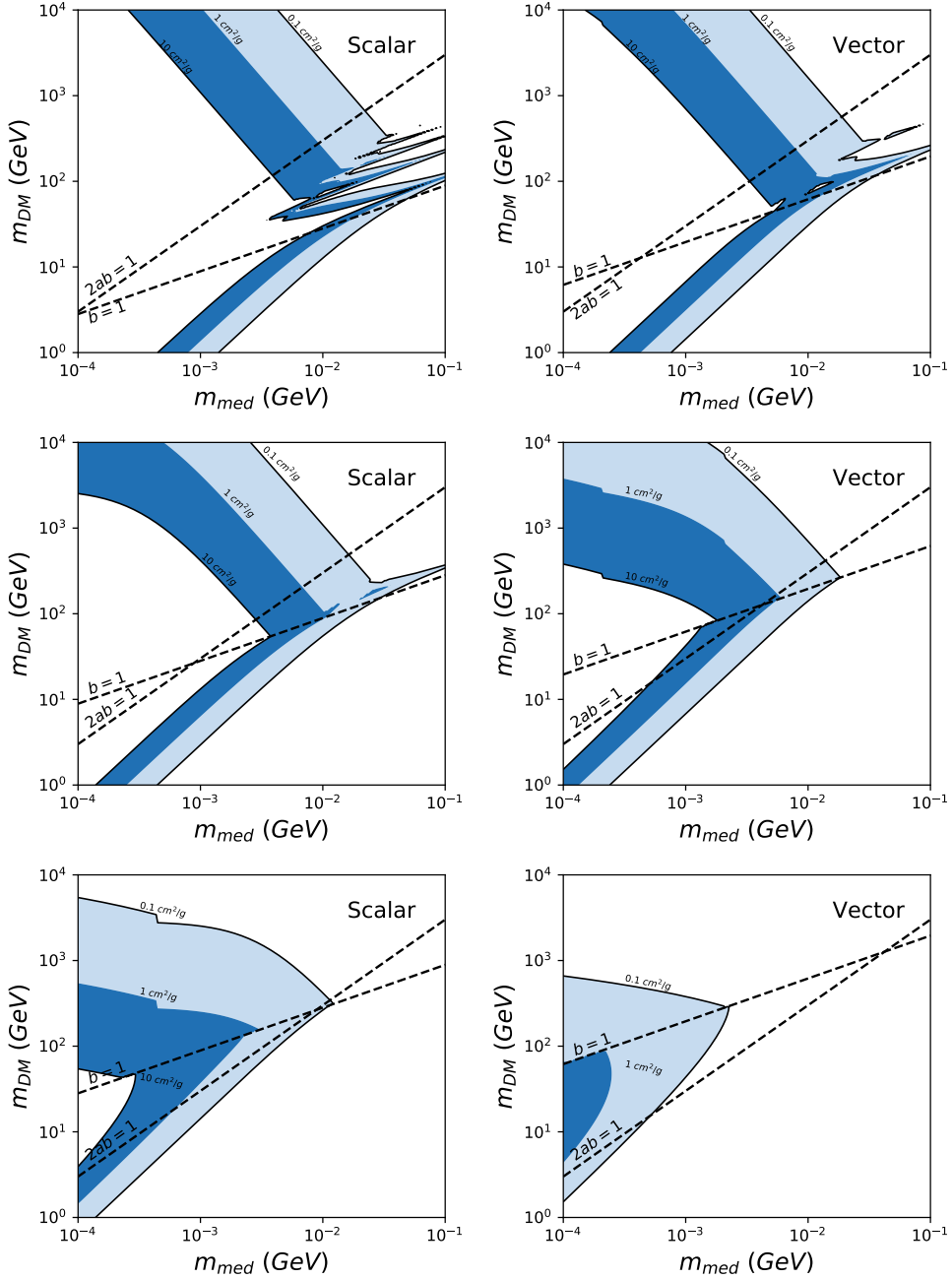


FIGURE 2.7: Contour of the self-scattering cross section divided by the DM mass for the scalar (left) and vector (right) portal models. The DM-to-med coupling has been fixed requiring that the self-interacting particle abundance today is $10^2 \times \Omega_{\text{DM}}$ (top), $10^4 \times \Omega_{\text{DM}}$ (middle) and $10^6 \times \Omega_{\text{DM}}$ (bottom).

such that one can factorise the Sommerfeld effect from the thermally average annihilation cross section: $\langle\sigma v\rangle \simeq S_F \times \langle\sigma v\rangle_{TL}$ where TL stands for the cross section at tree level, i.e. without taking the Sommerfeld effect into account and S_F is the Sommerfeld factor which encodes the contribution of the Sommerfeld effect in the process, see below.

As we are now interested in DM annihilation processes, one must pay attention to the typical values of the DM relative velocity in such processes. As we have seen in Chapter 1, DM annihilations are relevant at the DM decoupling in FO scenario, but also later on at CMB recombination (see Section 1.4) or today for indirect detection when annihilating in the centre of the Milky Way or in dwarf galaxies (see Section 1.8). In all of these contexts, DM relative velocity is much smaller than at DM decoupling:

$$v \sim \begin{cases} 2 \times 10^{-3} & \text{in the Milky Way,} \\ 3 \times 10^{-5} & \text{in dwarf galaxies,} \\ 10^{-7} & \text{at CMB recombination.} \end{cases} \quad (2.29)$$

Then, as the DM relative velocity is small, one can always consider the leading order in the expansion of the annihilation cross section given in Eq. 2.20. In this case, as the final process is largely dominated by the leading wave, it is not necessary to solve the Schrödinger equation for all waves as we did for the self-interaction cross section, but simply solve the one corresponding to the dominant wave in the process.

2.2.1 The Sommerfeld factor

The result of the above assumption that one can factorise the Sommerfeld effect from the tree-level annihilation process is that one can define the Sommerfeld factor as the ratio between the full cross-section including the Sommerfeld effect (σ) and the tree-level cross-section without the Sommerfeld enhancement (σ_{TL}),

$$S_k \equiv \frac{\sigma}{\sigma_{TL}}, \quad (2.30)$$

with \vec{k} the relative impulsion of the incoming particles.

The ratio given in Eq. 2.30 can be related to the wave function found with and without the Sommerfeld effect. Indeed, as we already discussed above, the Sommerfeld effect does nothing but to modify the Schrödinger equation of the incoming

wave function by adding a potential term which represents the exchange of particles in the initial state. Moreover, since the cross section represents the probability for a process to occur, it is proportional to the square of the module of the wave function evaluated at the interaction point: $\sigma \propto |\psi(0)|^2$. Thus, the Sommerfeld factor is also given by,

$$S_k = \frac{|\psi_k(0)|^2}{|\psi_{k,TL}(0)|^2}, \quad (2.31)$$

where $\psi_{k,TL}$ stands for the wave function without any perturbation (i.e. at tree level) and ψ_k takes the Sommerfeld effect into account. Performing the same expansion of the wave function in terms of the partial wave as done in Eq. 2.8, one can compute the Sommerfeld factor corresponding to each wave in terms of the solution of Eq. 2.19 taken at $x \rightarrow 0$, see [176] for an in depth discussion,

$$S_l = \left| \frac{(2l+1)!!}{2^{l+1}(l+1)!} \lim_{x \rightarrow 0} \frac{\chi^{(l+1)}(x)}{a^{l+1}} \right|, \quad (2.32)$$

where χ^n stands for the n th derivative of χ with respect to the dimensionless variable x . At the end of the day, the final annihilation cross section which takes the Sommerfeld enhancement into account can be written as,

$$\langle \sigma v \rangle \simeq \sum_{l=0}^{\infty} S_l \langle \sigma v \rangle_l v^{2l}. \quad (2.33)$$

2.2.2 s-wave annihilation

The Sommerfeld factor expressed in Eq. 2.32 can be close to unity or be very large depending on the wave and on the values of the dimensionless parameters a and b ⁸. Thus, let us first determine in more details what are the values that can take this factor for the simplest case, the s-wave.

The left panel of Figure 2.8 shows contours of the Sommerfeld factor for the s-wave annihilation in the $a - b$ plane. One can also distinguish in Figure 2.8 the two lines already met above defined by $b = 1$ and $2ab = 1$ which delimit the Born, the resonant and the classical regimes of the Sommerfeld effect. The values of the Sommerfeld factor shown in this Figure are obtained by solving numerically Eq. 2.19 for

⁸Let us recall that S_l does depend on a and b through $\lim_{x \rightarrow 0} \chi^{(l+1)}(x)$ which is the solution of Eq. 2.11.

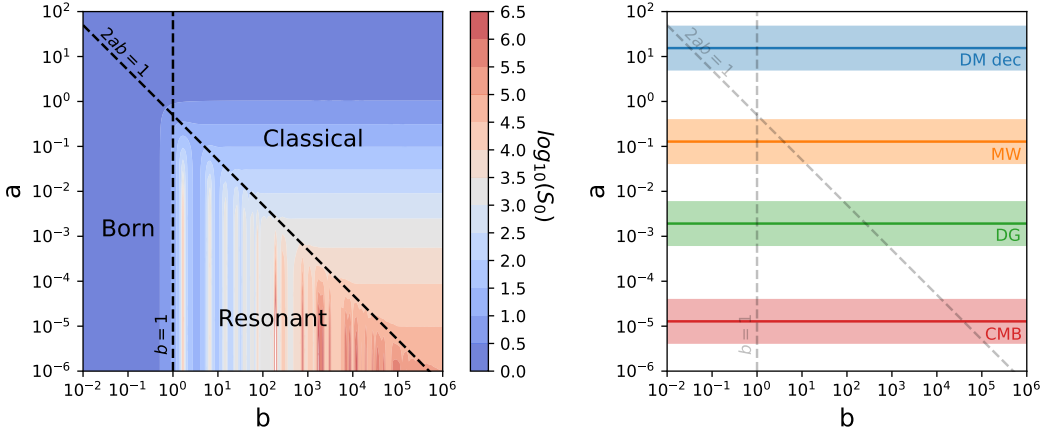


FIGURE 2.8: Left: contour of the Sommerfeld factor for s-wave annihilation in the Born, resonant and classical regimes in the $a - b$ plane. Right: relevant regions of the $a - b$ plane when considering DM freeze-out (blue), DM indirect detection in the Milky Way (orange) and in dwarf galaxies (green) and CMB constraints on DM annihilation (red) with $\alpha_{\text{med}} \simeq \alpha_{EW}$.

the s-wave contribution ($l = 0$) and plugging the solution into Eq. 2.32, that is to say that we did not use any analytic approximation. From this panel, we see that we recover behaviours similar to the ones observed for the self-interacting cross section. Indeed, in the Born regime the Sommerfeld factor for the s-wave contribution is constant $S_0^{\text{Born}} \simeq 1$. In the resonant regime the factor highly depends on the values of a and b and lies between $S_0^{\text{Resonant}} \gtrsim 10$ and $S_0^{\text{Resonant}} \lesssim 10^7$. This factor could of course be even larger if one does consider larger values of b and smaller values of a , but this would require a very large coupling which may become non-perturbative at some point. Finally, in the classical regime the Sommerfeld factor does not depend on $b = \alpha_{\text{med}} m_{\text{DM}} / m_{\text{med}}$ since the mediator is basically massless when compared to the DM and the mass ratio does not play any role. We recover the solution one can obtain with a Coulombian potential.

We have briefly mentioned that the DM relative velocity is not the same in the various contexts where the Sommerfeld effect can be relevant for DM annihilations, see Eq. 2.29. Thus, in general, different regions of the $a - b$ plane are relevant. On the right panel of Figure 2.8, we show which region of the parameter space (i.e. the $a - b$ plane) is relevant for which type of situation. We considered DM annihilation at freeze-out (blue), in the Milky way or in dwarf galaxies today (orange and green respectively) and at CMB recombination (red). In order to delimit an area for each of those situations such as we did in this plot, we fixed the DM-to-med coupling

to the electroweak fine structure constant $\alpha_{\text{med}} = \alpha_{EW} \simeq 1/128$. Indeed, as the velocity is fixed for each situation, fixing the DM-to-med coupling allow us to fix the dimensionless parameter a . The wide bands correspond to a variation of one order of magnitude in the DM-to-med coupling. Hence, in each coloured region of right panel of Figure 2.8, the DM-to-med coupling lies in the following range: $\alpha_{\text{med}} \in [\alpha_{EW}/\sqrt{10}, \alpha_{EW}\sqrt{10}]$.

Thanks to the right panel of Figure 2.8, we see that in the s-wave case, for a DM-to-med coupling of order of the electroweak fine structure constant, the Sommerfeld effect is negligible when considering the DM freeze-out (as already mentioned in Section 2.1.2) and starts to be relevant when considering indirect detection experiments looking for DM annihilation in the Milky Way. Moreover, it becomes really important and could change the whole picture for DM annihilation in dwarf galaxies and when considering CMB constraints on the DM annihilation cross section⁹. Considering a smaller or a larger DM-to-med coupling would move up or move down respectively the four coloured regions of right panel of Figure 2.8 simultaneously.

2.2.3 p-wave annihilation

Now that we have learned more about the simplest case, the s-wave, we can take a look to the next step: the p-wave case. Once one consider non-zero angular momentum quantum number ($l > 0$), since the angular momentum starts to play a role, this make the Schrödinger equation of Eq. 2.19 more unstable (numerically speaking). However, it still can be solved numerically relatively easily for the p-wave contribution. We give in the left panel of Figure 2.9 contours of the Sommerfeld factor in the p-wave case ($l = 1$) in the $a - b$ plane. Note that the colour scale is different than in the s-wave case of Figure 2.8. Here the Sommerfeld factor goes up to 10^{15} .

We give in the right panel of Figure 2.9 the regions of the $a - b$ plane that are relevant for the various contexts similarly to the right panel of Figure 2.8. Then one can compare both panels of Figure 2.9 and see that, as in the s-wave case, the Sommerfeld factor is not much larger than one at DM decoupling if we fix the DM-to-med coupling to the electroweak fine structure constant. However, as the Sommerfeld factor is globally much much larger in the p-wave case than in the s-wave case, one could think that it becomes highly non-negligible even for DM annihilation in the Milky Way today. Indeed, the Sommerfeld factor can already multiply the p-wave annihilation cross section by 3 or even 4 orders of magnitude. It goes even to 10

⁹Note that it is due to this effect that s-wave annihilation processes during the recombination epoch can be constrained by CMB, see Section 1.4 and Eq. 1.62

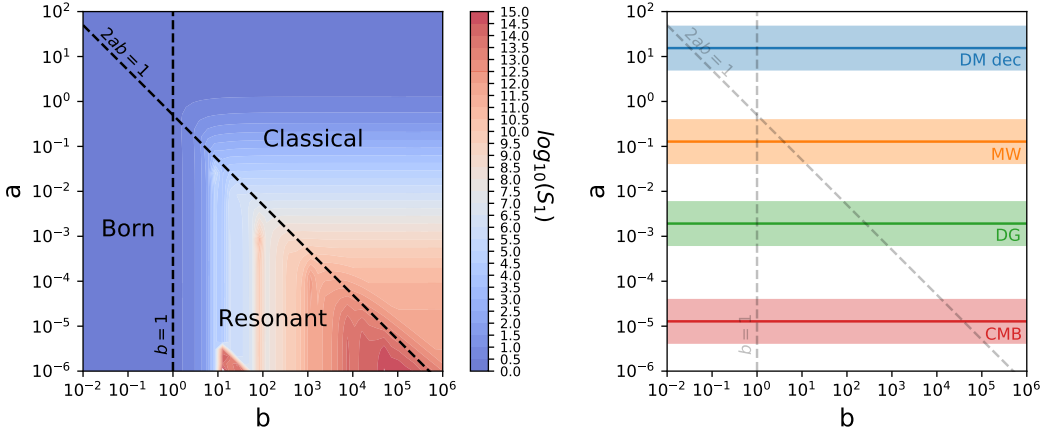


FIGURE 2.9: Left: contour of the Sommerfeld factor for p-wave annihilation in the Born, resonant and classical regimes in the $a - b$ plane. Right: relevant regions of the $a - b$ plane when considering DM freeze-out (blue), DM indirect detection in the Milky Way (orange) and in dwarf galaxies (green) and CMB constraints on DM annihilation (red) with $\alpha_{\text{med}} \simeq \alpha_{EW}$.

orders of magnitude for DM annihilations in dwarf galaxies and up to 15 for annihilations at CMB recombination.

However, one has to be more careful as in the p-wave case the annihilation cross section contains an additional factor of v^2 which compensates the Sommerfeld factor as it is well known. This is why indirect detection constraints are usually neglected in DM models in which the DM annihilates through a p-wave. Thus, in order to know if the Sommerfeld enhancement is in fact relevant or not for a given wave, one should study $S_1 v^{2l}$ instead of S_l alone. This is what we do in Figure 2.10 which shows, for the four situations we considered individually, contours of $S_1 v^{2l}$ in the $a - b$ plane. In the four panels of Figure 2.10, the grey regions are where $S_1 v^{2l} < 1$ such that the p-wave contribution is negligible.

Now, we can compare the results for p-wave annihilation presented in Figure 2.10 to the one obtained for s-wave annihilation shown in Figure 2.8. For a given choice of the dimensionless parameters a and b , it is clear from this comparison that if both s-wave and p-wave are present, the s-wave annihilation always easily dominates over the p-wave annihilation. Thus, one can always neglect the p-wave

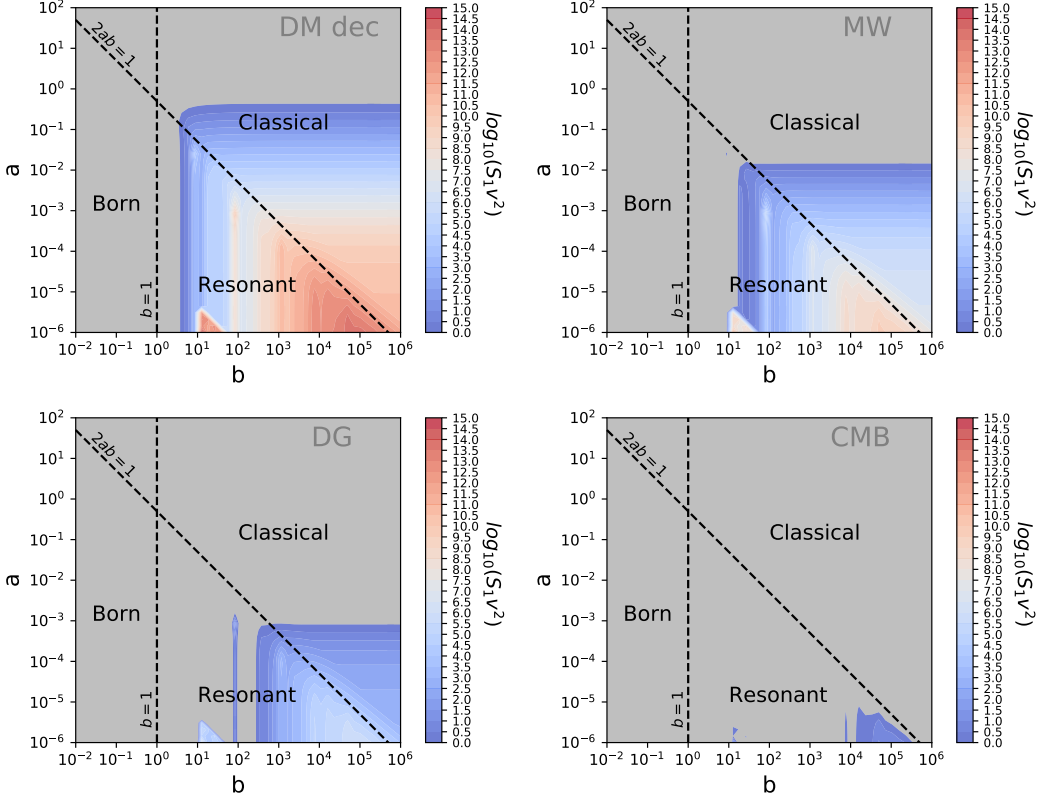


FIGURE 2.10: Contour of the Sommerfeld factor times v^2 for p-wave annihilation in the Born, resonant plane and classical regimes in the $a - b$ plane.

contribution even taking the Sommerfeld effect into account. However, if the s-wave annihilation is forbidden¹⁰, the DM p-wave annihilation cross section could be largely enhanced by the Sommerfeld effect if the DM-to-med coupling is large enough. This can be seen on the bottom left panel of Figure 2.10 in which the product $S_1 v^2$ can be of order of ~ 10 in dwarf galaxies if $\alpha_{\text{med}} \sim \alpha_{EW} \times \sqrt{10}$. This effect can thus be relevant for a DM candidate as we can see in the scalar portal model for example. Indeed, this can be seen for example if we fix the DM-to-med coupling from the DM relic density constraint of Section 1.1, if we fix the mediator (a real scalar) mass to $m_\phi = 1$ GeV for example¹¹ and then if we compute the DM

¹⁰This can be the case due to angular momentum conservation considerations for specific initial and final states. For example this is the case for the annihilation of a pair of Majorana fermions into a pair of Dirac fermions or in annihilation of a pair of Dirac fermions into a pair of real scalars.

¹¹The only requirement is that the light mediator must be much lighter than the DM.

annihilation cross section as a function of the DM mass, taking the Sommerfeld enhancement into account.

The result is shown in Figure 2.11 which displays the values of the DM annihilation cross section with (solid coloured) and without (dashed coloured) the Sommerfeld factor for DM annihilations in the Milky Way (left panel) and in dwarf galaxies (right panel) together with the corresponding constraints coming from indirect detection experiments (see Section 1.8 for more details on these constraints). The colour scheme of Figure 2.11 follows the one of Figure 1.31 for simplicity. The solid dots ending the curves of both panels of Figure 2.11 indicate where the DM relic density constraint requires a DM-to-med coupling larger than unity. Continuing the line beyond this dot would then be untrustworthy as a perturbative calculus. On the left panel (and less easily on the right panel) of this Figure, one can recognize the previously discussed Born, resonant and classical regimes. Indeed, the annihilation cross section starts by being flat because the mediator mass is not much lighter than the DM one and the DM-to-med coupling is still quite low¹². The Sommerfeld factor is thus close to one as the solid and dashed coloured line merge. At higher DM mass, the mediator versus DM mass ratio decrease and the DM-to-med coupling increase such that one enters the classical regime. The Sommerfeld factor now strongly depends on the precise values of the parameters. At even higher DM mass, the mediator is effectively massless, this is the classical regime where the curve flatten.

These results show a concrete and very simple example along which, contrary to what is usually admitted in the literature, a p-wave annihilation can be constrained by indirect detection. As we have seen in the first chapter of this thesis, this model is nevertheless already excluded in many ways before being constrained by indirect detection, but this simply illustrates the importance of the Sommerfeld enhancement even for p-wave annihilations. We will see in the following that this effect can be fully relevant for other concrete p-wave models in the context of self-interacting DM. For which some part of the parameter space will be constrained precisely by indirect detection, see Chapter 6.

In summary, in this chapter we have introduced the Sommerfeld effect and emphasised the fact that it is important in several different contexts, for self-interactions in particular as well as for DM annihilation processes that could take place at CMB recombination or in the MW and DG. We finished this chapter in showing that contrary to common belief in general in the literature, p-wave annihilation scenarios

¹²We recall that fixing this coupling from the DM relic density constraint makes the coupling to increase linearly with the DM mass.

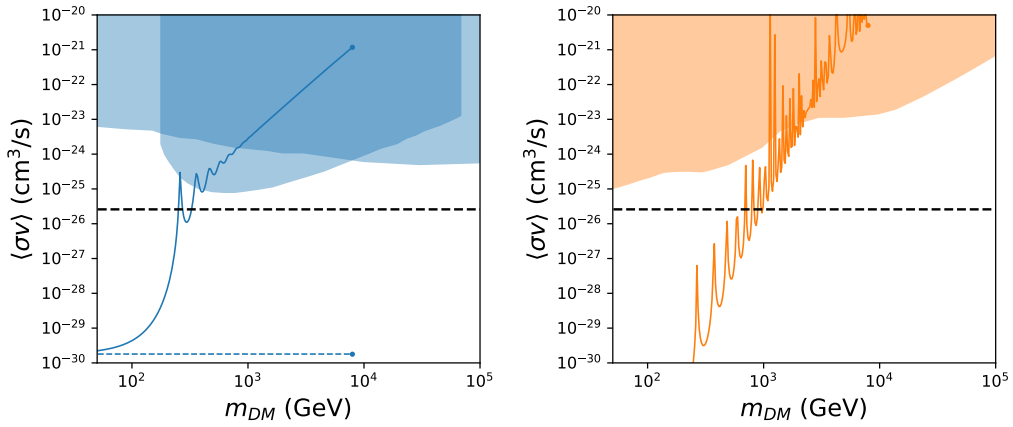


FIGURE 2.11: DM annihilation cross section with (solid line) and without (dashed coloured line) the Sommerfeld factor as a function of the DM mass for annihilation in the Milky way (left) and in dwarf galaxies (right). Are also shown the constraints coming from indirect detection experiments as explained in Section 1.8 and the value of the annihilation cross section at freeze-out (black dashed).


can be tested by indirect detection experiments thanks to the Sommerfeld enhancement.

Part II

DM production and Hidden Sector

Chapter 3

Dark Matter production mechanisms

 In this third Chapter, we will present how to account for the relic abundance of DM when it interacts with the SM through portals as we did in [177], [178]¹. In particular, we consider the possibility for the mediator to be massive and its implications on the DM relic abundance production mechanism in a generic way for both the scalar and the vector portal models of Subsection 1.3.4. In this context and using the formalism of the Boltzmann equation developed above (see Subsection 1.2.1), we will detail the phase diagram of DM production. Next, we will discuss some specificities of the two portal models we consider.

3.1 The three sectors and their connections

The underlying structure is the same for the Higgs portal model in the fully broken case (i.e. $0 < m_\phi < m_{\text{DM}} < v_H < v_\Phi$) and for the kinetic mixing portal model in the massive mediator case (i.e. $0 < m_{\gamma'} < m_{\text{DM}}$). This structure is composed of three sectors connected to each other by three different couplings resulting from two interactions. This can be seen in Figure 3.2.

We would like to draw the reader's attention on the fact that this three sector and three connections structure (depicted in Figure 3.2) for the kinetic mixing portal model is specific to the massive mediator case. Indeed, if the dark photon is massless, one can see from Eq. 1.55 that the dark photon does not couple to any SM

¹These works threaten the vector portal case, the scalar portal case is then an unpublished original work.

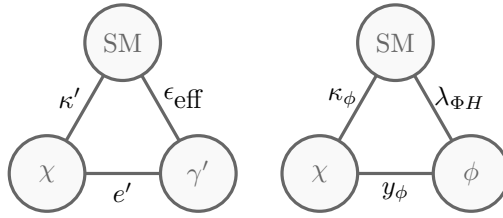


FIGURE 3.1: The three sectors (blobs) and their three connections (lines) for the vector (left) and scalar (right) portal models.

particle such that the only way to produce dark photon is to go through the production of DM particles. As already said above, the smooth transition between massive and massless mediator cases goes through the proper treatment of thermal effects. This will be done in Section 3.3 where we will see that the effective coupling ϵ_{eff} in Figure 3.2 goes to zero with the dark photon mass. That is to say that in the massless mediator case, the line (i.e. the connection) between the SM and dark photon baths no longer exists.

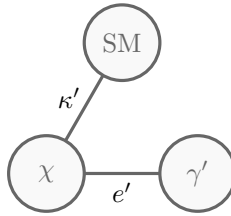


FIGURE 3.2: The three sectors (blobs) and their two connections (lines) for the kinetic mixing portal model in the massless dark photon case.

3.2 Phase diagram of dark matter production

We will now discuss how the DM relic abundance depends on this "three sectors-three connectors" structure. We will start with an empty hidden sector (i.e. no DM and no mediator in the thermal bath at the end of inflation or a negligible amount of them), and from this initial condition we will go through all production regimes (or "phases") all the way from phases where the DM never thermalises with any other

particles to phases where all particles thermalise with each other².

In this chapter, we aim to illustrate the fact that the final phase diagram of DM production is quite general for portal models which present a "three sectors-three connectors" behaviour. We will make this discussion for both vector and scalar portal models. Note that for the sake of clarity and generality, thermal effects will not be included in the analysis as they are specific to the dark photon portal model. However we will discuss results including thermal effects in Section 3.3 and refer to [177] for a more in-depth analysis of consequences of thermal effects on DM production mechanisms.

There are only four free parameters on which the DM relic abundance can depend on: the DM and the mediator masses ($m_{\gamma'}$ or m_ϕ) and the two couplings between the DM and the mediator (α' or α_ϕ) and between the mediator and the SM (ϵ or $\lambda_{\phi H}$). These parameters rule all possible interactions of the theory. In particular, the connection between the DM and SM baths is going through the production of the mediator in the s-channel, see Figure 3.3.

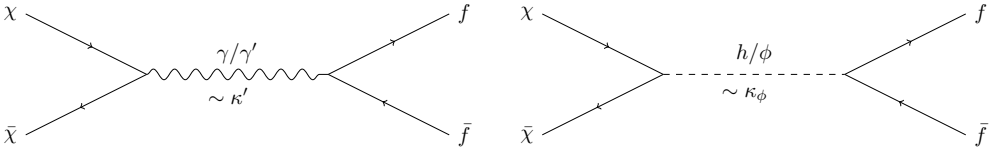


FIGURE 3.3: Connection between the DM and SM baths goes through the production of the mediator in the s-channel for both the kinetic mixing portal (left) and the Higgs portal (right) models. f indicates a SM fermion.

The strength of these interactions is set by the DM-to-SM connector:

$$\kappa' \equiv \epsilon \sqrt{\alpha' / \alpha}, \quad (3.1)$$

$$\kappa_\phi \equiv \sin(2\theta) \sqrt{\pi \alpha_\phi}. \quad (3.2)$$

In the hidden sector, the connection between the DM and the mediator baths is set by a DM annihilation in the t-channel which is driven by α' and α_ϕ for the vector

²If the visible and hidden sectors are feebly coupled with each others, it would not be surprising that the reheating at the end of inflation took place mostly into one of the sectors rather than both of them. We assume here that reheating happened in the VS.

and scalar portal respectively, see Figure 3.4.

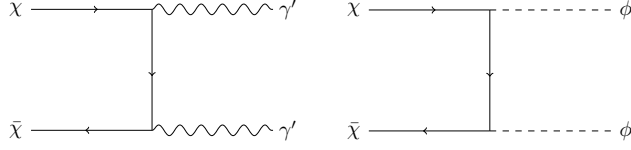


FIGURE 3.4: Connection between the DM and mediator baths goes through the annihilation of two DM particles into two mediator particles in the t-channel for both the kinetic mixing portal (left) and the Higgs portal (right) models.

Finally, the connection between the mediator and SM baths goes through several processes for which the dominant ones are shown in Figure 3.5. We recall here that for the vector portal model, the processes given in Figure 3.5 are valid only in the massive mediator case as the connection between SM fermions and the dark photon no longer exists in the massless dark photon case. However, these processes are driven by the mixing parameter ϵ and $\lambda_{\Phi H}$ for the kinetic mixing portal and the Higgs portal models respectively such that they are not independent of the two other connectors. Indeed, as we have introduced the SM-to-DM connectors κ' and κ_ϕ in Eqs. 3.1 and 3.2, one can see the SM-to-med couplings as function of the DM-to-SM and the DM-to-med connectors:

$$\epsilon' = \kappa' \sqrt{\alpha/\alpha'}, \quad (3.3)$$

$$\lambda_{\Phi H} = \frac{\kappa_\phi}{\sqrt{\pi\alpha_\phi}} \left(\frac{m_H^2 - m_\Phi^2}{v_\Phi v_H} \right), \quad (3.4)$$

where in the second equation we have used the definition of the mixing angle given in Eq. 1.52.

As a consequence of this structure, for a given set of masses, one can represent the DM relic abundance as contour line in the $\kappa' - \alpha'$ (or $\kappa_\phi - \alpha_\phi$) plane, that is to say as a function of the strength of the SM-to-DM connector and purely hidden sector interactions. This will lead to a "phase diagram" with various interesting regimes. To get this phase diagram we need to integrate a set of Boltzmann equations for

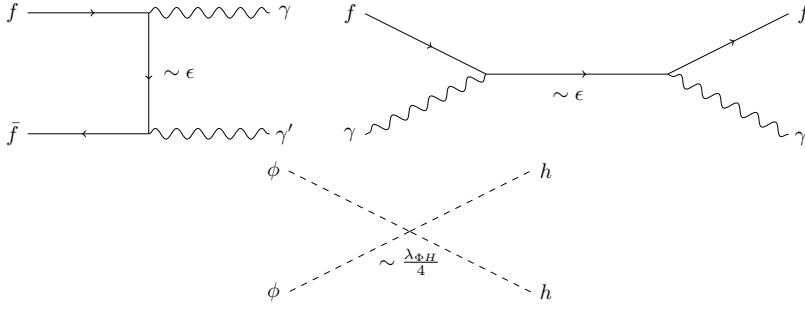


FIGURE 3.5: Dominant processes connecting the SM and mediator baths for the kinetic mixing portal (top) and the Higgs portal (bottom) models. f indicates a SM fermion.

the DM and the mediator yields. Once it is done, one can distinguish nine regimes along five distinct dynamical mechanisms³.

These five mechanisms are freeze-in (I), sequential freeze-in (II), reannihilation (III), secluded freeze-out (IV) and freeze-out (V). These regimes differ depending on which of the three connections thermalises the two reservoirs it connects or instead remains out of equilibrium at all times. In the latter case, a connection can be either totally irrelevant or, on the contrary, induce a relevant out-of-equilibrium production of a reservoir from another one. The most generic sequence of regimes, in the massive mediator case, appearing along the phase diagram is the one shown in Figures 3.6. Left (right) panel of this figure shows contour lines of the DM relic abundance in the $\kappa' - \alpha'$ ($\kappa_\phi - \alpha_\phi$) plane for the vector (scalar) portal model. We have always assumed DM to be heavier than the mediator and we present results obtained with a weak mass hierarchy.

This sequence of regimes can be illustrated by the following chain,

$$\text{Ia} \rightarrow \text{Ib} \rightarrow \text{II} \rightarrow \text{IIIb} \rightarrow \text{Vb} \rightarrow \text{Va}, \quad (3.5)$$

where the "a" and "b" labels refer to a process going through the visible sector or the hidden sector respectively and will be defined properly below⁴. Using the "three

³In the massless mediator case, five regimes and four dynamical mechanisms were already found and discussed in [179] for the Kinetic Mixing model and another type of scalar portal.

⁴Note however that the "a" and "b" notations here differ from the one defined in [177]

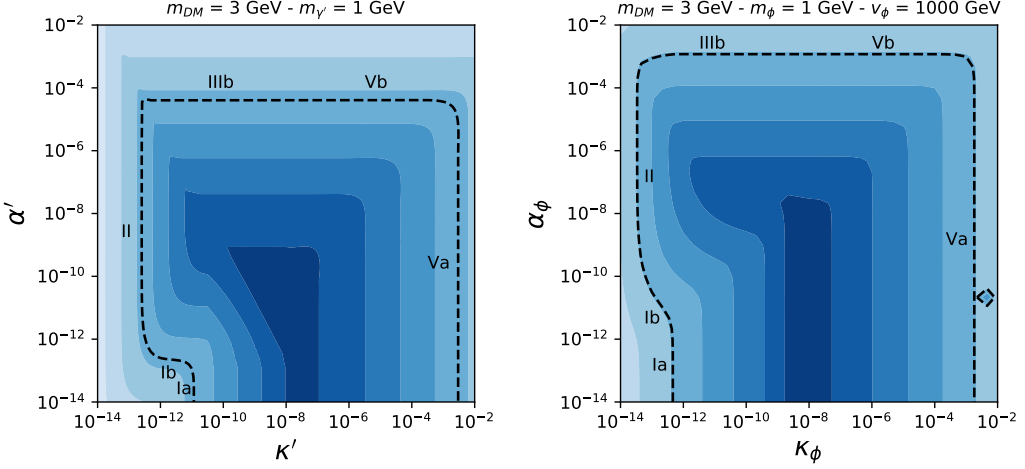


FIGURE 3.6: DM relic density obtained as a function of κ'/κ_ϕ and α'/α_ϕ for $m_{\text{DM}} = 3 \text{ GeV}$ and $m_{\text{med}} = 1 \text{ GeV}$. This diagram displays the various different production regimes which can lead to the observed relic density. For this particular choice of masses one obtains 6 different production regimes along 4 dynamical ways: freeze-in (Ia & Ib), sequential freeze-in (II), reannihilation (IIIb) and freeze-out (Va & Vb).

sectors-three connectors" representation as in Figure 3.2, the Figure 3.7 gives all mechanisms we found, to be explained below.

This specific structure involves three new regimes (Ib, II and IIIb), on top of those already existing in the massless case (Ia, Va and Vb). The fourth new regime (IVb) and the two other regimes existing in the massless case (IIIa and IVa) will appear for other models. In all cases, the shape of the phase diagram is generic.

3.2.1 Set of Boltzmann equation

Let us now discuss how the parameter space (i.e. the $\kappa'/\kappa_\phi - \alpha'/\alpha_\phi$ plane) is naturally divided in different phases. In order to understand which process will dominate and when it will, we present in this subsection the set of Boltzmann equations in a three sectors three connectors scenario. Since the global behaviour of the parameter space is the same for both portal models, we will use a generic notation for the analysis and we will present results for both the vector and the scalar portal models.

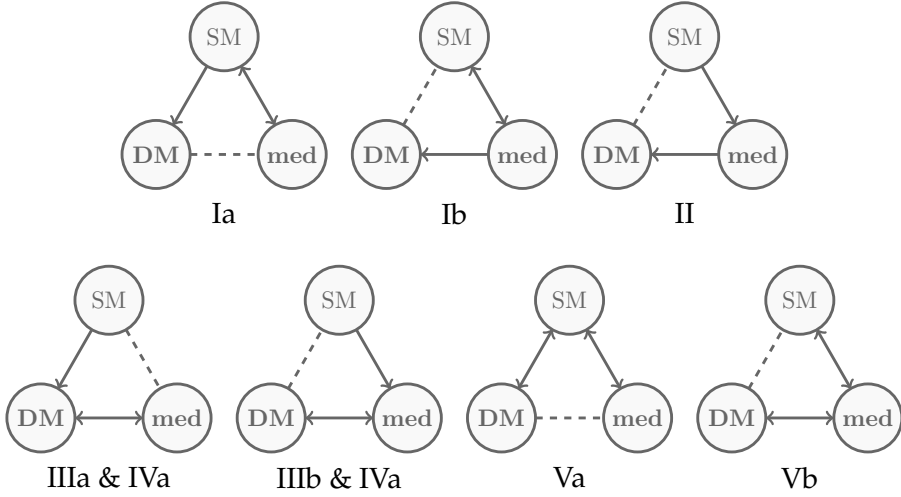


FIGURE 3.7: The 9 possible DM production regimes in the three sectors three connectors scenario. A double sided arrow means that the two corresponding sectors have reached chemical equilibrium; a single sided arrow indicates slow out-of-equilibrium production of one sector by the other one; a dashed line corresponds to a subdominant (i.e. irrelevant) interaction between the sectors. Regimes Ia and Ib, II, IIIa and IIIb, IVa and IVb, Va and Vb are associated to 5 distinct mechanisms to produce the DM abundance: the freeze-in (I), sequential freeze-in (II), reannihilation (III), secluded freeze-out (IV) and freeze-out (V) mechanisms respectively (see Sections 3.2.2 to 3.2.6). Note that the diagrams are identical for the reannihilation and secluded freeze-out mechanisms.

The set of Boltzmann equations that determine the time evolution of the DM and the light mediator yields is given by⁵

⁵Here and in subsequent Boltzmann equations, we have included factors of $1/2$, typical of Dirac DM particles, into the definitions of the cross-sections [166].

$$\begin{aligned}
xHs \frac{dY_{\text{DM}}}{dx} &= \langle \sigma_{\text{med} \rightarrow \text{DM}} v \rangle n_{\text{med}}^2 - \langle \sigma_{\text{DM} \rightarrow \text{med}} v \rangle n_{\text{DM}}^2 \\
&+ \langle \sigma_{\text{DM} \rightarrow \text{SM}} v \rangle [(n_{\text{DM}}^{\text{eq}})^2 - n_{\text{DM}}^2] + \langle \Gamma_{\text{SM} \rightarrow \text{DM}}^D \rangle \frac{n_{\text{SM}}^{\text{eq}}}{(n_{\text{DM}}^{\text{eq}})^2} [(n_{\text{DM}}^{\text{eq}})^2 - n_{\text{DM}}^2] + \dots,
\end{aligned} \tag{3.6}$$

$$\begin{aligned}
xHs \frac{dY_{\text{med}}}{dx} &= \langle \sigma_{\text{DM} \rightarrow \text{med}} v \rangle n_{\text{DM}}^2 - \langle \sigma_{\text{med} \rightarrow \text{DM}} v \rangle n_{\text{med}}^2 \\
&+ \langle \sigma_{\text{med} \rightarrow \text{SM}} v \rangle [(n_{\text{med}}^{\text{eq}})^2 - n_{\text{med}}^2] + \langle \Gamma_{\text{SM} \rightarrow \text{med}}^D \rangle \frac{n_{\text{SM}}^{\text{eq}}}{(n_{\text{med}}^{\text{eq}})^2} [(n_{\text{med}}^{\text{eq}})^2 - n_{\text{med}}^2] + \dots
\end{aligned} \tag{3.7}$$

where Γ^D refers to the decay rate of a SM particle into two DM particles or two mediator particles. We kept a sum over all $\text{SM} \leftrightarrow \text{DM}$ and $\text{SM} \leftrightarrow \text{med}$ channels implicit for clarity. The dots in equations 3.6 and 3.7 stand for possible additional terms which could arise in one model or another⁶. However, in this thesis, we will limit ourself to leading order processes on the relevant couplings⁷. Moreover, in order to avoid cluttering of the equations let us define

$$\gamma_{\text{SM} \leftrightarrow \text{DM}}^{\text{eq}} \equiv \langle \sigma_{\text{DM} \rightarrow \text{SM}} v \rangle (n_{\text{DM}}^{\text{eq}})^2 + \langle \Gamma_{\text{SM} \rightarrow \text{DM}}^D \rangle n_{\text{SM}}^{\text{eq}} + \dots, \tag{3.8}$$

and

$$\gamma_{\text{SM} \leftrightarrow \text{med}}^{\text{eq}} \equiv \langle \sigma_{\text{med} \rightarrow \text{SM}} v \rangle (n_{\text{med}}^{\text{eq}})^2 + \langle \Gamma_{\text{SM} \rightarrow \text{med}}^D \rangle n_{\text{SM}}^{\text{eq}} + \dots \tag{3.9}$$

Although the Boltzmann equations contain in general many terms, only one or two terms are relevant for production regimes we are interested in. At the opposite, these equations are not sufficient to determine the amount of DM produced in the reannihilation regimes. Indeed, these regimes are characterised by a different temperature for the hidden and the visible sectors. Thus, we also need to evaluate the amount of energy which has been transferred from one sector to the other. We will discuss the additional needed equation when we will discuss the reannihilation regimes (see subsection 3.2.4).

The parameter space can be divided in several regions depending on whether the various connecting processes lead, or not, to thermalisation. Delimiting those

⁶For example, in the vector portal model we have $f + \gamma' \rightarrow f + \gamma$ for f a SM fermion. In the scalar portal, we have $h + h \rightarrow h + \phi$ for example.

⁷For example, in the vector portal model, we have $f + f \rightarrow \gamma' + \gamma$ which dominates over $f + f \rightarrow \gamma' + \gamma'$ as only one mixing parameter is required in the first and two are required in the second process.

regions will help us to understand the distinction between the various production regimes. Notice also that kinetic and chemical equilibrium are reached almost at the same time for relativistic species [179] such that one can use the kinetic equilibrium condition to check if two baths thermalised prior to DM decoupling. The "three sector - three connectors" structure gives us three thermalisation conditions:

$$\Gamma_{\text{SM} \leftrightarrow \text{DM}} \gtrsim H \quad - \quad \Gamma_{\text{SM} \leftrightarrow \text{med}} \gtrsim H \quad - \quad \Gamma_{\text{DM} \leftrightarrow \text{med}} \gtrsim H. \quad (3.10)$$

Note that, for the case of SM bath thermalising with one of the two "dark" particles (DM or mediator), the thermalisation conditions of Eq. 3.10 have to be evaluated at $T \sim m_{\text{DM}}$ since we aim to look for thermalisation when the DM abundance will freeze which typically happens when the temperature cools down to the DM mass. On the other hand, for the last case, where we focus on the possible thermalisation within the hidden sector, we could face two distinct temperatures T and T' for the visible and hidden sector respectively. This would happen if the hidden sector thermalises but is not in thermal equilibrium with the SM, i.e. the two first conditions of Eq. 3.10 are not satisfied while the last one is. In this case, the last thermalisation conditions of Eq. 3.10 has to be evaluated at $T' \sim m_{\text{DM}}$. The interaction rates in Eq. 3.10 are given by,

$$\Gamma_{\text{SM} \leftrightarrow \text{DM}} = \frac{\gamma_{\text{SM} \leftrightarrow \text{DM}}^{\text{eq}}}{n_{\text{DM}}^{\text{eq}}}, \quad (3.11)$$

$$\Gamma_{\text{SM} \leftrightarrow \text{med}} = \frac{\gamma_{\text{SM} \leftrightarrow \text{med}}^{\text{eq}}}{n_{\text{med}}^{\text{eq}}}, \quad (3.12)$$

$$\Gamma_{\text{DM} \leftrightarrow \text{med}} = \langle \sigma_{\text{med} \rightarrow \text{DM}} v \rangle n_{\text{med}}. \quad (3.13)$$

Those thermalisation conditions can all be converted into a condition on the involved coupling. Indeed, we have seen from the relevant Feynman diagrams of Figures 3.3, 3.4 and 3.5 that these three thermalisation conditions are driven by κ'/κ_ϕ , $\epsilon/\lambda_{\Phi H}$ and α'/α_ϕ respectively such that one can extract a lower bound on these couplings from thermalisation conditions. Figure 3.8 gives the minimal value for each coupling required for thermalisation in both the vector and scalar portal models, shown in dashed and solid respectively.

The reason that in Eq. 3.13 we do not evaluate quantities at equilibrium is due to fact that mediator particles are still being produced by slow $\text{SM} \rightarrow \text{med}$ processes.

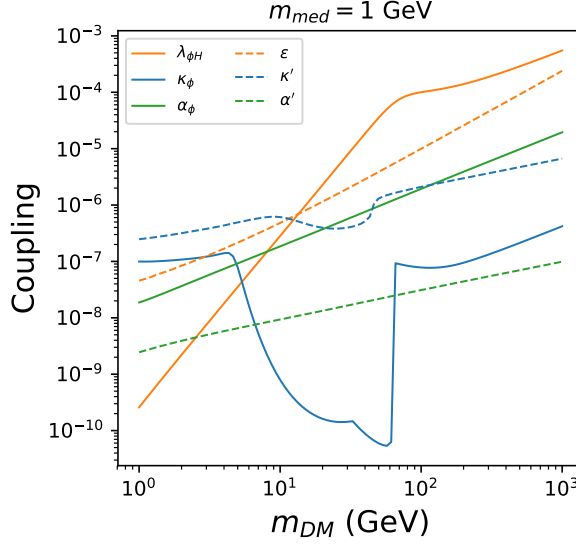


FIGURE 3.8: Value of the couplings needed to have thermalisation between DM and SM baths (blue), DM and mediator baths (green) and SM and mediator baths (orange). The solid and dashed lines show results for the vector and scalar portal models respectively.

So, we could have situation where neither the mediator nor the DM is at equilibrium and we need to consider out-of-equilibrium quantities. We then have two situations depending on if the mediator has reached equilibrium or not. If the SM and the mediator bath are in thermal equilibrium, quantities appearing in 3.13 are at equilibrium and the value of α'/α_ϕ required for thermalisation does not depend on the connector between the SM and the mediator, $\epsilon/\lambda_{\Phi H}$. On the other hand, if the SM and mediator baths are not in thermal equilibrium, there is a slow production of mediator particles from the SM which is still occurring and the value of α'/α_ϕ required for thermalisation depends on $\epsilon/\lambda_{\Phi H}$.

If we consider thermalisation or not, there are only eight possibilities with three sectors. Figure 3.9 shows how the three thermalisation lines generically divide the parameter space for a chosen set of DM and mediator masses. We do not show scale on the x- and y-axis as we aim to provide a qualitative understanding for now. Six of the eight possibilities are visible on the Figure 3.9, but two are missing. The one which connects all sector but the mediator to the SM lies above the part of the parameter space we are presenting. Indeed, it lies in the non-perturbative region

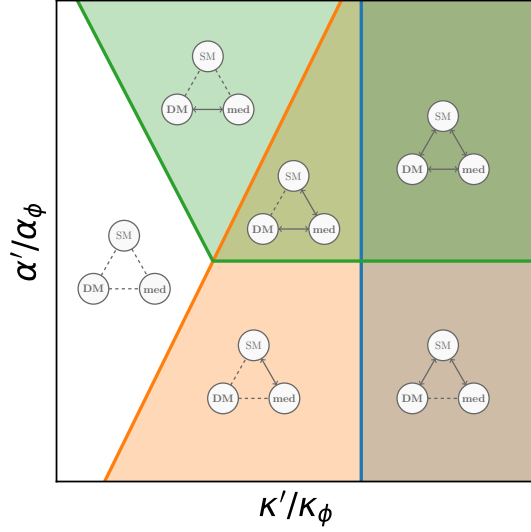


FIGURE 3.9: DM-to-med coupling versus DM-to-SM coupling and subdivision made by the three thermalisation conditions. In blue: the SM and DM baths thermalise, in orange: the SM and mediator baths thermalise and in green: the DM and mediator baths thermalise.

($\alpha'/\alpha_\phi > 1$) and will not be considered. The other possibility we are missing requires a thermalisation only between the DM and the SM baths. This is not possible as the value of κ'/κ_ϕ it requires to thermalise implies either a thermalisation between the SM and the mediator baths either a thermalisation between the DM and the mediator baths. Thus, we argue here that Figure 3.9 shows, in a qualitative way, all possible combination of thermalisations which could arise in a "three sectors-three connectors" structure. Note that since $\epsilon \propto 1/\sqrt{\alpha'}$ (resp. $\lambda_{\Phi H} \propto 1/\sqrt{\alpha_\phi}$), the smaller α' (resp. α_ϕ), the larger ϵ (resp. $\lambda_{\Phi H}$) for fixed values of κ' (resp. κ_ϕ). This explains why, in Figure 3.9, we have that SM-to-med interactions thermalise more easily for small values of α' (resp. α_ϕ).

In order to know how the relic abundance is generated, it is not enough to know which interaction does thermalise. As mentioned already above, out-of-equilibrium processes can also play a crucial role. The later can slowly produce particles from a filled reservoir to a more empty reservoir. Thus in Figure 3.9, one must also indicate these processes whenever they are relevant, pointing in which direction they are relevant. One would also leave the irrelevant out-of-equilibrium processes in dashed line. This is what we do in Figure 3.10. This implies that some regions of Figure 3.9 will be now divided in two. For instance, the orange only region in Figure 3.9 will be split into two regions depending on which of the two out-of-equilibrium

channels (DM-to-SM or DM-to-med) will dominate. Indeed, when the DM is connected in the same way to both the SM and the mediator baths⁸, we have to know the hierarchy of those interactions. Is the DM more connected to the SM or to the mediator? This can be answered by looking at the following condition,

$$\gamma_{\text{DM} \leftrightarrow \text{med}} = \gamma_{\text{DM} \leftrightarrow \text{SM}}. \quad (3.14)$$

We face the same issue in regimes where several processes are in thermal equilibrium. These regimes have also to be divided into two regions depending on which channel is dominant. Then, in these cases, these divisions in sub-regions are driven by,

$$\gamma_{\text{DM} \leftrightarrow \text{med}}^{\text{eq}} = \gamma_{\text{DM} \leftrightarrow \text{SM}}^{\text{eq}}, \quad (3.15)$$

with $\gamma_{\text{DM} \leftrightarrow \text{med}}^{\text{eq}} \equiv \langle \sigma_{\text{DM} \leftrightarrow \text{med}} v \rangle (n_{\text{med}}^{\text{eq}})^2$.

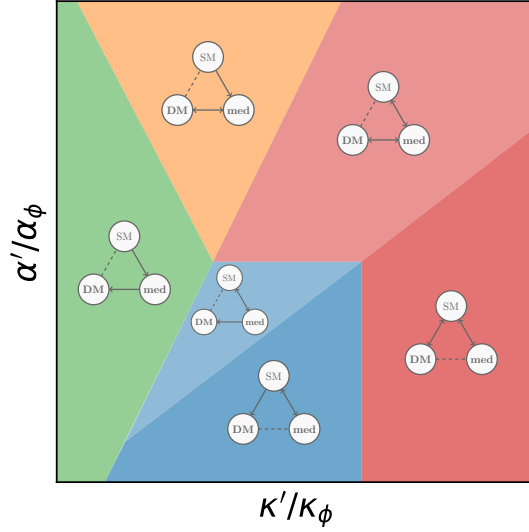


FIGURE 3.10: DM-to-med coupling versus DM-to-SM coupling and subdivision made by the three thermalisation conditions and considering the dominant connection to the DM bath only.

⁸i.e. if the lines connecting DM to the SM and DM to the mediator in Figure 3.9 are both dashed (no thermalisation) or both solid (thermalisation).

Let us detail a little bit more the transition from Figure 3.9 to Figure 3.10. Indeed, we still have six different regions in the latter one but they are not exactly the same than in the first one. Indeed, let us look at the orange subdivision in Figure 3.9 where the SM and mediator baths are in thermal equilibrium but not with the DM bath. The condition given by Eq. 3.14 divide this subsection in two in Figure 3.10: the dark blue regime where the DM-to-SM connection is stronger than the DM-to-med connection and the light blue regime where the DM-to-med connection is stronger than the DM-to-SM connection.

The white region in Figure 3.9, where there is no thermal contact between any of the three baths, is unchanged as well as the green only region where only the DM and mediator baths are in thermal contact (green and orange respectively in Figure 3.10). In the orange and green region in Figure 3.9 the mediator bath thermalise with the DM and SM ones. Now, the fully thermalised region (orange, green and blue in Figure 3.9), because of the condition given in Eq. 3.14, is split in two and in one of these two subdivision, the DM stronger connects to the mediator bath than to the SM one. Thus, in this region, one can neglect the effect of the DM connection to the SM bath and one gets back to the same physical situation than in the orange and green region. Moreover, in the other part of the fully thermalised region, the DM is stronger connected to the mediator bath and one gets back to the same physical situation than in the orange and blue region where the DM and mediator baths are not thermally connected. This behaviour explains the rearrangement of these three subdivision in Figure 3.9 into two in Figure 3.10.

Now that we have an overall idea of the picture, let us analyse all of the six regimes shown in Figure 3.10.

3.2.2 Freeze-in: regimes Ia and Ib

Let us first consider very small values for the DM-to-SM (κ'/κ_ϕ) and DM-to-med (α'/α_ϕ) couplings. In this case, the DM-to-SM and DM-to-med processes do not thermalise, but nevertheless the SM-to-med processes do thermalise because $\epsilon \sim \kappa'/\sqrt{\alpha'}$ (or $\lambda_{\Phi H} \sim \kappa_\phi/\sqrt{\alpha_\phi}$). Thus, the mediator is a part of the SM thermal bath. Then, either the DM bath is already there just after the inflation and the DM relic abundance has to be set by the initial condition. Or the DM reservoir was empty or negligible at the end of inflation. The DM could then only be slowly produced through out-of-equilibrium processes $\text{SM} \rightarrow \text{DM}$ and $\text{med} \rightarrow \text{DM}$ parametrised by κ'/κ_ϕ and α'/α_ϕ respectively. This is the so-called Freeze-In regime that we have already met in Subsection 3.2.2. The Boltzmann equation for the DM yield (Eq. 3.6) becomes:

$$\text{Regime I : } xHs \frac{dY_{\text{DM}}}{dx} \simeq \gamma_{\text{SM} \leftrightarrow \text{DM}}^{\text{eq}}(x) + \gamma_{\text{med} \leftrightarrow \text{DM}}^{\text{eq}}(x), \quad (3.16)$$

where we simplified the right hand side as the DM yield will always be much smaller than equilibrium yields. Now, depending on which process dominates (i.e. on which side of the line defined by Eq. 3.14 we sit), we get two different dynamical production mechanisms for DM. The first one is:

$$\text{Regime Ia : } xHs \frac{dY_{\text{DM}}}{dx} \simeq \gamma_{\text{SM} \leftrightarrow \text{DM}}^{\text{eq}}(x). \quad (3.17)$$

In the first case (Ia), DM production is dominated by slow $\text{SM} \rightarrow \text{DM}$ out-of-equilibrium processes (in dark blue in Figure 3.10). These processes depend only on the connector κ'/κ_ϕ . As a consequence, the DM relic abundance depends only on κ'/κ_ϕ and it gives a vertical line in the phase diagram, see left panel of Figure 3.11.

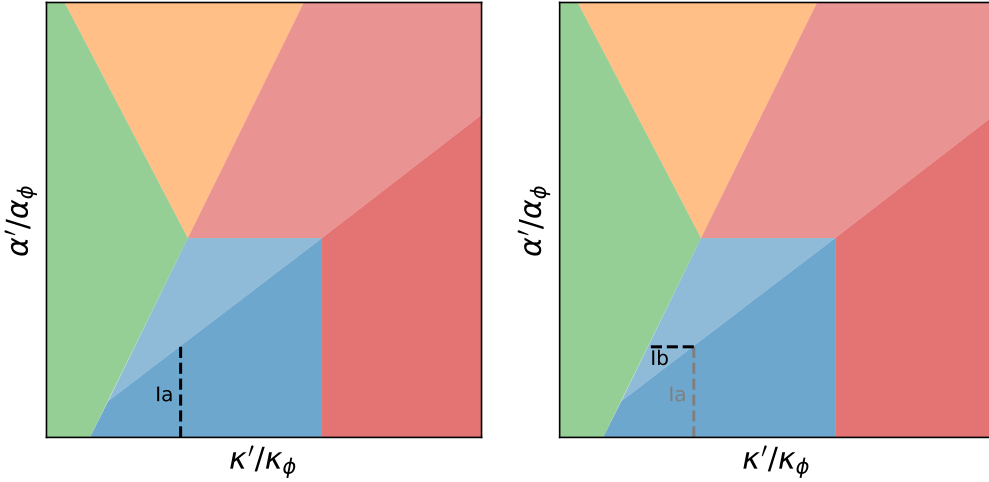


FIGURE 3.11: Qualitative representation of the parameter space of a three sectors three connectors scenario for the regime Ia (left) and Ib (right).

Note that the fact that there is here thermalisation between the SM and the mediator baths does not change anything to the dynamics of this freeze-in regime. Indeed, since the DM particles are dominantly produced by the SM particles it

does not matter if the mediator bath thermalises with the SM. The only effect this thermalisation can have is that the thermalised mediator particles will modify the number of relativistic degrees of freedom and thus the Hubble expansion rate. The modification of the Hubble rate is of order⁹ $g_{\text{med}}/g_{*}^{\text{eff}} \sim 10^{-2}$. As this effect is of percent level, we neglect it. In the left panel of Fig. 3.12 we show as a function of m_{DM} the value of the SM-to-DM connector required to reach the observed relic abundance in the Ia regime, which we note κ_{Ia} ¹⁰. For the vector portal model, as the thermalised dark photons role is negligible in the production of the DM particles, this solid blue line is essentially the same as in the massless dark photon case [179]. The step in this figure is due to the closing of the production of DM through the Z boson channel. Indeed, if $m_{\text{DM}} > m_Z$, this production channel is no longer available. The production of DM from SM is then less efficient and a bigger value for the coupling is required. For the scalar portal model, the first step is due to the closing of the production of DM through the H boson channel. The second step is due to the closing of channels through the SM scalar VEV (v_H). The fact that the line stops at $m_{\text{DM}} = 1000$ GeV in the scalar case is due to the choice of the new scalar VEV ($v_\Phi = 1000$ GeV) in this example. Indeed, when $m_{\text{DM}} > v_\Phi$, the freeze-in process stops to be efficient before the symmetry breaking because there is no scalar mixing in this case. It is then no longer possible to produce DM from SM and the freeze-in regime does not exist for $m_{\text{DM}} > v_\Phi$. See section 3.4 for a more in depth analysis.

In both models, the dependence of κ_{Ia} on the DM mass can be complicated because the dominant production channels depend also on m_{DM} . But the number of DM particles produced through $\text{SM}_i \text{SM}_i \rightarrow \text{DM DM}$ is related in a simple way to equilibrium quantities evaluated at a temperature $T \ll \max\{m_i, m_{\text{DM}}\}$,

$$Y_{\text{DM}}^{\text{Ia}}(x) = \sum_i c_i \frac{(n_i^{\text{eq}})^2 \langle \sigma_{\text{SM}_i \rightarrow \text{DM} \bar{\text{DM}}} \rangle}{Hs} \Big|_{T=\max\{T, m_i, m_{\text{DM}}\}}, \quad (3.18)$$

where the c_i are order unity coefficients [179]. Eq. 3.18 allows us to understand easily why $\Omega_{\text{DM}} = 26\%$ requires a small value of the DM-to-SM coupling. Indeed, as already mentioned, one needs a suppressed amount of DM with respect to the amount it has if it thermalises and is relativistic. Thus one requires a small value for the DM yield and then a small production cross section $\langle \sigma_{\text{SM}_i \rightarrow \text{DM} \bar{\text{DM}}} \rangle \sim \kappa'^2$ (or κ_ϕ^2).

Going up along the vertical line of the Ia regime depicted in Fig. 3.11, the value of α'/α_ϕ increases while that of $\epsilon/\lambda_{\Phi H}$ decreases. Thus, at some point, the SM

⁹We remind here that $g_\phi = 0$ and $g_{\gamma'} = 3$ (in the massive vector case).

¹⁰Note that we have shown in Section 1.7 and Figure 1.30 that direct detection can probe values of κ down to 3×10^{-11} and 10^{-9} for the vector and scalar portal respectively. We see now that it implies that direct detection experiments are able to probe FI regime, see [84] for more details.

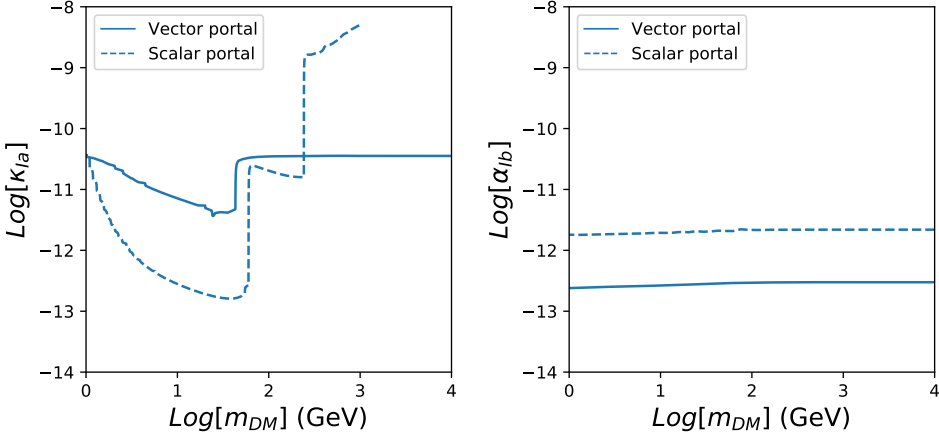


FIGURE 3.12: Left: Values of κ'/κ_ϕ needed to account for the observed relic density, as a function of the DM mass m_{DM} , for the standard freeze-in (regime Ia) for the vector portal (solid) and the scalar portal (dashed) models. Right: Values of α'/α_ϕ needed to account for the observed relic density, as a function of the DM mass m_{DM} , for the freeze-in from mediators (regime Ib) for the vector portal (solid) and the scalar portal (dashed) models.

and the mediator baths stop to thermalise, $\epsilon/\lambda_{\Phi H} < \epsilon_{\text{th}}/\lambda_{\Phi H_{\text{th}}}$. However, before this could happen and while the mediator particles are still in thermal equilibrium with the SM bath, α'/α_ϕ becomes large enough for the $\text{med} \rightarrow \text{DM}$ processes to overcome the $\text{SM} \rightarrow \text{DM}$ production and to dominate the DM production. Clearly, in this case a smaller value of the DM-to-SM connector κ'/κ_ϕ is required to avoid overproduction of DM particles and moreover, the DM relic abundance depends only on α'/α_ϕ . This gives rise to the horizontal line depicted in Fig. 3.11¹¹.

$$\text{Regime Ib : } x H s \frac{dY_{DM}}{dx} \simeq \gamma_{\text{med} \leftrightarrow \text{DM}}^{\text{eq}}(x). \quad (3.19)$$

In other words for this second case (Ib), the DM production is dominated by the $\text{med} \rightarrow \text{DM}$ process (in light blue in Figure 3.10), and the process depends only on the connector α'/α_ϕ . As said above, the DM relic abundance depends only on α'/α_ϕ and it gives a horizontal line in the phase diagram, see right panel of Figure 3.11. In the right panel of Fig. 3.12 we show as a function of m_{DM} the value of the med-to-DM connector required to reach the observed relic abundance in the Ib regime,

¹¹This regime has been briefly discussed in [180], where it is dubbed "inverse annihilation", and in [181], in a model with a scalar singlet that mixes with the Higgs. It is also considered in a scenario with a Z' based on a $B - L$ gauge symmetry, which appeared simultaneously with our work [182].

which we note α_{Ib} . This time, there is no particular feature since there is only one production channel which is an annihilation and that it occurs in the t-channel (i.e. no *on-shell* resonance).

As in the Ia regime, the DM yield can be simply written in the Ib regime,

$$Y_{\text{DM}}^{\text{Ib}}(x) = c_{\text{med}} \frac{(n_{\text{med}}^{\text{eq}})^2(x) \langle \sigma_{\text{med} \rightarrow \text{DM} \bar{\nu}} \rangle}{Hs} \Big|_{T=\text{Max}[T, m_{\text{DM}}]}, \quad (3.20)$$

with $c_{\text{med}} = \mathcal{O}(1)$.

Note that this production regime is not new as a dynamical regime (it is a simple freeze-in) but is new in the sense that source particles here are not SM particles but hidden sector particles.

3.2.3 Sequential freeze-in: regime II

As we move toward smaller values of the DM-to-SM coupling κ'/κ_ϕ , the value of the med-to-SM coupling $\epsilon/\lambda_{\Phi H}$ decreases. This will imply that, at some point, the value of this last connector will not be high enough to allow thermalisation between the SM and the mediator baths anymore: $\epsilon/\lambda_{\Phi H} < \epsilon_{\text{th}}/\lambda_{\Phi H_{\text{th}}}$. At this moment, the mediator yield is no longer given by the equilibrium quantity and one has to compute the actual mediator yield as a function of time. In this new regime, shown in green in Figure 3.10, none of the three sector thermalises with an other one.

One could think that, like in the previous regime, this regime could be split in two distinct phases depending on to which bath the DM one is more coupled to (see Eq. 3.14). But, if the DM bath is more connected to the SM bath, as the DM-to-SM coupling is already much smaller than the one required in the standard freeze-in phase, $\kappa'/\kappa_\phi \ll \kappa_{\text{Ia}}$, the DM relic abundance could not be produced directly from SM. Thus, there is, in practice, only one possibility for the phase "II". It turns out that this slow out-of-equilibrium production of mediator particles from SM directly followed by the slow out-of-equilibrium production of DM particles from these unthermalised mediator particles can produce the observed DM relic abundance.

This chain of successive freeze-in processes has been dubbed "sequential freeze-in" and constitute a new dynamical way of accounting for the DM relic density. As in standard freeze-in, the reverse processes can be neglected as they have a minor impact on the final DM yield. The Boltzman equations take then the following form,

$$\text{Regime II : } \begin{cases} xHs \frac{dY_{\text{med}}}{dx} \simeq \gamma_{\text{SM} \leftrightarrow \text{med}}^{\text{eq}} \\ xHs \frac{dY_{\text{DM}}}{dx} \simeq \gamma_{\text{med} \leftrightarrow \text{DM}} \end{cases} \quad (3.21)$$

There is a suppression factor on this reaction density with respect to the equilibrium density, as the DM production rate will be proportional to $\propto (n_{\text{med}}/n_{\text{med}}^{\text{eq}})^2$ with n_{med} determined by the first Boltzmann equation. The number of mediator produced by freeze-in from SM particles is proportional to ϵ^2 and $\lambda_{\Phi H}^2$ in the vector and scalar portal models respectively. Putting it in the DM particles production rate which is proportional to $n_{\text{med}}^2 \langle \sigma_{\text{med} \rightarrow \text{DM}} v \rangle$, in the vector portal model we get $n_{\text{DM}} \sim \epsilon^4 \alpha'^2 \sim \kappa'^4$ and, in the scalar portal model, $n_{\text{DM}} \sim \lambda_{\Phi H}^4 \alpha_\phi^2 \sim \kappa_\phi^4$. We get then that, in the sequential freeze-in regime, the DM relic density depends on the magnitude of the DM-to-SM connector only. This feature is again translated into a vertical line in the phase diagram, see Figure 3.13.

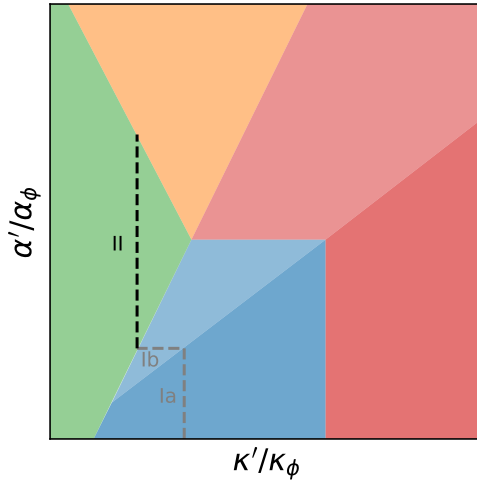


FIGURE 3.13: Qualitative representation of the parameter space of a three sectors three connectors scenario for the regime II.

These results show that along the sequential freeze-in it is possible to have a DM-to-SM connector orders of magnitude below the one required in the standard freeze-in regime. Figure 3.14 gives the required value of the DM-to-SM connector κ'/κ_ϕ , dept κ_{II} , to produce the observed DM relic abundance in the sequential freeze-in regime (II). We also show results in the standard freeze-in regime (Ia) for

comparison. One can see that for large values of $m_{\text{DM}}/m_{\text{med}}$, κ_{II} tends to κ_{Ia} . The merging of the sequential freeze-in regime (II) with the very well known standard freeze-in regime (Ia) is easy to understand. Heavier DM particles stop to be produced at higher temperature and thus earlier in the Universe history. The SM had then less time to produce mediator particles prior the temperature T reaches the DM mass scale. With less mediator particles in the bath, one need to increase the sequential freeze-in efficiency. As we have seen, this efficiency is ruled only by the DM-to-SM connector κ'/κ_ϕ . Then, increasing the mass ratio $m_{\text{DM}}/m_{\text{med}}$ requires to increase κ_{II} . Increasing κ_{II} will imply that, at some point, the production of DM directly from SM particles will be comparable to the sequential freeze-in production such that the two regimes will merge. This feature can also be understood looking at the $m_{\text{DM}}/m_{\text{med}}$ mass ratio. As $m_{\text{DM}}/m_{\text{med}} \rightarrow \infty$, one gets back to the massless mediator case where the mediator cannot be directly produced from the SM. The sequential FI regime does not exist or is much less efficient in the case of the scalar portal model. Indeed, one sees that the sequential freeze-in regime exists for $m_{\text{DM}} > v_\phi$ while it was not the case for the standard freeze-in regime. This is due to the fact that mediator particles can be produced without scalar mixing, directly from the quartic coupling. Thus, enough mediator particles could have been produce at high temperature for the DM to freeze-in from the mediator bath, even before the hidden and visible sector symmetry breaking temperature. The difference at high DM masses between the curves for the scalar model in the regime Ia (light dashed blue) and the regime II (dark dashed blue) stems from the fact that sequential freeze-in starts to be relevant for DM particles lighter than the hidden sector symmetry breaking and this was not taken into account in the pure freeze-in regime (regime Ia). That is to say that the pure freeze-in curve in Figure 3.14 (dashed light blue) is pure freeze-in and does not take sequential freeze-in contribution into account.

3.2.4 Reannihilation: regimes IIIa and IIIb

In the regime II, if we increase the DM-to-med connector α'/α_ϕ , the DM and mediator baths will start to thermalise at some point. Here, one has two different thermal baths because the HS does not thermalise with the SM. That is to say that the HS bath has no reason to have the same temperature as the SM one, we have $T_{\text{HS}} \equiv T' \neq T_{\text{SM}} \equiv T$. In this regime, clearly since the DM thermalises with the mediator, its abundance will be Boltzmann suppressed when the temperature goes below its mass ($T' < m_{\text{DM}}$). But then it turns out that it will not undergo a standard freeze-out mechanism and this for two reasons: first this happens in a sector with $T' \neq T$. Second, at the time the DM abundance gets Boltzmann suppressed, HS particles are still slowly produced out-of-equilibrium from the SM. One faces thus a DM production regime called "reannihilation" in which this small source of dark

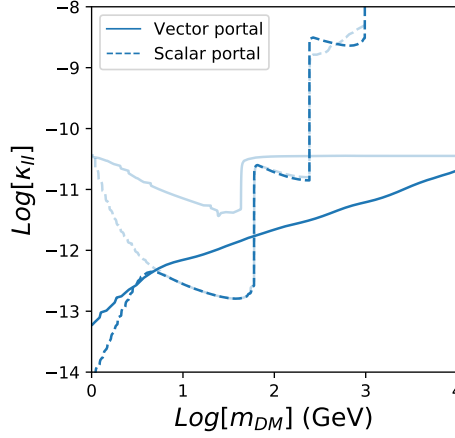


FIGURE 3.14: Values of κ'/κ_ϕ needed to account for the observed relic density, as a function of the DM mass m_{DM} , for the sequential freeze-in (regime II) for the vector portal (solid) and the scalar portal (dashed) models. Solutions obtained in the regime Ia are also shown in light blue.

sector particles forced the DM to freeze-out somewhat later than during standard freeze-out (actually when $T \sim m_{DM}$ rather than when $T' \sim m_{DM}/(\text{a few})$). This regime takes place already in the vector portal model for a massless mediator (see [179]).

As in the freeze-in regime (I), the reannihilation regime (III) is also made of two sub-regimes. Indeed, the source of dark sector particles could produce either DM particles (IIIa) either mediator particles (IIIb), depending on which connection is the strongest one. In practice, in the two models we are interested in, moving towards larger values of α'/α_ϕ , the system enters into the regime IIIb and not the regime IIIa. This is due to the value of the DM-to-SM connector which is very small in this part of the parameter space. Indeed, the value of κ'/κ_ϕ is smaller than the one required in the regime Ia. That is to say that DM cannot be efficiently produced from SM in this region of the parameter space. Thus, we first discuss the regime IIIb and discuss next the regime IIIa.

As said above, in the regime IIIb (shown in orange in Figure 3.10) one has to consider quantities in the hidden sector at a different temperature $x' \neq x$ and a source term from SM for the mediator. The Boltzmann equations can thus be written as,

$$\text{Regime IIIb : } \begin{cases} xHs \frac{dY_{\text{med}}}{dx} \simeq \gamma_{\text{SM} \leftrightarrow \text{med}}^{\text{eq}}(x) - \gamma_{\text{med} \leftrightarrow \text{DM}}^{\text{eq}}(x') \left[1 - \left(\frac{Y_{\text{DM}}}{Y_{\text{DM}}^{\text{eq}}(x')} \right)^2 \right], \\ xHs \frac{dY_{\text{DM}}}{dx} \simeq \gamma_{\text{med} \leftrightarrow \text{DM}}^{\text{eq}}(x') \left[1 - \left(\frac{Y_{\text{DM}}}{Y_{\text{DM}}^{\text{eq}}(x')} \right)^2 \right]. \end{cases} \quad (3.22)$$

Clearly, these equations can be solved only if one knows T' as a function of T . Thus, one also needs to provide the dark sector temperature as a function of the temperature of the visible sector. This is done by integrating the Boltzmann equation for the SM-to-hidden sector energy transfer (see [179]),

$$xH \frac{d\rho'}{dx} + 4H(\rho' + p') \simeq (n_{\text{SM}}^{\text{eq}}(x))^2 \langle \sigma_{\text{SM} \rightarrow \text{med}} v \Delta E \rangle. \quad (3.23)$$

One can plug into this equation, the hidden sector equation of state $p' = p'(\rho')$ which is given by

$$p' = \frac{1}{3} (\rho' - m_{\text{DM}} Y_{\text{DM}} s), \quad (3.24)$$

$$\rho_{\text{DM}}(x') = \rho_{\text{DM}}^{\text{eq}}(x) \frac{Y_{\text{DM}}}{Y_{\text{DM}}^{\text{eq}}(x)}. \quad (3.25)$$

The final DM relic density obtained in the regime IIIb approximately scale as

$$\Omega_{\text{DM}} \propto \frac{\log \left(\sqrt{\langle \sigma_{\text{SM} \rightarrow \text{med}} v \rangle \langle \sigma_{\text{DM} \rightarrow \text{med}} v \rangle} \right)}{\langle \sigma_{\text{med} \rightarrow \text{DM}} v \rangle}, \quad (3.26)$$

which goes like $\propto \log(\alpha' \epsilon) / \alpha'^2$ in the vector portal model or like $\propto \log(\alpha_\phi \lambda_{\Phi H}) / \alpha_\phi^2$ in the scalar portal model. This explains why this regime leads to a line which is close to be horizontal in the phase diagram, see Figure 3.15.

The IIIb reannihilation regime is new¹² as it does not occur in the massless mediator case. Alternatively, in the massless mediator case, the system enters in the

¹²It has not been discussed in [179] as it does not exist in the massless dark photon case and as authors did not considered the scalar portal we are considering. Indeed, in this work, authors considered a scalar DM directly mixing with the SM scalar.

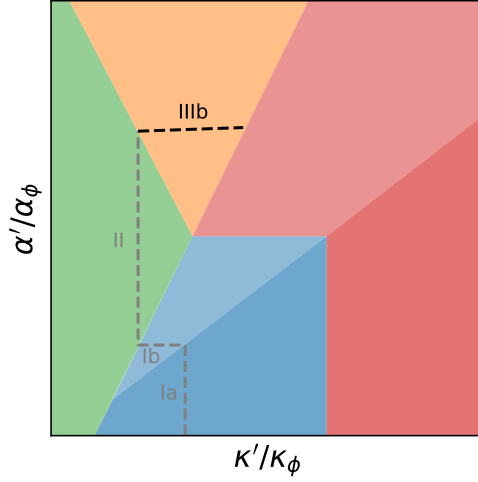


FIGURE 3.15: Qualitative representation of the parameter space of a three sectors three connectors scenario for the regime IIIb.

regime IIIa instead of IIIb. This stems from the fact that the massless mediator does not directly couple to SM particles such that the source of dark sector particles goes through $\text{SM} \rightarrow \text{DM}$ slow out-of-equilibrium processes. In this regime IIIa, the hidden sector is then populated from SM-to-DM processes (see [179]) and the Boltzmann equations are given by,

$$\text{Regime IIIa : } \begin{cases} xHs \frac{dY_{\text{med}}}{dx} \simeq -\gamma_{\text{med} \leftrightarrow \text{DM}}^{\text{eq}}(x') \left[1 - \left(\frac{Y_{\text{DM}}}{Y_{\text{DM}}^{\text{eq}}(x')} \right)^2 \right], \\ xHs \frac{dY_{\text{DM}}}{dx} \simeq \gamma_{\text{SM} \rightarrow \text{DM}}^{\text{eq}}(x) + \gamma_{\text{med} \leftrightarrow \text{DM}}^{\text{eq}}(x') \left[1 - \left(\frac{Y_{\text{DM}}}{Y_{\text{DM}}^{\text{eq}}(x')} \right)^2 \right]. \end{cases} \quad (3.27)$$

As in the regime IIIb, one has also to compute the transferred energy from one sector to the other. This time, this transfer is dominated by the SM-to-DM process,

$$xH \frac{d\rho'}{dx} + 4H(\rho' + p') \simeq (n_{\text{SM}}^{\text{eq}}(x))^2 \langle \sigma_{\text{SM} \rightarrow \text{DM}} v \Delta E \rangle. \quad (3.28)$$

In the massive mediator case, the slow production of the mediator from SM is always more efficient than the slow production of DM from SM in this part of the parameter space. Thus, this regime can only show up in the massless mediator case where the production of mediator from SM is not possible. Thus, we will not discuss the regime IIIa further, see [179] for a detailed analysis. We will just mention that in

this regime, as said in [179], the final DM abundance, which is set at $T \sim m_{\text{DM}}$ rather than at $T' \sim m_{\text{DM}} / (\text{a few})$, scales as $\sim \log(\alpha' \kappa') / \alpha'^2$ in the vector portal model and we found a similar behaviour in the scalar portal model $\sim \log(\alpha_\phi \kappa_\phi) / \alpha_\phi^2$.

3.2.5 Secluded freeze-out: regimes IVa and IVb

As we have seen in the previous subsection, the two reannihilation regimes (IIIa and IIIb) occur when a slow production of hidden sector particles from SM particles is still active when the DM freezes-out, that is to say when T' becomes smaller than m_{DM} . If such a source term becomes negligible before $T' \sim m_{\text{DM}}$, the system does not enter in one of the two reannihilation regimes. Here too, once the source term from the SM has created enough DM or mediator particles, these particles thermalise with each other forming a hidden thermal bath with temperature T' . But, since the same term from SM has stopped to be active at $T' \gtrsim m_{\text{DM}}$, there is no period of reannihilation. Instead, the DM particles undergo a simple “secluded freeze-out”. Here we refer to standard text-books freeze-out, except that it takes place in a hidden sector, characterised by a temperature T' which differs from that of the visible sector, T (see Ref. [179] for details).

In practice, in the mass ranges we are considering in this chapter, secluded freeze-out does not occur in the instances depicted in Figures 3.6. This stems from the fact that, for the considered mass ranges, the SM-to-DM source term is always still active at $T' \sim m_{\text{DM}}$. Indeed, since we are always considering DM candidates heavier than the electron, the slow out-of-equilibrium production of DM particles from electron annihilation is always occurring at $T' \sim m_{\text{DM}}$ ¹³. Nevertheless, there are of course values of the masses for which the secluded freeze-out regime clearly dominates. This is the case for example if $m_{\text{med}} \ll m_{\text{DM}}$ and if the hidden sector was produced by some processes at the end of inflation. In fact, a general way for the secluded freeze-out to dominate would be to have an IR¹⁴ mass scale which would cut-off the hidden sector particles source term at a higher temperature, $T' > m_{\text{DM}}$. An other example, would be if the mass hierarchy is as following: $m_{\text{med}} < m_{\text{DM}} < m_e$, the SM-to-DM and SM-to-mediator potential source terms would be cut when the SM temperature reach the electron mass, $T \sim m_e$.

As in the previous dynamical ways, one can in principle distinguish two regimes, depending on whether the dominant dark sector particles source term produces DM particles or mediator particles, corresponding to IVa and IVb regimes respectively. The Boltzmann equations for the DM yield in the secluded freeze-out regimes are similar than the one in the reannihilation regimes. Here too, once the source term

¹³Other production channels are still active if the DM is heavier than other SM leptons.

¹⁴Infrared.

has stopped to be active, the Boltzmann equations for the DM yield are the same in both IVa and IVb regimes:

$$\text{Regimes IVa \& IVb : } \begin{cases} xHs \frac{dY_{\text{med}}}{dx} \simeq -\gamma_{\text{med} \leftrightarrow \text{DM}}^{\text{eq}}(x') \left[1 - \left(\frac{Y_{\text{DM}}}{Y_{\text{DM}}^{\text{eq}}(x')} \right)^2 \right], \\ xHs \frac{dY_{\text{DM}}}{dx} \simeq \gamma_{\text{med} \leftrightarrow \text{DM}}^{\text{eq}}(x') \left[1 - \left(\frac{Y_{\text{DM}}}{Y_{\text{DM}}^{\text{eq}}(x')} \right)^2 \right]. \end{cases} \quad (3.29)$$

In regimes regimes IVa and IVb, one can neglect the production terms at time DM freezes, see eqs 3.29. In all cases, the relic density is essentially determined by the value of the DM-to-med coupling (α' or α_ϕ), which would lead to a horizontal line in the phase diagram (if the choice of masses was allowing these regimes), see [179].

3.2.6 Freeze-out: regimes Va and Vb

Finally, from the reannihilation or secluded freeze-out regimes, if we keep increasing the DM-to-SM connector κ'/κ_ϕ (and consequently the SM-to-med connector $\epsilon/\lambda_{\Phi H}$), at some point all particles will thermalise and will form a unique thermal bath, characterised by a unique temperature T . Thus, DM particles will have no other choice to undergo a standard freeze-out. This freeze-out regimes will happen when, on top of the α'/α_ϕ driven processes which were already in thermal equilibrium in the previous regimes, the κ'/κ_ϕ driven processes and/or the $\epsilon/\lambda_{\Phi H}$ driven processes thermalise. Thus, such a transition into the freeze-out regime takes place when either κ'/κ_ϕ becomes larger than κ_{th} or $\epsilon/\lambda_{\Phi H}$ becomes larger than $\epsilon_{\text{th}}/\lambda_{\Phi H_{\text{th}}}$, see Figure 3.8.

Once again, the freeze-out regime can be dominated either by the med \leftrightarrow DM annihilation process (regime Vb, in light red in Figure 3.10) with the following Boltzmann equation,

$$\text{Regime Vb : } xHs \frac{dY_{\text{DM}}}{dx} \simeq \gamma_{\text{med} \leftrightarrow \text{DM}}^{\text{eq}}(x) \left[1 - \left(\frac{Y_{\text{DM}}}{Y_{\text{DM}}^{\text{eq}}(x)} \right)^2 \right], \quad (3.30)$$

or by the SM \leftrightarrow DM processes for larger values of κ'/κ_ϕ (regime Va, in dark red in Figure 3.10) with

$$\text{Regime Va : } xHs \frac{dY_{\text{DM}}}{dx} \simeq \gamma_{\text{SM} \leftrightarrow \text{DM}}^{\text{eq}}(x) \left[1 - \left(\frac{Y_{\text{DM}}}{Y_{\text{DM}}^{\text{eq}}(x)} \right)^2 \right]. \quad (3.31)$$

These two Boltzmann equations are very similar to the one applying in the secluded regimes except that this time there is only an equation for the DM yield since the mediator thermalises with both the DM and the SM particles. The other difference comes in the unique variable x instead of having both x and x' . This stems again from the fact that all populations thermalise with each other such that there is a unique temperature T .

Depending on which process dominates, the DM relic abundance will be either driven by α'/α_ϕ leading to a horizontal line in the phase diagram for the regime Vb (see left panel of Figure 3.16), either driven by $\kappa'/\kappa_{\Phi H}$ leading to a vertical line in the phase diagram for the regime Va (see right panel of Figure 3.16). In the latest case, if we keep decreasing the DM-to-med connector α'/α_ϕ , the hidden sector will eventually stop to thermalise, but this will have no impact on the DM final relic abundance since the connection of the DM to the mediator bath was already subdominant in this part of the parameter space.

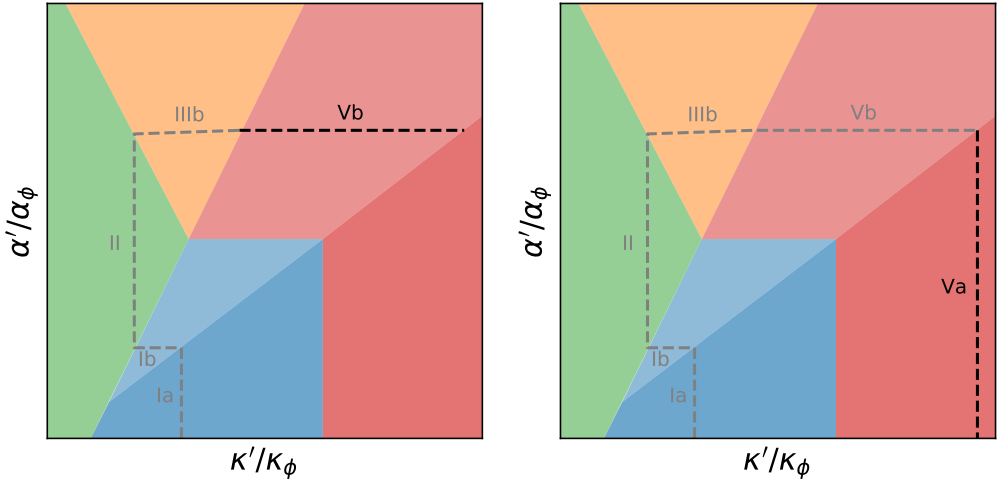


FIGURE 3.16: Qualitative representation of the parameter space of a three sectors three connectors scenario for the regime Vb (left) and Va (right).

We show in Figure 3.17 the needed values for the relevant coupling in order to account for the observed DM relic density in both regimes Vb (left) and Va (right).

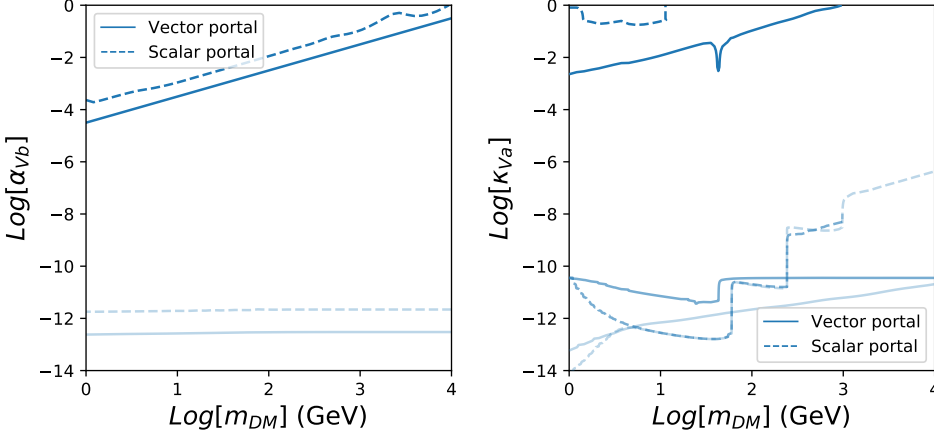


FIGURE 3.17: Values of κ'/κ_ϕ needed to account for the observed relic density, as a function of the DM mass m_{DM} , in the freeze-out regimes: regime Vb (left) and regime Va (right) for the vector portal (solid) and the scalar portal (dashed) models. Solutions obtained in the regime Ia and II/Ib are also shown for comparison in light blue and very light blue respectively.

3.3 Specificity of the vector portal model

3.3.1 Thermal effects

The vector portal model, also known as the dark photon model, is known for displaying thermal effects. These effects can be important when considering the dark photon production rates (in particular in stars, see Refs. [106]–[111]). As a consequence, taking these thermal effects into account could be very relevant in the determination of the DM final relic abundance. We will thus now review these thermal effects, in particular for dark photons production during the early Universe. In the next subsections, we will see what these effects imply on the DM relic abundance.

As we briefly mention in Subsection 1.3.4, the most important issue when considering thermal effects concerns how to treat the massless dark photon limit (i.e. $m_{\gamma'} \rightarrow 0$). Indeed, on the one hand, we have seen that, in the case of a massive dark photon, one can dissociate the dark photon propagation eigenstate basis from

the mass eigenstate basis. On the other hand, we have also seen that in the massless dark photon limit, the propagation and mass eigenstates are degenerate and one cannot distinguish the two basis anymore. This major difference between the massless and massive dark photon cases is expressed, in practice, by the fact that the dark photon does not couple directly to any SM particles in the massless case. Naively, taking the massless limit of the massive case does not display this property. This apparently contradictory phenomenon has been extensively studied in the literature in presence of a medium¹⁵ (see Refs. [106]–[111]). For our purpose, the important practical consequence of this absence of SM-to-med interaction in the massless case is that it imply that mediator particles cannot be produced directly from the SM bath. As a consequence, the sequential freeze-in regime (II) does not exist.

When a dark photon propagates through a thermal bath, it can oscillate into a SM photon and interact with charged particles from the plasma. This interaction of a propagating dark photon with the plasma is illustrated in Figure 3.18. The single and double wiggly lines represent a propagating photon and dark photon respectively. The oscillation from one particle to the other is shown by crossed circles while the photon polarisation in the thermal bath is depicted by the blob (made of SM charged fermions for example). The cut in the blob is associated to the imaginary part of the photon polarisation tensor. Indeed, in vacuum this cut is related to the dark photon decay rate and in a medium it also takes the dark photon production rate (coalescence) into account [106], [183]. In the same way, the dark photon production rate from Compton scattering and pair annihilation would be considered by a cut in the two-loop diagram with photon exchange within the blob.

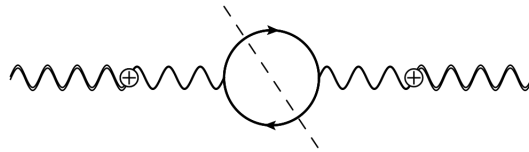


FIGURE 3.18: The imaginary part of the dark photon propagator (double wiggly lines) in a medium includes both its decay rate and creation rates.

When considering thermal effect, one has also to consider separately the transverse and the longitudinal components of the photon polarisation tensor. Indeed,

¹⁵As it is the case in stars or in the early Universe.

in a medium, the longitudinal mode corresponds to the proper excitation of the medium which is known as plasmons (see [184] for example). In most of the dark photon mass range we are interested in, the dark photon production is mostly dominated by production through transverse photons [109], [110]. In a thermal bath, the transverse mode of propagating photons behave essentially like massive particles with a thermal mass (noted ω_T) [185].

$$\text{Re } \Pi_{\gamma,T} \equiv \omega_T^2 \sim \sum_i e_i^2 T^2, \quad (3.32)$$

is the real part of $\Pi_{\gamma,T}$ the self-energy of the transverse photons with e_i the relativistic particles electric charge. Taking this into account, the creation of transverse dark photons proceeds through an effective mixing parameter $\epsilon \rightarrow \epsilon_{\text{eff}}$, with

$$\epsilon \rightarrow \epsilon_{\text{eff}} = \epsilon \times \frac{m_{\gamma'}^2}{m_{\gamma'}^2 - \Pi_{\gamma,T}}, \quad (3.33)$$

where the denominator comes from the propagator in Figure 3.18 and the numerator comes from the $\gamma \rightarrow \gamma'$ transition in this figure too, see Eq. 1.55 (see also Appendix B for more details on ϵ_{eff}). This effective coupling displays a resonance, when $m_{\gamma'} \approx \omega_{\gamma,T}$, one should also consider the transverse photon modes finite width in a medium: $\propto \text{Im } \Pi_{\gamma,T} \ll \text{Re } \Pi_{\gamma,T}$. This effective coupling also displays a suppression at high temperature (or low dark photon mass, $m_{\gamma'} \ll \omega_T$) of the dark photon production from SM coming from the fact that in the numerator we have $m_{\gamma'}^2 \sim T^2$. This latter behaviour, moreover also implies a smooth transition in the physical massless dark photon limit as the effective coupling goes to zero in this limit. Indeed, when $m_{\gamma'} \rightarrow 0$, the dark photon does not couple to the SM anymore since $\epsilon_{\text{eff}} \rightarrow 0$, just as in the massless case. In the opposite limit, when $m_{\gamma'} \gg \omega_T$, the effective mixing parameter goes back to the usual mixing parameter we have in vacuum, $\epsilon_{\text{eff}} \rightarrow \epsilon$. For off-shell dark photon, this effective coupling is simply given by ϵ since such process are essentially insensitive to the dark photon mass quicker (i.e. for smaller DM masses) than without taking thermal effects into account.

Practically, the major consequence of the above is that the dark photon production rate is highly suppressed at high temperature ($T \gg m_{\gamma'}$) and is strongly enhanced when the temperature approximately reaches the dark photon mass (i.e. when $\omega_T \approx m_{\gamma'}$). Thus, if the DM is much heavier than the dark photon, the processes which will set the DM relic abundance will freeze before that the dark photons are significantly produced from the SM bath and thermal effects are irrelevant

such that one recovers the massless case results.

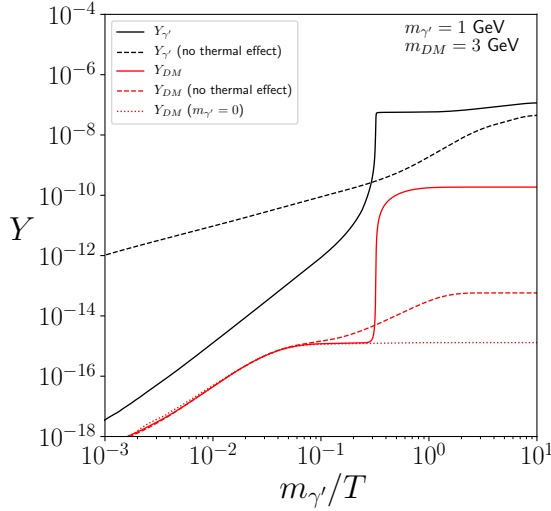


FIGURE 3.19: Comparison of the evolution of the dark photon (black lines) and DM abundances (red lines), with (solid) and without (dashed) thermal effects on dark photon production. The dotted lines give the abundance of dark photon in the massless limit. We consider values of the couplings which lead to the observed relic density when the thermal corrections are taken into account (solid red lines): $\kappa_{\text{II}} = 3.6 \times 10^{-14}$ and $\epsilon = 10^{-11}$.

Figure 3.19 shows the difference in the dark photon and DM yields ($Y_{\gamma'}$ and Y_{DM} respectively) evolution with (solid) and without (dashed) taking thermal effects into account for dark photon production. On this figure we see how thermal effects can be relevant when the DM and dark photons masses are taken to be close, here we fixed: $m_{\gamma'} = 1 \text{ GeV}$, $m_{\text{DM}} = 3 \text{ GeV}$. For this particular example, the DM-to-SM connector has been fixed such that this set of values lead to the observed relic density taking into account thermal corrections: $\kappa_{\text{II}} = 3.6 \times 10^{-14}$ and $\epsilon = 10^{-11}$. One can see that most of the dark photons are produced at a temperature close to the DM mass scale. As the DM production rate from dark photons is not yet Boltzmann suppressed at this time, the DM yield is strongly enhanced and follows the dark photon yield curve. Thus, the DM production from dark photon is strongly enhanced compared to the massive case without thermal correction and to the massless case. See Appendix B for more technical details of the effect of the resonance on the DM production.

Moreover, the dark photon production rate is not the only rate which is impacted by thermal effects. Indeed, it also affects the dark photon thermalisation with the SM bath. It will be easier for them to thermalise with SM particles as their production is boosted. Thus, a smaller value of the SM-to-med connector will be required to thermalise.

Figure 3.20 shows the same phase diagram than the one depicted in the left panel of Figure 3.6, but taking thermal effects into account. We will now review what these thermal effects change for every regime one by one.

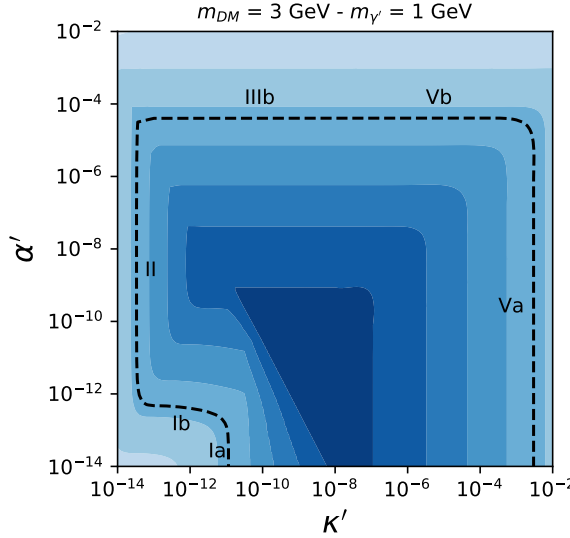


FIGURE 3.20: Same as Figure 3.6, $m_{\text{DM}} = 3 \text{ GeV}$ and $m_{\gamma'} = 1 \text{ GeV}$, but taking into account thermal effects on dark photon production.

3.3.2 Freeze-in regimes

In the first regime we considered, the regime Ia, the DM is produced by slow out-of-equilibrium processes from annihilation or decay of SM particles. On the one hand, in this regime, the dark photon bath plays a negligible role and taking thermal effects into account has no impact on the DM final relic abundance. On the other hand, in the second freeze-in regime, the regime Ib, the DM is produced by a slow out-of-equilibrium process from annihilation of dark photons. Since these dark photons are in thermal equilibrium with the SM, thermal effects will play a role and have an impact on the DM abundance. Indeed, if $m_{\text{DM}} \gtrsim m_{\gamma'}$, the dark

photon number density will be strongly enhanced by the resonance such that dark photons will be able to reach equilibrium with SM for even smaller values of the SM-to-med coupling ϵ . Thus, if dark photons are in thermal equilibrium with the SM for smaller ϵ , the regime Ib will be relevant for smaller ϵ or, equivalently, smaller DM-to-SM coupling κ' .

3.3.3 Sequential freeze-in regime

As in the regime Ib, thermal corrections will play an important role in the sequential freeze-in regime, regime II. For a DM particle not much heavier than the dark photon, the slow out-of-equilibrium production of DM particles from dark photon will coincide with the resonant enhancement of the slow out-of-equilibrium production of dark photons from the annihilation or the decay of SM particles. This will then make this chain of freeze-in more efficient and one will have to lower the DM-to-SM connector in order to not overproduce DM. This will lead to an even more pronounced extension towards the left of the mesa shaped phase diagram. This feature can also be seen on the Figure 3.21 which shows the same as Figure 3.14 taking thermal effects into account. We see that thermal effects are mostly relevant when the dark photon is not much lighter than the DM. Otherwise, we get approximately back to the massless dark photon case.

3.3.4 Reannihilation regimes

As for the regime Ib, in the reannihilation from dark photon regime, regime IIIb, since the production of dark photon from SM is enhanced, this regime will dominates over the production of DM from SM. The regime IIIb will thus be relevant for a wider range of the DM-to-SM coupling. On the other hand, the regime IIIa in which the SM sources the dark sector producing directly DM particles is unchanged as the production rate of dark photons from SM is negligible.

3.3.5 Secluded freeze-out regimes

For $m_{\gamma'} < m_{\text{DM}} < m_e$, the regime IVb is not relevant anymore with thermal corrections. This stems from the fact that at a temperature much bigger than the dark photon mass scale, the dark photon production is considerably suppressed once taking thermal effects into account and that at a temperature close to the dark photon mass scale, the production is Boltzmann suppressed as the dark photons are lighter than the electrons¹⁶. Remember that the production stops when $T' \sim m_{\text{DM}}$.

¹⁶The electrons are thus already Boltzmann suppressed when the resonant dark photon production should have started.

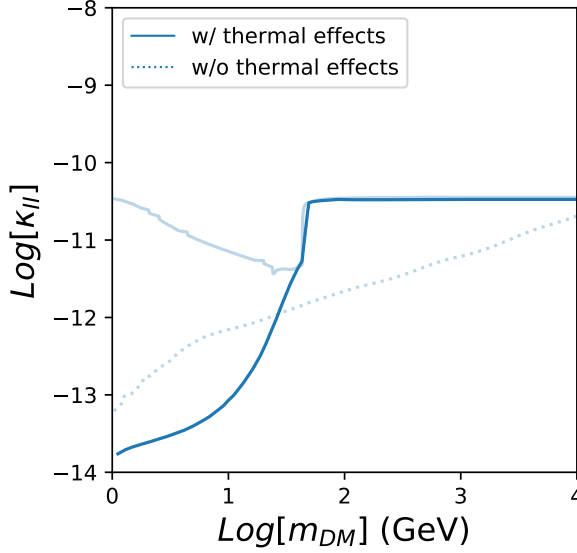


FIGURE 3.21: Dark matter candidates as shown in Figure 3.14 but taking thermal effects in the dark photon production rates. The additional dashed lines are given for the sake of comparison. They correspond to the curves shown in Fig. 3.14, thus without thermal effects.

Nevertheless, the regime IVa still apply for scenario where dark photon particles are much lighter than the DM particles, as in the massless case (see [179]).

3.3.6 Freeze-out regimes

Since all particles are thermalised in a single thermal bath, the effects of the above thermal corrections on the dynamics of these regimes are negligible.

3.4 Specificity of the scalar portal model

Introducing a new scalar and a new VEV bring some new dynamics to the system. As we have already mentioned earlier, depending on the value of this new VEV and the value of the DM mass with respect to the two VEV's, we will face different phases of the model. In practice, we have considered the new VEV to always be bigger than the electroweak symmetry breaking scale ($v_H < v_\Phi$). Indeed, a new symmetry breaking is not expected at the electroweak scale. Thus, there are essentially three possibilities,

- The broken phase: $m_{DM} < v_H < v_\Phi$

- The semi-broken phase: $v_H < m_{\text{DM}} < v_\Phi$
- The symmetric phase: $v_H < v_\Phi < m_{\text{DM}}$

We will see in the following that for most of the dynamical regimes we studied in Section 3.2, only the broken phase is relevant and this is why this is the phase we focused on in Section 3.2. However, we will also see that for two freeze-in regimes (Ia and II), discussing in which phase a DM candidate sits is relevant. For this reason, we will go through the three phases (broken, semi-broken and symmetric) one by one and explain, for each of them, what does it imply for regimes Ia and II.

3.4.1 The broken phase

If the DM mass is smaller than the new and SM scalar VEV's (i.e. $m_{\text{DM}} < v_H < v_\Phi$), the DM production mechanism through which the DM abundance is set (see Section 3.2) will occur when both hidden and visible sector symmetries are broken: $T \lesssim m_{\text{DM}} < v_H < v_\Phi$. Thus, the mixing between the two scalars of the theory is achieved as we have seen in Subsection 1.3.4 for which we remind all relevant couplings in Figure 3.22.

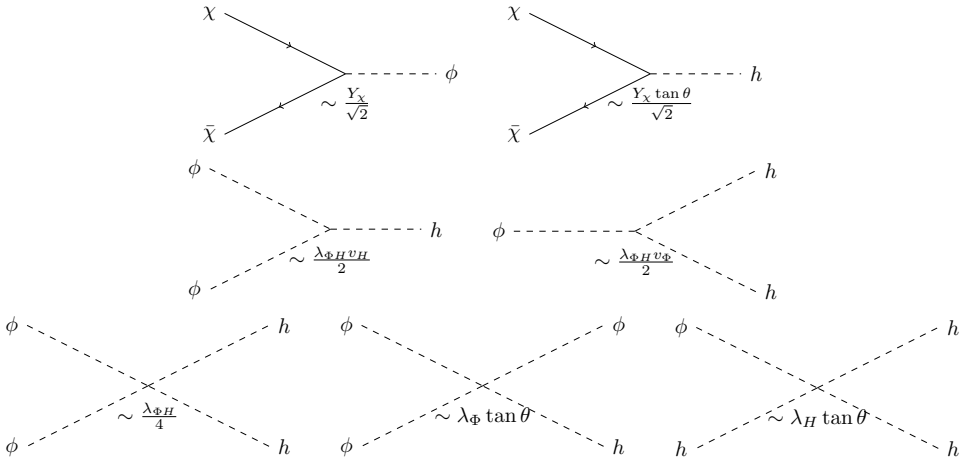


FIGURE 3.22: Couplings (at leading order for a small mixing angle) between the DM, the mediator and the visible sector in the fully broken phase.

Results have already been discussed at length in Section 3.2 where we have seen that this phase is allowing all regimes we discussed in in this section. Focusing on

the low DM-to-SM connector region, we recap in Figure 3.23 results we had in Section 3.2 highlighting the broken phase and to which we refer for more explanations on this figure.

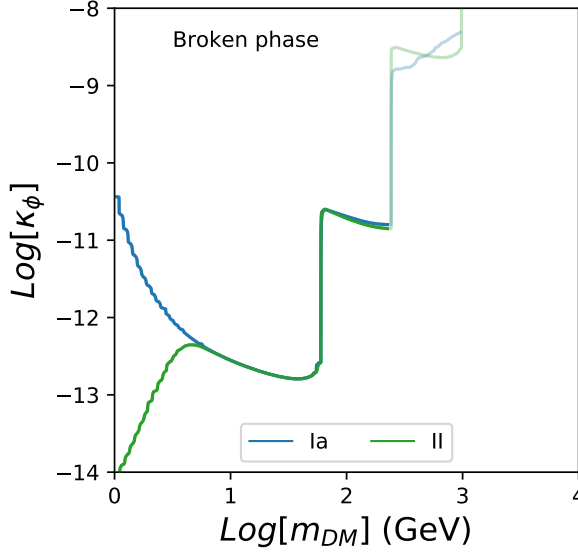


FIGURE 3.23: Values of the DM-to-SM connector to account for the observed DM relic abundance in the broken phase in the regimes Ia (blue) and II (green). The mediator mass has been taken to $m_{\text{med}} = 1$ GeV.

3.4.2 The semi-broken phase

If the DM mass is bigger than the SM scalar VEV but smaller than the new scalar VEV (i.e. $v_H < m_{\text{DM}} < v_\Phi$), the DM abundance will be set at a temperature higher than the SM broken symmetry scale such that the SM will still be in his symmetric phase while the hidden sector symmetry will be broken. As a consequence, only the new scalar Φ acquires a VEV,

$$\Phi = \frac{v_\Phi + \tilde{\phi}}{\sqrt{2}}, \quad (3.34)$$

where the λ_3 parameter from Eq. 1.48 is again traded for the v_Φ one, as in Subsection 1.3.4. There is then no mixing since the mass matrix, given by

$$M_{\Phi H}^2 = \begin{pmatrix} 0 & 0 \\ 0 & 2\lambda_{\Phi} v_{\Phi}^2 \end{pmatrix}, \quad (3.35)$$

is already diagonal. One can then get rid of the *tilde* notation $\phi \equiv \tilde{\phi}$ and has now to consider the real scalar ϕ and the complex scalar H . The relevant couplings in this phase are shown in Figure 3.24.

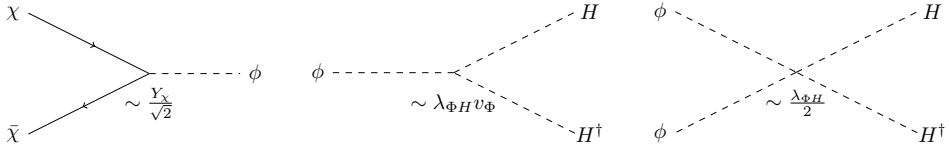


FIGURE 3.24: Couplings between the DM, the mediator and the visible sector in the broken hidden sector phase.

In this phase, it is still possible to produce DM directly from SM and the standard freeze-in regime still exists (regime Ia). Indeed, one can build from Figure 3.24 an annihilation process of two H 's into two DM particles through the production of a ϕ particle in the s-channel. Since this is the only way to produce DM directly from SM, the required value for the DM-to-SM coupling κ_{ϕ} has to be somewhat increased compared to the one required in the broken phase in which there are more DM production channels. The sequential freeze-in, regime II, is unchanged as it is still possible to produce the new scalar from slow out-of-equilibrium annihilation of two H 's through the quartic coupling and since the DM can still be frozen-in from slow out-of-equilibrium annihilation of two ϕ 's through the Yukawa coupling. This can be seen in Figure 3.25.

3.4.3 The symmetric phase

Finally, if the DM mass lies above both VEV's of the theory, the DM abundance will be frozen before any symmetry breaking could occur. As a consequence, the only remnant couplings are the one directly readable from the Lagrangian given in Eq. 1.48 and shown in Figure 3.26.

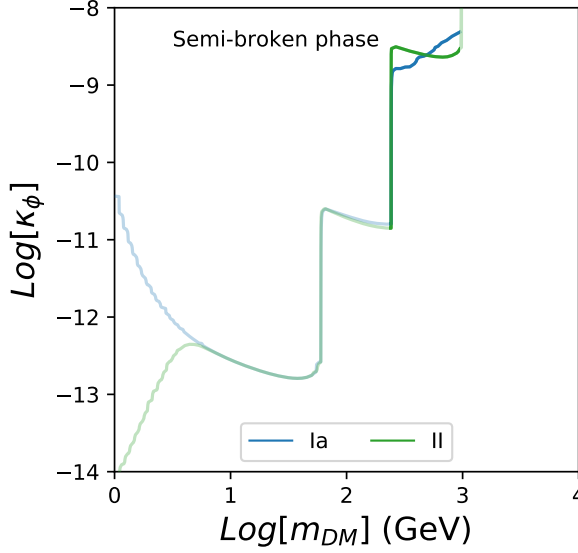


FIGURE 3.25: Values of the DM-to-SM connector to account for the observed DM relic abundance in the semi-broken phase in the regimes Ia (blue) and II (green).

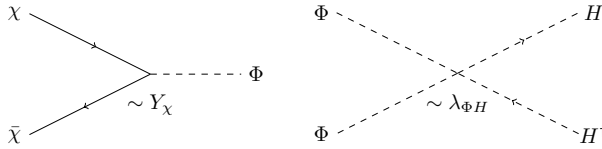


FIGURE 3.26: Couplings between the DM to the mediator and the mediator to the visible sector in the symmetric phase.

From this figure, one can conclude that it is no longer possible to produce DM directly (i.e. in an unsuppressed way) from SM in the symmetric phase. Thus, the only way to account for the observed DM relic abundance starting from an empty hidden sector is through the sequential freeze-in, regime II. Thus, this regime we discovered plays a crucial role for heavy DM candidates. Again, as it is now the only way to produce DM, one needs a stronger DM-to-SM connector in order to produce enough DM particles with respect to couplings required in the semi-broken phase. Results one would obtain in this phase are shown in Figure 3.27 where there is no dark blue line as there is no solution in the regime Ia.

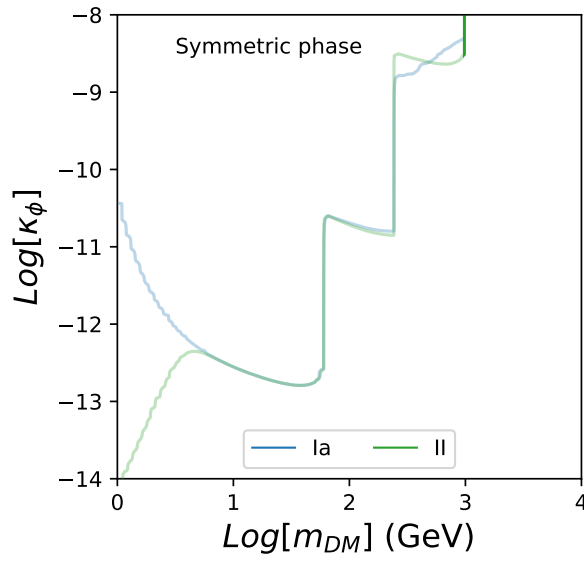



FIGURE 3.27: Values of the DM-to-SM connector to account for the observed DM relic abundance in the symmetric phase in the regime II (green).

Chapter 4

Thermally disconnected HS

 In Chapter 3, we have seen that, even if the DM particles have never been in thermal equilibrium with the SM thermal bath, one can account for the DM relic density in several ways. Indeed, the DM could be part of a HS made of particles which would not be in thermal equilibrium with the SM, the VS. In such scenarios, we have seen that there are various DM production mechanisms: FI, sequential FI, reannihilation and secluded FO, see Subsections 3.2.2, 3.2.3, 3.2.4 and 3.2.5 respectively. All this analysis we have made in Chapter 3 was based on the assumption that at the end of inflation, the HS was negligible and that the HS has been created from the SM thermal bath afterwards. Thus, the portal was essential, thermalising or not both sectors with each other, depending on the regime considered. Here, in this chapter based on [85], [186], [187], we would like to consider a scenario which, like everywhere in this thesis, is based on a VS-HS portal structure, but which is different in the sense that, here, we will neglect the portal interactions. We assume instead that the HS was already there at the end of inflation or, at least, that the portal ceased to be relevant long before the DM relic density was frozen. Neglecting the portal in this way, we will also assume that DM particles thermalise with an additional particle within the HS. Thus, one looks at the situation where we have two distinct and thermally disconnected baths, one composed of SM particles (VS) and one composed of dark sector particles such as DM and possibly other new particles (HS). Each bath would thus have its own temperature, T and T' for the VS and HS respectively.

Under these assumptions, one is left with a scenario where the DM freezes-out within the HS which gives rise to two possibilities. Either, the DM decouples while non-relativistic as in the secluded FO of Subsection 3.2.5 (since the portal ceases to have any effect long before DM decouples in the thermal HS bath, as we have seen), or it freezes-out while still relativistic. It turns out that these simple and very generic scenarios have never been studied in much detail. In this chapter, we determine the full DM mass and hidden-to-visible temperature ratio ranges which are allowed in such case. We call this available parameter space the "domain" of all DM thermal

candidates.

4.1 Theoretical constraints

4.1.1 Relativistic decoupling floor

Before discussing concrete models in which the DM thermalises within a hidden sector with its own temperature T' , let us study the DM relic density constraint in a model independent way in the context of thermally disconnected HS. In this section, we will see that this constraint gives, for the case of a relativistic decoupling in the HS, a lower bound on the hidden-to-visible temperature ratio. This is to be expected since a too low temperature ratio means a too small amount of DM particles with respect to SM particles and since the maximum of DM particles one can get when thermalised within the HS is when it decouples relativistically. Indeed, in the non-relativistic decoupling case, the number of DM particles left is Boltzmann suppressed. This lower bound on the hidden-to-visible temperature ratio can be translated in a lower bound on the DM mass for a given temperature ratio. This would thus give the generalisation of the Cowsik-McClelland [188] bound to cases where $T'/T \neq 1$.

If the DM decouples relativistically in the HS, the DM number density before decoupling is simply given by its relativistic value

$$n_{\text{DM}} = \frac{\zeta(3)}{\pi^2} g_{\text{DM}}^n T'^3, \quad (4.1)$$

where the effective degeneracy of the relativistic degrees of freedom are as usual: $g_{\text{DM}}^n = g_{\text{DM}}$ for a boson and $g_{\text{DM}}^n = 3g_{\text{DM}}/4$ for a fermion. The Riemann zeta function of three is approximately given by $\zeta(3) \simeq 1.202$. This scenario has the nice feature of giving a relic density which does not depend on the value of the DM annihilation cross section, simply because Eq. 4.1 is independent of it. Imposing that the DM number density given in Eq. 4.1 leads to (at least) the observed DM relic density, we get the following lower bound

$$\frac{T'_{\text{dec}}}{T_{\text{dec}}} \geq 2.46 \times 10^{-4} \times \left(\frac{100 \text{ GeV}}{m_{\text{DM}}} \right)^{1/3} \times \left(\frac{G_*^S(T_{\text{dec}})}{g_{\text{DM}}^n(T'_{\text{dec}})} \right)^{1/3}, \quad (4.2)$$

where T_{dec} and T'_{dec} indicate the value of the VS and the HS temperature at DM decoupling respectively while G_*^S stems for the total effective relativistic degrees

of freedom contained in both the visible and hidden sectors¹. It is defined in the same way than g_*^S (see Eq. 1.40), but taking HS relativistic degrees of freedom into account. This bound is saturated for a relativistic decoupling, but not for a non-relativistic one.

Note that such relativistic decoupling can be realised in two different ways. In the first possibility, which is analogous to the neutrino decoupling in the SM, the DM interaction rate could have been $\propto T'^5/\Lambda^4$ below some scale $T' \sim \Lambda$,² with $\Lambda > T'_{\text{dec}} \gg m_{\text{DM}}$ in the same way as the interaction rate for SM neutrinos changed from $\Gamma \propto \alpha_W^2 T$ to $\Gamma \propto G_F^2 T^5$ for $T \lesssim M_W$ [167]. In the second possibility, the mass of particles the DM is annihilating into could play the role of the heavy "cut-off" scale. If these particles are heavier than the DM, the annihilation rate became Boltzmann suppressed when T' went below their mass. Schematically, this relativistic freeze-out possibility is analogous to non-relativistic DM decoupling in the sense that decoupling was due to a Boltzmann suppression. Then, in this case, the DM is reheated just before its decoupling since the heavier particle (final states) are becoming non-relativistic³. Then, the initial value of the hidden-to-visible temperature ratio $T'_{\text{in}}/T_{\text{in}}$, i.e. before the heavier particle became non-relativistic, differs from the value of this ratio at DM decoupling, $T'_{\text{dec}}/T_{\text{dec}}$. They differ by

$$\frac{T'_{\text{dec}}}{T_{\text{dec}}} = \left(\frac{g_*^S(T'_{\text{in}})}{g_*^S(T'_{\text{dec}})} \right)^{1/3} \times \frac{T'_{\text{in}}}{T_{\text{in}}}. \quad (4.3)$$

In the first scenario instead there is no such reheating of the HS and $T'_{\text{in}}/T_{\text{in}} = T'_{\text{dec}}/T_{\text{dec}}$ as $g_*^S(T'_{\text{in}}) = g_*^S(T'_{\text{dec}})$.

Let us emphasises the fact that the factor of g_*^S in Eq. 4.1.1 takes into account all relativistic degrees of freedom contained in the HS and not only the DM. This is due to the fact that the HS may be composed of numerous particles on top of the DM one, such that theoretically, the HS could be made of several decoupled sector.

Figure 4.1 shows contours of the normalised DM relic abundance ($\Omega_{\text{DM}} h^2 / 0.1188$) in the T'/T vs DM mass plane for a relativistic decoupling. The blue shaded area indicates where the initial amount of DM (i.e. before it decouples relativistically) lies

¹Depending on which sector dominates the energy and entropy distributions of the Universe implies two types of solutions. See Subsection 4.1.2 for more details.

² Λ would typically be the mass of some heavy mediator.

³This reheating is similar to the photon reheating which occurred during the e^+e^- annihilation catastrophe in the VS

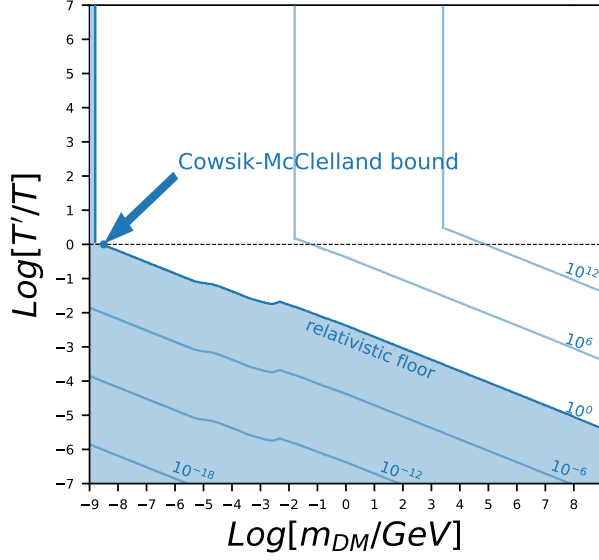


FIGURE 4.1: Contour of the normalised DM relic abundance $\Omega_{\text{DM}} h^2 / 0.1188$ in the T'/T vs DM mass plane for a relativistic decoupling.

already below the observed abundance today. In that sense and for a chosen DM mass, the contour $\Omega_{\text{DM}} h^2 = 0.1188$ (depicted by the solid dark blue line in Figure 4.1) gives the minimal temperature ratio one can consider for a DM thermal candidate as given in Eq. 4.2. Alternatively, for a given hidden-to-visible temperature ratio, the very same contour gives the minimal DM mass for a thermal candidate. One can also see in Figure 4.1, the Cowsik-McClelland [188] bound which gives a lower bound on the DM mass for a thermal candidate which was in equilibrium with the visible sector (i.e. only one bath with $T' = T$, black dashed line in Figure 4.1). Note that this very simple relativistic floor scenario has, to our knowledge, surprisingly not been previously presented in the literature in any published paper. After presenting it, we became aware of a preprint [189] where this scenario has been partially presented.

4.1.2 Unitarity wall

After having considered the extreme case of a relativistic decoupling, let us consider the opposite case in which the DM decouples while well non-relativistic (i.e. $m_{\text{DM}}/T'_{\text{dec}} \gg 1$). In this type of scenario, the final DM abundance depends on the annihilation cross section as we have seen in Subsection 3.2.6. However, the expression given in Eq. 1.41 is only valid in a standard FO scenario in which the DM

thermalises with the SM, i.e. $T' = T$. Thus, in Appendix C, we generalise the instantaneous freeze-out approximation for the thermally disconnected HS case, i.e. fixing $x'_{\text{dec}} = m_{\text{DM}}/T'_{\text{dec}}$ from the condition $\Gamma/H|_{T'=T'_{\text{dec}}} = 1$ and determining Y_{DM} by assuming that the yield after freeze-out is equal to $n_{\text{DM}}^{eq}/s|_{T'=T'_{\text{dec}}}$. Here, the outcome of this scenario is somewhat more complicated than for the standard FO case because the Universe expansion rate as well as its energy and entropy densities get contributions from both the visible and the hidden sectors,

$$H(x') = \sqrt{\frac{8\pi}{3M_{\text{pl}}^2}} \sqrt{\rho_{\text{VS}}(x') + \rho_{\text{HS}}(x')}, \quad (4.4)$$

$$s(x') = s_{\text{VS}}(x') + s_{\text{HS}}(x'). \quad (4.5)$$

In terms of the inverse hidden temperature $x' \equiv m_{\text{DM}}/T'$ and the hidden-to-visible temperature ratio $\xi \equiv T'/T$, the energy and entropy densities of both sectors are given by,

$$\rho_{\text{VS}}(x') = \frac{\pi^2}{30} g_*^{\text{eff}}(m_{\text{DM}}/x' \xi) \left(\frac{m_{\text{DM}}}{x' \xi} \right)^4, \quad (4.6)$$

$$\rho_{\text{HS}}(x') = \frac{\pi^2}{30} g_*'^{\text{eff}}(m_{\text{DM}}/x') \left(\frac{m_{\text{DM}}}{x'} \right)^4, \quad (4.7)$$

$$s_{\text{VS}}(x') = \frac{2\pi}{45} g_*^S(m_{\text{DM}}/x' \xi) \left(\frac{m_{\text{DM}}}{x' \xi} \right)^3, \quad (4.8)$$

$$s_{\text{HS}}(x') = \frac{2\pi}{45} g_*'^S(m_{\text{DM}}/x') \left(\frac{m_{\text{DM}}}{x'} \right)^3. \quad (4.9)$$

Using the instantaneous freeze-out approximation described above and presented in Appendix C, one obtains

$$\Omega_{\text{DM}} h^2 = 4.7 \cdot 10^8 \frac{g_{\text{DM}}^n \sqrt{G_*^{\text{eff}}(T_{\text{dec}})} x'_{\text{dec}}}{G_*^S(T_{\text{dec}}) M_{\text{pl}} \langle \sigma v \rangle \text{ GeV}} \times \frac{T'_{\text{dec}}}{T_{\text{dec}}} \quad (4.10)$$

with x'_{dec} given by (see Appendix C),

$$\begin{aligned} x'_{\text{dec}} \simeq & \ln \left[0.038 \left(\frac{T'_{\text{dec}}}{T_{\text{dec}}} \right)^2 \langle \sigma v \rangle m_{\text{pl}} M_{\text{DM}} \left(\frac{g_{\text{DM}}}{\sqrt{G_*^{\text{eff}}(T_{\text{dec}})}} \right) \right] \\ & + \frac{1}{2} \ln \ln \left[0.038 \left(\frac{T'_{\text{dec}}}{T_{\text{dec}}} \right)^2 \langle \sigma v \rangle M_{\text{pl}} m_{\text{DM}} \left(\frac{g_{\text{DM}}}{\sqrt{G_*^{\text{eff}}(T_{\text{dec}})}} \right) \right]. \end{aligned} \quad (4.11)$$

In the non-relativistic regime, the initial amount of DM may lie well above the abundance we will ultimately need such that one needs a large Boltzmann suppression, i.e. a large enough annihilation cross section. For large DM masses, the needed DM annihilation cross section could eventually violate the unitarity constraint [190]. The unitarity upper bound on the cross section is given by [190],

$$\sigma_{\text{ann.}} v < \frac{\pi(2l+1)}{p_{\text{DM}}^2} v = \frac{\pi(2l+1)}{m_{\text{DM}}^2} \frac{(1-v^2/4)}{v/4}, \quad (4.12)$$

where v is the relative velocity between both annihilating DM particles and l is the angular momentum quantum number, as in Chapter 2, between the in-going particles. Since in Eq. 4.10, it is the thermally average cross section which is involved, we have to take the thermally average of Eq. 4.12. This can be done by integrating Eq. 4.12 over all possible velocities

$$\langle \sigma v \rangle \equiv \frac{\int \sigma_{\text{ann.}} v f_v(E_1) f_v(E_2) dp_1^3 dp_2^3}{\int f_v(E_1) f_v(E_2) dp_1^3 dp_2^3}, \quad (4.13)$$

where 1 and 2 refer to the two in-going particles of energy $E_{1,2}$ and momentum $\vec{p}_{1,2}$. The velocity distribution, f_v , can be either the Fermi-Dirac or the Bose-Einstein distribution depending on the spin of the incident particles. This integration gives the following upper bound on the annihilation cross section,

$$\langle \sigma v \rangle < \frac{\pi(2l+1)}{4m_{\text{DM}}^2} x'^2 \mathcal{I}_\epsilon(x'), \quad (4.14)$$

with $\epsilon = \pm 1$ for a fermion or a boson respectively and where the function \mathcal{I} in Eq. 4.14 is defined as following,

$$\mathcal{I}_\epsilon(x') \equiv \frac{1}{N^2} \cdot \int_{4x'^2}^{\infty} dw \int_{\sqrt{w}}^{\infty} dk_+ \int_{-k_{-,max}}^{k_{-,max}} dk_- \times \left\{ \frac{\sqrt{w/(w-4x'^2)}}{\left(e^{\frac{k_++k_-}{2}} + \epsilon\right) \left(e^{\frac{k_+-k_-}{2}} + \epsilon\right)} \right\}. \quad (4.15)$$

with $k_{\pm} \equiv (E_1 \pm E_2)/T'_{\text{dec}}$, $w \equiv s/T_{\text{dec}}'^2$, $k_{-,max} \equiv \sqrt{1-4x'^2/w} \sqrt{k_+^2 - w}$, $s \equiv (p_1 + p_2)^2$ and $N \equiv \int_{x'}^{\infty} \frac{\sqrt{k^2 - x'^2}}{e^k + \epsilon} k dk$. Note that in the classical regime where one can use the Maxwell-Boltzmann distribution instead of the Fermi-Dirac or Bose-Einstein ones, one can take the relativistic and the non-relativistic limits. This would greatly simplify this expression for \mathcal{I}_ϵ . In the relativistic regime we get,

$$\langle \sigma v \rangle \simeq \frac{n_\epsilon}{T'^2}, \quad (4.16)$$

with $n_\epsilon = 5\pi/12$ for a fermion and $n_\epsilon = 15\pi/16$ for a boson in the relativistic limit $T' \gg m_{\text{DM}}$. In the non-relativistic limit $T' \ll m_{\text{DM}}$, we have instead

$$\langle \sigma v \rangle \simeq \frac{4\pi}{m_{\text{DM}}^2} \frac{K_2(2x')}{K_2^2(x')}, \quad (4.17)$$

with $x' = m_{\text{DM}}/T'$.

Now, one can use the unitarity upper bound of Eq. 4.14 on the DM annihilation cross section to constraint the hidden-to-visible temperature ratio at DM decoupling as a function of the DM mass. Depending on which of the visible and the hidden sectors dominates at DM decoupling, one face two distinct physical situations. To understand which one dominates, let us compare their energy and entropy densities (see Eqs. 4.6 to 4.9):

$$r_\rho(x') \equiv \frac{\rho_{\text{HS}}(x')}{\rho_{\text{VS}}(x')}, \quad (4.18)$$

$$r_S(x') \equiv \frac{s_{\text{HS}}(x')}{s_{\text{VS}}(x')}. \quad (4.19)$$

As a result, the HS dominates the expansion rate and entropy density of the Universe if,

$$r_\rho > 1 \quad \Rightarrow \quad \left(\frac{T'}{T} \right) > \left(\frac{g_*^{\text{eff}}(m_{\text{DM}}/x'\xi)}{g_*'^{\text{eff}}(m_{\text{DM}}/x')} \right)^{1/4}, \quad (4.20)$$

$$r_S > 1 \quad \Rightarrow \quad \left(\frac{T'}{T} \right) > \left(\frac{g_*^S(m_{\text{DM}}/x'\xi)}{g_*'^S(m_{\text{DM}}/x')} \right)^{1/3}. \quad (4.21)$$

The transition between a Universe dominated by the HS or by the VS is model dependent as it depends on the number of relativistic degrees of freedom in the HS. However, this number cannot be smaller than one and in a VS where there are only SM particles it is smaller than ~ 106 . In this case, the Eqs. 4.20 and 4.21 hold as soon as T'/T is above $\sim (\text{a few})^4$.

⁴Note that the two conditions $r_\rho > 1$ and $r_S > 1$ are very similar and differ from a factor of order unity.

Now that we know that, if $T'/T < (\text{a few})$, the Universe expansion rate and its entropy density are dominated by the VS and by the HS otherwise, one can plug the maximum annihilation cross section allowed by unitarity in Eq. 4.10 for both cases. Saturating Eq. 4.14 gives,

$$\frac{T'_{\text{dec}}}{T_{\text{dec}}} = 1.18 \times 10^5 \times \left(\frac{100 \text{ GeV}}{m_{\text{DM}}} \right)^2 \times \left(\frac{g_*^S(T_{\text{dec}})}{\sqrt{g_*^{\text{eff}}(T_{\text{dec}})}} \right) \times \mathcal{I}_\epsilon(x'_{\text{dec}}) \times x'_{\text{dec}}, \quad (4.22)$$

for a Universe dominated by the VS and

$$m_{\text{DM}} = 35 \text{ TeV} \times \left(\frac{g_*'^S(T'_{\text{dec}})}{\sqrt{g_*'^{\text{eff}}(T'_{\text{dec}})}} \right)^{1/2} \times (\mathcal{I}_\epsilon(x'_{\text{dec}}) \times x'_{\text{dec}})^{1/2}, \quad (4.23)$$

for a Universe dominated by the HS. Let us emphasise that in the latter case, the DM abundance does not depend on the hidden-to-visible temperature ratio. This is to be expected as in this case, the VS contribution can be totally neglected, i.e. neither the energy nor the entropy densities depend on this ratio (see Eq. 4.7 and 4.9 respectively). As a consequence, the maximal DM mass has a unique value which does not depend on the temperature ratio.

Figure 4.2 shows contours of the normalised DM relic abundance $\Omega_{\text{DM}} h^2 / 0.1188$ in the T'/T vs DM mass plane for a non-relativistic decoupling in which the annihilation process saturates the unitarity bound. This figure indicates how the temperature ratio versus DM mass plane is constrained by the unitarity bounds obtained in the case of a Universe dominated by the VS, $T'/T < (\text{a few})$, and the case where it is dominated by the HS, $T'/T > (\text{a few})$. On the same Figure, is also shown the Griest-Kamionkowski bound [190] which is the very well known upper bound on the mass of a DM thermal candidate, resulting from unitarity, in the case where there is only one bath, i.e. everything thermalised together such that $T' = T$.

4.1.3 Thermalised Hidden Sector requirement

Now that we have seen how the parameter space is constrained in a model independent way by the *relativistic floor* and the *unitarity wall*, one should add one last theoretical constraint to this picture. Indeed, as we are interested in thermal DM candidate, we should impose that the HS thermalised at some point in the early

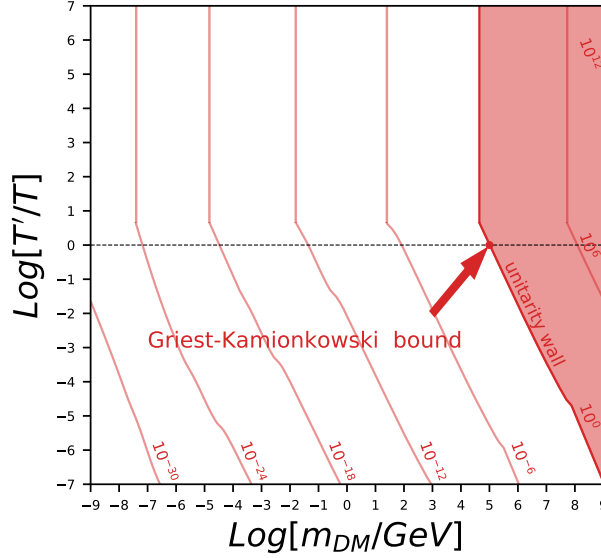


FIGURE 4.2: Contour of the normalised DM relic abundance $\Omega_{\text{DM}} h^2 / 0.1188$ in the T'/T vs DM mass plane for a non-relativistic decoupling in which the annihilation process saturates the unitarity bound.

Universe. This can be done using the maximal cross section allowed by unitarity (Eq. 4.14) and imposing that the interaction rate was larger than the expansion rate at some point before DM decoupling (i.e. for $T'_{\text{th}} > T'_{\text{dec}}$ with T'_{th} the temperature of thermalisation). In practice we checked for every point of the parameter space if the following condition was fulfilled,

$$(n_{\text{DM}} \langle \sigma v \rangle)_{T' > T'_{\text{dec}}} > H|_{T > T_{\text{dec}}}, \quad (4.24)$$

where $\langle \sigma v \rangle$ is given by Eq. 4.14, H by Eq. 4.4 and n_{DM} by its full non-relativistic form,

$$n_{\text{DM}}(T') = \frac{g_{\text{DM}} T'^3}{2\pi^2} \int_{x'}^{\infty} \frac{\sqrt{w^2 - x'^2}}{e^w \pm 1} w dw, \quad (4.25)$$

where the \pm sign stems for a fermion and a boson respectively.

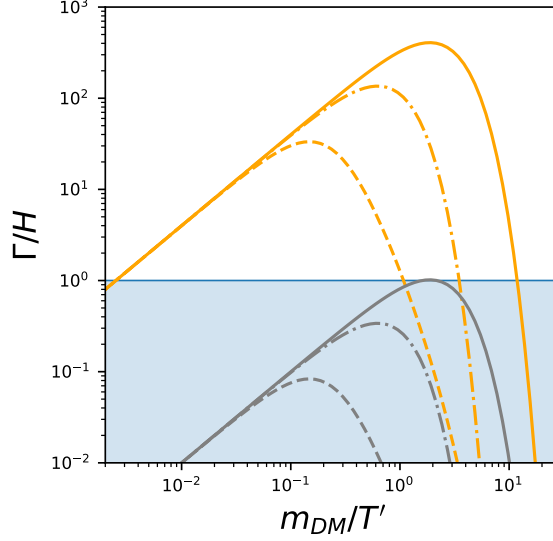


FIGURE 4.3: Schematic behaviour of interaction rates, Γ , with respect to the expansion rate, as function of m_{DM}/T' for three scenarios for DM decoupling: the DM particles become non-relativistic (solid lines), the DM annihilates into heavier particles of mass m' (here chosen to be $m'/m_{\text{DM}} = 3$) (dot-dashed lines) and the DM interacts through some heavy mediator and decouples while still relativistic (dashed lines). We show these three cases for the same DM mass but for two choices of T'/T (orange and grey lines, respectively), see text for more details.

Even though we aim to be as model independent as possible, the way that DM decouples is model dependent such that we will here consider three generic scenarios. The first possibility we consider is the usual non-relativistic DM decoupling, see solid lines in Figure 4.3 which shows Γ/H as a function of m_{DM}/T' for the three DM decoupling scenarios we consider here and for two choices of T'/T . That is to say that the DM particles were still in thermal equilibrium when $T' \sim m_{\text{DM}}$ and that its number density changed from $n_{\text{DM}} \propto T'^3$ to being Boltzmann suppressed $n_{\text{DM}} \propto \exp(-m_{\text{DM}}/T')$. The two other DM decoupling possibilities we consider are the two relativistic decoupling scenarios already mentioned in Subsection 4.1.1: the DM annihilation process is cut off either by a heavy mediator mass or by the mass of the final state particles, see the dashed and dot-dashed lines respectively in Figure 4.3.

Figure 4.3 shows the three DM decoupling scenarios just introduced assuming the same DM mass and for two choices of the hidden-to-visible temperature ratio

T'/T (orange and grey lines). The orange curves describe the behaviour of DM candidate which where in thermal equilibrium at a temperature T' with $T'_{\text{eq}} > T' > T'_{\text{dec}}$. Decreasing (increasing) the temperature ratio would move down (up) the orange curves such that one can conclude from Figure 4.3 that the temperature range within which the DM was in chemical equilibrium shrinks (resp. expands) as T'/T decreases (resp. increases). If one keep decreasing T'/T , one will end up with the limit case where the equilibrium and decoupling temperatures are equal $T_{\text{eq}} = T_{\text{dec}}$, see the solid grey curve in Figure 4.3. This corresponds to the case of a mildly non-relativistic DM particle freeze-out such that the candidate lies close to the relativistic floor and such that the relativistic form of Eq. 4.25 given in Eq. 4.1 can be used as a very good proxy. In such an approximation, one can solve analytically Eq. 4.24 and get the temperature ratio as a function of the DM mass for which the unitarity cross section is not strong enough to allow any thermalisation within the HS. We have,

$$\frac{T'_{\text{th}}}{T_{\text{th}}} > 1.2 \times 10^{-8} \times \left(\frac{m_{\text{DM}}}{100 \text{ GeV}} \right)^{1/2} \left(\frac{\sqrt{G_*^{\text{eff}}(T_{\text{th}})}}{g_{\text{DM}}} \right)^{1/2} \left(\frac{1}{x'_{\text{th}} \mathcal{I}_\epsilon(x'_{\text{th}})} \right)^{1/2}. \quad (4.26)$$

This gives the diagonal and vertical dark orange lines in Figure 4.4. Note also that for smaller values of the DM annihilation cross section than the one allowed by unitarity of Eq. 4.14, the thermalisation condition requires the DM mass to be smaller. This is also shown in Figure 4.4 for various values of the annihilation cross section with respect to the maximum value of it allowed by unitarity (Eq. 4.14).

4.1.4 Thermal DM mass range

One can now bring together the three model independent constraints on the temperature ratio versus DM mass plane. This has been done in Figure 4.5 where one can see how the relativistic floor (blue), the unitarity wall (red) and the thermalisation condition (orange) constrain the parameter space. From Figure 4.5, one can see how the mass range of a thermal DM candidate evolves with the hidden-to-visible temperature ratio. As said above, for a unique bath in which the DM thermalises with the SM, the DM mass was constrained below by the Cowsik-McClelland bound [188] and above by the Griest-Kamionkowski bound [190],

$$\text{eV} \lesssim m_{\text{DM}} \lesssim 100 \text{ TeV} \quad \text{for } T' = T. \quad (4.27)$$

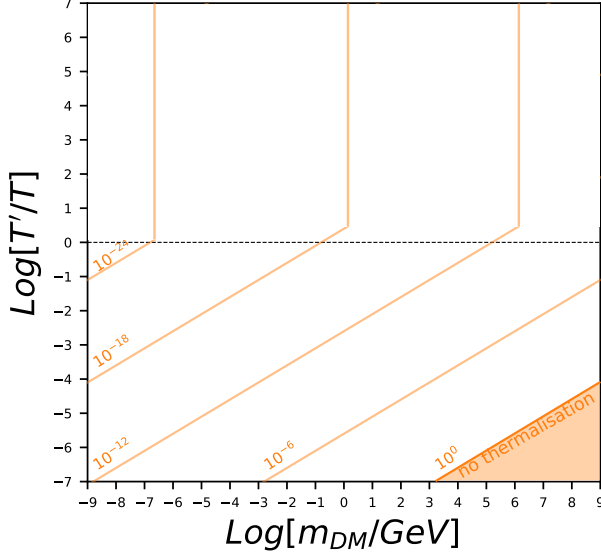


FIGURE 4.4: Contour of the normalised DM annihilation cross section $\langle\sigma v\rangle/\langle\sigma v\rangle_{ub}$ (with $\langle\sigma v\rangle_{ub}$ given by Eq. 4.14) in the T'/T vs DM mass plane for a non-relativistic decoupling.

Thanks to Eqs. 4.2 and 4.22 one can now constrain the mass range of a DM thermal candidate for a more generic scenario in which the DM did not necessarily thermalise with the VS, but did within the HS. We have, $m_{\text{CM}}\left(\frac{T'_{\text{dec}}}{T_{\text{dec}}}\right) \lesssim m_{\text{DM}} \lesssim m_{\text{GK}}\left(\frac{T'_{\text{dec}}}{T_{\text{dec}}}\right)$, where the generalisation of the Cowsik-McClelland and Griest-Kamionkowski masses are function of the hidden-to-visible temperature ratio at DM decoupling. These masses are defined for a Universe dominated by the VS as

$$m_{\text{CM}} \equiv 1.5 \text{ eV} \times \left(\frac{T_{\text{dec}}}{T'_{\text{dec}}}\right)^3 \times \frac{g_*^S(T_{\text{dec}})g_*'^S(T'_0)}{g_{\text{DM}}^n(T'_{\text{dec}})g_*'^S(T'_{\text{dec}})}, \quad (4.28)$$

$$m_{\text{GK}} \equiv 34 \text{ TeV} \times \left(\frac{T_{\text{dec}}}{T'_{\text{dec}}}\right)^{1/2} \times \left(\frac{g_*^S(T_{\text{dec}})}{\sqrt{g_*^{\text{eff}}(T_{\text{dec}})}}\right)^{1/2} \times (\mathcal{I}_\epsilon(x'_{\text{dec}}) \times x'_{\text{dec}})^{1/2}, \quad (4.29)$$

while for a Universe dominated by the HS, we have instead

$$m_{\text{CM}} \equiv 1.5 \text{ eV} \times \left(\frac{T_{\text{dec}}}{T'_{\text{dec}}} \right)^3 \times \frac{g_*^S(T_{\text{dec}})g_*'^S(T'_0)}{g_{\text{DM}}^n(T'_{\text{dec}})g_*'^S(T'_{\text{dec}})}, \quad (4.30)$$

$$m_{\text{GK}} \equiv 35 \text{ TeV} \times \left(\frac{g_*'^S(T'_{\text{dec}})}{\sqrt{g_*'^{\text{eff}}(T'_{\text{dec}})}} \right)^{1/2} \times (\mathcal{I}_\epsilon(x'_{\text{dec}}) \times x'_{\text{dec}})^{1/2}. \quad (4.31)$$

Note that the width of the mass range for a thermal DM candidate decreases with the hidden-to-visible temperature ratio (as it can be seen in Figure 4.5), but this mass range move to higher masses.

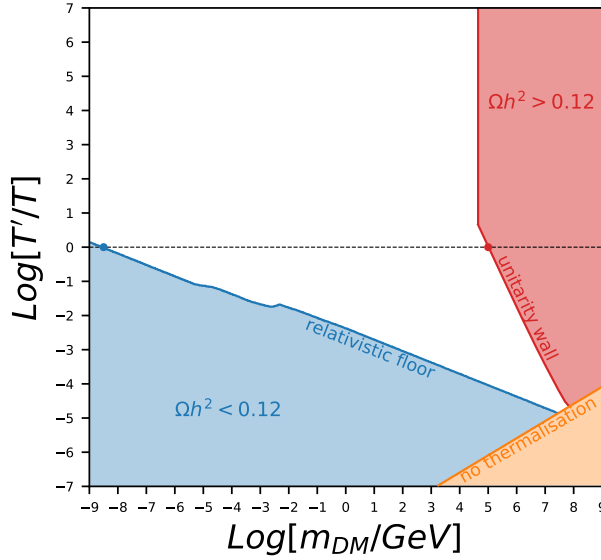


FIGURE 4.5: Theoretical constraints from the relativistic floor (blue), the unitarity wall (red) and the thermalisation condition (orange) on the temperature ratio versus DM mass plane.

Finally, let us emphasise that the maximum mass allowed for a DM thermal candidate does not exactly correspond to the minimum allowed value of the hidden-to-visible temperature ratio. Indeed, the maximum DM mass one can reach corresponds to the intersection of the unitarity wall and the thermalisation line of Figure 4.5 and is given by Eq. 4.29. One gets

$$m_{\text{DM}}^{\text{max}} \simeq 52 \text{ PeV}, \quad (4.32)$$

which corresponds to a temperature ratio at decoupling of

$$\frac{T'_{\text{dec}}}{T_{\text{dec}}} \simeq 6.9 \times 10^{-5}. \quad (4.33)$$

Instead, the minimum allowed value of the temperature ratio corresponds to the intersection of the relativistic floor and the thermalisation line. It can be obtained using Eqs. 4.2 and 4.26, we have

$$\left(\frac{T'_{\text{dec}}}{T_{\text{dec}}} \right)_{\text{min}} \simeq 1.4 \times 10^{-5}, \quad (4.34)$$

which corresponds to a slightly lower DM mass of

$$m_{\text{DM}} \simeq 30 \text{ PeV}. \quad (4.35)$$

Although this 30 PeV is not an absolute upper bound on the DM mass, it nevertheless constitutes an upper bound on the DM mass for all relativistic decoupling scenario discussed above.

4.2 Observational constraints

Let us now take a look at some observations which can further constrain the DM thermal candidate parameter space, still in a model independent way.

4.2.1 N_{eff}

We have already discussed the N_{eff} constraint from CMB data in Section 1.4 showing that the effective number of relativistic degrees of freedom can play an important role in the Universe expansion. Indeed, it is well known that the Universe used to be in a radiation dominated era at the time of BBN. Thus, adding new relativistic degrees of freedom in the early Universe would increase the total energy density of the Universe and, consequently, the Hubble expansion rate. This would therefore modify the well measured relative abundances of light nuclei which were fixed by the BBN process. Thus, to avoid that those additional particles are still relativistic at the time of BBN, one could require that $T'_{\text{dec}} > T'_{\text{BBN}}$ such that one would be sure, in a model independent way, that DM was non-relativistic at BBN. However, we will

see in Chapters 5 and 6 that it is not necessarily required. There are other ways to fulfil the N_{eff} constraint making the DM abundance negligible at BBN, but this is model dependent, see below.

Focusing on a model independent N_{eff} constraint, we write the extra contribution to N_{eff} due to DM at $T_{\text{BBN}} \simeq 1$ MeV using $\Delta N_{\text{eff}} \equiv \rho_{\text{DM}}(T'_{\text{BBN}})/\rho_{\nu}(T_{\text{BBN}})$. The DM energy density is given by its integral form at equilibrium while the neutrino energy density is simply given in terms of the photon energy density as they already have decoupled from the SM thermal bath, $\rho_{\nu} = \frac{7}{8} \left(\frac{4}{11}\right)^{4/3} \rho_{\gamma}$. We have,

$$\rho_{\text{DM}}(T') = \frac{g_{\text{DM}} T'^4}{2\pi^2} \int_{x'}^{\infty} \frac{\sqrt{w^2 - x'^2}}{e^w \pm 1} w^2 dw, \quad (4.36)$$

$$\rho_{\nu}(T) = \frac{7\pi^2}{240} \left(\frac{4}{11}\right)^{4/3} g_{\gamma} T^4, \quad (4.37)$$

where $g_{\gamma} = 2$ is the photon number of degrees of freedom. The additional contribution to N_{eff} from DM is therefore given by,

$$\Delta N_{\text{eff}} \simeq g_{\text{DM}} \frac{60}{7\pi^4} \left(\frac{11}{4}\right)^{4/3} \left(\frac{T'_{\text{BBN}}}{T_{\text{BBN}}}\right)^4 \int_{x'_{\text{BBN}}}^{\infty} \frac{\sqrt{w^2 - x'^2_{\text{BBN}}}}{e^w \pm 1} w^2 dw, \quad (4.38)$$

where $x'_{\text{BBN}} \equiv m_{\text{DM}}/T'_{\text{BBN}}$. The latest constraint given by the Planck collaboration [94] is $N_{\text{eff}} = 2.99 \pm 0.17$ which is similar to the one obtained from BBN [191]. SM predictions give $N_{\text{eff}} = 3.04$ (see [192] for example) such that one can constrain the quantity given in Eq. 4.38: $\Delta N_{\text{eff}} \leq 0.29$ at 2σ .

We emphasise the fact that we are, for the moment, considering only contributions to ΔN_{eff} from the DM. Indeed, contributions from additional degrees of freedom within the HS are possible, but are also much more model dependent. For this reason, we will start discussing, in a model independent way, contributions from DM and later we will discuss how the picture would change if there are additional degrees of freedom within the HS.

Applying the constraint $\Delta N_{\text{eff}} \leq 0.29$ on the DM contribution leads to the green region of Figure 4.8 which presents two distinct features. These features can be understood if one considers the relativistic and non-relativistic behaviour of Eq. 4.38. Indeed, lower the DM mass is (left hand side of Figure 4.8) more relativistic the DM was at BBN. In the limit where the DM was relativistic at BBN, Eq. 4.38 and $\Delta N_{\text{eff}} \leq 0.29$ give

$$\frac{T'_{\text{BBN}}}{T_{\text{BBN}}} \leq 0.44 \times \left(\frac{3.5}{g_{\text{DM}}^{\text{eff}}} \right)^{1/4}, \quad (4.39)$$

where $g_{\text{DM}}^{\text{eff}} = g_{\text{DM}}$ for a boson and $g_{\text{DM}}^{\text{eff}} = 7g_{\text{DM}}/8$ for a fermion. This gives the constraint on the temperature ratio at DM decoupling,

$$\frac{T'_{\text{dec}}}{T_{\text{dec}}} \leq 0.44 \times \left(\frac{3.5}{g_{\text{DM}}^{\text{eff}}} \right)^{1/4} \times \left(\frac{g'^S(T'_{\text{BBN}})}{g'^S(T'_{\text{dec}})} \right)^{1/3} \left(\frac{g'^S(T'_{\text{dec}})}{g'^S(T_{\text{BBN}})} \right)^{1/3}, \quad (4.40)$$

From Eq. 4.40, one can see that the bound on the hidden-to-visible temperature ratio at DM decoupling does not depend on the DM mass for a relativistic decoupling as expected. This regime is relevant for a DM which is relativistic at BBN, that is to say for $m_{\text{DM}} \lesssim \text{MeV}$ and it can be seen in Figure 4.6 as the horizontal plateau of the green region.

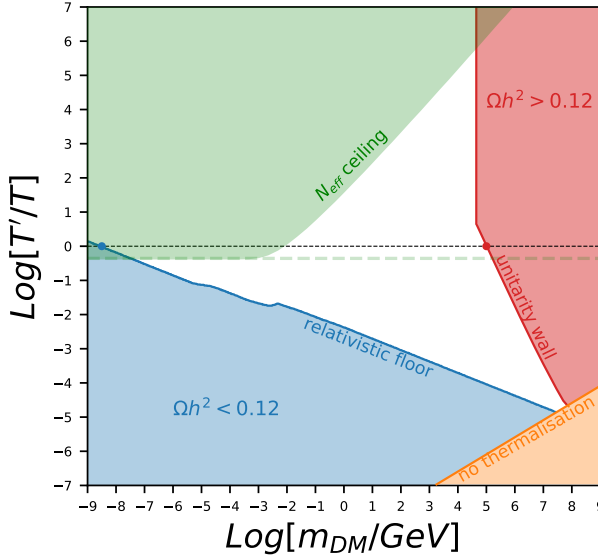


FIGURE 4.6: N_{eff} exclusion area (green) together with the relativistic floor, unitarity wall and thermalisation condition.

On the other hand, if the DM mass lies above the MeV scale, the DM may have been already non-relativistic at BBN and its abundance would have been further suppressed. In this regime, using Eq. 4.38 the constraint at BBN is

$$\frac{T'_{\text{BBN}}}{T_{\text{BBN}}} \leq 0.51 \times \left(\frac{4}{g_{\text{DM}}} \right)^{1/4} (x'_{\text{BBN}})^{-5/8} e^{x'_{\text{BBN}}/4}, \quad (4.41)$$

while at DM decoupling we have,

$$\frac{T'_{\text{dec}}}{T_{\text{dec}}} \leq 0.51 \times \left(\frac{4}{g_{\text{DM}}} \right)^{1/4} (x'_{\text{BBN}})^{-5/8} e^{x'_{\text{BBN}}/4} \times \left(\frac{g'^S_{*}(T'_{\text{BBN}})}{g'^S_{*}(T'_{\text{dec}})} \right)^{1/3} \left(\frac{g'^S_{*}(T'_{\text{dec}})}{g^S_{*}(T_{\text{BBN}})} \right)^{1/3}. \quad (4.42)$$

Eq. 4.42 gives us a more complicated upper bound on the temperature ratio as it depends non trivially on the DM mass (through x'_{BBN}). However, one can rewrite $x'_{\text{BBN}} = m_{\text{DM}}/T_{\text{BBN}} \times (T_{\text{BBN}}/T'_{\text{BBN}})$ such that one can solve Eq. 4.42 for $T'_{\text{dec}}/T_{\text{dec}}$ as a function of m_{DM} if we fix $T_{\text{BBN}} \simeq 1$ MeV. The result of this operation can be translated into the diagonal part of the green region of Figure 4.6.

Now, we consider the possibility of extra degrees of freedom which may be contained in the HS. Contributions to ΔN_{eff} from other HS particles is much more model dependent as it depends on how numerous they are at DM decoupling and if they are still relativistic or not. However, one can consider the simplest case where the DM annihilates into lighter particles which can decay or annihilate into SM particles. In this case, if they decay or annihilate into SM particles for example before the BBN occurs they will have no impact on BBN. Otherwise, their mass should be larger than T'_{BBN} in order to become non-relativistic before BBN and to have their abundance to be Boltzmann suppressed. However, if the mediator mass is of the same scale than the DM mass, the N_{eff} constraint is still relevant, see Eqs. 4.40 and 4.42 and the green area in Figure 4.6. Instead, if the mediator is lighter than the DM and if the ratio of the masses is fixed, the diagonal part moves to the right by a factor of $m_{\text{DM}}/m_{\text{med}}$. Alternatively, if one fixes the mass of the mediator and not the mass ratio, one gets an unique upper bound on the hidden-to-visible temperature ratio: $T'/T < m_{\text{med}}/T_{\text{BBN}}$, in the same way that we obtained the horizontal part of the green area of Figure 4.6, see Eq. 4.40. In the massless mediator limit, we have

$$\frac{T'_{\text{dec}}}{T_{\text{dec}}} \leq 0.60 \times \left(\frac{1}{g'^{\text{eff}}_{*}} \right)^{1/4} \times \left(\frac{g'^S_{*}(T'_{\text{BBN}})}{g'^S_{*}(T'_{\text{dec}})} \right)^{1/3} \left(\frac{g'^S_{*}(T'_{\text{dec}})}{g^S_{*}(T_{\text{BBN}})} \right)^{1/3}, \quad (4.43)$$

where g_*^{eff} includes all HS degrees of freedom which are still unsuppressed at the BBN time (see also [100]). This last constraint gives rise to an additional horizontal line depicted in light green in Figure 4.6. This extra line lies within the exclusion line from the contribution of DM for $m_{\text{DM}} < \text{MeV}$. This is due to the fact that we consider a Dirac DM ($g_{\text{DM}}^{\text{eff}} = 3.5$) and a scalar mediator ($g_{\text{med}}^{\text{eff}} = 1$). Thus, on the one hand, the region allowed by BBN extends to the white domain depicted in Figure 4.6 if there are no extra degrees of freedom left at BBN epoch. On the other hand, values of the hidden-to-visible temperature ratio at DM decoupling larger than ~ 1 are excluded if there are still some extra degrees of freedom remaining at BBN time. We made this discussion as generic as possible, but of course, constraints from BBN can be much more restrictive in explicit models. For example, one could be worry if HS particles (DM or other) annihilate and/or decay during BBN. This could greatly impact the expansion rate and the energy transfer into the VS, see [130], [193], [194]. However, this would require a concrete model and it goes out of the context of this chapter which is dedicated to model independent constraints on thermal DM candidate.

4.2.2 Free-streaming constraints

The second and last observational constraint we will consider in a model independent way is the so-called free-streaming (FS) constraint. This bound comes from the fact that a too light DM particle would have been relativistic for so long that it would have not permitted the formation of large scale structure which are observed today. The usual bound is given by data extracted from Lyman- α forest and gives $m_{\text{DM}} > 5.3 \text{ keV}$ [195]. But, it is assuming a unique thermal bath in the early Universe, i.e. with $T' = T$. In this section, we will generalise this constraint for the case where $T' \neq T$ by converting the constraint on the average distance a collisionless DM particle travels after production, that is to say on the DM free-streaming horizon.

The average momentum of a boson or a fermion population in thermal equilibrium with temperature T' is given by

$$\langle p \rangle \equiv \frac{\int d^3p f(p) p}{\int d^3p f(p)} = T' \times \begin{cases} 3.15 \text{ for a fermion,} \\ 2.70 \text{ for a boson.} \end{cases} \quad (4.44)$$

Since a species can be characterised as non-relativistic when its average momentum lies around its mass, $\langle p \rangle \sim m$, the temperature for which a DM fermion candidate becomes non-relativistic (NR) is about $T'_{\text{NR}} \simeq m_{\text{DM}}/3.15$. This temperature can be converted in time unit thanks to the following relation: $t = 1/2H(T')$ such that one can compute when the DM candidate stops to be relativistic. Depending on if this

transition happens before or after the time of matter-radiation (MR) equality (i.e. $t_{\text{MR}} = 1.9 \times 10^{11}$ s), the free-streaming horizon is given by $\lambda_{\text{FS}} \equiv \int_{t_{\text{dec}}}^{t_0} \langle v(t) \rangle / a(t) dt$ such that one has,

$$\lambda_{\text{FS}} \simeq \frac{\sqrt{t_{\text{MR}} t_{\text{NR}}}}{a_{\text{MR}}} \left(5 + \log \frac{t_{\text{MR}}}{t_{\text{NR}}} \right) \left(\frac{g_*^S(T_0) + (\xi_0)^3 g_*'^S(T'_0)}{g_*^S(T_{\text{dec}}) + (\xi_{\text{dec}})^3 g_*'^S(T'_{\text{dec}})} \right)^{1/3}, \quad (4.45)$$

if $t_{\text{NR}} < t_{\text{MR}}$ and where $a_{\text{MR}} = 8.3 \times 10^{-5}$ is the scale factor at the time of matter-radiation equality. If $t_{\text{NR}} > t_{\text{MR}}$ we have instead,

$$\lambda_{\text{FS}} \simeq \left(\frac{6(t_{\text{MR}}^2 t_{\text{NR}})^{1/3} - t_{\text{MR}}}{a_{\text{MR}}} \right) \left(\frac{g_*^S(T_0) + (\xi_0)^3 g_*'^S(T'_0)}{g_*^S(T_{\text{dec}}) + (\xi_{\text{dec}})^3 g_*'^S(T'_{\text{dec}})} \right)^{1/3}. \quad (4.46)$$

In the last expression we used $\langle v(t) \rangle \simeq a_{\text{NR}}/a \simeq (t_{\text{NR}}/t)^{2/3}$ which is true only if $t > t_{\text{NR}}$. Finally, one can verify that Eq. 4.45 coincides with Eq. 4.46 when $t_{\text{NR}} = t_{\text{MR}}$ as it should.

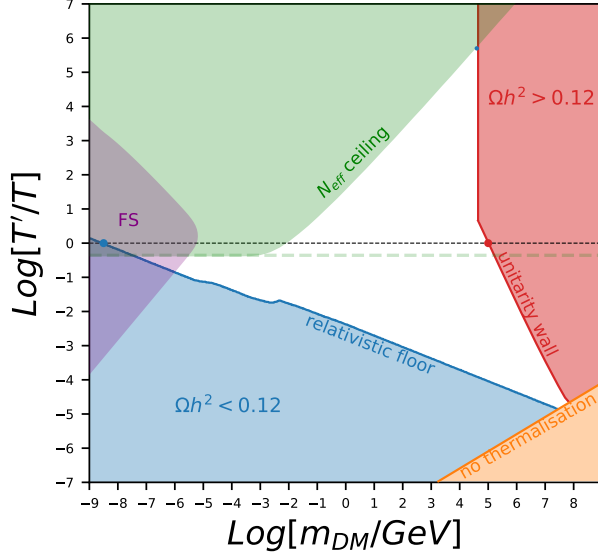


FIGURE 4.7: Free-streaming exclusion area (purple) together with the N_{eff} ceiling, the relativistic floor, unitarity wall and thermalisation condition.

In order to obtain the free-streaming bound given in purple in Figure 4.7, we imposed the usual free-streaming horizon upper bound given by $\lambda_{\text{FS}} \simeq 0.066$ Mpc, see [195]. The very specific behaviours of the purple exclusion area can be understood as following: if the hidden-to-visible temperature ratio is much smaller than unity ($T' \ll T$), the time when DM becomes non-relativistic goes like $t_{\text{NR}} \sim (T'/T)^2/m_{\text{DM}}^2$ such that the free-streaming length increases with the temperature ratio, $\lambda_{\text{FS}} \propto (T'/T)/m_{\text{DM}}$, up to the logarithm in Eq. 4.45. We have then that $T'/T < (m_{\text{DM}} \times \text{factor})$ if we impose that $\lambda_{\text{FS}} < 0.066$ Mpc. On the other hand, if the temperature ratio is larger than unity ($T' \gg T$), the time when DM becomes non-relativistic goes like $t_{\text{NR}} \propto 1/T'^2$ such that the free-streaming length decreases with the temperature ratio, $\lambda_{\text{FS}} \propto (T'/T)^{-4/3}/m_{\text{DM}}$. The free-streaming horizon constraint gives then $T'/T > (\text{factor}/m_{\text{DM}}^{3/4})$.

4.3 The 2D domain

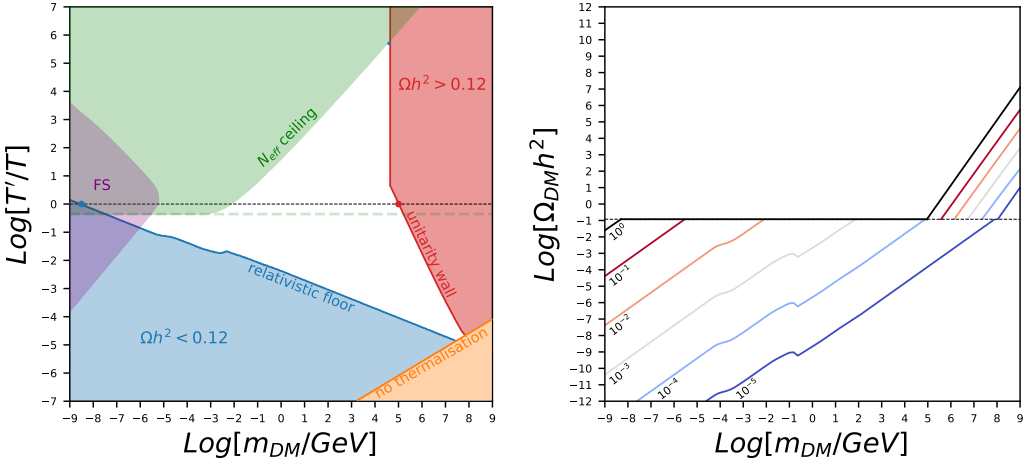


FIGURE 4.8: Domain of thermal DM candidates (white). Left: Temperature ratio (at the time of DM decoupling) as function of the DM mass. Right: Relic density versus DM mass plane for various temperature ratios.

In this section, we will summarise the various theoretical and observational constraints discussed in Sections 4.1 and 4.2. Left panel of Figure 4.8 shows bounds obtained from the relativistic floor of Eq. 4.2 (blue), the unitarity wall of Eqs. 4.22 and 4.23 (red), the thermalisation line of Eq. 4.26 (orange), the N_{eff} ceiling of Eqs. 4.40 and 4.42 (green) and, finally, the free-streaming constraint of Eqs. 4.45 and 4.46 (purple). Along the horizontal black dashed line for which $T' = T$, we recover the

well known 1D mass range for a DM thermal candidate which was in equilibrium with the SM bath at decoupling and for which DM masses smaller than a few MeV are already excluded by BBN.

This figure shows that the DM relic density lies below observations in the blue region (below the relativistic floor) and above observations in the red region (right of the unitarity wall). This means that suitable DM candidate should live within the white region of left panel of Figure 4.8. That is to say that the DM mass and the hidden-to-visible temperature ratio at DM decoupling are bounded;

$$m_{\text{DM}} \in [1.1 \text{ keV}, 53 \text{ PeV}], \quad (4.47)$$

$$\frac{T'_{\text{dec}}}{T_{\text{dec}}} \in [1.6 \times 10^{-5}, 5.0 \times 10^5]. \quad (4.48)$$

Note that the upper bound we get is as high as 53 PeV, which is about a factor 500 larger than the one we have for ordinary $T' = T$ freeze-out. The lower bound being as low as 1.1 keV, it is about a factor 1000 lower than for ordinary FO.

Right panel of Figure 4.8 shows contour of the hidden-to-visible temperature ratio as a function of the DM mass and the DM relic density. The horizontal black dashed line indicates the observed DM relic density, i.e. $\Omega_{\text{DM}} h^2 = 0.1188$. Below this line, the contours of the temperature ratio are obtained from a relativistic decoupling such that intersection of those contours with the horizontal dashed line correspond to the relativistic floor of left panel. Above the line $\Omega_{\text{DM}} h^2 = 0.1188$, contours are the one obtained considering a non-relativistic freeze-out and assuming the maximal cross section allowed by unitarity (see Eq. 4.14). Again, intersections of those lines with the horizontal dashed line correspond to the unitarity wall shown in the left panel of Fig. 4.8.

For $T' = T$, we recover the 1D bounds on the DM mass range given in Eq. 4.27. For $T' \leq T$, the allowed mass range shrinks, but also slowly shifts toward higher DM masses. As a consequence, the merging point of the relativistic floor and the unitarity wall gives a DM candidate around the PeV scale which corresponds to a hidden-to-visible temperature ratio at decoupling of order $T'/T \sim 10^{-5}$, see darkest blue line of bottom panel of Figure 4.8.

4.4 Explicit models in the 2D domain

Now that we have drawn the 2D domain of all DM thermal candidate, we can study how concrete DM models can live in the domain depicted in Figure 4.8. In all of

these models, DM will annihilate into HS particles, and the way it will do so will distinguish the models.

4.4.1 Scenario 1 : t-channel

We first consider a very popular model that we have already studied in this thesis; The vector portal model (benchmark model B of Eq. 1.53) where the DM is a Dirac fermion charged under a new gauge group $U(1)'$. As above, the DM relic abundance is set by the freeze-out of the annihilation process of a pair of DM particles into a pair of massive vector bosons (see Figure 3.4 above), the new gauge boson. Here, in contrast to what we did in Eq. 1.53, we will not consider any kinetic mixing term as we are not interested by the fate of the mediator for the moment. Figure 4.9 shows, in the 2D domain of the left panel of Figure 4.8, the hidden-to-visible temperature ratio as a function of the DM mass for two choices of the free parameters which are the DM-to-med coupling α' and the vector boson mass $m_{\gamma'}$.

The black solid line of Figure 4.9 is for $\alpha' = 3 \times 10^{-4}$ and $m_{\gamma'} = 10$ GeV. Let us explain the several features visible of this solid line. First, in the $T' < T$ region of the parameter space, the HS content never plays a major role in the expansion of the Universe and the HS energy and entropy densities can be neglected when solving the Boltzmann equation for the DM yield. Second, as long as the DM is lighter than the vector boson, the only possible DM annihilation process in the theory is totally inefficient such that DM decouples while still relativistic, that is to say that $T'_{\text{dec}} > m_{\text{DM}}$. The DM relic abundance is then given by the relativistic floor of Eq. 4.2. Once the DM and the vector boson have the same mass, the DM annihilation process starts to be extremely efficient such that one needs that it induces a non-relativistic FO with a large Boltzmann suppression, which must be compensated with a larger value of the temperature ratio. For $m_{\text{DM}} > m_{\gamma'}$, the DM annihilation cross section decreases with the DM mass $\langle\sigma v\rangle \sim 1/m_{\text{DM}}^2$ such that the temperature ratio also has to decrease with the DM mass giving rise to the diagonal. Finally, at some point, the DM annihilation cross section will be so small that it could never thermalised the HS. At such an high DM mass, neither a non-relativistic decoupling nor a relativistic decoupling is possible and the curve stops (little black dot at the extreme right of the dashed black curve). This dot is the equivalent of the little red dot which lies at the intersection of the unitarity wall and the thermalization line, but for a smaller value of the DM-to-med coupling α' .

The black dashed line of Figure 4.9 is for $\alpha' = 0.1$ and $m_{\gamma'} = 30$ MeV. In this case, as the vector boson is lighter than in the previous case, the threshold where the DM annihilation process starts to be efficient happens for a lighter DM mass, at $m_{\text{DM}} = 30$ MeV. The increase in the annihilation cross section is so large than

one need a HS temperature larger than the VS temperature, $T' > T$. In this part of the parameter space, the HS sector may dominate very quickly the Universe's expansion rate. Hence, the DM relic abundance is no longer impacted by the VS as the freeze-out occurs in the HS without feeling the presence of the VS through the expansion rate and the energy and entropy densities are dominated by the HS. As a consequence, the DM relic abundance does not depend on the VS temperature nor the hidden-to-visible temperature ratio. This behaviour is translated by vertical lines in the 2D domain of Figure 4.9. Finally, the fact that the right branch of the black dashed line of Figure 4.9 is shifted to the right compared to the dashed black line is also easy to understand. This comes from the large increase in the DM-to-med coupling α' . As the DM and the vector boson are more strongly coupled, they remain longer in chemical equilibrium and DM abundance is further suppressed. Thus, the DM mass can be larger before that the annihilation process stops to allow any thermalisation within the HS.

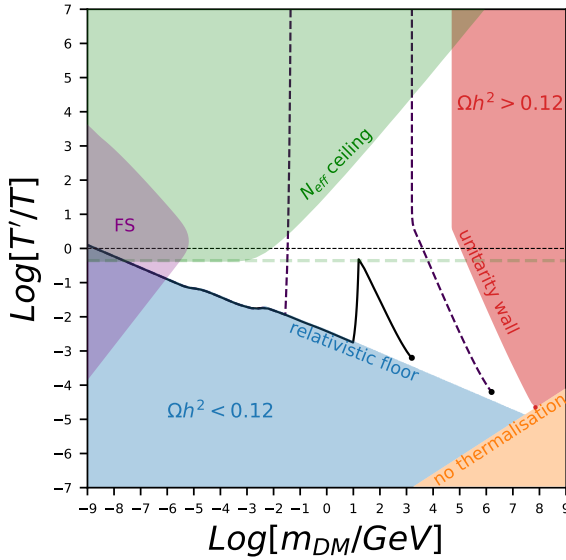


FIGURE 4.9: Parameter space for DM freeze-out driven by DM annihilating into two dark photons in the t-channel. The parameters are $\alpha' = 3 \cdot 10^{-4}$ and $m_{\gamma'} = 10$ GeV for the solid curve while $\alpha' = 0.1$ and $m_{\gamma'} = 30$ MeV for the black dashed curve.

4.4.2 Scenario 2: s-channel

The second model we consider is none of the two benchmark models above. However, it is still built on a Dirac fermion DM, but which annihilates into lighter Dirac

fermions through the production of a scalar state in the s-channel. This time the Lagrangian is given by

$$\mathcal{L} = \mathcal{L}_{SM} + i\bar{\chi}\gamma_\mu\partial^\mu\chi - m_{DM}\bar{\chi}\chi + i\bar{\psi}\gamma_\mu\partial^\mu\psi - m_\psi\bar{\psi}\psi + \partial^\mu\phi\partial_\mu\phi - m_\phi^2\phi^2 - y_\chi\phi\bar{\chi}\chi - y_\psi\phi\bar{\psi}\psi, \quad (4.49)$$

and the DM annihilation cross section, in the non-relativistic limit, by

$$\langle\sigma v\rangle = \frac{\pi\alpha_x^2}{m_{DM}^2} \sqrt{1 - \frac{m_\psi^2}{m_{DM}^2}} \frac{1 - \frac{m_\psi^2}{2m_{DM}^2}}{\left(1 - \frac{m_\phi^2}{4m_{DM}^2}\right)^2 + \frac{\Gamma_\phi^2 m_\phi^2}{16m_{DM}^4}}, \quad (4.50)$$

where we defined $\alpha_x \equiv y_\chi y_\phi / 4\pi$.

We give in Figure 4.10 the results obtained in this model. As one can see comparing Figures 4.9 and 4.10, results are very similar in both models. The important difference with the previous model is the presence of a resonance when the mediator mass is twice the DM one. When this happens, the DM annihilation cross section is resonantly enhanced such that one need to largely increase the hidden-to-visible temperature ratio in order to not annihilate too much DM particles. As a result, around the resonance, the dependence of the temperature ratio as a function of the DM mass is different. This can be seen from Eq. 4.50 neglecting the DM mass ($m_{DM} \ll m_\phi$) or neglecting the mediator mass ($m_\phi \ll m_{DM}$). This gives a cross section going like $\langle\sigma v\rangle \sim m_{DM}^2/m_\phi^4$ or like $\langle\sigma v\rangle \sim 1/m_{DM}^2$ respectively. This behaviour is only visible on the black solid line ($\alpha_x = 0.001$, $m_\psi = 10$ GeV and $m_\phi = 100$ GeV) as the choice of the parameters is such that the curve lies entirely in the region of the parameter space where the HS never dominates the energy nor the entropy density of the Universe. The dashed black line, on the other hand, does not show this behaviour as the resonance occurs when the expansion of the Universe is dominated by the HS.

4.4.3 The role of the heavy mediator

As seen in Section 4.1.1, DM can decouple in a relativistic way in two main ways, depending on whether the annihilation cross section is cut off at $T' > m_{DM}$ by the mass of a heavy mediator it involves or by the mass of its (heavier) annihilation products. Here, we will look a bit more in details the scenario with heavy mediator. In particular, we will look at the interplay between the heavy mediator mass, the DM mass and the decoupling temperature T'_{dec} . To this end, we keep considering

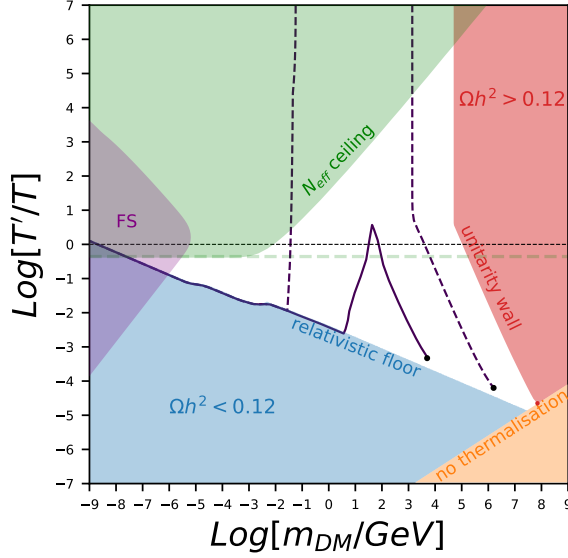


FIGURE 4.10: Parameter space for DM freeze-out driven by DM annihilating into two Dirac fermions in the s-channel mediated by a scalar. We used $\alpha_x = 0.001$, $m_\psi = 5\text{ MeV}$ and $m_\phi = 100\text{ GeV}$ for the dashed line and $\alpha_x = 0.1$ and $m_\psi = 30\text{ MeV}$ with $m_\phi = 1\text{ GeV}$ for the solid line.

the s-channel model of the previous subsection.

To analyse in details what this relativistic decoupling mechanism implies for the parameter space of this explicit example of DM model, one can take the relativistic counterpart of the non-relativistic form of the DM annihilation cross section of Eq. 4.50. Neglecting this time the width of the real scalar ϕ and the DM and final states masses, we have,

$$\langle\sigma v\rangle \simeq \frac{8\pi\alpha_x^2 T'^2}{m_\phi^4}, \quad (4.51)$$

in the range $m_{\text{DM}} \lesssim T' \lesssim m_\phi$ which applies when the DM decouples while still relativistic. With an explicit annihilation cross section at hand, one can compute the absolute value of the temperature at DM decoupling solving the standard thermalisation condition $\Gamma/H = n_{\text{DM}}^{\text{eq}}(T')\langle\sigma v\rangle/H = 1$ along the relativistic floor (i.e. plugging 4.2 and 4.51 in the thermalisation condition). We get,

$$T'_{\text{dec}} = 19.5 \text{ TeV} \times \left(\frac{1}{\alpha_x}\right)^{2/3} \left(\frac{m_\phi}{\text{PeV}}\right)^{4/3} \left(\frac{m_{\text{DM}}}{10 \text{ TeV}}\right)^{2/9} \left(\frac{100}{g_*^S(T_{\text{dec}})}\right)^{1/18} \left(\frac{1}{g_{\text{DM}}^n}\right)^{1/9}. \quad (4.52)$$

We can still use the unitarity bound of Eq. 4.14 for this model as it was a model independent approach. Hence, the upper bound on the DM mass for this model goes down to

$$m_{\text{DM}} \lesssim 30 \text{ PeV} \times (\mathcal{I}_1(x'_{\text{dec}}) \times x'_{\text{dec}})^{3/5}. \quad (4.53)$$

where $(\mathcal{I}_1(x'_{\text{dec}}) \times x'_{\text{dec}})^{3/5}$ is of order unity such that we get back the absolute upper bound on the DM mass for a relativistic decoupling, see Eq. 4.35. As already said above, the fact that this upper bound is slightly smaller than the absolute upper bound on the mass of any DM thermal candidate (Eq. 4.29) is to be expected as Eq. 4.53 sits on the intersection of the relativistic floor and the thermalisation line while Eq. 4.29 sits on the intersection of the unitarity wall and the thermalisation line, see Figure 4.5. Actually, we get back to the 30 PeV upper bound of Eq. 4.35 as it should for a relativistic decoupling

The absolute upper bound on the DM mass coming from unitarity for this model given in Eq. 4.53 also gives an upper bound on the heavy mediator versus DM mass ratio m_ϕ/m_{DM} through the relationship between the decoupling temperature and the DM and heavy mediator masses, see Eq. 4.52. We have,

$$\frac{m_\phi}{m_{\text{DM}}} < 680 \times (\alpha_x)^{1/2} \left(\frac{\text{PeV}}{m_{\text{DM}}}\right)^{5/3} (\mathcal{I}_1(x'_{\text{dec}}))^{3/4}. \quad (4.54)$$

Moreover, one can impose that the decoupling temperature is larger than the DM mass, $T'_{\text{dec}} \gtrsim m_{\text{DM}}$, in order to ensure a relativistic decoupling for the DM. We thus obtain a lower bound on the heavy mediator versus DM mass ratio,

$$\frac{m_\phi}{m_{\text{DM}}} \gtrsim 9.78 \times (\alpha_x)^{1/2} \left(\frac{\text{PeV}}{m_{\text{DM}}}\right)^{5/12}. \quad (4.55)$$

Note that importantly, this last equation indicates that the smaller the DM mass the larger the heavy mediator-to-DM mass ratio has to be for DM to decouple relativistically. This stems from the fact that smaller the DM mass, larger the hidden-to-visible temperature ratio has to be in order to have enough DM abundance today (i.e. to keep sitting on the relativistic floor). Larger the temperature ratio, later the DM will

decouple as its annihilation rate will stay longer more efficient than the Hubble rate. As we want the DM to decouple relativistically, we need to compensate this gain in the annihilation rate by decreasing the heavy mediator mass with respect to the DM one to make the DM to still decouple while relativistic.

Finally, one can check that the unitarity bound also constraints the mass of the heavy mediator as a function of the decoupling temperature thanks to the explicit form of the annihilation cross section. The lower bound is thus given by,

$$\frac{m_\phi}{T'_{\text{dec}}} > 2.38 \times (\alpha_x)^{1/2} (\mathcal{I}_1(x'_{\text{dec}}))^{-1/4}. \quad (4.56)$$

This last bound is automatically satisfied for typical perturbative coupling, as expected.

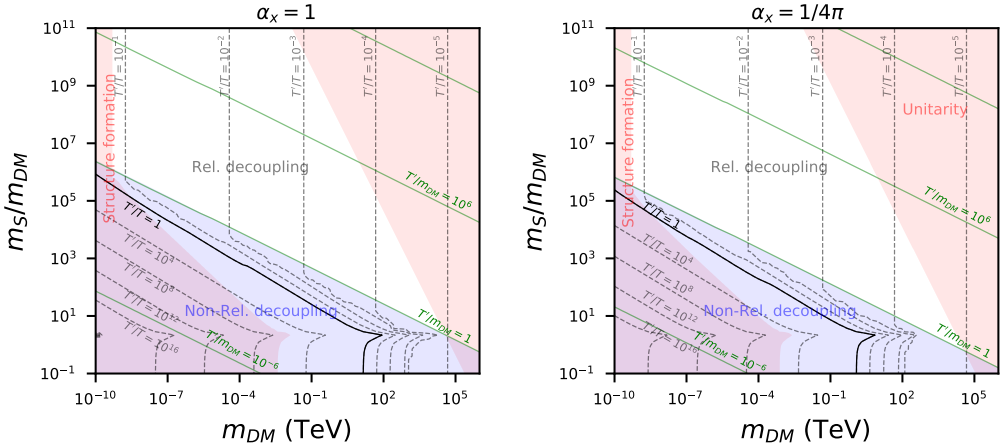


FIGURE 4.11: Allowed parameter space for two choices of the couplings, $\alpha_x = 1$ (left) and $\alpha_x = 1/4\pi$ (right). The regions excluded by the structure formation and unitarity constraints are shown in red, while the blue region indicates the non-relativistic regime. We also show various contour of $T'_{\text{dec}}/m_{\text{DM}}$ and $T'_{\text{dec}}/T_{\text{dec}}$.

Figure 4.11 shows as a function of the DM mass and the heavy mediator-to-DM mass ratio, the value of the temperature ratio at decoupling one needs to account for the observed relic density in this model for two choices of the coupling $\alpha_x = 1$ (left) and $\alpha_x = 1/4\pi$ (right). Are also visible in Figure 4.11, the lower (blue) and upper (red) bounds on the mass ratio given by Eq. 4.55 and Eq. 4.54 respectively. Constraint from large scale structure is also shown in red, as well as the isocontours

of $T'_{\text{dec}}/T_{\text{dec}}$ and $T'_{\text{dec}}/m_{\text{DM}}$. Let us explain various features visible in Figure 4.11. When DM decouples while still relativistic (i.e. white region), the isocontour of the temperature ratio at decoupling, $T'_{\text{dec}}/T_{\text{dec}}$, are vertical because this ratio does not depend on the heavy mediator mass m_ϕ as the model saturates the relativistic floor of Eq. 4.2. The absolute unitarity bound given in Eq. 4.14 which corresponds to Eq. 4.53 is saturated close to the floor ($T'_{\text{dec}}/m_{\text{DM}} \simeq 1$) as expected and for $m_\phi/m_{\text{DM}} \sim 2$.

As said above, for smaller DM masses, the heavy mediator has to be much heavier than the DM $m_\phi \gg m_{\text{DM}}$ so that the DM decouples while still relativistic, see Eq. 4.55.

If the heavy mediator versus DM mass ratio is smaller, one enters in the non-relativistic decoupling regime shown in blue in Figure 4.11. This regime corresponds to a secluded freeze-out regime (see Subsection 3.2.5 for more details) and results in this regime follow the analytical results of [179] (see also [85], [100], [177]). As we have seen in Chapter 3, in the secluded freeze-out (as in the ordinary freeze-out), the DM final relic abundance also depends on the annihilation cross section and not only on the DM mass and the hidden-to-visible temperature ratio as in the relativistic decoupling regime. Hence, since the annihilation cross section decreases quickly with the heavy mediator mass, $\langle\sigma v\rangle \propto 1/m_\phi^4$ when $m_\phi \gtrsim m_{\text{DM}}$, the DM relic density will decrease quickly when m_ϕ/m_{DM} decreases. This has to be compensated by a larger value of the hidden-to-visible temperature ratio in order to balance this fall of the annihilation cross section strength. This specific feature explains the behaviour of the temperature ratio isocontours in the non-relativistic regime for $m_\phi \gtrsim m_{\text{DM}}$. One can also distinguish in Figure 4.11 the effect of the resonance at $m_\phi \simeq 2m_{\text{DM}}$ for which the DM annihilation cross section is resonantly boosted and this requires a larger value of the temperature ratio.


Finally, if the mediator ϕ is no longer heavier than the DM, $m_\phi < m_{\text{DM}}$, the DM relic density becomes very quickly independent of the mediator ϕ mass as the model is now in a "light mediator" regime where the cross section is independent of the mediator mass m_ϕ . This is why the contours of the temperature ratio are vertical in this region of the parameter space as it is the case in the relativistic regime. Note the large difference in the magnitude of the hidden-to-visible temperature ratio in those two regions. In fact, the T'/T isocontours should be even more shifted towards the right than in Figure 4.11 due to the fact that in the $m_\phi < m_{\text{DM}}$ region, the DM can also annihilate into two ϕ 's ($\text{DMDM} \rightarrow \phi\phi$). This effect has not been taken into account as, here, we aimed to show how the results behave from a unique annihilation channel everywhere (i.e. from $\text{DMDM} \rightarrow \psi\psi$ mediated by a s-channel scalar ϕ).

Part III

Self-Interacting Dark Matter ways-out

Chapter 5

SIDM in a colder Hidden Sector

 In the two first chapters, we have considered and motivated the possibility that DM undergoes self-interactions. One has seen in the framework of the two particularly simple explicit benchmark models A and B that many constraints apply to this setup and, actually, excluding that these models could have enough self-interactions as suggested by small scale structure anomalies. In the previous chapter, one has considered and motivated the possibility that the HS does not thermalise with the SM thermal bath, as a result of a feeble DM-to-SM connection. Having all of these chapters in mind, one will now ask the following question: What about self-interacting DM in a HS not thermally connected to the SM thermal bath? In particular, what become the constraints developed in Chapter 1 in the hidden-to-visible temperature ratio versus DM mass plane? Indeed, constraints as considered in Chapter 1 assumed a thermal connection between the dark sector and the SM, so that $T' = T$. But what happens for $T' \neq T$? To illustrate this, we consider here too the two portal models that we presented in Section 1.3.4 and defined by Eqs. 1.48 and 1.53 for the Higgs portal and the kinetic mixing portal models respectively. The following discussion is mainly based on [85] for the vector case, but also contain original unpublished work (scalar case) and use results from [84].

5.1 Hidden sector temperature

The first thing to do when considering a different temperature for the HS and the SM is to ensure that the HS bath has thermalised before DM decoupling such that a temperature for the HS can be defined at this moment. We have then to compute the minimal value of the HS sector coupling (corresponding to the DM-to-med coupling in the two benchmark models we consider) which allows a thermalisation of particles within the HS. That is to say that we look for the equivalent of the thermalisation condition in orange in Figure 4.8. Since, we already discussed thermalisation conditions in Chapter 3, we simply recall here the condition which is of our interest in this section given first in Eq. 3.10,

$$\Gamma_{\text{DM} \leftrightarrow \text{med}}|_{T' \simeq m_{\text{DM}}} \gtrsim H|_{T' \simeq m_{\text{DM}}}, \quad (5.1)$$

with H the Hubble rate as previously. Neglecting the portal connection to the SM there is no significant production of DM or mediator particles from the SM and the interaction rate in Eq. 5.1 is simply given by

$$\Gamma_{\text{DM} \leftrightarrow \text{med}} = \langle \sigma_{\text{DM} \rightarrow \text{med}} v \rangle n_{\text{DM}}^{\text{eq}}. \quad (5.2)$$

The thermally averaged DM annihilation cross sections at tree level (see corresponding Feynman diagrams in Figure 2.2 above which we reproduce again in Figure 5.1 for convenience) for the vector and the scalar portal models are given in Eqs. 2.21 and 2.22 and that we repeat here,

$$\langle \sigma v \rangle_{\bar{\chi}\chi \rightarrow \gamma'\gamma'} = \frac{\pi \alpha'^2}{m_{\text{DM}}^2} \sqrt{1 - \frac{m_{\gamma'^2}}{m_{\text{DM}}^2}}, \quad (5.3)$$

$$\langle \sigma v \rangle_{\bar{\chi}\chi \rightarrow \phi\phi} = \frac{3v^2}{4} \frac{\pi \alpha_\phi^2}{m_{\text{DM}}^2} \sqrt{1 - \frac{m_\phi^2}{m_{\text{DM}}^2}}, \quad (5.4)$$

where we kept same notations as previously, with v the Møller velocity (see Chapter 2).

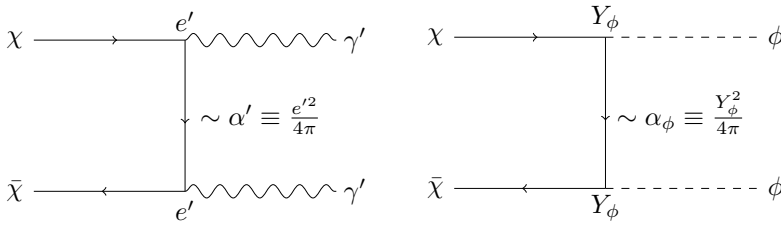


FIGURE 5.1: Feynman diagrams corresponding to the DM annihilation processes responsible for the freeze-out mechanism for both the kinetic mixing portal (left) and the Higgs portal (right) models.

In the same way that we obtained, for a cross section which saturates the unitarity bound, the thermalisation line of Eq. 4.26 and depicted in Figure 4.5, one can determine the minimal allowed value of the DM-to-med coupling in those specific

benchmark models we consider. In order to do that, one must plug the expressions for the DM annihilation cross section of Eqs. 5.3 and 5.4 and the DM relativistic number density into the thermalisation condition given in Eq. 5.1. These lower bounds are given as a function of the hidden-to-visible temperature ratio and the DM mass by,

$$\alpha' \gtrsim 5.98 \times 10^{-9} \frac{T}{T'} \left(\frac{\sqrt{g_{\star}^{eff}(T)}}{g_{DM}^{eff}(T')} \right)^{1/2} \left(\frac{m_{DM}}{100 \text{ GeV}} \right)^{1/2}, \quad (5.5)$$

$$\alpha_{\phi} \gtrsim 3.95 \times 10^{-9} \frac{T}{T'} \left(\frac{\sqrt{g_{\star}^{eff}(T)}}{g_{DM}^{eff}(T')} \right)^{1/2} \left(\frac{m_{DM}}{100 \text{ GeV}} \right)^{1/2}. \quad (5.6)$$

As long as the DM-to-med coupling is bigger than these lower bounds and if the connection to the SM is negligible, the dark sector will be totally decoupled from the SM and enters into a simple freeze-out phase within the HS. The source of the HS has not to be necessarily the SM as in the secluded freeze-out regime such as considered above (regime IV of Section 3.2.5). Indeed, as discussed in Chapter 3, the HS could have been produced just after the inflation in the same way that it is usually assumed that the SM is produced just after inflation. However, in practice, the dynamics is the same as in the secluded freeze-out mechanism because the source of the bath has no role other than setting the initial conditions. Thus, in order to have an analytic approximation of the DM relic density, one can use the formula obtained assuming an instantaneous FO (see Eq. 4.10), but for the DM annihilation cross section of Eqs. 5.3 and 5.4 for the vector and scalar portal models respectively. For the former one we have,

$$\frac{T'_{\text{dec}}}{T_{\text{dec}}} \simeq 1.73 \times 10^{-2} \times \left(\frac{\alpha'}{10^{-3}} \right)^2 \left(\frac{g_{\star}^S(T_{\text{dec}})}{100} \right) \left(\frac{100}{g_{\star}^{eff}(T_{\text{dec}})} \right)^{1/2} \left(\frac{23}{x'_{\text{dec}}} \right) \left(\frac{\text{TeV}}{m_{DM}} \right)^2, \quad (5.7)$$

in which we neglected the mediator mass as we are interested in the light mediator regime where $m_{\text{med}} \ll m_{DM}$. Similarly, for the scalar portal model using the cross section given in 5.4 we get,

$$\frac{T'_{\text{dec}}}{T_{\text{dec}}} \simeq 1.70 \times 10^{-3} \times \left(\frac{\alpha_{\phi}}{10^{-3}} \right)^2 \left(\frac{g_{\star}^S(T_{\text{dec}})}{100} \right) \left(\frac{100}{g_{\star}^{eff}(T_{\text{dec}})} \right)^{1/2} \left(\frac{23}{x'_{\text{dec}}} \right)^2 \left(\frac{\text{TeV}}{m_{DM}} \right)^2. \quad (5.8)$$

Note the power of two on x'_{dec} in the scalar portal case which differs from the vector portal case. This is due to the velocity dependence of the annihilation cross section as $v^2 \sim T'/m_{\text{DM}} = 1/x'$. Figure 5.2 shows, within the domain of thermal DM candidates of Figure 4.8, contours of the DM-to-med coupling which account for the DM relic density today. Note that in Figure 5.2 we focus on the GeV to TeV DM mass range such that one cannot see the unitarity wall neither the thermalisation line. However, one can still recognise the relativistic floor in blue.

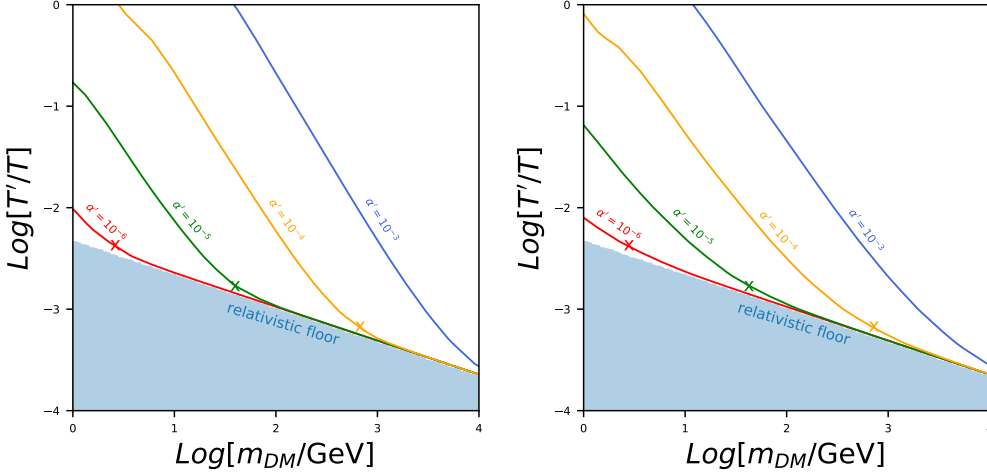


FIGURE 5.2: Needed value of $(T'/T)_{T=T_{\text{dec}}}$ as a function of the DM mass in order to satisfy the relic density constraint for four different values of the DM-to-med coupling. Results are obtained neglecting all connection to the SM for both the vector portal model (left) and the scalar portal model (right). The black solid line shows the model independent relativistic floor obtained in Eq. (4.2). The crosses show the value of m_{DM} above which Eqs. (5.5) and (5.6) are no longer satisfied, i.e. above which $\Gamma/H|_{T'=m_{\text{DM}}} < 1$.

Behaviours of curves shown in Figure 5.2 are easy to understand with the help of Eqs. 5.7 to 5.8. Indeed, from these equations one can see that the DM relic density scales as $\Omega_{\text{DM}} \propto (T'/T)/\langle\sigma v\rangle$ such that, for a fixed value of the DM-to-med coupling, the larger the DM mass is, the smaller the temperature ratio must be. As a consequence, the larger the DM mass is, the smaller the Boltzmann suppression must be in order to not deplete too much the DM abundance after it becomes non-relativistic. If one keeps increasing the DM mass, one will reach the point where the needed value of the temperature ratio is so small that the initial DM abundance is the same of what one would expect from a particle which decouples while still relativistic. In other words, the temperature ratio curve as a function of the DM

mass will reach asymptotically the "relativistic floor" of Eq 4.2 (shown in blue in Figure 5.2). We also indicate with crosses in both panels of Figure 5.2 where the approximate condition for the HS to thermalise ($\Gamma/H|_{T'=m_{DM}} = 1$) stops to hold, in the same way we ended the curves with dots in Section 4.4. Thus, for a fixed value of the DM-to-med coupling, on the one hand the HS thermalises if the DM mass is lighter than the mass shown by the cross. On the other hand, the HS does not thermalise for heavier DM masses. This is due to the fact that the annihilation rate scales as the cross section which decreases with the mass. Since the process responsible of the DM freeze-out cannot be responsible for the HS thermalisation for heavy DM masses, one needs to assume an additional interaction in the UV in order to satisfy the HS thermalisation hypothesis. The fact that the crosses lie close to the relativistic floor is to be expected. Indeed, looking at the heaviest DM mass (for a fixed value of the DM-to-med coupling) which allows the HS to thermalise, the thermalisation condition holds such that when the DM decouples, its number density has already been a little bit Boltzmann suppressed. This indicates that its associated temperature ratio has to be a little bit bigger than the one expected for relativistic decoupling. Conversely, looking at the lightest DM mass for which the thermalisation condition does not hold, one does not expect any sizeable Boltzmann suppression since in this case, the DM thermalises when $T' \sim m_{DM}$ (and not before already). That is to say when the Γ/H ratio is maximum. In this case, the needed temperature ratio lies very close to the relativistic floor.

5.2 Portal strength to the visible sector

Results shown in Figure 5.2 were obtained assuming a negligible SM-to-med coupling and thus a negligible SM-to-DM coupling. The purpose of this section is to determinate the maximal allowed value of the mixing parameter $\epsilon/\lambda_{\Phi H}$ for previous results still being valid. Indeed, if one increases the mixing parameter, the SM could produce more DM and/or mediator particles such that the HS would be reheated. In that case, the hidden-to-visible temperature ratio would become bigger than the one assumed in Figure 5.2. The criteria we used is to impose that the DM and mediator yields obtained by freeze-in from SM particles does not exceed the yields obtained at DM decoupling when neglecting the SM source terms. That is to say that we imposed that:

$$Y_{DM}^{SM}(T'_{dec}) < Y_{DM}^{HS}(T'_{dec}), \quad (5.9)$$

$$Y_{med}^{SM}(T'_{dec}) < Y_{med}^{HS}(T'_{dec}), \quad (5.10)$$

where $Y^{SM}(T'_{dec})$ indicates the yield obtained through a freeze-in from SM particles at DM decoupling (given by Eq. 3.18) while $Y^{HS}(T'_{dec})$ stems for the yield obtained

after a freeze-out in the HS at DM decoupling when neglecting the SM source terms (given by solution of Eq. 3.29).

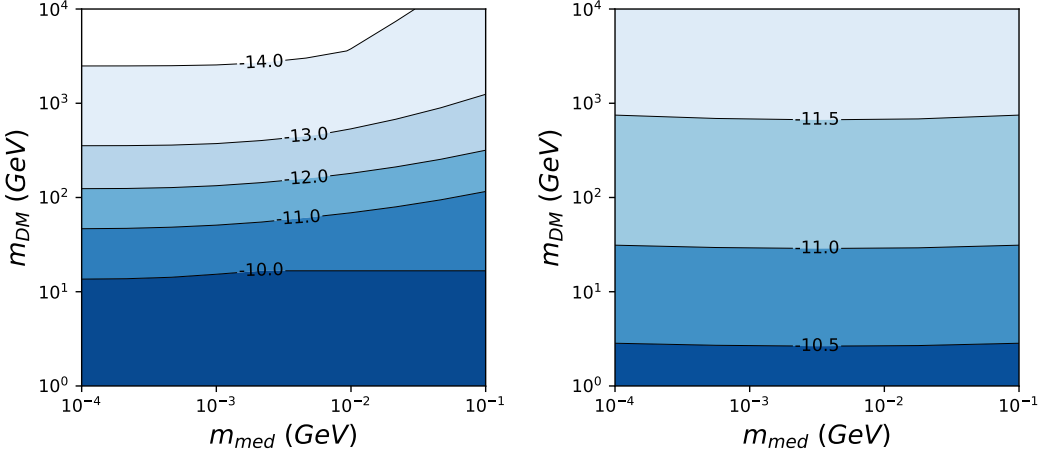


FIGURE 5.3: Maximal allowed value of the SM-to-med coupling such that the production of HS particles from SM never exceeds what one would have without the portal interaction. For the whole shown parameter space, we fixed $\alpha' = 10^{-4}$ for the vector portal model (left) and for the scalar portal model $\alpha_\phi = 10^{-4}$ (right) and used the temperature ratio given by Figure 5.2.

Figure 5.3 shows the upper bound on the SM-to-med coupling $\epsilon/\lambda_{\Phi H}$ in the DM versus mediator mass plane one has when assuming that the portal interaction never produce more DM and mediator that one would get without this connection to the SM. Every point in this plane is a DM candidate in the sense that, fixing the DM-to-med coupling to $\alpha' = 10^{-4}$ for the vector portal model (left) and to $\alpha_\phi = 10^{-4}$ as well as for the scalar portal model (right), we used the temperature ratio given by Figure 5.2¹. From Figure 5.3, one can conclude for example that for $m_{\text{DM}} = 100$ GeV and $m_{\text{med}} = 0.1$ GeV, the maximal allowed value for results shown on Figure 5.2 still being valid is $\epsilon \lesssim 10^{-11}$ in the vector portal model and $\lambda_{\Phi H} \lesssim 6.3 \times 10^{-12}$ in the scalar portal model.

¹We recall that this temperature ratio were fixed in order to satisfy the DM relic abundance constraint.

5.3 Constraints

In Chapter 1, we have reviewed all relevant constraints one should take care of while considering SIDM models. But, during the whole chapter, we have considered a dark sector which is in thermal equilibrium with the SM or, at least, with the same temperature T . However, as we discussed already above, this requirement is not mandatory at all and one could have a HS with its own temperature. In such scenarios, some of the constraints reviewed in Chapter 1 may change. In this section, we will go through all relevant constraints which are impacted if the HS thermal bath has a different temperature as the SM thermal bath.

5.3.1 CMB

DM annihilation rate

Let us start our analysis on changes of CMB constraints with the upper bound on the DM annihilation cross section into two mediators which could give rise to photons at recombination, see Eq. 1.62. In the case where both sector thermalise and if we only have one thermal bath and thus one temperature (i.e. $T' = T$), this constraint is already strong enough to exclude the whole vector portal model as soon as the dark photon is heavier than twice the electron mass, $m_{\gamma'} > 2m_e$. Indeed, in this scenario, the new mediator decays into charged SM leptons and this would produce too many photons. This has already been studied at length, see [123] for a deeper analysis. However, this bound does not entirely exclude the scalar portal model as the annihilation cross section of DM into two scalars proceeds in p-wave. Thus, the cross section is suppressed compared to a s-wave annihilation. In practice, both s-wave and p-wave cross sections are boosted thanks to the Sommerfeld effect, but, as we have seen in Chapter 2, it turns out that the p-wave cross section is much less boosted than the s-wave one at recombination as a result of small velocities at this time, see Figure 1 of [123]. As a consequence, the scalar portal model does really not suffer from this constraint.

On the other hand, in the case where the connection between the two sectors is not strong enough to allow thermalisation between the two baths, the HS has its own temperature, $T' \neq T$. As we have seen above, the required annihilation cross section in order to get the observed DM relic abundance is changed by a factor of T'/T , see Eq. 4.10. Thus, if the HS thermal bath temperature is smaller than the SM thermal bath temperature, the annihilation cross section needed is suppressed with respect to the case $T'/T = 1$, since it has been less Boltzmann suppressed in this case (its number density before Boltzmann suppression being smaller by a factor of $(T'/T)^3$). This suppression could potentially be strong enough to avoid the upper bound on the annihilation cross section given by the CMB. Figure 5.4

gives for the vector portal model (left) and the scalar portal model (right) contour of $\log_{10} \left[\frac{\langle \sigma v \rangle_{rec}}{\text{cm}^3 \text{s}^{-1}} \frac{\text{GeV}}{m_{\text{DM}}} \right]$ at recombination in the DM versus mediator mass plane. As previously, we used the temperature ratio given by Figure 5.2 for all points in this parameter space. The key feature is given by the solid black line which indicates where the upper bound on this quantity sits in this plane. Every candidate below this line has an annihilation cross section into light mediators too strong at recombination and is excluded by CMB data.

One can conclude from these results that the CMB constraints on the DM annihilation cross section at recombination is strongly relaxed as now it excludes DM masses below a few tens of GeV for the vector portal model. While the parameter space we consider for the scalar portal model is totally allowed by this constraint.

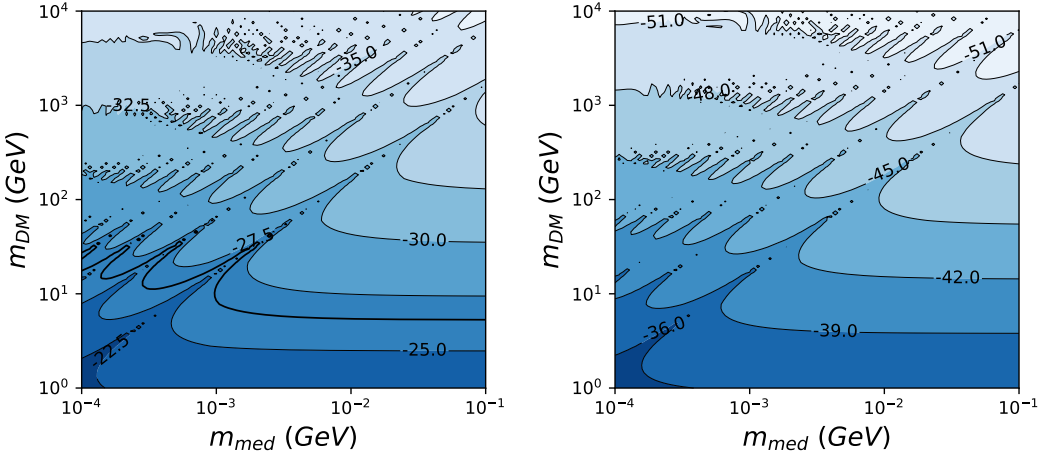


FIGURE 5.4: Contours of $\log_{10} \left[\frac{\langle \sigma v \rangle_{rec}}{\text{cm}^3 \text{s}^{-1}} \frac{\text{GeV}}{m_{\text{DM}}} \right]$ at recombination as a function of DM and mediator masses for the vector with $\alpha_{\gamma'} = 10^{-4}$ (left) and scalar with $\alpha_{\phi} = 10^{-4}$ (right) portal models. The solid black line gives the upper bound given by Eq. 1.62: $\langle \sigma v \rangle_{rec} / m_{\text{DM}} = 4 \times 10^{-27} \text{ cm}^3 \text{s}^{-1} \text{GeV}^{-1}$ such that the region below this line is excluded.

Mediator decay

The constraints from CMB on the mediator decay were summarised in Figure 1.22 and Eq. 1.63. They both suggested two simple ways out: either one can reduce the mediator lifetime in order to make it decay long before recombination era, either one can reduce the mediator abundance when at the last scattering surface. The problem with the first way out is that if one shorten the mediator lifetime, one must increase

its connection to the SM and this usually requires SM-to-med couplings above the upper limit given by the no thermalisation condition (see Figure 5.3). However, the second way out is automatically included in the thermally disconnected HS scenario. Indeed, if $T' < T$ the mediator number density left after having decoupled from the DM particles is suppressed by a factor of $(T'/T)^3$. This factor can be small enough to suppress the mediator number density and to make it below the upper bound given by CMB. Fixing the value of the SM-to-med coupling as given in Figure 5.3 and the temperature ratio as given in Figure 5.2, one can check that the mediator lifetime is short enough in order to avoid the bound on the mediator decay from CMB. As an example,

$$m_{\text{med}} = 10 \text{ MeV} \quad \text{and} \quad \frac{T'}{T} \lesssim 0.02 \quad \Rightarrow \quad m_{\text{DM}} \gtrsim 117 \text{ GeV}, \quad (5.11)$$

$$m_{\text{med}} = 1.5 \text{ MeV} \quad \text{and} \quad \frac{T'}{T} \lesssim 0.04 \quad \Rightarrow \quad m_{\text{DM}} \gtrsim 74 \text{ GeV}. \quad (5.12)$$

This shows how this CMB constraint on the mediator decay can be easily avoided once the hidden-to-visible temperature ratio is sizeably smaller than unity.

N_{eff}

Since the mediator number density is suppressed by a factor of $(T'/T)^3$ at recombination, this suppression also applies for the CMB constraint on the number of light degrees of freedom encoded in the value of N_{eff} . In practice, this constraint will also become quickly irrelevant for portal models like those we are considering. However, this suppression in the mediator number density is not the only effect that the thermally disconnected HS scenario brings with it. Indeed, if the new light mediator decays while still relativistic after neutrino decoupling, each decay process will inject less energy in the visible sector than in the case where the HS and SM baths are thermally connected. This is simply due to the fact that the mediator reservoir contains less energy since it is decreased by a suppression factor of $(T'/T)^4$ and that its decay is less boosted. As a consequence, there are much less decays which happen after neutrino decoupling such that constraints from CMB on N_{eff} are even more weakened.

The upper bound on the mediator number density as a function of its lifetime which actually applied when $T' < T$ requires a deeper analysis, but a conservative upper bound can be obtained by multiplying the upper bound got in the $T' = T$ case by the suppression factor $(T'/T)^3$. Thus, if one assumes that the mediator decouples while still relativistic (as it is the case in the light mediator scenario), one

gets the upper bound on the lifetime given in Table 5.1.

τ_{med} (sec)		$m_{\gamma'} \text{ (MeV)}$				$m_{\phi} \text{ (MeV)}$			
		3	10	30	100	3	10	30	100
$\frac{T'}{T}$	1	$10^{1.1}$	$10^{0.1}$	$10^{-0.4}$	$10^{-0.7}$	$10^{2.1}$	$10^{1.1}$	$10^{0.1}$	$10^{-0.5}$
	0.1	$10^{7.3}$	$10^{6.3}$	$10^{5.3}$	$10^{4.3}$	$10^{8.3}$	$10^{7.3}$	$10^{6.3}$	$10^{5.3}$
	0.01	>	>	>	>	>	>	>	>
	0.001	>	>	>	>	>	>	>	>

TABLE 5.1: Upper bound on the light mediator lifetime from N_{eff} at CMB for several values of the hidden-to-visible temperature ratio at DM decoupling. This bounds are given for both the vector portal (left) and the scalar portal (right) models assuming a relativistic decoupling. The mention ">" indicates an upper bound greater than 10^8 sec.

From the upper bounds given in Table 5.1, it is easy to conclude that the thermally disconnected HS scenario fulfill easily the N_{eff} constraint at recombination. Indeed, as the mention of ">" indicates an upper bound greater than 10^8 sec, a temperature ratio smaller than 0.01 is enough to guarantee that this constraint is avoided.

Note that for a stable mediator (or with a lifetime longer than the age of the Universe), as it is the case if the mediator is lighter than twice the electron mass or if there is no SM-to-med connection at all, the only relevant constraints are given by the requirement that the mediator relic abundance is negligible compared to the DM and by the Hubble constant. In both cases, the extra $(T'/T)^3$ suppression factor of the mediator number density makes those constraints easier to be fulfilled.

5.3.2 BBN

As in the case of constraints coming from CMB, BBN constraints such that the Hubble constant, the entropy injection and the photodisintegration are all relaxed by the extra factor of $(T'/T)^3$ in the light mediator number density. One could then also consider a conservative upper bound by multiplying the light mediator number density by $(T'/T)^3$. This has been done in Table 5.2 which gives the maximal value of the mediator lifetime allowed by the Hubble constant/entropy injection and photodisintegration constraints. As explained in Subsection 1.5.2, photodisintegration constraint does not apply if the mediator mass is smaller than the photodisintegration threshold (i.e. if $m_{med} < 4.4$ MeV). In the same way, none of these constraints apply if the mediator is stable or if the mediator is already non-relativistic at BBN

(its number density would have been Boltzmann suppressed).

One can thus conclude that BBN constraints become quickly irrelevant in the case of a thermally disconnected HS. Typically, a hidden-to-visible temperature ratio below $T'/T < 0.01$ is low enough to avoid all BBN constraints for most of the parameter space.

τ_{med} (sec)		$m_{\gamma'} \text{ (MeV)}$				$m_\phi \text{ (MeV)}$			
		3	10	30	100	3	10	30	100
$\frac{T'}{T}$	1	$10^{2.0}$	$10^{1.0}$	$10^{0.0}$	$10^{-0.4}$	$10^{2.4}$	$10^{2.0}$	$10^{1.0}$	$10^{-0.1}$
	0.1	$10^{6.9}$	$10^{4.1}$	$10^{3.9}$	$10^{3.8}$	$10^{7.8}$	$10^{4.2}$	$10^{4.0}$	$10^{3.9}$
	0.01	$>$	$>$	$10^{4.7}$	$10^{4.5}$	$>$	$10^{7.6}$	$10^{4.9}$	$10^{4.7}$
	0.001	$>$	$>$	$>$	$10^{7.0}$	$>$	$>$	$>$	$>$

TABLE 5.2: Upper bound on the light mediator lifetime from photodisintegration and Hubble constant/entropy injection during BBN for several values of the hidden-to-visible temperature ratio at DM decoupling. This bounds are given for both the vector portal (left) and the scalar portal (right) models assuming a relativistic decoupling. The mention ">" indicates an upper bound greater than 10^8 sec.

5.3.3 Direct detection

For the whole DM versus mediator mass plane we consider in Figure 5.3, the DM-to-SM connector κ'/κ_ϕ appears to be below or almost below current direct detection constraints given in Figure 1.30. Indeed, we have $\kappa_{KM} \lesssim 10^{-10.5}$ for the vector portal model and $\kappa_{HP} \lesssim 10^{-13} \left(\frac{v_\phi}{\text{GeV}} \right)$ for the scalar portal model. This stems from the fact that, as we have already seen above (see Section Eqs. 5.5 and 5.6), if the temperature ratio is smaller than one, the DM-to-med coupling which is required by the relic density constraint, is smaller than the one one should expect in the thermally connected case (i.e. when $T' = T$). As a direct consequence, the DM scattering cross section on nucleon (given in Eqs. 1.72 and 1.73 for the vector and scalar portal models respectively) will be suppressed such that it is easier to satisfy the direct detection constraints in the thermally disconnected scenario. Note that it has already been suggested some time ago that considering a hidden-to-visible temperature ratio smaller than unity could relax the direct detection (see [196]). A value of T'/T slightly below unity has also been considered in [98], [197], along another general ("dissipative") framework.

5.3.4 Indirect detection

Once again, in the thermally disconnected scenario ($T' < T$), the required DM-to-med coupling is smaller than in the thermally connected scenario ($T' = T$). Thus, the DM annihilation cross section into two mediator particles is also smaller and constraints coming from indirect detection experiments becomes easy to be fulfilled. Such constraints are then relevant only for smaller DM masses (smaller than a few GeV), see Section 5.4 below.

5.4 Summary plot

Let us now present how all of these constraints look like in the DM versus mediator mass plane together with the other constraints developed in Chapter 1.

5.4.1 Kinetic mixing portal

Starting with the vector portal model, Figure 5.5 shows in the DM versus mediator mass plane which part of this parameter space all constraints previously discussed exclude for two values of the DM-to-med coupling: $\alpha' = 10^{-4}$ (left) and $\alpha' = 10^{-5}$ (right) and for three values of the SM-to-med connector: $\epsilon = 10^{-11}$ (top), $\epsilon = 10^{-12}$ (middle) and $\epsilon = 10^{-13}$ (bottom).

In each plot of Figure 5.5, the light blue region is excluded by photodisintegration and/or Hubble constant/entropy injection at BBN combined with the N_{eff} constraint. As explained above, these constraints have been determined by applying the $(T'/T)^3$ suppression factor to the dark photon number density of existing bounds in the thermally connected case (see [130]), as we believe constraints obtained in this way are conservative. The red region on the same plot shows the indirect detection constraints while the grey region indicates where the self-interactions constraints are not satisfied. As for direct detection constraints, they are not visible since they are satisfied for the whole DM versus mediator mass plane for these choices of the DM-to-med and SM-to-med couplings. Indeed, as we have seen in 1.30, the direct detection constraints can be translated into an upper bound on the DM-to-SM coupling κ' as a function of the DM. The maximal allowed value of this coupling is $\kappa' \lesssim 3 \times 10^{-11}$ while this coupling is at most 1.13×10^{-12} (top left) and at least 3.58×10^{-15} (bottom right). The relic density constraint is automatically satisfied for the whole parameter space visible in these plots as we have fixed the value of the temperature ratio according to Figure 5.2. Since all this has been done assuming that the portal interaction has a negligible impact on both DM and mediator relic abundance, the green dashed line indicates the maximal value of the DM mass for which this assumption holds (obtained as in Figure 5.3). Above this line

the portal interaction starts to have more and more impact as we increase the DM mass. However this does not necessarily exclude this part of the parameter space, on the contrary, we expect that a sizeably region above the green dashed line is still allowed. To show that, one would have to compute the relic abundance including portal interactions, which is beyond the scope of this thesis. One would then enter a reannihilation (3.2.4) or a secluded freeze-out (3.2.5) production regime (see [179]).

The differences between the left and right plots of Figure 5.5 can be easily understood. A lower DM-to-med coupling means a smaller DM annihilation rate and a smaller Boltzmann suppression of the DM number density at freeze-out. Once again, this imply a smaller hidden-to-visible temperature ratio (see Figure 5.2) and finally a smaller mediator density. This explain why the overclosure constraint as well as the BBN and CMB constraints are excluding a smaller part of the parameter space when $\alpha' = 10^{-5}$ than when $\alpha' = 10^{-4}$. The indirect detection constraint is also relevant for a smaller part of the parameter space; this is simply due to the smaller DM annihilation rate. The self-interaction constraints are more difficult to satisfy and require a smaller DM mass, but since the other constraints are not excluding this part of the parameter space anymore, we still have an order of magnitude in the DM mass and in the mediator mass which is allowed. Finally, the fact that the green dashed line appears to go down as we decrease the DM-to-med coupling is understood as following: as one decreases the DM connection to the mediator, the DM and mediator number densities become more sensitive to the small source term from SM.

5.4.2 Higgs portal

Switching now to the scalar portal model, Figure 5.6 shows the same parameter space as in Figure 5.5, but for the Higgs portal. The DM-to-med coupling has also been fixed to $\alpha_\phi = 10^{-4}$ for panels on the left while panels on the right are for $\alpha_\phi = 10^{-5}$. Again, these plots are for three values of the SM-to-med connector: $\lambda_{\Phi H} = 10^{-11}$ (top), $\lambda_{\Phi H} = 10^{-11.5}$ (middle) and $\lambda_{\Phi H} = 10^{-12}$ (bottom).

As in the previous case, when the mediator is heavier than twice the electron mass (i.e. $m_{med} > 2m_e$), the mediator decay width² is suppressed by the mixing parameter. Furthermore, it is also suppressed due to the electron Yukawa coupling. As a consequence, the BBN constraints on the mediator lifetime impose to the mixing angle and thus the SM-to-med coupling to be large such that the mediator does not decay during or after BBN. However, hidden sector particles can still be actively produced from SM thanks to the quartic interaction ($HH \rightarrow \phi\phi$) which involves the SM-to-med coupling only. This can force thermalisation between the hidden and

²All relevant decay widths and cross sections can be found in Appendix A.

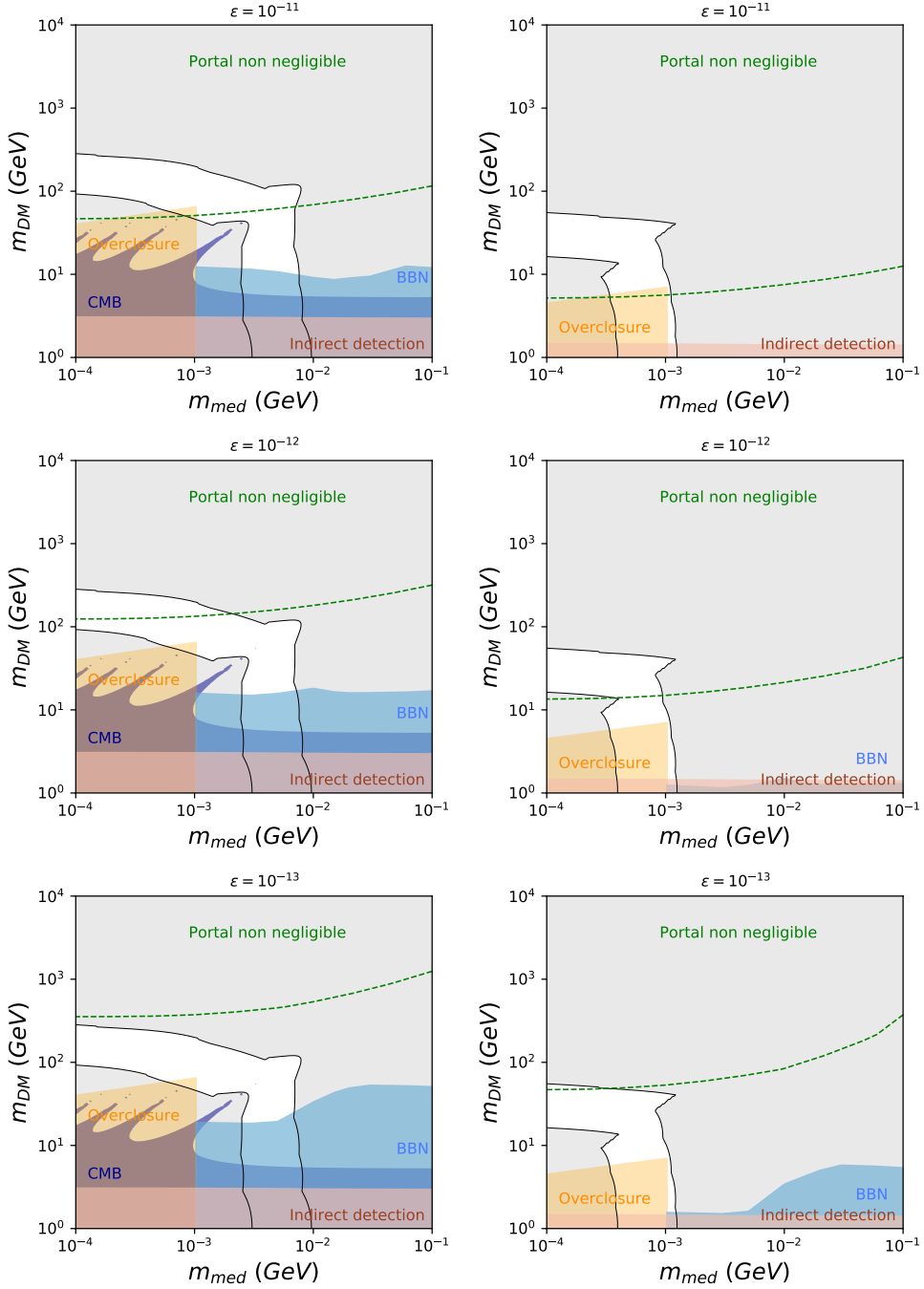


FIGURE 5.5: Constraints from CMB, BBN, self-interaction, indirect and direct detection all together for the vector portal model with $\alpha' = 10^{-4}$ (left) and $\alpha' = 10^{-5}$ (right), for three different values of ϵ .

the visible sectors which contradicts the assumption of a thermally decoupled HS. The major consequence of this is that the whole parameter space is excluded by BBN constraints as soon as the mediator is heavier than twice the electron mass. This can be seen in Figure 5.6. One can also see that the narrow region which in the case where both sector thermalise with each other is still not excluded (for $m_{DM} \sim 0.5$ GeV and $m_{med} \sim 1.1$ MeV [130]) disappears when the HS is colder than the visible sector. This is due to the fact that this region is viable thanks to a large value of the SM-to-med coupling (so that the light mediator can decay before BBN and avoid its constraints) but this large value of the Higgs portal deeply thermalises both sectors, such that $T'/T = 1$.

However, as one can conclude from Figure 5.6, the scalar portal model is now widely open for mediator lighter than twice the electron mass, unlike for the case where both bath thermalise with each other. Below the electron threshold, the decay width is suppressed by loop processes and this leads to lifetime so large than they are forbidden in the $T'/T = 1$ case but not anymore in the $T'/T < 1$ case, i.e. from the suppression by a factor of $(T'/T)^3$. For $\alpha' = 10^{-5}$ this even allows values of m_{DM} below the GeV scale.

5.5 What if no portal at all?

As a final comment for this chapter, let us stress that from the discussion above, it appears that both the vector portal model and the scalar portal model are perfectly viable without any portal at all (i.e. with a stable mediator). In this case all constraints related to the decay of the light mediator, as well as direct and indirect detection, disappear and only the modification of the Hubble constant that the light mediator implies at BBN and CMB times, as well as the non-overclosure constraint are relevant. On the one hand, the former constraint can be easily satisfied by requiring that the mediator is non relativistic enough at these relevant times. This would then require a sufficiently high mediator mass. On the other hand, the latter constraint can be satisfied by requiring that the mediator constitutes a negligible fraction of the DM relic abundance today. This can be done imposing $\Omega_{med} < \Omega_{DM}$ which implies

$$\frac{T'_{dec}}{T_{dec}} \leq 1.14 \times 10^{-2} \times \left(\frac{\text{MeV}}{m_{med}} \right)^{1/3} \times \left(\frac{g_*^S(T_{dec})}{g_{med}^{eff}(T'_{dec})} \right)^{1/3}, \quad (5.13)$$

where all quantities are taken at the DM decoupling. This upper bound lies well above the relativistic floor of Eq. 4.2, as a result of the fact that $m_{med} \ll m_{DM}$, so that this scenario is perfectly viable.

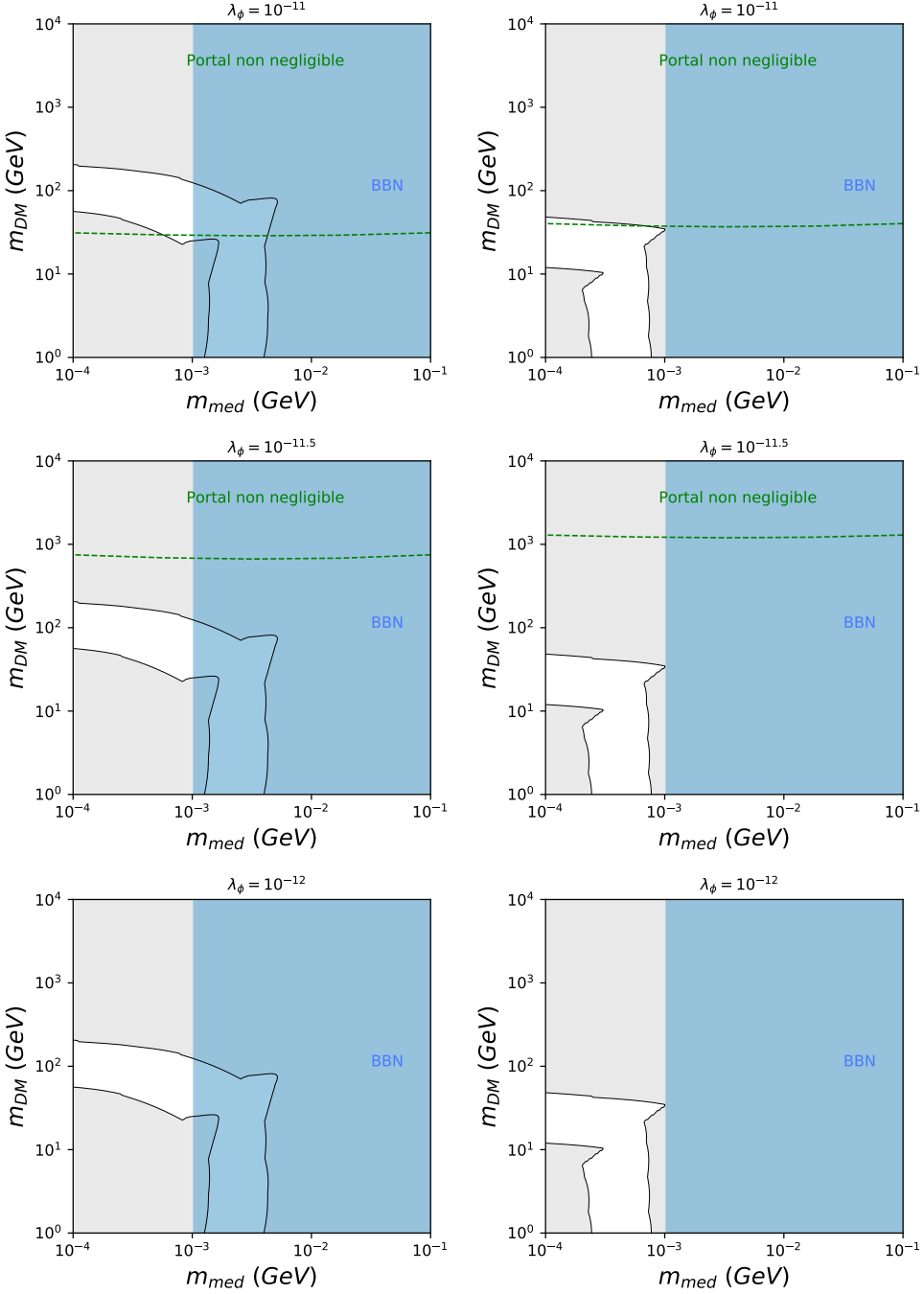



FIGURE 5.6: Constraints from CMB, BBN, self-interaction, indirect and direct detection all together for the scalar A_ϕ model with $\alpha_\phi = 10^{-4}$ (left) and $\alpha_\phi = 10^{-5}$ (right), for three different values of $\lambda_{\Phi H}$.

Chapter 6

Additional minimal solutions for SIDM

 In the previous chapter, the fact that the HS was thermally decoupled from the SM bath was used as a way to circumvent various constraints applying on SIDM with light mediator models. Indeed, we have seen at the end of Chapter 1 (see more specifically Section 1.10) that particle physics experimental constraints were incompatible with small scale structure and cosmological constraints. Basically, a colder and thermally decoupled HS greatly weakens the cosmological constraints such that the tensions can be alleviated. Through this final chapter, we are going to see that even if there is no decoupled DM hidden sector, one can also alleviate the various tensions applying to SIDM in several other ways by introducing an additional particle on top of the DM and the light mediator particles. The way we will invoke an extra particle will differ in each scenario, but the general idea remains the same in all cases: to decouple the small scale structure constraint from the cosmological constraints (see below). We will end this chapter by seeing what could still be done if one does not introduce any extra degree of freedom and consider thermally coupled dark sector. This final chapter is based on [85] and on results from [84] and unpublished results (see Chapter 2).

6.1 Subleading DM annihilation into light mediators

Let us start with the simplest way to decouple small scale structure constraints from cosmological constraints. As we said above, this makes the use of at least one extra new particle on top of the DM and the light mediator particles. This extra particle does not need necessarily to be light¹, which allows this extra particle to easily fulfil all cosmological constraints in a much easier way than the light mediator. The simple idea is to assume that the coupling between the DM and the new heavy mediator

¹In the sense that this extra particle can be heavier than the light mediator, but has still to be lighter than the DM.

is the one which fixes the DM relic density from a freeze-out of DM annihilation into heavy mediators, say $DM DM \rightarrow X X$. Thus in such a scenario, the DM annihilation rate into a pair of light mediators can be much smaller than the thermal value. This does not cause any problem for the small scale structure constraints as these can still be easily fulfilled for a large part of the DM versus mediator mass plane with couplings to the light mediator much smaller than the ones required to account for the DM relic density, see Figure 2.6. Thus, even if it proceeds in a s-wave way, this allow to fulfil the CMB constraints on the DM annihilation rate into light mediators as seen in Figure 1.21. Alternatively, the annihilation channel responsible for the DM relic density, could be p-wave in order to satisfy this CMB constraint such that the heavy mediator should be a scalar boson. Moreover, the direct detection constraint is relaxed by the fact that the DM-to-med coupling is reduced. The simplest option of this kind we have found turns out to have as DM candidate a Dirac fermion, as a light mediator, a vector boson or a scalar boson and as a real or complex scalar S as extra particle (we took it to be real and consider only interactions which contains an even number of them). Those two versions are simply the usual vector and scalar portal model we are used to, but with an additional scalar boson. Their Lagrangian are given by

$$\mathcal{L} \ni -g\gamma'_\mu i\bar{\psi}\gamma^\mu\psi - \frac{\epsilon}{2}F_{\mu\nu}^Y F'^{\mu\nu} - y_S S\bar{\psi}\psi + \lambda_{HS}H^\dagger HS^2, \quad (6.1)$$

$$\mathcal{L} \ni -y_\phi\phi\bar{\chi}\chi + h.c. - \lambda\phi^\dagger\phi H^\dagger H - y_S S\bar{\psi}\psi + \lambda_{HS}H^\dagger HS^2 + \lambda_{\phi S}\phi^\dagger\phi S^2. \quad (6.2)$$

Now, we will see how such a structure allows us to avoid each constraints. We present results obtained for the vector and the scalar models in Figures 6.1 and 6.2 respectively. For each figures, the left (resp. right) panels show results for the DM-to-med coupling fixed to $\alpha'/\alpha_\phi = 10^{-4}$ (resp. $\alpha'/\alpha_\phi = 10^{-5}$) and this for three values of the new heavy mediator mass: $m_S = 3$ GeV (top), $m_S = 30$ GeV (middle) and $m_S = 300$ GeV (bottom). On these figures, the small scale structure exclusion areas are shown in shaded grey while the green hatched regions indicate the part of the parameter space which is kinetically forbidden as the heavy mediator is heavier than the DM. In this region, the DM freezes-out when the temperature reaches the heavy mediator mass scale (i.e. when $T \simeq m_S$) instead of the DM mass scale. Thus, the DM decouples while still relativistic and does not undergo through the usual Boltzmann suppression. As a consequence, its relic abundance is much bigger than the one required by observations. We also show the overclosure constraint in yellow which arises when the light mediator is stable which happens once its mass is smaller than twice the electron mass: $m_{\text{med}} < 2m_e$. This part of the parameter space is then also excluded.

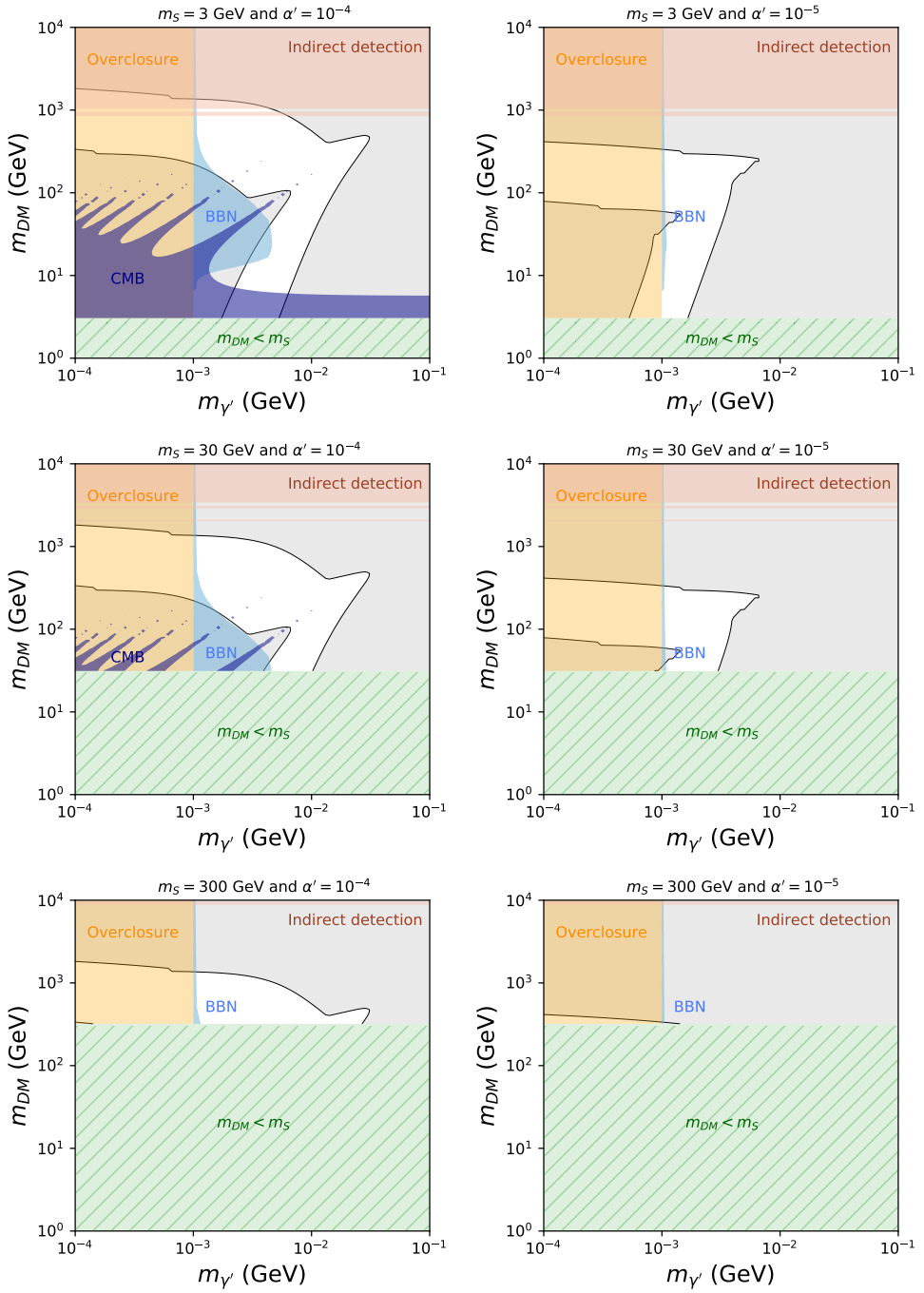


FIGURE 6.1: Constraints from CMB, BBN, self-interaction, indirect and direct detection all together for the subleading DM annihilation into light mediators with $\alpha' = 10^{-4}$ (left) and $\alpha' = 10^{-5}$ (right), for three different values of m_S .

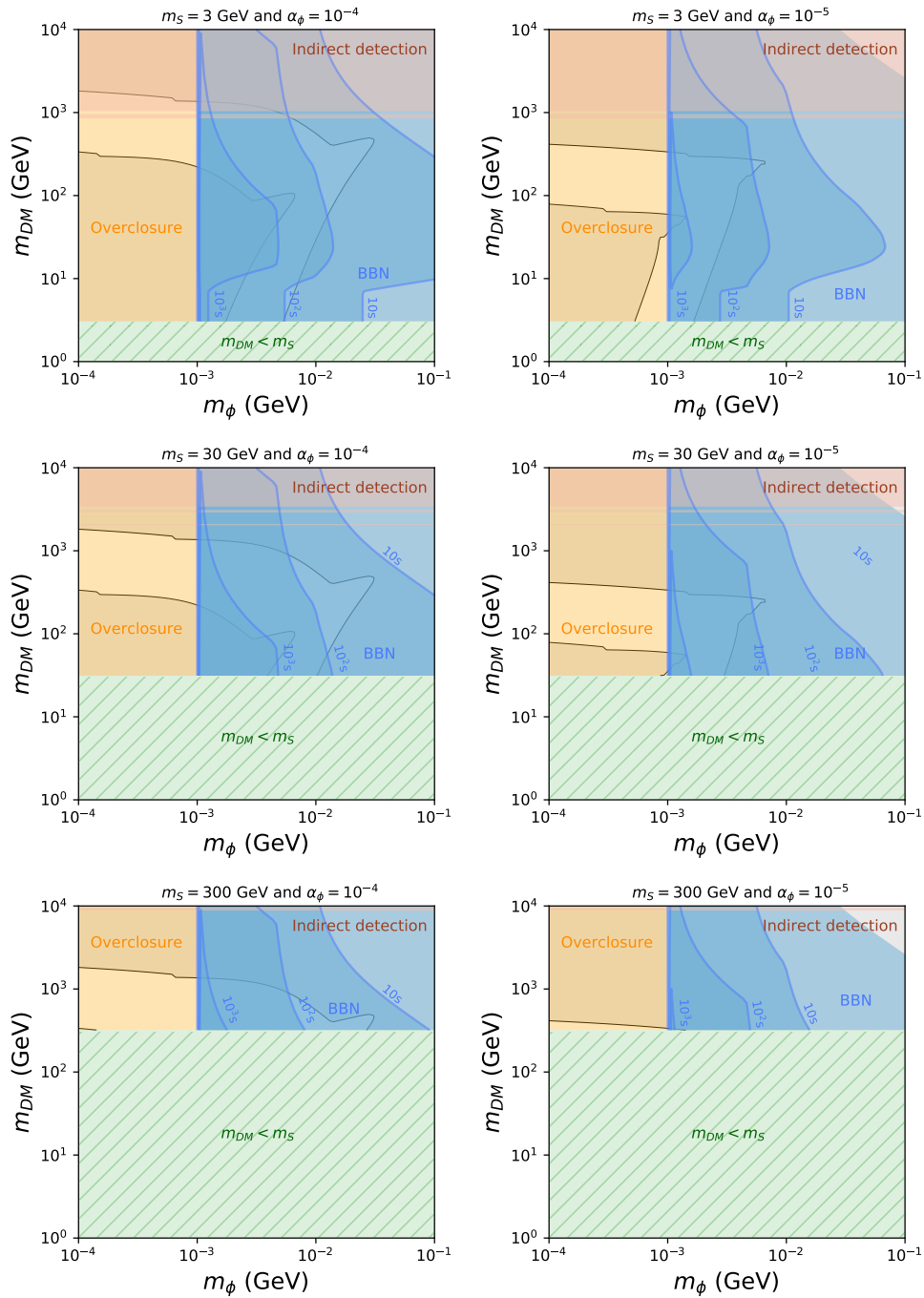


FIGURE 6.2: Constraints from CMB, BBN, self-interaction, indirect and direct detection all together for the subleading DM annihilation into light mediators with $\alpha_\phi = 10^{-4}$ (left) and $\alpha_\phi = 10^{-5}$ (right), for three different values of m_S .

6.1.1 CMB

As the new heavy mediator is a scalar boson in both the vector and the scalar models, the CMB does not suffer from any large distortion from DM annihilation into a pair of this heavy mediator. Indeed, we have seen in Eq. 1.62 that p-wave annihilations do not produce enough charged particles at recombination in order to spoil the CMB spectra. Thus, it is the same than for the case of a DM annihilation into light scalar mediators. The scalar model is then not further constrained by the upper bound on the annihilation rate at recombination, this explains the absence of CMB constraint for all panels of Figure 6.2. The light mediator could still perturb the CMB in the vector model in which the DM annihilation into a pair of light mediators is of s-wave type. However, since this annihilation rate is subleading, its corresponding cross section is smaller than the thermal value such that it can easily fulfill the upper bound given Eq. 1.62 and depicted in Figure 1.21. The CMB bound is shown in dark blue in Figure 6.1.

Moreover, in both models the heavy and light mediators are connected to the SM through a kinetic mixing portal or a Higgs portal depending on if it is a vector or a scalar boson respectively. These mixing interactions do not have to be particularly small as one does not impose to the two baths to be thermally disconnected. As a consequence, all of these light and heavy mediators can decay fast enough into a pair of charged fermions to have any effect on the CMB or N_{eff} .

6.1.2 BBN

In both the vector and the scalar model, on the one hand we have that the mass of the new heavy mediator particle lies much above the MeV scale (from 3 GeV to 300 GeV in Figures 6.1 and 6.2) such that it can easily decay before it would cause any problems for BBN at all. On the other hand, the light mediator mass still lies around the MeV scale and could be constrained. However, as in models presented in the previous chapter (see Section 5.1), the vector mediator can still decay fast enough to avoid BBN constraints in most of the parameter space, the forbidden part of the parameter space is depicted in light blue in 6.1. The scalar mediator model is a little bit more challenging if one keep requiring that its lifetime should not exceed one second ($\tau_\phi < 1$ sec). If one relaxes slightly this bound, one can find some non-negligible part of the parameter space to be allowed. This can be seen in Figure 6.2, where we show in light blue several contours of the light mediator lifetime in seconds which excludes less and less of the parameter space if one relaxes more and more the $\tau_\phi < 1$ sec constraint.

6.1.3 Direct detection

As for the previously defined vector and scalar portal models (see Subsection 1.3.4 and Section 1.7), one can define a DM-to-SM coupling parameter which here, through the exchange of a S scalar particle, is

$$\kappa_S \equiv \frac{y_S}{2} \sin(2\theta), \quad (6.3)$$

where θ is the $H - S$ mixing angle and where we follow the same procedure for the VEV's definitions as detailed in Subsection 1.3.4 for the portal model with a scalar ϕ , see Eqs. 1.48 to 1.52. In terms of Lagrangian parameters (Eq. 6.2), the mixing angle is thus given by

$$\tan(2\theta) = \frac{\lambda_{HS} v_H v_S}{\lambda_S v_S^2 - \lambda_H v_H^2}. \quad (6.4)$$

Even if the new heavy mediator S brings a new direct detection channel, since it is much heavier than the light mediator threshold, $m_S \gg 40$ MeV (see Section 1.7 and Eq. 1.68), the DM scattering on nucleon process is strongly suppressed and direct detection experiments are not sensitive to this channel. There is thus no constraints coming from direct detection on the DM-to-SM coupling from this channel, $\kappa_S \ll \kappa_{HP}$ for considered mass ranges. Moreover, as the coupling between the DM and the light mediator particle is reduced in this scenario, the direct detection constraints for the light mediator exchanged channel are relaxed. Thus, tensions between direct detection constraints and BBN constraints are relaxed compared to models analysed in Chapter 4, which explains why the region allowed by BBN are wider in the present case. This behaviour is true for both vector and scalar portal, but since the constraints were much stronger in the scalar model than in the vector model, the resulting allowed region is still wider in the vector model than in the scalar one. These models illustrate well the fact that if one makes the light mediator to have a negligible impact on the DM production mechanism, it can be easy to fulfil all constraints, specially to alleviate the BBN versus direct detection tensions. For all plots shown in Figures 6.1 and 6.2, the magnitude of the DM-to-SM connection occurring through the light mediator has been chosen such that we have the largest part of the parameter space which is allowed. In other words, the direct detection constraints are saturated for the whole parameter space, i.e. $\kappa' \sim \kappa_{KM}/(\text{a few})$ and $\kappa_\phi \sim (\text{a few}) \times \kappa_{HP}$. However, we would like to emphasise that it is a choice in the way of presenting the results. One can decide to lower the DM-to-SM connection which would shrink a bit the parameter space allowed by BBN constraints.

m_{DM} (GeV)	$m_{\gamma'}$ (MeV)	m_S (GeV)	α'	y_S	σ_T/m_{DM} (cm ² /g)	$\frac{\sigma_{\text{DMDM} \rightarrow \gamma' \gamma'}}{\sigma_{\text{thermal}}}$	$\kappa' \left(\frac{\kappa'}{\kappa_{\text{KM}}^{DD}} \right)$	$\kappa_S \left(\frac{\kappa_S}{\kappa_{\text{HP}}^{DD}} \right)$	$\tau_{\gamma'}$ (sec)	τ_S (sec)
83	18	31	1.7×10^{-4}	0.25	0.18	1.2×10^{-2}	1.8×10^{-11} (0.55)	1.1×10^{-10} ($\ll 1$)	0.30	0.089
326	12	62	6.5×10^{-5}	0.51	0.35	1.2×10^{-4}	2.3×10^{-11} (0.35)	1.8×10^{-10} ($\ll 1$)	0.12	0.006
617	11	12	3.8×10^{-4}	0.70	0.13	1.0×10^{-3}	4.4×10^{-11} (0.47)	4.4×10^{-10} ($\ll 1$)	0.22	0.020
m_{DM} (GeV)	m_ϕ (MeV)	m_S (GeV)	α_ϕ	y_S	σ_T/m_{DM} (cm ² /g)	$\frac{\sigma_{\text{DMDM} \rightarrow \phi\phi}}{\sigma_{\text{thermal}}}$	$\kappa_\phi \left(\frac{\kappa_\phi}{\kappa_{\text{HP}}^{DD}} \right)$	$\kappa_S \left(\frac{\kappa_S}{\kappa_{\text{HP}}^{DD}} \right)$	τ_ϕ (sec)	τ_S (sec)
0.5	1.1	0.01	1.5×10^{-5}	0.02	0.19	0.23	6.8×10^{-7} (0.60)	9.4×10^{-8} (0.09)	27	1
2	3	0.01	4.5×10^{-5}	0.04	0.13	0.13	1.9×10^{-7} (0.99)	1.9×10^{-7} (0.99)	24	1
326	12	62	6.5×10^{-5}	0.51	0.35	1.0×10^{-5}	1.4×10^{-8} (6.17)	1.8×10^{-10} ($\ll 1$)	38	0.006

TABLE 6.1: Examples of parameters values which satisfy the various constraints for the vector (top) and the scalar (bottom) models. κ_{HP}^{DD} and κ_{KM}^{DD} stand for the current experimental upper limit on κ_S and κ' respectively, see Figure 1.30. That these sets of couplings satisfy the CMB constraint of Eq. (1.62) can be seen straightforwardly from comparing the value of $\sigma_{\text{DMDM} \rightarrow \gamma' \gamma'} / \sigma_{\text{thermal}}$ (or $\sigma_{\text{DMDM} \rightarrow \phi\phi} / \sigma_{\text{thermal}}$) above with Figure 1.21. For all of these examples, the indirect detection signal is at least two orders of magnitudes below current experimental sensitivities (see Figure 1.31).

6.1.4 Indirect detection

Since the DM annihilation into a pair of light mediators cross section at freeze-out is sub-dominant, the corresponding annihilation rate today is also reduced. As a consequence, indirect detection signal from DM annihilation into a pair of light mediators is reduced and there is no indirect detection constraint coming from this channel. Moreover, DM annihilation into a pair of heavy mediator is p-wave and so suppressed too. However, as explained in details in Subsection 2.2.3, when the heavy mediator S becomes massless compared to the DM (that is to say when $m_S \ll m_{\text{DM}}$), the Sommerfeld effect can be important, even for p-wave annihilation and one still finds some part of the parameter space that are excluded by indirect detection, depicted in red in Figures 6.1 and 6.2.

6.1.5 Detailed results

Figures 6.1 and 6.2 are used to globally show what the allowed parameter space can look like, but does not give explicitly all parameters. Thus, we present in Table 6.1 numerical examples of sets of parameters which satisfy all constraints for both the vector (top lines) and the scalar models (bottom lines).

Finally we give in Table 6.2 a schematic summary of how various constraint are evaded in this model.

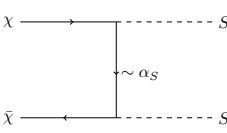
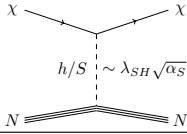
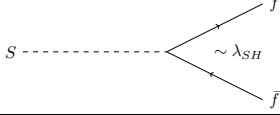
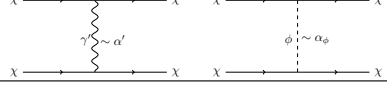
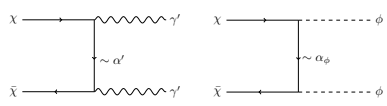
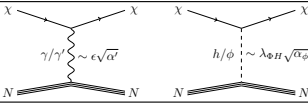
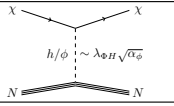
Subleading DM annihilation into light mediators	
Process diagram	Constraint
	<ul style="list-style-type: none"> • α_S fixed by relic density • p-wave \Rightarrow small enough for CMB • small enough for indirect detection
	<ul style="list-style-type: none"> • λ_{SH} fixed by direct detection
	<ul style="list-style-type: none"> • $m_S > \text{GeV} \Rightarrow$ fast enough for BBN
	<ul style="list-style-type: none"> • α' / α_ϕ fixed by small scale structure
	<ul style="list-style-type: none"> • α' / α_ϕ small enough for indirect detection • α' / α_ϕ small enough for CMB
	<ul style="list-style-type: none"> • $\epsilon / \lambda_{\Phi H}$ fixed by direct detection
	<ul style="list-style-type: none"> • $\epsilon / \lambda_{\Phi H}$ fast enough for BBN

TABLE 6.2: Summary of how tensions are alleviated in the subleading annihilation option.

6.2 The *p*-wave option

Another possibility is to consider models in which the DM annihilation into a pair of light mediators is *p*-wave, but still dominates the freeze-out. Thus for a Dirac DM candidate, the light mediator must be a scalar boson, ϕ . Here, we do not decouple the channel responsible for the relic density and the one responsible for the strong self-interactions. As discussed above in Section 1.10, this could be problematic because these two constraints together generally impose a relatively strong connection between DM and the light mediator which would imply a relatively strong DM-to-SM connection. This would then be directly in opposition with cosmological constraints and particle physics experiments, see Figure 1.32. Thus here instead, the extra degree of freedom is assumed to be lighter (i.e. extra-light) than the already existing light mediator ϕ and will be used to reduce the light mediator number density. This reduction can be done through a decay of the light mediator into two extra light mediator particles ($\phi \rightarrow XX$) and/or through an annihilation process of two light mediators into two extra-light mediator particles ($\phi\phi \rightarrow XX$). The simplest model we could think of along these hypothesis is to assume that the extra-light mediator is a scalar boson S (which we take here too to be real for definiteness, with an even number of them in all interactions), as following,

$$\mathcal{L} \ni -(y_\phi \phi \bar{\chi} \chi + h.c.) - \lambda_{\phi H} \phi^\dagger \phi H^\dagger H - \lambda_{\phi S} \phi^\dagger \phi S^2 - \lambda_{HS} H^\dagger H S^2, \quad (6.5)$$

with ϕ the light mediator and S the extra-light scalar into which the light mediator decays and/or annihilates. For simplicity, we assume that the DM does not directly couple to the extra-light scalar (or that this coupling is negligible) which can be justified on the basis of a symmetry. Depending on the values of the coupling between the light and the extra-light scalars, the reduction of the number density of the light one will be dominated either by its decay or its annihilation. Note that, in order to decay, the light mediator ϕ must have a VEV.

Figure 6.3 gives the allowed parameter space for this model for two choices of the extra-light scalar mass and for two opposite cases: a feeble (top panels) and a strong (bottom panels) coupling between the light and the extra-light scalars. One can see that contrary to the previous model, here the different panels are very similar. This was to be expected as for a given choice of the couple (m_{DM}, m_ϕ) , the self-interaction cross section is only a function of the DM-to-med coupling. Since this coupling is always fixed by the relic density constrained for all panels of Figure 6.3, the self-interaction cross section is the same whatever the choice of the other parameters is (i.e. m_S , $\lambda_{\phi H}$, $\lambda_{\phi S}$ and λ_{HS}).

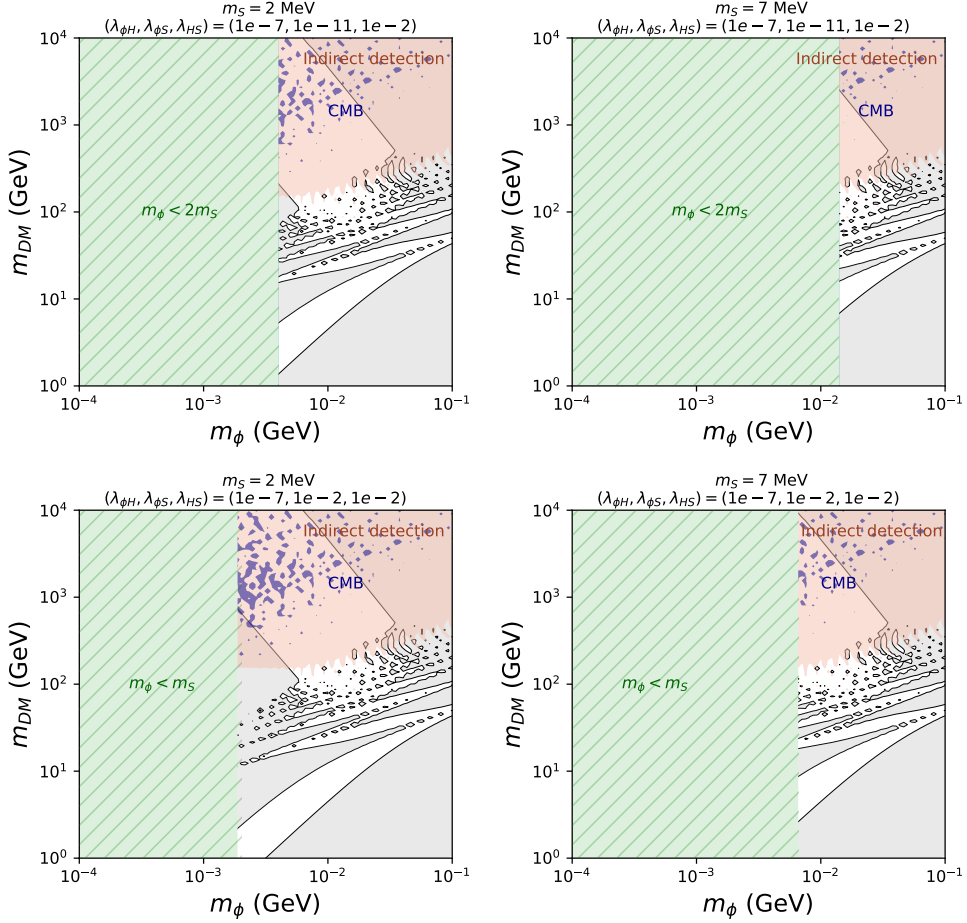


FIGURE 6.3: Constraints from CMB, BBN, self-interaction, indirect and direct detection all together for the DM p-wave annihilation into light mediators with $m_S = 2$ MeV (left) and $m_S = 7$ MeV (right), for the decaying (top panels) and the annihilating (bottom panels) regimes (see below).

6.2.1 CMB

Since the DM annihilation into a pair of scalar bosons is of the p-wave type and since the DM annihilates only into a pair of scalar bosons, the model cannot be constrained too strongly by CMB constraints on the DM annihilation cross section at recombination. However, the DM abundance is set by the freezing of the DM annihilation process into a pair of light mediator (i.e. a pair of ϕ 's) such that the DM-to-med coupling can be big and that the annihilation at recombination can still be too high in some part of the parameter space, see darkblue contour in Figure

6.3. This also explains why the CMB constraint is the same for all panels of the very same figure: it only depends on the DM-to-med interaction which is the same as explain above. This is at the opposite than in the previous model where the DM abundance were fixed by the freezing of another process. Thus, on the one hand, the DM annihilation into ϕ 's was negligible as seen in Table 6.3 and could not be constrained by the upper bound on the DM annihilation cross section at recombination (see Eq. 1.62). On the other hand, the light and the extra-light scalars (ϕ and S respectively) can both decay fast enough to have any sizable effect on the CMB. The N_{eff} constraint is also satisfied from fast enough decay of the two new scalars of the theory.

6.2.2 BBN

The BBN and N_{eff} constraints are solved in a similar way. Indeed, as said above, if the mediator ϕ has a relic density resulting from the DM annihilation into a pair of these mediators, this relic density must be decreased by the BBN time. A decay exclusively into SM particles through the Higgs portal is forbidden by direct detection (for $m_{DM} \gtrsim 1$ GeV). A decay into extra hidden sector particles solves this problem. On the one hand the $\phi \rightarrow SS$ decay can be fast enough if $\lambda_{\phi S}$ is not too small. On the other hand, the $S \rightarrow SMSM$ decay can also be fast enough, through the mixing of the extra-light and the SM scalars ($S - h$) if the coupling between these particles (i.e. λ_{HS}) is large enough. The later feature can be realised without inducing a too large Higgs boson invisible decay width. For instance, if the extra-light scalar S has a mass above the e^+e^- threshold one has the following lifetime

$$\tau_{\phi \rightarrow SS} \simeq 1s \cdot \left(\frac{m_\phi}{20 \text{ MeV}} \right) \left(\frac{2.3 \times 10^{-12}}{\lambda_{\phi S}} \right)^2 \left(\frac{500 \text{ MeV}}{v_\phi} \right)^2, \quad (6.6)$$

$$\tau_{S \rightarrow e^+e^-} \simeq 1s \cdot \left(\frac{2 \text{ MeV}}{m_S} \right) \left(\frac{7.8 \times 10^{-3}}{\lambda_{HS}} \right)^2 \left(\frac{500 \text{ MeV}}{v_S} \right)^2. \quad (6.7)$$

From these expressions, one can see that it is easy to have the two scalars to decay before BBN such that BBN do not further constrain the model. Indeed, the mixing parameter between the light and the extra-light scalars $\lambda_{\phi S}$ does not have to be large (see Eq. 6.6). However, if the light mediator VEV is very small (that is to say if $v_\phi \ll 1$ MeV), the ϕ boson becomes stable and one would need a large mixing parameter between the light and the extra-light scalars in order to deplete the abundance of ϕ 's through a two-to-two annihilation process, $\phi\phi \rightarrow SS$. We have thus here two types of solution emerging from this unique model. The solution were the light mediator abundance is depleted due to its decay into a pair of extra-light scalars and the solution were its abundance is depleted thanks to a fast annihilation

into a pair of S 's.

In both solutions, BBN constraints are easily avoided for the considered parameter space. This explains the total absence of constraint labeled as BBN in all panels of Figure 6.3.

6.2.3 Direct detection

Since the small scale structure constraints did not require any coupling between the DM and the extra-light scalar S , direct detection through DM-to- S coupling is small if this coupling is small or nonexistent. But, direct detection constraints could still be relevant for scattering of DM on nucleon through the mixing of the light mediator ϕ and the SM Higgs scalar. However, this interaction can also easily be suppressed, even if the mixing parameters $\lambda_{\phi S}$ and λ_{HS} are sizable to account for BBN. Indeed, it would only require that the transitions from light mediators ϕ 's to SM scalars H 's are suppressed enough, i.e. that the $\lambda_{\phi H}$ coupling is small enough, as well as the product of $\lambda_{\phi S}$ and λ_{HS} .

These requirements which allow us to avoid direct detection constraints are very easy to achieve in the "annihilating" solution because the mixing is suppressed by the very small VEV of ϕ . They can also be fulfilled in the "decaying" solution, but a small tension remains between direct detection and the ϕ lifetime which tends to be too long for being in agreement with BBN constraints.

6.2.4 Indirect detection

As for the previous model, even if the DM annihilation cross section is p-wave, the Sommerfeld effect can considerably increase the annihilation rate in the same way that explained above in Subsection 2.2.3. It is even more true here, as the two light scalars can participate to the Sommerfeld effect and enhance the DM annihilation cross section and lead in this model to a large indirect detection rate which can be tested (and actually rules out a large part of the parameter space). Indirect detection constraints are shown in red in Figure 6.3 and vary with the light mediator as the light mediator has to decay and/or annihilate into S 's for this model to be constrained.

6.2.5 Results

To sum up, all constraints are satisfied if both mixing parameter $\lambda_{\phi S}$ and λ_{HS} are large enough (but not too large so that their product is small enough) and $\lambda_{\phi H}$ is small enough.

m_{DM} (GeV)	m_ϕ (MeV)	m_S (MeV)	v_ϕ (MeV)	v_S (MeV)	$\lambda_{\phi H}$	$\lambda_{\phi S}$	λ_{HS}	σ_T/m_{DM} (cm ² /g)	$\frac{\kappa_{HP}}{\kappa_{HP}^{DIP}}$	τ_ϕ (sec)	τ_S (sec)	Γ_h^{inv} (MeV)	$\langle\sigma_{\phi\phi\rightarrow SSv}\rangle$ (GeV ⁻²)	$\Omega_{med}^0 h^2$
126	20	2	500	500	5.4×10^{-8}	6.2×10^{-12}	0.016	0.28	0.05	0.14	0.76	1.23	$\ll \sigma_{thermal}$	0
382	71	7	436	83	6.3×10^{-7}	3.2×10^{-11}	0.014	0.21	0.49	0.03	0.68	0.94	$\ll \sigma_{thermal}$	0
83	50	2	$\ll 1$	500	6.3×10^{-8}	0.010	0.015	0.11	$\ll 1$	$\gg 1$	0.87	1.08	2.5×10^{-5}	2.5×10^{-5}
173	300	10	$\ll 1$	50	1.0×10^{-6}	0.015	0.010	0.21	$\ll 1$	$\gg 1$	1.44	0.48	1.5×10^{-6}	4.0×10^{-4}

TABLE 6.3: Examples of parameter values which satisfy the various constraints for a model with two light scalars. κ_{HP}^{DIP} stands for the current experimental upper limit on κ_{HP} for the masses considered, see Fig. 1.30. $\Omega_{med}^0 h^2$ refers to the relic density value of the mediator today.

As previously, a couple of numerical examples which satisfy all constraints are given in the two first lines of Table 6.3. For the second example the annihilation cross section of DM into ϕ 's is of order $\langle\sigma v\rangle_{DMDM\rightarrow\phi\phi} \simeq 10^{-25} \text{ cm}^3\text{s}^{-1}$ in dwarf galaxies². As can be seen from Fig. 1.31, this can be constrained by indirect detection experiments. This is due to the fact, as discussed above (see Chapter 2), that the Sommerfeld effect brings a $\sim 1/v^3$ enhancement for p-wave processes which compensates for the v^2 suppression which appears in p-wave cross section. For further details on this setup, note that with for example the first set of couplings in Table 6.3, the S scalar thermalises with the SM thermal bath through λ_{HS} , whereas DM and ϕ thermalise through y_ϕ . Both visible and hidden sector never thermalise through the $\lambda_{\phi S}$ interaction but does so through $\lambda_{\phi H}$ until $T \simeq 35 \text{ MeV}$. Later on, the T'/T ratio does not remain equal to unity but remains close to it. For instance, at $t \simeq 1 \text{ sec}$, one has $T'/T \simeq 0.95$.

Finally and as for previous solution, we give in Table 6.4 a summary of how various constraints are evaded in this model.

6.3 Stable mediator option

As discussed in the above section, if the mediator is absolutely stable, the main constraints are the non overclosure and modification of the Hubble constant once as all other constraints above do not apply. A simple way to avoid these constraints is to consider a scenario where the hidden-to-visible temperature ratio is sizably smaller than unity, as we have done in Chapter 4, see Eq. 4.2 in particular. Instead, if one consider a HS with a temperature similar to the one of the visible sector (i.e. $T'/T \sim 1$), a more complicated possibility arises if the stable light mediator number density is reduced after its decoupling from an annihilation into extra lighter particles. This possibility would imply new constraints related to the existence of

²This cross section has to be multiplied by four in order to get the DM annihilation cross section into SM charged fermions since each of the ϕ 's will decay into two charged fermions.

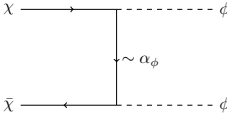
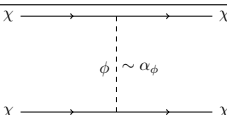
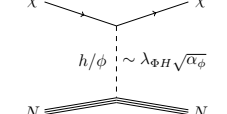
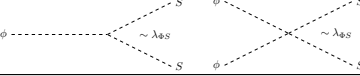
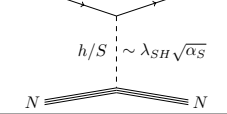
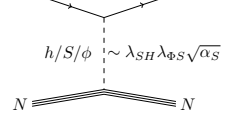
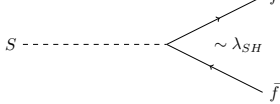
P-wave option	
Process diagram	Constraint
	<ul style="list-style-type: none"> • α_ϕ fixed by relic density • p-wave \Rightarrow small enough for CMB • small enough for indirect detection
	<ul style="list-style-type: none"> • α_ϕ large enough for small scale structure
	<ul style="list-style-type: none"> • $\lambda_{\Phi H}$ fixed by direct detection
	<ul style="list-style-type: none"> • $\lambda_{\Phi S}$ large enough to deplete ϕ
	<ul style="list-style-type: none"> • λ_{SH} fixed by direct detection
	<ul style="list-style-type: none"> • $\lambda_{\Phi S}$ fixed by direct detection
	<ul style="list-style-type: none"> • λ_{SH} fast enough for BBN

TABLE 6.4: Summary of how tensions are alleviated in the p-wave option.

this extra light particle. One finds two minimal models realising this scenario. The first one has already been proposed in [198] (see also [199]). It involves a s-wave annihilation of DM into a γ' light mediator, followed by an annihilation of this γ' into a lighter scalar S , followed by decay of this scalar S into SM particles. Omitting less relevant scalar interactions, the Lagrangian of this model is:

$$\mathcal{L} \ni -g\gamma'_\mu i\bar{\psi}\gamma^\mu\psi - g\gamma'_\mu iQ'_S(S^*\partial_\mu S - S\partial_\mu S^*) - \frac{\epsilon}{2}F_{\mu\nu}^\gamma F'^{\mu\nu} - \lambda_{HS}S^\dagger SH^\dagger H, \quad (6.8)$$

with ψ the Dirac DM candidate and S the additional extra-light scalar. The mass of the light mediator γ' comes from spontaneous breaking of the $U(1)'$ gauge symmetry once the extra-light scalar S acquires a VEV. The stability of the γ' light mediator requires here an extra (charged conjugation) symmetry, in order that a kinetic mixing between the γ' and the hypercharge gauge boson is forbidden. A nice feature of this model is that the extra-light scalar S is the one one has anyway to introduce in the model if one assumes that the $U(1)'$ symmetry is spontaneously broken through the Brout-Englert-Higgs mechanism. The other minimal model where this turns out to be possible is nothing but the model of the previous section of Eq. 6.5, in other regions of the parameter space as already discussed, assuming in particular now that the scalar mediator ϕ has no VEV, so that it doesn't decay.

The phenomenology of the model described by the Lagrangian given in Eq. 6.8 has been analysed in detail in [198]. Once the non-overclosure constraint is satisfied for the light mediator γ' , from annihilation of this light mediator into a pair of extra-light scalars S , $\gamma'\gamma' \rightarrow SS$, one is left essentially with constraints on the extra-light particles, the S 's. On the one hand the mass of this extra particle must be larger than twice the electron mass $m_S > 2m_e$, otherwise its decay is loop suppressed and therefore too slow for CMB or BBN constraints to be satisfied. On the other hand, its mass must be below the 4.4 MeV threshold to avoid the BBN photodisintegration constraint. The N_{eff} , the Hubble constant and the entropy injection constraints are just enough satisfied from the fact that when the two mediators (S and γ') decouple, the hidden-to-visible temperature ratio T'/T (which is equal to unity at DM decoupling) is already not anymore equal to unity, but slightly smaller (from decoupling of SM particles in between). The CMB constraint on the DM annihilation cross section given in Eq 1.62 does not apply for DM annihilation into a pair of light mediator $DMDM \rightarrow \gamma'\gamma'$ because the γ' is stable but applies for the $DMDM \rightarrow \gamma'S$ scattering, as well as for $\gamma'\gamma' \rightarrow SS$ scattering since it is the S 's particles which are connected to the SM. For the last scattering it is easily satisfied since this scattering is not enhanced by the Sommerfeld effect. For the former scattering, this constraint still leaves an allowed parameter space. Direct detection is satisfied from the fact

that DM communicates with SM particles only through a $\text{DM}-\gamma'-S\text{-SM}$ chain.

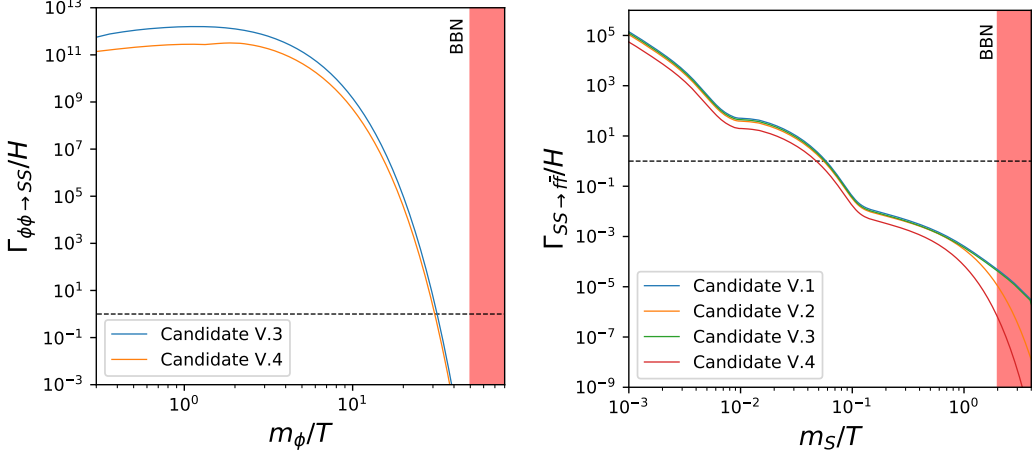


FIGURE 6.4: Left: Evolution of the annihilation rate of a pair of ϕ 's into a pair of S 's, normalised to the Hubble rate for the last two candidates of Table 6.3. The black dashed line represents the thermalisation line, ie: when $\Gamma_{\phi\phi \rightarrow SS} = H$. Right: Evolution of the annihilation rate of a pair of S 's into a pair of SM fermions normalised to the Hubble rate for all candidates of Table 6.3. The black dashed line represents the thermalisation line, ie: when $\Gamma_{SS \rightarrow f\bar{f}} = H$. One can also see when BBN starts in red in both plots.

As for the model of the previous section with a stable scalar mediator ϕ , Eq. 6.5, it can be successful in a perhaps less squeezed way. The first constraint it has to fulfill is that the annihilation process into a pair of extra-light scalars $\phi\phi \rightarrow SS$, which must be in thermal equilibrium at temperature of order $T \sim m_\phi$, such that the ϕ number density is later on Boltzmann suppressed. This will be the case for model described by Eq. 6.5 in another parameter regime than for the decay option of Section 6.2. As already mentioned above, one has to assume much larger values of the mixing between the two scalars $\lambda_{\phi S}$ than above in the decay option (i.e. for instance $\lambda_{\phi S} > \lambda_{\phi S}^{th} \simeq 6 \times 10^{-9}$ for $m_{\text{med}} = 30$ MeV). Note that S can annihilate into a pair of SM particles through the Higgs portal, but these $SS \rightarrow f\bar{f}$ annihilation processes decouple before the $\phi\phi \rightarrow SS$ process. The latter process decouples when $m_\phi/T \sim 30$. This is shown in Figure 6.4 for two examples sets of parameters which satisfy all constraints and are given in Table 6.3. Thus, for these two examples (where $m_\phi/m_S \lesssim 30$), the S scalar is a hot relic and its number density is not Boltzmann suppressed. Now, we are going to see how the various constraints are fulfilled which would make this stable mediator scenario easily viable.

6.3.1 Non-overclosure

The light mediator annihilation process into a pair of extra-light scalars (i.e. the $\phi\phi \rightarrow SS$ scattering through $\lambda_{\phi S}$ coupling of Eq. 6.8) is fast enough in order to reduce the population of stable light mediator ϕ and to avoid the Universe to over-close. There is then no reduction of the parameter space coming from this constraint.

6.3.2 CMB

The DM annihilation into a pair of light mediators does not cause any large CMB distortion because the mediator is a scalar such that the annihilation is of p-wave type (see Eq. 1.62). Moreover, the light mediator annihilation process, from $\lambda_{\phi S}$ coupling, into a pair of extra-light scalars also reduces enough the light mediator population to fulfill the related N_{eff} constraint. Finally, the decay of the extra-light scalar S is fast enough to satisfy the N_{eff} constraint associated to its decay.

6.3.3 BBN

The decay rate of the extra-light particle S decay, from λ_{HS} coupling, is also fast enough to satisfy BBN Hubble constant and entropy injection constraints altogether with photodisintegration constraints. This requires to take a large enough mixing parameter between the extra-light scalar and the SM scalar boson λ_{HS} , see Eq. 6.7. All this can be realised without inducing a too large Higgs boson invisible decay width.

6.3.4 Direct detection

As in Section 6.2, the self-interaction constraints require a sizable DM-to-med coupling but does not require any connection between the DM and the extra-light scalar S . Thus, direct detection through DM-to- S coupling is small if the corresponding coupling, $\bar{\psi}\psi S$, is small or is irrelevant (i.e. if there is no coupling at all between these two particles). Moreover, the DM cannot scatter on nucleon at tree level through the DM-to-med coupling because the light mediator has no VEV.

6.3.5 Indirect detection

If the ϕ has no VEV and is stable, the annihilation of DM into ϕ does not produce any SM particles and DM annihilation produce SM particles only at the loop level. There is thus basically no relevant constraint coming from indirect detection experiments.

6.4 The neutrino option

If one does not introduce any other extra particle on top of the DM and the light mediator particles, the only possibility³ for the light mediator to not spoil BBN observations while decaying is that it decays into neutrinos. For the decay to proceed into neutrinos exclusively without producing any electron/positron pairs, there are two simple possibilities. One needs either an *electronphobic* light mediator such that it does not couple to the electron lepton doublet and that the decay proceeds only into muon or tau neutrinos, or that the mediator is lighter than twice the electron mass. With a light scalar mediator it is not easy to have a dominant and fast enough decay into neutrinos. As for the vector light mediator option (i.e. the γ' option), the possible portals which can make the vector mediator to decay into neutrinos are the kinetic mixing portal or the so-called "mass mixing portal". As already mentioned above, through kinetic mixing, and below the e^+e^- threshold, the γ' decays dominantly to three photons at a rate far too slow to proceed before BBN and even slower to neutrinos. Through the more involved mass mixing scenario, the decay can dominantly proceed into neutrinos at a rate fast enough to decay before the BBN occurs. The relevant interactions of the "mass mixing portal" are therefore

$$\mathcal{L} \ni -g\gamma'_\mu J_{\text{DM}}^\mu - \delta m^2 \gamma'_\mu Z_\mu, \quad (6.9)$$

where $J_{\text{DM}}^\mu = \bar{\psi}\gamma^\mu\psi$, $J_{\text{DM}}^\mu = \bar{\chi}\gamma^\mu\gamma^5\chi$ and $J_{\text{DM}}^\mu = i(S^*\partial_\mu S - S\partial_\mu S^*)$ for a Dirac, Majorana and scalar DM particle respectively. This model for the Dirac DM case has already been considered in Appendix B of [123], as a way out to the CMB constraints above summarised by Eq. 1.62, see the various constraints holding on it in Figure 4 of this reference.

The kinetic mixing option does not allow the light mediator to decay into muon and/or tau neutrinos without producing electron neutrinos as well. However, the production of electron neutrinos can be avoided in models with an extra $U(1)'$ gauge symmetry, along which the corresponding gauge boson Z' couples only to μ and τ flavours, as well as to DM. The most straightforward possibility is to assume a $L_\mu - L_\tau$ flavour symmetry so that gauge anomalies cancel,

$$\mathcal{L} \ni -\frac{1}{4}F'_{\mu\nu}F'^{\mu\nu} - ig' \sum_i Q'_i \bar{\psi}_i \gamma^\mu Z'_\mu \psi_i + ig' Q'_{\text{DM}} \bar{\chi} \gamma^\mu \chi Z'_\mu, \quad (6.10)$$

where the sum is over the muon and tau left-handed doublets, as well as over the muon and tau right-handed singlets (with $Q' = 1$ for muon spinors and $Q' = -1$ for

³Except for the $T'/T \neq 1$ solution discussed in Chapter 4.

tau spinors). Here, for definiteness, χ is taken to be a Dirac fermion, but in principle the DM candidate could also be a scalar boson charged under the $U(1)'$. The gauge part of this model has been considered in many different contexts (see [200]–[203]), including as a possibility of explanation for the $(g - 2)_\mu$ anomaly, [204]–[207]. This requires a Z' with mass 10-100 MeV and $g' \sim 5 \times 10^{-4}$. With the adjunction of a DM particle, as in Eq. 6.10, it has also been considered for various purposes [208]–[210]. In [210] it has been noted that the values of $m_{Z'}$ and g' which fit well the $(g - 2)_\mu$ anomaly, see above, can also lead to DM self-interactions with $\sigma_T/m_{\text{DM}} \sim 1\text{cm}^2/\text{g}$ (once Q'_{DM} has been fixed for the annihilation of DM into leptons to have the thermal value). Here we would like to point out that this model turns out to be good also to avoid the CMB and BBN constraints above. In particular, as already said, a decay of the light mediator into muon and/or tau neutrinos allow to avoid the CMB constraint of Eq. 1.62. The other CMB and the BBN constraints are avoided in a way similar to the way the first model we considered (see vector portal model of Chapter 4) avoids these constraints above (for $T'/T = 1$). Note that all this has been analyzed in [211] in the framework of a model where, on top of the interactions of Eq. 6.10, the scalar whose vev breaks spontaneously the $U(1)_{L_\mu - L_\tau}$ gauge symmetry is considered explicitly, assuming in addition that this scalar has Yukawa interactions with DM, so that for self-interactions the light mediator is this extra scalar, rather than the Z' .

6.5 The asymmetric dark matter option

So far we have assumed everywhere that there is an equal number of DM particles and antiparticles. If instead we assume that DM is asymmetric, some of the constraints will change drastically. This possibility has been considered in [212] in the context of a model where a dark proton and a dark electron couple to a dark photon. On the one hand, all constraints related to DM annihilation are trivially removed, since DM does not annihilate anymore. This concerns in particular the CMB constraint of Eq. 1.62 and the indirect detection constraints. On the other hand, the constraints on the number of mediators and on its decay remain. In an asymmetric setup, still, DM thermalises with the light mediator at $T \gtrsim m_{\text{DM}}$, and the resulting important symmetric DM component must be suppressed afterwards through an annihilation catastrophe. This annihilation catastrophe leaves the mediator as a hot relic, so one is left with as many light mediator as in the symmetric case. Thus, if the mediator is stable, the non-overclosure constraint remains fully relevant. Similarly, for an unstable mediator, remain relevant the N_{eff} and mediator decay CMB constraints above, as well as the Hubble constant and entropy injection and photodisintegration BBN constraints, as well as direct detection constraints. In Refs. [130], [212], authors have not considered in details the N_{eff} CMB constraint,

as well as Hubble constant and entropy injection BBN constraints. However, as already said above, if for the minimal vector model of Chapter 4 (and similarly for the more involved vector model of Ref. [212]), one removes the CMB constraint given in Eq. 1.62, a proper incorporation of these constraints leaves allowed a relatively wide region of parameter space. However, for the scalar mediator model, to assume an asymmetric setup instead of a symmetric one does not change much the picture because in this model this CMB constraint was already avoided (from the fact that the annihilation is p-wave). In particular the strong tension between direct detection and BBN constraints remains.

Summary and outlooks

Along this thesis we have studied various aspects, and put forward several possible new properties, of models where the DM belongs to a HS that may be connected to the SM sector through portal interactions. These new properties and scenarios concern in particular the way models of this type can account for the DM relic abundance observed today in the Universe and/or the way they could allow large DM self-interactions. We have started by presenting the many relevant constraints which apply to scenarios where the large self-interactions needed to account for the small scale anomalies result from the exchange of a light mediator. To do so, we presented two very well known portal models which are the Higgs portal and the kinetic mixing portal models. Both of them have been used in this work as representatives of scalar and vector portal models respectively. The global study we have performed for these two portal models is also representative of what would happen in other portal-like models. At the end of the first chapter, it appeared that self-interacting DM models with light mediator are strongly constrained from three types of constraints which are in tensions with each other [84], [85]. First, to alleviate small scale structure constraints, one requires a relatively strong connection between the DM and the light mediator. Second, cosmological and astrophysical observations suggest a short lifetime for the light mediator and thus a strong connection between the light mediator and SM particles. Third, particle physics experiments which try to detect or produce DM (or light mediator particles) have still not found any prove of the existence of such particles. This non-observation indicates that the DM should be not so strongly connected to the SM.

The second chapter introduced in detail the so-called Sommerfeld effect and its consequences on DM portal models. This effect is at the origin of the enhancement of the DM self-interaction in presence of a light mediator and to look at it in more details, as we did in this chapter, allowed us to see how one could take advantage of this effect in order to reduce the tensions discussed in Chapter 1. In particular, we have shown (as a first main result) that the Sommerfeld enhancement can still be largely operative for a DM-to-med coupling quite smaller than the ones that we considered in Chapter 1, [85]. This will be used later in Chapters 5 and 6 to build simple SIDM frameworks that account for all constraints. In this chapter 2, we also stressed the fact that the Sommerfeld effect is important for the annihilation of DM

particles in various contexts, at the time of the recombination (constrained by CMB data), as well as for production of cosmic rays today in the MW galactic centre or in DG (constrained by indirect detection). We showed here, in particular, that contrary to common belief, a DM p-wave annihilation could lead to observable signals in indirect detection experiments thanks to the Sommerfeld effect in the case of a large DM-to-med coupling, [85]. This second main result will also be used in Chapter 6 to constraints models discussed within.

The third chapter was dedicated to the way one could account for the amount of DM observed in the Universe in HS models. In these models, the HS does not contain the DM particles only, but it also contains other particles with which the DM can interact. Thus, in this chapter, we studied models containing, in full generality, three reservoirs (SM, DM and extra HS particles) with potentially three connections between them. The scalar and vector portal models considered in Chapter 1 are perfect prototype models of this kind. Thus, to study how we account for the DM relic density in these models, as we did in Chapter 3, is interesting in itself as it studies a generic situation. It is also fully relevant for SIDM models based on a light mediator since these models have generically the very same three sector-three connections structure. We have then shown, as a third result, that with such a structure the DM relic abundance can be produced through no less than five distinct mechanisms which are the freeze-in, the sequential freeze-in (which is new), the reannihilation, the secluded freeze-out and finally the freeze-out [177], [178]. Four of those production mechanisms have two different realisations depending on if the DM is dominantly connected to the mediator or SM particles. This makes nine regimes among which four are new and for five of the nine regimes the DM is feebly connected to the SM.

In Chapter 4, we looked in more details at the possibility that the DM relic density stems from a freeze-out in the HS which would occur when a possible portal between the HS and the VS has ceased to have any sizeable effect. This was already the case of one of the DM production mechanism that we saw in Chapter 3, the so-called secluded FO regime. Here, we developed more this possibility which holds also in general for models where there would be no connection at all between both the visible and hidden sectors, but where both sectors would be already there at the end of inflation. The purpose of this chapter was to determine, in a model independent way (i.e. beyond the two benchmark portal models) what is the domain of all DM thermal candidate. This domain stems from the two possibilities of FO that can hold in this case, the non-relativistic secluded FO and the relativistic secluded FO. The latter which is extremely simple and leads to a relic density which does not depend on the annihilation cross section, but only on the DM mass and on the hidden-to-visible temperature ratio, had, as mentioned above, strangely

not be considered in any published paper before, which makes its study our fourth result and the general study of the domain to be our fifth result [186], [187]. The full $m_{\text{DM}} - T'/T$ domain of possibilities we presented is bounded from below (for T'/T) by the "relativistic floor" (i.e. the relativistic FO case), from above (for T'/T) by the "unitarity wall" and the " N_{eff} ceiling", from below (for m_{DM}) by the generalisation of the Cowsik-McClelland bound and from above (for m_{DM}) by generalisation of the Griest-Kamionkowski bound.

From all these discussions in Chapters 1 to 4, in Chapter 5 we come back to the problematic of conciliating all constraints that apply to the SIDM scenarios with light mediator. This necessarily requires to relax one of the assumptions made in Chapter 1. In this chapter, we considered what is probably the simplest possibility. This is to say that this possibility does not require to enlarge the Lagrangian of the two benchmark models with any extra new field. It only requires to give up the assumption that the HS is thermally connected to the SM thermal bath, just as we considered already in Chapters 3 and 4 for the DM relic density issue. So, we argue that this solution is minimal because it does not require any additional degree of freedom and moreover it is natural because it is what observations suggest: feebly coupled to the VS and strongly self-interacting. Indeed, we have seen that if the mixing parameter (the SM-to-med coupling) lies below the thermalisation threshold, such portal models can easily satisfy the DM relic abundance constraint, and avoid all kinds of other constraints still alleviating the tensions at small scale. We found, as a sixth result, that all free parameters can live in ranges of several orders of magnitude without difficulties which makes this solution totally viable and really interesting [85].

In chapter 6, other minimal solutions to the SIDM tensions have been studied at length. The general idea behind such scenarios is either to deplete the light mediator abundance prior to BBN by decay or further annihilations into lighter particles or to decrease its impact on the BBN and/or CMB using p-wave processes or neutrinos particles in the final state. These solutions are less minimal as they require extra degrees of freedom and in most cases their allowed parameter space is more squeezed, but remain simple solutions to the SIDM issue and constitute the final result of this thesis [85].

The several aspects and new properties/scenarios of setups based on a VS-HS portal structure discussed here could be further studied in many ways, along several new avenues. Through this thesis, we have studied many aspects of self-interacting DM models with light mediator, from production mechanisms, to experimental constraints passing by a theoretical model building phase. A simple thermalised HS brings a lot of new and open questions. One could worry about

what happens in more details in the transition regime between the relativistic and non-relativistic DM decoupling cases, close to the relativistic floor. One could also study further the fate of the light mediator in the hotter HS scenario. We hope that these works, and many others, could, step by step, ultimately lead to the elucidation of the fundamental question of what DM is made of, in terms of particles.

Part IV

Appendices

Appendix A

Cross sections

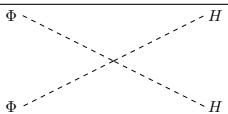
In this first appendix, we give all relevant cross sections we may used in this thesis, for both the scalar and vector portal models.

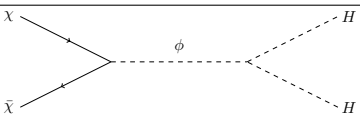
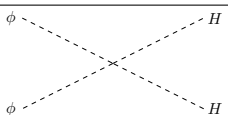
A.1 Higgs portal

The scalar portal model detailed in Subsection 1.3.4 is described by the following Lagrangian,

$$\begin{aligned} \mathcal{L} = \mathcal{L}_{SM} + i\bar{\chi}\not{D}\chi - m_{DM}\bar{\chi}\chi + Y_{\chi}\Phi\bar{\chi}\chi - \mu_{\Phi}^2\Phi^2 + \lambda_{\Phi}\Phi^4 - \mu_H^2H^{\dagger}H \\ + \lambda_H\left(H^{\dagger}H\right)^2 + \lambda_3\Phi H^{\dagger}H + \lambda_{\Phi H}\Phi^2H^{\dagger}H, \end{aligned} \quad (\text{A.1})$$

such that relevant processes in the symmetric, semi-symmetric and broken phases are as given in the following tables.

$T_{EW} < T_{\Phi} < m_{DM}$ (fully symmetric phase): $v_{\Phi} = 0 = v_H$	
Process	Cross section
	$\frac{\lambda_{\Phi H}^2}{\pi s}$

$T_{EW} < m_{DM} < T_{\Phi}$ (semi-symmetric phase): $v_{\Phi} \neq 0 = v_H$	
Process	Cross section
	$\frac{\lambda^2 v_{\Phi}^2 Y_{\chi}^2}{64\pi s^2} \left(1 - \frac{4m_{DM}^2}{s}\right)^{3/2}$
	$\frac{\lambda_{\Phi H}^2}{4\pi s} \frac{1}{\sqrt{1 - 4\frac{m_{\Phi}^2}{s}}}$

$m_{\text{DM}} < T_{EW} < T_{\Phi}$ (broken phase): $v_{\Phi} \neq 0 \neq v_H$	
Process	Cross section
	$N_c \frac{\kappa^2}{8\pi s^3} \left(m_f^2 m_h^2 \right) \frac{\sqrt{1 - \frac{4m_f^2}{s} \left(1 - \frac{4m_{\text{DM}}^2}{s} \right)}}{\left(1 - \frac{m_h^2}{s} \right)^2 + \frac{\Gamma_h^2 m_h^2}{s^2}}^{3/2}$
	$\frac{\kappa^2}{32\pi s^4} \left(\frac{m_h^8}{v_H^2} \right) \frac{\sqrt{1 - \frac{4m_h^2}{s} \left(1 - \frac{4m_{\text{DM}}^2}{s} \right)}}{\left(1 - \frac{m_h^2}{s} \right)^2 + \frac{\Gamma_h^2 m_h^2}{s^2}}^{3/2}$
	$\frac{\kappa^2}{288\pi s^2} \left(\frac{g^2}{m_Z^2 c_w^2} \right) \frac{\sqrt{1 - \frac{4m_Z^2}{s} \left(1 - \frac{4m_{\text{DM}}^2}{s} \right)}}{\left(1 - \frac{m_h^2}{s} \right)^2 + \frac{\Gamma_h^2 m_h^2}{s^2}}^{3/2} \times \left(1 - 4 \frac{m_Z^2}{s} + 12 \frac{m_Z^4}{s^2} \right)$
	$\frac{\kappa^2}{288\pi s^2} \left(\frac{g^2}{m_W^2} \right) \frac{\sqrt{1 - \frac{4m_W^2}{s} \left(1 - \frac{4m_{\text{DM}}^2}{s} \right)}}{\left(1 - \frac{m_h^2}{s} \right)^2 + \frac{\Gamma_h^2 m_h^2}{s^2}}^{3/2} \times \left(1 - 4 \frac{m_W^2}{s} + 12 \frac{m_W^4}{s^2} \right)$
	$\frac{\kappa^2}{8\pi} m_h \left(1 - \frac{4m_{\text{DM}}^2}{m_h^2} \right)^{3/2}$
	$\frac{\sin^2(2\beta_{\Phi H})}{32\pi} \frac{m_h^2}{v_{\Phi}} \sqrt{1 - \frac{4m_{\phi}^2}{m_h^2}} \left(1 - \frac{m_{\phi}^2}{m_h^2} \right)^2$
	$\frac{Y_f^2 \sin^2(\beta_{\Phi H})}{16\pi} m_{\phi} \left(1 - \frac{4m_f^2}{m_{\phi}^2} \right)^{3/2}$
	$\frac{Y_{\chi}^4}{2\pi s} \left[\left(1 + 16 \frac{m_{\text{DM}}^2}{s} - 32 \frac{m_{\text{DM}}^4}{s^2} \right) \tanh^{-1} \sqrt{1 - \frac{4m_{\text{DM}}^2}{s}} - \left(1 + 8 \frac{m_{\text{DM}}^2}{s} \right) \sqrt{1 - 4 \frac{m_{\text{DM}}^2}{s}} \right]$
	$\frac{\lambda_{\Phi H}^2}{16\pi s} \frac{\sqrt{1 - 4 \frac{m_h^2}{s}}}{\sqrt{1 - 4 \frac{m_{\phi}^2}{s}}}$

A.2 Kinetic mixing

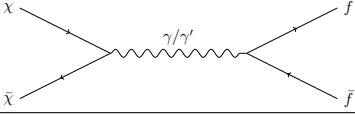
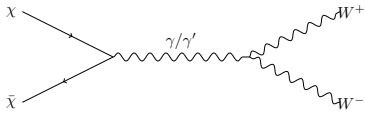
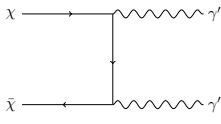
The vector portal model detailed in Subsection 1.3.4 is described by the following Lagrangian,

$$\mathcal{L} \subset -\frac{1}{4}B'^{\mu\nu}B'_{\mu\nu} + \frac{1}{2}m_{\gamma'}^2 B'^{\mu}B'_{\mu} - \hat{e} m_{\gamma'}^2 B'^{\mu}B'_{\mu} - e' \bar{\chi} \gamma^{\mu} \chi (B'_{\mu} - \hat{e} B_{\mu}), \quad (\text{A.2})$$

such that relevant processes are as given in the following table for the massive dark photon case:

Process	Cross section
	$16\pi N_c \frac{\alpha^2 \kappa^2}{s} \frac{\left(1 - \frac{2m_f^2}{s}\right) \left(1 - \frac{2m_{\text{DM}}^2}{s}\right)}{\left(1 - \frac{m_{\gamma'}^2}{s}\right)^2 + \frac{\Gamma_{\gamma'}^2 m_{\gamma'}^2}{s^2}} \sqrt{\frac{1 - \frac{4m_f^2}{s}}{1 - \frac{4m_{\text{DM}}^2}{s}}}$
	$\frac{\pi \alpha^2 \kappa^2 s}{m_W^4} \left(1 - 4\frac{m_W^2}{s} + 12\frac{m_W^4}{s^2}\right) \left(1 - \frac{m_{\text{DM}}^2}{s} - 6\frac{m_W^4}{s^2}\right) + 2\frac{m_W^2}{s} \left(1 - 4\frac{m_{\text{DM}}^2}{s}\right) \sqrt{\frac{1 - \frac{4m_W^2}{s}}{1 - \frac{4m_{\text{DM}}^2}{s}}}$
	$N_c \cos^2 \theta_W Q^2 \frac{\alpha \epsilon^2}{3} m_{\gamma'} \left(1 - \frac{4m_f^2}{m_{\gamma'}^2}\right)^{1/2}$
	$\frac{32\pi \alpha'^2}{s \left(1 - \frac{4m_{\text{DM}}^2}{s}\right)} \left[\left(1 - 8\frac{m_{\text{DM}}^2}{s}\right) \tanh^{-1} \sqrt{1 - 4\frac{m_{\text{DM}}^2}{s}} + \frac{m_{\text{DM}}^2}{s} \sqrt{1 - 4\frac{m_{\text{DM}}^2}{s}} \right]$
	$\frac{32\pi \alpha^2 \epsilon^2}{s \left(1 - \frac{4m_f^2}{s}\right)} \left[\left(1 - 8\frac{m_f^2}{s}\right) \tanh^{-1} \sqrt{1 - 4\frac{m_f^2}{s}} + \frac{m_f^2}{s} \sqrt{1 - 4\frac{m_f^2}{s}} \right]$
	$\frac{4\pi \alpha^2 \epsilon^2}{s} \frac{\left(1 + \frac{m_f^2}{s}\right) \left(1 - 5\frac{m_f^2}{s} + 2\frac{m_f^4}{s^2}\right)}{1 - \frac{m_f^2}{s}}$

In the case of a massless dark photon, one has instead:

Process	Cross section
	$16\pi N_c \frac{\alpha^2 \kappa^2}{s} \left(1 - \frac{2m_f^2}{s}\right) \left(1 - \frac{2m_{DM}^2}{s}\right) \sqrt{\frac{1 - \frac{4m_f^2}{s}}{1 - \frac{4m_{DM}^2}{s}}}$
	$\frac{\pi \alpha^2 \kappa^2 s}{m_W^4} \left(1 - 4\frac{m_W^2}{s} + 12\frac{m_W^4}{s^2}\right) \left(1 - \frac{m_{DM}^2}{s} - 6\frac{m_W^4}{s^2} + 2\frac{m_W^2}{s} \left(1 - 4\frac{m_{DM}^2}{s}\right)\right) \sqrt{\frac{1 - \frac{4m_W^2}{s}}{1 - \frac{4m_{DM}^2}{s}}}$
	$\frac{32\pi \alpha'^2}{s \left(1 - \frac{4m_{DM}^2}{s}\right)} \left[\left(1 - 8\frac{m_{DM}^2}{s}\right) \tanh^{-1} \sqrt{1 - 4\frac{m_{DM}^2}{s}} + \frac{m_{DM}^2}{s} \sqrt{1 - 4\frac{m_{DM}^2}{s}} \right]$

Appendix B

Thermal effects

For comprehensiveness and completeness we will review in this appendix the main features of the dark photon production rate, extensively studied in e.g. [106]–[111].

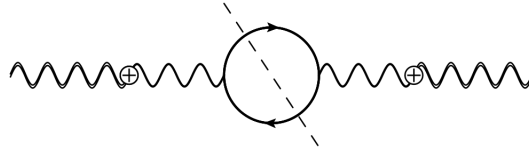


FIGURE B.1: The imaginary part of the dark photon propagator (double wiggly lines) in a medium includes both its decay rate and creation rates.

As we did in Chapter 3, we will treat the kinetic mixing as a perturbation and we will work in the interaction basis. Thus, in such a framework, the dark photon self-energy of Figure B.1 captures thermal effects through those of the photons. We have,

$$\Pi_{\gamma'} = m_{\gamma'}^2 + \frac{\epsilon^2 m_{\gamma'}^4}{(K^2 - \Pi_{\gamma})}, \quad (\text{B.1})$$

where the momentum of the virtual dark photon K is given by $K^2 \equiv \omega^2 - k^2$. The imaginary part of the dark photon propagator is given by,

$$\text{Im } \Pi_{\gamma'} = \frac{\epsilon^2 m_{\gamma'}^4 \text{Im } \Pi_{\gamma}}{(m_{\gamma'}^2 - \text{Re } \Pi_{\gamma})^2 + \text{Im } \Pi_{\gamma}^2}, \quad (\text{B.2})$$

where we used $K^2 = m_{\gamma'}^2$. This corresponds to a virtual photon which mixes into a dark photon on mass-shell. In vacuum, the imaginary part of the photon propagator $\text{Im } \Pi_{\gamma}$ is related to possible photon decay channels, but within a thermal bath, the

imaginary part of the photon propagator also gets contributions from the emission and the absorption rates of photons from the medium. Γ is the rate that rules the thermal equilibrium condition,

$$f(\omega, t) - f_{\text{eq}} \propto \exp(-\Gamma t), \quad (\text{B.3})$$

with f the distribution function of dark photons.

$$\text{Im } \Pi_\gamma = -\omega \Gamma_\gamma = -\omega(\Gamma_{\gamma, \text{em}} - \Gamma_{\gamma, \text{abs}}), \quad (\text{B.4})$$

where the minus sign between the rates of emission and of absorption stems for Bose-Einstein statistics while for Fermi-Dirac statistics one has [183],

$$\text{Im } \Pi_\gamma = -\omega \Gamma_\gamma = -\omega(\Gamma_{\gamma, \text{em}} + \Gamma_{\gamma, \text{abs}}). \quad (\text{B.5})$$

Due to unitarity [213], it is known that the amplitude squares for the emission and absorption process are equal. However, the emission rate of a photon of energy ω is Boltzmann suppressed compared to its corresponding absorption rate,

$$\Gamma_{\text{em}} = \exp(-\omega/T) \Gamma_{\text{abs}}, \quad (\text{B.6})$$

such that one can write

$$\Gamma_{\gamma', \text{em}} = \frac{\epsilon^2 m_{\gamma'}^4 \Gamma_{\gamma, \text{em}}}{(m_{\gamma'}^2 - \text{Re } \Pi_\gamma)^2 + \omega^2 (e^{\omega/T} - 1)^2 \Gamma_{\gamma, \text{em}}^2}. \quad (\text{B.7})$$

At finite temperature, the medium can also support the propagation of longitudinal modes or plasmon waves on top of transverse modes. These new modes describe the oscillations of charged particles which are contained in the thermal bath. Thus, one should definitively make the distinction between transverse (labeled with a T subscript) and longitudinal (labeled with a L subscript) self-energy such as emission and absorption rates, $(\Gamma, \Pi) \rightarrow (\Gamma_{T,L}, \Pi_{T,L})$ [109]. The simplest of the two is the transverse mode as transverse photons simply get a thermal mass with a small momentum dependence. In the relativistic regime and to leading order in the electroweak fine structure constant α , we have

$$\text{Re } \Pi_{\gamma, T} = \begin{cases} \omega_p^2 = \sum_i q_i^2 T^2 / 9 & \text{low } k \\ 3/2 \omega_p^2 & \text{large } k \end{cases}, \quad (\text{B.8})$$

where ω_p is the so-called plasma frequency and the sum is over relativistic charged particles [185].

The longitudinal mode of the photon self-energy is more complicated due to the fact that longitudinal photons do not propagate in vacuum. Staying in the relativistic regime and at leading order in the electroweak fine structure constant α , the photon self-energy takes the form [185]

$$\Pi_L(\omega, k) = 3\omega_p^2 \frac{K^2}{k^2} \left(\frac{\omega}{2k} \log \left(\frac{\omega + k}{\omega - k} \right) - 1 \right), \quad (\text{B.9})$$

where we used the definition of the longitudinal polarisation tensor given in [109], [110]: $\Pi_L \equiv \Pi_L^{\text{APP}}$, which differs from that of [185], $\Pi_L^{\text{BS}} = K^2/k^2 \Pi_L^{\text{APP}}$. One can thus solve for $\omega_L^2 - k^2 = \text{Re } \Pi_L(\omega_L(k), k)$ which leads to

$$\text{Re } \Pi_{\gamma, L} = \begin{cases} \omega_p^2 K^2 / \omega^2 & k \sim 0 \\ \sim 0 & k \gtrsim \omega_p \end{cases}. \quad (\text{B.10})$$

The behaviours of the dispersion relations of the transverse (solid blue) and longitudinal (solid orange) modes as functions of the momentum k are shown in Figure B.2.

One can write for a longitudinal plasmon mode close to be on-shell (i.e. having $\omega \sim \omega_L$, $\text{Re } \Pi_{\gamma, L} \approx \omega_L^2 K^2 / \omega^2$) [109], [110], [185],

$$\frac{1}{K^2 - \Pi_L} \approx \frac{\omega^2 Z_L}{K^2(\omega^2 - \omega_L^2) - iZ_L \omega^2 \text{Im } \Pi_L}, \quad (\text{B.11})$$

where, using Eq. B.9, the wave-function normalisation Z_L is given by

$$Z_L^{-1} = 1 + \frac{k^2}{\omega_L} \frac{3\omega_p^2 - \omega_L^2 + k^2}{2(\omega_L^2 - k^2)}, \quad (\text{B.12})$$

which satisfies $Z_L \rightarrow 1$ as $k \rightarrow 0$ but tends to zero for $k \gtrsim \omega_p$, as one can see from the green solid line in Figure B.2. Note that, we considered the real part of the self-energy only at leading order in the electroweak fine structure constant α , but the imaginary part $\text{Im } \Pi_L$ may include higher order corrections in α (Compton emission, etc.). The fact that Z_L goes to zero when $k \gtrsim \omega_p$ reflects the fact that the longitudinal mode mostly exists for moderate momenta. From this and from Eq. B.7 we get

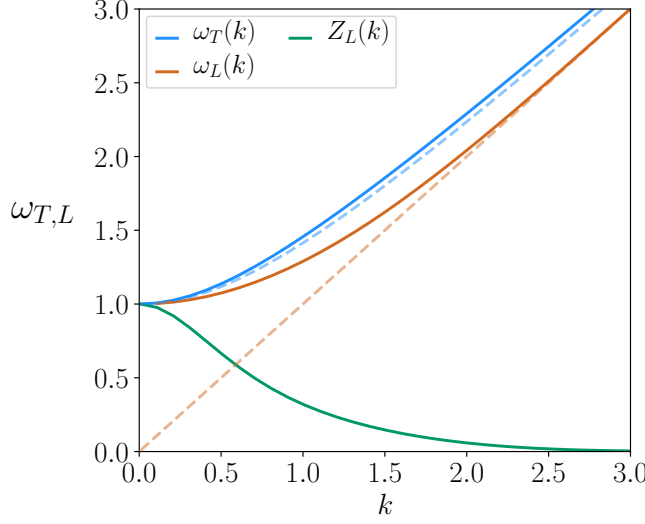


FIGURE B.2: Dispersion relations for $\omega_T(k)$ (blue solid) and $\omega_L(k)$ (orange solid) in the relativistic regime $T \ll m_e$. They are normalised to $\omega_p = 1$. The dashed orange line is the dispersion relation of a standard massive particle. The dispersion relation of the transverse mode has $\omega_T = \omega_p$ for small k and $\omega_T \approx \sqrt{3/2\omega_p^2 + k^2}$ for large k . That of the longitudinal mode has $\omega_L = \omega_p$ for small k but asymptotically to $\omega_L \approx k$ for large k . Also shown is the wave-function normalisation Z_L (green solid) which goes to zero at large k , revealing that the longitudinal mode propagates only for small enough momenta.

$$\Gamma_{\gamma',\text{em}}^L = \frac{\epsilon^2 m_{\gamma'}^4 \tilde{Z}_L^2 \Gamma_{\gamma,\text{em}}^L}{(\omega^2 - \omega_L^2)^2 + \omega^2 (e^{\omega/T} - 1)^2 (\tilde{Z}_L \Gamma_{\gamma,\text{em}}^L)^2}, \quad (\text{B.13})$$

with $\tilde{Z}_L = \omega^2 / m_{\gamma'}^2 Z_L$. Expression given in Eq. B.13 agrees with the literature [109], [110], [214]. However, it may be compared with Eq. 2.7 of [110] using the fact that in Eq. B.13 the longitudinal photon emission rates are to be calculated as in vacuum while in [110] they include factors interpreted as wave-function normalisation: $\tilde{Z}_L \Gamma_{\gamma,\text{em}}^L|_{\text{us}} = \Gamma_{\gamma,\text{em}}^L|_{\text{RR}}$.

Eq. B.13 has to be compared to

$$\Gamma_{\gamma',\text{em}}^T = \frac{\epsilon^2 m_{\gamma'}^4 \Gamma_{\gamma,\text{em}}^T}{(m_{\gamma'}^2 - \omega_T^2)^2 + \omega^2 (e^{\omega/T} - 1)^2 (\Gamma_{\gamma,\text{em}}^T)^2}. \quad (\text{B.14})$$

Comparing these expressions, one sees that at large T , $\omega_P \gg m_{\gamma'}$ and $\omega \sim \omega_P$, such as the ratio of longitudinal and transversal modes of the rate scales as,

$$\frac{\Gamma_{\gamma',\text{em}}^L}{\Gamma_{\gamma',\text{em}}^T} \approx \frac{\omega^4}{m_{\gamma'}^4} \frac{\Gamma_{\gamma,\text{em}}^L}{\Gamma_{\gamma,\text{em}}^T}. \quad (\text{B.15})$$

Furthermore, as the longitudinal production rate itself is proportional to $\propto m_{\gamma'}^2$ ¹, one finds that the overall scaling of the ratio given in Eq. B.15 is $\omega^2/m_{\gamma'}^2 \gg 1$. Hence, at the end of the day, the dark photons production rate occurs dominantly through production of longitudinal photons at high temperature, $\omega_P \gtrsim m_{\gamma'}$ [109], [110]. On the other hand, at lower temperatures, which is the regime relevant for infra-red dominated freeze-in production, one has

$$\frac{\Gamma_{\gamma',\text{em}}^L}{\Gamma_{\gamma',\text{em}}^T} \approx Z_L^2 \frac{\Gamma_{\gamma,\text{em}}^L}{\Gamma_{\gamma,\text{em}}^T} \sim Z_L^2 \frac{m_{\gamma'}}{\omega} \ll 1, \quad (\text{B.16})$$

because $Z_L \gtrsim 1$. Thus the dark photon production is dominated by production of transverse photons as explained above, see also [109], [110]. One can then use the following replacement rule for the on-shell dark photon production as it proceeds essentially as in vacuum,

$$\epsilon \rightarrow \epsilon_{\text{eff}}^2 = \frac{\epsilon^2 m_{\gamma'}^4}{(m_{\gamma'}^2 - \text{Re} \Pi_\gamma)^2 + \omega^2 (e^{\omega/T} - 1)^2 \Gamma_\gamma^2}, \quad (\text{B.17})$$

which basically explains the substitution rule stated in Eq. (3.33).

Finally, we give in Figure B.3 the time evolution of the dark photon yield highlighting all contributions to dark photon production. One can recognise the high temperature suppression of transversal modes and the low temperature suppression of the longitudinal mode of Eqs. B.15 and B.16 respectively.

¹This is due to current conservation: $k_\mu J^\mu = 0 \rightarrow \epsilon_\mu^L J^\mu \propto m_{\gamma'}$.

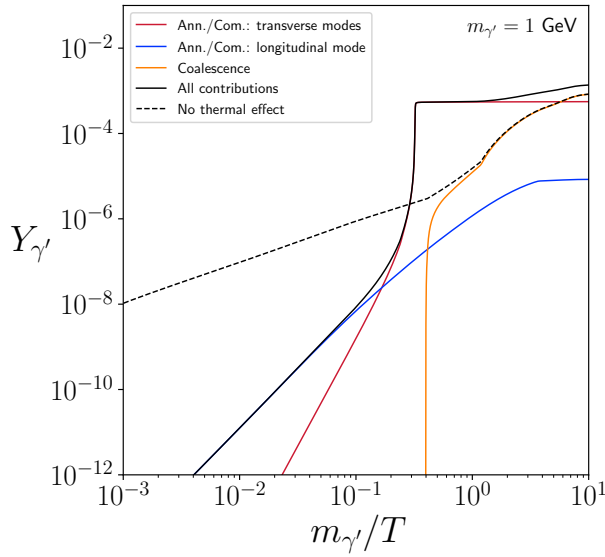


FIGURE B.3: For $\epsilon = 10^{-9}$, all contributions to the dark photon yield as a function of the inverse temperature. One can distinguish contributions from pair annihilation and Compton processes for both transverses (red dashed) and longitudinal modes (blue dashed), from the coalescence process (orange dashed) and from all contributions together (solid black). For the coalescence, we have taken into account the thermal corrections to the mass of the SM particles that annihilate into a dark photon [108].

Appendix C

Instantaneous freeze-out approximation

C.1 The thermally connected HS case

In this Appendix, we derive the DM relic abundance for a non-relativistic FO as a function of the DM annihilation cross section and the hidden-to-visible temperature ratio. Let us first review the very well known case (see e.g. [167]) for which the DM is in thermal equilibrium with the SM bath.

We assume that the DM FO occurs instantaneously such that the instant of DM decoupling is set when the Hubble expansion rate becomes larger than the DM annihilation rate: $\Gamma|_{T_{\text{dec}}} \lesssim H|_{T_{\text{dec}}}$. Defining T_{dec} as the exact instant where the two rates stop to be equal, one has

$$n^{eq}(T_{\text{dec}})\langle\sigma v\rangle = \sqrt{\frac{8\pi}{3M_{\text{pl}}^2}}\sqrt{\rho(x_{\text{dec}})}, \quad (\text{C.1})$$

with $x_{\text{dec}} \equiv m_{\text{DM}}/T_{\text{dec}}$, M_{pl} the Planck mass and where the DM number density is given by $n^{eq}(T_{\text{dec}}) \equiv g_{\text{DM}}(m_{\text{DM}}T_{\text{dec}}/2\pi)^{3/2}e^{-m_{\text{DM}}/T_{\text{dec}}}$, using the non-relativistic approximation. Taking the logarithm of Eq. C.1, one can approximate the instant of DM decoupling x_{dec} by

$$x_{\text{dec}} \simeq \ln \left[0.038 \langle\sigma v\rangle m_{\text{pl}} m_{\text{DM}} \left(\frac{g_{\text{DM}}}{\sqrt{g_{*}^{\text{eff}}(T_{\text{dec}})}} \right) \right] + \frac{1}{2} \ln \ln \left[0.038 \langle\sigma v\rangle m_{\text{pl}} m_{\text{DM}} \left(\frac{g_{\text{DM}}}{\sqrt{g_{*}^{\text{eff}}(T_{\text{dec}})}} \right) \right]. \quad (\text{C.2})$$

The DM relic density is defined by the DM energy density relative abundance today and can be related to the DM yield today [167]: $\Omega_{\text{DM}} h^2 = 2.5 \times Y_{\text{DM}}(T_0)(m_{\text{DM}}/\text{GeV})$. Then, assuming an instantaneous one has: $Y_{\text{DM}}(T_0) = Y_{\text{DM}}(T_{\text{dec}}) = H(T_{\text{dec}})/s(T_{\text{dec}})\langle\sigma v\rangle$. Finally, plugging the expressions for the Hubble expansion rate as well as for the entropy energy density, we find the DM relic abundance in the instantaneous freeze-out approximation:

$$\Omega_{\text{DM}} h^2 = 4.7 \cdot 10^8 \frac{g_{\text{DM}}^n \sqrt{g_*^{\text{eff}}(T_{\text{dec}})} x_{\text{dec}}}{g_*^S(T_{\text{dec}}) m_{\text{pl}} \langle\sigma v\rangle \text{GeV}}, \quad (\text{C.3})$$

where x_{dec} is given by Eq. C.2.

C.2 The thermally disconnected HS case

The procedure to obtain the DM relic abundance in the instantaneous FO approximation when the DM particle is part of a HS which has never thermalised with the VS is exactly the same as in the previous section. The only difference is that one must take the HS contributions in the energy and entropy densities. We have,

$$H(x') = \sqrt{\frac{8\pi}{3M_{\text{pl}}^2}} \sqrt{\rho_{\text{VS}}(x') + \rho_{\text{HS}}(x')}, \quad (\text{C.4})$$

$$s(x') = s_{\text{VS}}(x') + s_{\text{HS}}(x'). \quad (\text{C.5})$$

In terms of the inverse hidden temperature $x' \equiv m_{\text{DM}}/T'$ and the hidden-to-visible temperature ratio $\xi \equiv T'/T$, the energy and entropy densities of both sectors are given by,

$$\rho_{\text{VS}}(x') = \frac{\pi^2}{30} g_*^{\text{eff}} (m_{\text{DM}}/x' \xi) \left(\frac{m_{\text{DM}}}{x' \xi} \right)^4, \quad (\text{C.6})$$

$$\rho_{\text{HS}}(x') = \frac{\pi^2}{30} g_*'^{\text{eff}} (m_{\text{DM}}/x') \left(\frac{m_{\text{DM}}}{x'} \right)^4, \quad (\text{C.7})$$

$$s_{\text{VS}}(x') = \frac{2\pi^2}{45} g_*^S (m_{\text{DM}}/x' \xi) \left(\frac{m_{\text{DM}}}{x' \xi} \right)^3, \quad (\text{C.8})$$

$$s_{\text{HS}}(x') = \frac{2\pi^2}{45} g_*'^S (m_{\text{DM}}/x') \left(\frac{m_{\text{DM}}}{x'} \right)^3. \quad (\text{C.9})$$

In that case, the instantaneous freeze-out approximation gives,

$$\Omega_{\text{DM}} h^2 = 4.7 \cdot 10^8 \frac{g_{\text{DM}} \sqrt{g_*^{\text{eff}}(T_{\text{dec}}) + \tilde{\zeta}_{\text{dec}}^4 g'^{\text{eff}}(T'_{\text{dec}})} x'_{\text{dec}} \tilde{\zeta}_{\text{dec}}}{(g_*^S(T_{\text{dec}}) + \tilde{\zeta}_{\text{dec}}^3 g'^S(T'_{\text{dec}})) (T_{\text{dec}}) m_{\text{pl}} \langle \sigma v \rangle \text{ GeV}}, \quad (\text{C.10})$$

with x'_{dec} given by,

$$x'_{\text{dec}} \simeq \ln \left[0.038 \tilde{\zeta}_{\text{dec}}^2 \langle \sigma v \rangle m_{\text{pl}} m_{\text{DM}} \left(\frac{g_{\text{DM}}}{\sqrt{g_*^{\text{eff}}(T_{\text{dec}}) + \tilde{\zeta}_{\text{dec}}^4 g'^{\text{eff}}(T'_{\text{dec}})}} \right) \right] \\ + \frac{1}{2} \ln \ln \left[0.038 \tilde{\zeta}_{\text{dec}}^2 \langle \sigma v \rangle m_{\text{pl}} m_{\text{DM}} \left(\frac{g_{\text{DM}}}{\sqrt{g_*^{\text{eff}}(T_{\text{dec}}) + \tilde{\zeta}_{\text{dec}}^4 g'^{\text{eff}}(T'_{\text{dec}})}} \right) \right]. \quad (\text{C.11})$$

C.3 Further the instantaneous freeze-out approximation

Let us now derive a slightly improved formula for the DM relic abundance. We no longer assume the instantaneous FO, but we will not have a fully analytical formula.

Starting with the Boltzmann equation on the DM yield (Eq. 1.36),

$$\frac{dY}{dx} = - \frac{\langle \sigma v \rangle_{\tilde{\chi}\chi \rightarrow \chi\chi} s}{xH} \left[Y_{\chi}^2 - (Y_{\chi}^{eq})^2 \right]. \quad (\text{C.12})$$

One can use the HS temperature $x' \equiv m_{\text{DM}}/T'$ instead of the visible one ($x = m_{\text{DM}}/T$), we have

$$\frac{dY}{dx'} = -\mathcal{G}(x') \left[Y_{\chi}^2 - (Y_{\chi}^{eq})^2 \right], \quad (\text{C.13})$$

where now all quantities are seen as a function of x' and where we have defined $\mathcal{G}(x') \equiv \langle \sigma v \rangle s(x')/x'H(x')$.

At late times, long after the freeze-out, the equilibrium Yield is totally negligible (Boltzmann suppressed) compared to the actual Yield. It is to say that $Y \gg Y^{eq}$ when $x' \gg x'_{\text{dec}}$ such that the Boltzmann equation can be approximated as following,

$$\frac{dY}{dx'} = -\mathcal{G}(x')Y_{\chi}^2. \quad (\text{C.14})$$

This last equation can be integrated from the instant of decoupling x'_{dec} to today x'_0 ,

$$Y(x'_0) \simeq \left(\int_{x'_{\text{dec}}}^{x'_0} \mathcal{G}(x') dx' \right)^{-1}. \quad (\text{C.15})$$

One gets the DM relic abundance,

$$\Omega_{\text{DM}} h^2 = 2.53 \times 10^8 \times \left(\frac{m_{\text{DM}}}{\text{GeV}} \right) \times \left(\int_{x'_{\text{dec}}}^{x'_0} \frac{\langle \sigma v \rangle s(x')}{x' H(x')} dx' \right)^{-1}, \quad (\text{C.16})$$

where an integral has still to be performed. As said above, the final formula obtained in this way is not fully analytical, but is numerically closer to what one would obtain solving the Boltzmann equation. However, one can check that it recovers the analytical formula obtained assuming an instantaneous FO by taking a constant cross section in C.16. If one further assumes that the entropy and energy densities of the Universe are dominated by the VS, one gets

$$H(x') \simeq 1.67 \sqrt{g_{\star}^{\text{eff}}(m_{\text{DM}}/x' \tilde{\zeta})} \frac{m_{\text{DM}}^2}{M_{\text{pl}} x'^2 \tilde{\zeta}^2}, \quad (\text{C.17})$$

$$s(x') \simeq \frac{2\pi^2}{45} g_{\star}^S(m_{\text{DM}}/x' \tilde{\zeta}) \frac{m_{\text{DM}}^3}{x'^3 \tilde{\zeta}^3}, \quad (\text{C.18})$$

such that we finally have,

$$\Omega_{\text{DM}} h^2 = 7.90 \times 10^{-11} \times \frac{T'_{\text{dec}}}{T_{\text{dec}}} \times x'_{\text{dec}} \times \left(\frac{\text{GeV}^{-2}}{\langle \sigma v \rangle} \right) \times \left(\frac{\sqrt{g_{\star}^{\text{eff}}(T_{\text{dec}})}}{g_{\star}^S(T_{\text{dec}})} \right). \quad (\text{C.19})$$

Bibliography

- [1] J. H. Oort, "The force exerted by the stellar system in the direction perpendicular to the galactic plane and some related problems," *Bull. Ast. Inst. Neth*, vol. 6, p. 249, Aug. 1932.
- [2] F. Zwicky, "Die Rotverschiebung von extragalaktischen Nebeln," *Helv. Phys. Acta*, vol. 6, pp. 110–127, 1933. DOI: 10.1007/s10714-008-0707-4.
- [3] V. C. Rubin and J. Ford W. Kent, "Rotation of the Andromeda Nebula from a Spectroscopic Survey of Emission Regions," *apj*, vol. 159, p. 379, Feb. 1970. DOI: 10.1086/150317.
- [4] E. Aprile, J. Aalbers, F. Agostini, *et al.*, "First Dark Matter Search Results from the XENON1T Experiment," *Physical Review Letters*, vol. 119, no. 18, p. 181301, 2017, ISSN: 10797114. DOI: 10.1103/PhysRevLett.119.181301. arXiv: 1705.06655.
- [5] D. S. Akerib *et al.*, "Results from a search for dark matter in the complete LUX exposure," *Phys. Rev. Lett.*, vol. 118, no. 2, p. 021303, 2017. DOI: 10.1103/PhysRevLett.118.021303. arXiv: 1608.07648 [astro-ph.CO].
- [6] X. Cui, A. Abdukerim, W. Chen, *et al.*, "Dark Matter Results from 54-Ton-Day Exposure of PandaX-II Experiment," *Physical Review Letters*, vol. 119, no. 18, p. 181302, 2017, ISSN: 10797114. DOI: 10.1103/PhysRevLett.119.181302. arXiv: 1708.06917.
- [7] A. M. Sirunyan *et al.*, "Search for dark matter particles produced in association with a top quark pair at $\sqrt{s} = 13$ TeV," *Phys. Rev. Lett.*, vol. 122, no. 1, p. 011803, 2019. DOI: 10.1103/PhysRevLett.122.011803. arXiv: 1807.06522 [hep-ex].
- [8] A. M. Sirunyan *et al.*, "Search for narrow and broad dijet resonances in proton-proton collisions at $\sqrt{s} = 13$ TeV and constraints on dark matter mediators and other new particles," *JHEP*, vol. 08, p. 130, 2018. DOI: 10.1007/JHEP08(2018)130. arXiv: 1806.00843 [hep-ex].
- [9] A. M. Sirunyan *et al.*, "Search for dark matter produced in association with a Higgs boson decaying to $\gamma\gamma$ or $\tau^+\tau^-$ at $\sqrt{s} = 13$ TeV," *JHEP*, vol. 09, p. 046, 2018. DOI: 10.1007/JHEP09(2018)046. arXiv: 1806.04771 [hep-ex].

- [10] A. M. Sirunyan *et al.*, “Search for new physics in dijet angular distributions using proton–proton collisions at $\sqrt{s} = 13$ TeV and constraints on dark matter and other models,” *Eur. Phys. J. C*, vol. 78, no. 9, p. 789, 2018. DOI: 10.1140/epjc/s10052-018-6242-x. arXiv: 1803.08030 [hep-ex].
- [11] A. M. Sirunyan *et al.*, “Search for dark matter in events with energetic, hadronically decaying top quarks and missing transverse momentum at $\sqrt{s} = 13$ TeV,” *JHEP*, vol. 06, p. 027, 2018. DOI: 10.1007/JHEP06(2018)027. arXiv: 1801.08427 [hep-ex].
- [12] M. Aaboud *et al.*, “Search for dark matter in events with a hadronically decaying vector boson and missing transverse momentum in pp collisions at $\sqrt{s} = 13$ TeV with the ATLAS detector,” *JHEP*, vol. 10, p. 180, 2018. DOI: 10.1007/JHEP10(2018)180. arXiv: 1807.11471 [hep-ex].
- [13] A. M. Sirunyan *et al.*, “Search for top squarks and dark matter particles in opposite-charge dilepton final states at $\sqrt{s} = 13$ TeV,” *Phys. Rev. D*, vol. 97, no. 3, p. 032009, 2018. DOI: 10.1103/PhysRevD.97.032009. arXiv: 1711.00752 [hep-ex].
- [14] M. Aaboud *et al.*, “Search for dark matter and other new phenomena in events with an energetic jet and large missing transverse momentum using the ATLAS detector,” *JHEP*, vol. 01, p. 126, 2018. DOI: 10.1007/JHEP01(2018)126. arXiv: 1711.03301 [hep-ex].
- [15] M. Aaboud *et al.*, “Search for dark matter produced in association with bottom or top quarks in $\sqrt{s} = 13$ TeV pp collisions with the ATLAS detector,” *Eur. Phys. J. C*, vol. 78, no. 1, p. 18, 2018. DOI: 10.1140/epjc/s10052-017-5486-1. arXiv: 1710.11412 [hep-ex].
- [16] M. Aaboud *et al.*, “Search for an invisibly decaying Higgs boson or dark matter candidates produced in association with a Z boson in pp collisions at $\sqrt{s} = 13$ TeV with the ATLAS detector,” *Phys. Lett. B*, vol. 776, pp. 318–337, 2018. DOI: 10.1016/j.physletb.2017.11.049. arXiv: 1708.09624 [hep-ex].
- [17] D. Hooper, R. K. Leane, Y.-D. Tsai, S. Wegsman, and S. J. Witte, “A systematic study of hidden sector dark matter: application to the gamma-ray and antiproton excesses,” *JHEP*, vol. 07, no. 07, p. 163, 2020. DOI: 10.1007/JHEP07(2020)163. arXiv: 1912.08821 [hep-ph].
- [18] D. J. H. Chung, E. W. Kolb, and A. Riotto, “Superheavy dark matter,” *Phys. Rev.*, vol. D59, p. 023501, 1998. DOI: 10.1103/PhysRevD.59.023501. arXiv: hep-ph/9802238 [hep-ph].
- [19] E. W. Kolb, D. J. H. Chung, and A. Riotto, “WIMPzillas!” *AIP Conf. Proc.*, vol. 484, no. 1, pp. 91–105, 1999, [592(1999)]. DOI: 10.1063/1.59655. arXiv: hep-ph/9810361 [hep-ph].

- [20] L. Randall, J. Scholtz, and J. Unwin, “Flooded Dark Matter and S Level Rise,” *JHEP*, vol. 03, p. 011, 2016. DOI: 10.1007/JHEP03(2016)011. arXiv: 1509.08477 [hep-ph].
- [21] A. Berlin, D. Hooper, and G. Krnjaic, “PeV-Scale Dark Matter as a Thermal Relic of a Decoupled Sector,” *Phys. Lett.*, vol. B760, pp. 106–111, 2016. DOI: 10.1016/j.physletb.2016.06.037. arXiv: 1602.08490 [hep-ph].
- [22] A. Berlin, D. Hooper, and G. Krnjaic, “Thermal Dark Matter From A Highly Decoupled Sector,” *Phys. Rev.*, vol. D94, no. 9, p. 095019, 2016. DOI: 10.1103/PhysRevD.94.095019. arXiv: 1609.02555 [hep-ph].
- [23] K. Harigaya, M. Ibe, K. Kaneta, W. Nakano, and M. Suzuki, “Thermal Relic Dark Matter Beyond the Unitarity Limit,” *JHEP*, vol. 08, p. 151, 2016. DOI: 10.1007/JHEP08(2016)151. arXiv: 1606.00159 [hep-ph].
- [24] T. Tenkanen and V. Vaskonen, “Reheating the Standard Model from a hidden sector,” *Phys. Rev.*, vol. D94, no. 8, p. 083516, 2016. DOI: 10.1103/PhysRevD.94.083516. arXiv: 1606.00192 [astro-ph.CO].
- [25] A. Berlin, “WIMPs with GUTs: Dark Matter Coannihilation with a Lighter Species,” *Phys. Rev. Lett.*, vol. 119, p. 121801, 2017. DOI: 10.1103/PhysRevLett.119.121801. arXiv: 1704.08256 [hep-ph].
- [26] J. Bramante and J. Unwin, “Superheavy Thermal Dark Matter and Primordial Asymmetries,” *JHEP*, vol. 02, p. 119, 2017. DOI: 10.1007/JHEP02(2017)119. arXiv: 1701.05859 [hep-ph].
- [27] E. W. Kolb and A. J. Long, “Superheavy dark matter through Higgs portal operators,” *Phys. Rev.*, vol. D96, no. 10, p. 103540, 2017. DOI: 10.1103/PhysRevD.96.103540. arXiv: 1708.04293 [astro-ph.CO].
- [28] C. Blanco, J. P. Harding, and D. Hooper, “Novel Gamma-Ray Signatures of PeV-Scale Dark Matter,” *JCAP*, vol. 1804, no. 04, p. 060, 2018. DOI: 10.1088/1475-7516/2018/04/060. arXiv: 1712.02805 [hep-ph].
- [29] M. Cirelli, Y. Gouttenoire, K. Petraki, and F. Sala, “Homeopathic Dark Matter, or how diluted heavy substances produce high energy cosmic rays,” *JCAP*, vol. 1902, p. 014, 2019. DOI: 10.1088/1475-7516/2019/02/014. arXiv: 1811.03608 [hep-ph].
- [30] H. Davoudiasl and G. Mohlabeng, “Getting a THUMP from a WIMP,” 2019. arXiv: 1912.05572 [hep-ph].
- [31] H. Kim and E. Kuflik, “Superheavy Thermal Dark Matter,” *Phys. Rev. Lett.*, vol. 123, no. 19, p. 191801, 2019. DOI: 10.1103/PhysRevLett.123.191801. arXiv: 1906.00981 [hep-ph].

- [32] L. Heurtier and F. Huang, "Inflaton portal to a highly decoupled EeV dark matter particle," *Phys. Rev.*, vol. D100, no. 4, p. 043 507, 2019. DOI: 10 . 1103/PhysRevD.100.043507. arXiv: 1905.05191 [hep-ph].
- [33] M. J. Baker, J. Kopp, and A. J. Long, "Filtered Dark Matter at a First Order Phase Transition," 2019. arXiv: 1912.02830 [hep-ph].
- [34] D. Chway, T. H. Jung, and C. S. Shin, "Dark matter filtering-out effect during a first-order phase transition," 2019. arXiv: 1912.04238 [hep-ph].
- [35] L. Heurtier and H. Partouche, "Spontaneous Freeze Out of Dark Matter From an Early Thermal Phase Transition," *Phys. Rev.*, vol. D101, no. 4, p. 043 527, 2020. DOI: 10 . 1103/PhysRevD.101.043527. arXiv: 1912.02828 [hep-ph].
- [36] V. V. Batyghin, "On the possibility of experimental observation of Hard Vavilov-Čerenkov radiation," *Physics Letters A*, vol. 28, no. 1, pp. 64–65, 1968, ISSN: 03759601. DOI: 10 . 1016/0375-9601(68)90603-8.
- [37] S. I. Blinnikov and M. Y. Khlopov, "ON POSSIBLE EFFECTS OF 'MIRROR' PARTICLES," *Sov. J. Nucl. Phys.*, vol. 36, p. 472, 1982.
- [38] R. Foot, H. Lew, and R. R. Volkas, "A Model with fundamental improper space-time symmetries," *Phys. Lett. B*, vol. 272, pp. 67–70, 1991. DOI: 10 . 1016/0370-2693(91)91013-L.
- [39] H. Hodges, "Mirror baryons as the dark matter," *Phys. Rev. D*, vol. 47, pp. 456–459, 1993. DOI: 10 . 1103/PhysRevD.47.456.
- [40] Z. Berezhiani, A. Dolgov, and R. Mohapatra, "Asymmetric inflationary reheating and the nature of mirror universe," *Phys. Lett. B*, vol. 375, pp. 26–36, 1996. DOI: 10 . 1016/0370-2693(96)00219-5. arXiv: hep-ph/9511221.
- [41] N. Arkani-Hamed, S. Dimopoulos, and S. Kachru, "Predictive landscapes and new physics at a TeV," Jan. 2005. arXiv: hep-th/0501082.
- [42] M. J. Strassler and K. M. Zurek, "Echoes of a hidden valley at hadron colliders," *Phys. Lett. B*, vol. 651, pp. 374–379, 2007. DOI: 10 . 1016/j . physletb . 2007 . 06 . 055. arXiv: hep-ph/0604261.
- [43] D. Hooper and K. M. Zurek, "A Natural Supersymmetric Model with MeV Dark Matter," *Phys. Rev. D*, vol. 77, p. 087 302, 2008. DOI: 10 . 1103/PhysRevD.77.087302. arXiv: 0801.3686 [hep-ph].
- [44] J. L. Feng and J. Kumar, "The WIMPlless Miracle: Dark-Matter Particles without Weak-Scale Masses or Weak Interactions," *Phys. Rev. Lett.*, vol. 101, p. 231 301, 2008. DOI: 10 . 1103/PhysRevLett.101.231301. arXiv: 0803.4196 [hep-ph].
- [45] M. Cvetič, J. Halverson, and H. Piragua, "Stringy Hidden Valleys," *JHEP*, vol. 02, p. 005, 2013. DOI: 10 . 1007 / JHEP02(2013)005. arXiv: 1210 . 5245 [hep-ph].

- [46] R. K. Kaul, “Technicolor,” *Rev. Mod. Phys.*, vol. 55, p. 449, 1983. DOI: 10.1103/RevModPhys.55.449.
- [47] M. Montull and F. Riva, “Higgs discovery: the beginning or the end of natural EWSB?” *JHEP*, vol. 11, p. 018, 2012. DOI: 10.1007/JHEP11(2012)018. arXiv: 1207.1716 [hep-ph].
- [48] D. Carmi, A. Falkowski, E. Kuflik, T. Volansky, and J. Zupan, “Higgs After the Discovery: A Status Report,” *JHEP*, vol. 10, p. 196, 2012. DOI: 10.1007/JHEP10(2012)196. arXiv: 1207.1718 [hep-ph].
- [49] R. Barbieri, D. Greco, R. Rattazzi, and A. Wulzer, “The Composite Twin Higgs scenario,” *JHEP*, vol. 08, p. 161, 2015. DOI: 10.1007/JHEP08(2015)161. arXiv: 1501.07803 [hep-ph].
- [50] G. Kauffmann, S. D. White, and B. Guiderdoni, “The Formation and Evolution of Galaxies Within Merging Dark Matter Haloes,” *Mon. Not. Roy. Astron. Soc.*, vol. 264, p. 201, 1993.
- [51] J. Zavala, Y. Jing, A. Faltenbacher, G. Yepes, Y. Hoffman, S. Gottlober, and B. Catinella, “The velocity function in the local environment from LCDM and LWDM constrained simulations,” *Astrophys. J.*, vol. 700, pp. 1779–1793, 2009. DOI: 10.1088/0004-637X/700/2/1779. arXiv: 0906.0585 [astro-ph.CO].
- [52] M. A. Zwaan, M. J. Meyer, and L. Staveley-Smith, “The velocity function of gas-rich galaxies,” *Mon. Not. Roy. Astron. Soc.*, vol. 403, p. 1969, 2010. DOI: 10.1111/j.1365-2966.2009.16188.x. arXiv: 0912.1754 [astro-ph.CO].
- [53] B. Moore, S. Ghigna, F. Governato, G. Lake, T. R. Quinn, J. Stadel, and P. Tozzi, “Dark matter substructure within galactic halos,” *Astrophys. J. Lett.*, vol. 524, pp. L19–L22, 1999. DOI: 10.1086/312287. arXiv: astro-ph/9907411.
- [54] A. A. Klypin, A. V. Kravtsov, O. Valenzuela, and F. Prada, “Where are the missing Galactic satellites?” *Astrophys. J.*, vol. 522, pp. 82–92, 1999. DOI: 10.1086/307643. arXiv: astro-ph/9901240.
- [55] M. Boylan-Kolchin, J. S. Bullock, and M. Kaplinghat, “Too big to fail? The puzzling darkness of massive Milky Way subhaloes,” *Mon. Not. Roy. Astron. Soc.*, vol. 415, p. L40, 2011. DOI: 10.1111/j.1745-3933.2011.01074.x. arXiv: 1103.0007 [astro-ph.CO].
- [56] M. Boylan-Kolchin, J. S. Bullock, and M. Kaplinghat, “The Milky Way’s bright satellites as an apparent failure of LCDM,” *Mon. Not. Roy. Astron. Soc.*, vol. 422, pp. 1203–1218, 2012. DOI: 10.1111/j.1365-2966.2012.20695.x. arXiv: 1111.2048 [astro-ph.CO].
- [57] E. J. Tollerud, M. Boylan-Kolchin, and J. S. Bullock, “M31 Satellite Masses Compared to LCDM Subhaloes,” *Mon. Not. Roy. Astron. Soc.*, vol. 440, no. 4, pp. 3511–3519, 2014. DOI: 10.1093/mnras/stu474. arXiv: 1403.6469 [astro-ph.GA].

- [58] S. Garrison-Kimmel, M. Boylan-Kolchin, J. S. Bullock, and E. N. Kirby, "Too Big to Fail in the Local Group," *Mon. Not. Roy. Astron. Soc.*, vol. 444, no. 1, pp. 222–236, 2014. DOI: 10.1093/mnras/stu1477. arXiv: 1404.5313 [astro-ph.GA].
- [59] J. Dubinski and R. Carlberg, "The Structure of cold dark matter halos," *Astrophys. J.*, vol. 378, p. 496, 1991. DOI: 10.1086/170451.
- [60] J. F. Navarro, C. S. Frenk, and S. D. White, "The Structure of cold dark matter halos," *Astrophys. J.*, vol. 462, pp. 563–575, 1996. DOI: 10.1086/177173. arXiv: astro-ph/9508025.
- [61] J. F. Navarro, C. S. Frenk, and S. D. White, "A Universal density profile from hierarchical clustering," *Astrophys. J.*, vol. 490, pp. 493–508, 1997. DOI: 10.1086/304888. arXiv: astro-ph/9611107.
- [62] R. A. Flores and J. R. Primack, "Observational and theoretical constraints on singular dark matter halos," *Astrophys. J. Lett.*, vol. 427, pp. L1–4, 1994. DOI: 10.1086/187350. arXiv: astro-ph/9402004.
- [63] B. Moore, "Evidence against dissipationless dark matter from observations of galaxy haloes," *Nature*, vol. 370, p. 629, 1994. DOI: 10.1038/370629a0.
- [64] B. Moore, T. R. Quinn, F. Governato, J. Stadel, and G. Lake, "Cold collapse and the core catastrophe," *Mon. Not. Roy. Astron. Soc.*, vol. 310, pp. 1147–1152, 1999. DOI: 10.1046/j.1365-8711.1999.03039.x. arXiv: astro-ph/9903164.
- [65] S. Tulin and H. B. Yu, "Dark matter self-interactions and small scale structure," *Physics Reports*, vol. 730, pp. 1–57, 2018, ISSN: 03701573. DOI: 10.1016/j.physrep.2017.11.004. arXiv: 1705.02358.
- [66] M. Kaplinghat, S. Tulin, and H. B. Yu, "Dark Matter Halos as Particle Colliders: Unified Solution to Small-Scale Structure Puzzles from Dwarfs to Clusters," *Physical Review Letters*, vol. 116, no. 4, p. 41 302, 2016, ISSN: 10797114. DOI: 10.1103/PhysRevLett.116.041302. arXiv: 1508.03339.
- [67] A. Kamada, M. Kaplinghat, A. B. Pace, and H. B. Yu, "Self-Interacting Dark Matter Can Explain Diverse Galactic Rotation Curves," *Physical Review Letters*, vol. 119, no. 11, p. 111 102, 2017, ISSN: 10797114. DOI: 10.1103/PhysRevLett.119.111102. arXiv: 1611.02716.
- [68] A. Burkert, "The Structure of dark matter halos in dwarf galaxies," *IAU Symp.*, vol. 171, p. 175, 1996. DOI: 10.1086/309560. arXiv: astro-ph/9504041.
- [69] S. S. McGaugh and W. de Blok, "Testing the dark matter hypothesis with low surface brightness galaxies and other evidence," *Astrophys. J.*, vol. 499, p. 41, 1998. DOI: 10.1086/305612. arXiv: astro-ph/9801123.

- [70] F. C. van den Bosch and R. A. Swaters, "Dwarf galaxy rotation curves and the core problem of dark matter halos," *Mon. Not. Roy. Astron. Soc.*, vol. 325, p. 1017, 2001. DOI: 10 . 1046 / j . 1365 - 8711 . 2001 . 04456 . x. arXiv: astro-ph/0006048.
- [71] A. Borriello and P. Salucci, "The Dark matter distribution in disk galaxies," *Mon. Not. Roy. Astron. Soc.*, vol. 323, p. 285, 2001. DOI: 10 . 1046 / j . 1365 - 8711 . 2001 . 04077 . x. arXiv: astro-ph/0001082.
- [72] W. de Blok, S. S. McGaugh, A. Bosma, and V. C. Rubin, "Mass density profiles of LSB galaxies," *Astrophys. J. Lett.*, vol. 552, pp. L23–L26, 2001. DOI: 10 . 1086 / 320262. arXiv: astro-ph/0103102.
- [73] W. de Blok, S. S. McGaugh, and V. C. Rubin, "High-Resolution Rotation Curves of Low Surface Brightness Galaxies. II. Mass Models," *Astron. J.*, vol. 122, pp. 2396–2427, 2001. DOI: 10 . 1086 / 323450.
- [74] D. Marchesini, E. D’Onghia, G. Chincarini, C. Firmani, P. Conconi, E. Molinari, and A. Zacchei, "H α rotation curves: the soft core question," *Astrophys. J.*, vol. 575, pp. 801–813, 2002. DOI: 10 . 1086 / 341475. arXiv: astro-ph/0202075.
- [75] G. Gentile, A. Burkert, P. Salucci, U. Klein, and F. Walter, "The dwarf galaxy DDO 47 as a dark matter laboratory: testing cusps hiding in triaxial halos," *Astrophys. J. Lett.*, vol. 634, pp. L145–L148, 2005. DOI: 10 . 1086 / 498939. arXiv: astro-ph/0506538.
- [76] G. Gentile, P. Salucci, U. Klein, and G. L. Granato, "NGC 3741: Dark halo profile from the most extended rotation curve," *Mon. Not. Roy. Astron. Soc.*, vol. 375, pp. 199–212, 2007. DOI: 10 . 1111 / j . 1365 - 2966 . 2006 . 11283 . x. arXiv: astro-ph/0611355.
- [77] R. Kuzio de Naray, S. S. McGaugh, W. de Blok, and A. Bosma, "High Resolution Optical Velocity Fields of 11 Low Surface Brightness Galaxies," *Astrophys. J. Suppl.*, vol. 165, pp. 461–479, 2006. DOI: 10 . 1086 / 505345. arXiv: astro-ph/0604576.
- [78] R. Kuzio de Naray, S. S. McGaugh, and W. de Blok, "Mass Models for Low Surface Brightness Galaxies with High Resolution Optical Velocity Fields," *Astrophys. J.*, vol. 676, pp. 920–943, 2008. DOI: 10 . 1086 / 527543. arXiv: 0712.0860 [astro-ph].
- [79] P. Salucci, A. Lapi, C. Tonini, G. Gentile, I. Yegorova, and U. Klein, "The Universal Rotation Curve of Spiral Galaxies. 2. The Dark Matter Distribution out to the Virial Radius," *Mon. Not. Roy. Astron. Soc.*, vol. 378, pp. 41–47, 2007. DOI: 10.1111/j.1365-2966.2007.11696.x. arXiv: astro-ph/0703115.

- [80] S.-H. Oh *et al.*, “High-resolution mass models of dwarf galaxies from LITTLE THINGS,” *Astron. J.*, vol. 149, p. 180, 2015. DOI: 10.1088/0004-6256/149/6/180. arXiv: 1502.01281 [astro-ph.GA].
- [81] K. A. Oman *et al.*, “The unexpected diversity of dwarf galaxy rotation curves,” *Mon. Not. Roy. Astron. Soc.*, vol. 452, no. 4, pp. 3650–3665, 2015. DOI: 10.1093/mnras/stv1504. arXiv: 1504.01437 [astro-ph.GA].
- [82] R. Kuzio de Naray, G. D. Martinez, J. S. Bullock, and M. Kaplinghat, “The Case Against Warm or Self-Interacting Dark Matter as Explanations for Cores in Low Surface Brightness Galaxies,” *Astrophys. J. Lett.*, vol. 710, p. L161, 2010. DOI: 10.1088/2041-8205/710/2/L161. arXiv: 0912.3518 [astro-ph.CO].
- [83] J. S. Bullock, T. S. Kolatt, Y. Sigad, R. S. Somerville, A. V. Kravtsov, A. A. Klypin, J. R. Primack, and A. Dekel, “Profiles of dark haloes. Evolution, scatter, and environment,” *Mon. Not. Roy. Astron. Soc.*, vol. 321, pp. 559–575, 2001. DOI: 10.1046/j.1365-8711.2001.04068.x. arXiv: astro-ph/9908159.
- [84] T. Hambye, M. H. Tytgat, J. Vandecasteele, and L. Vanderheyden, “Dark matter direct detection is testing freeze-in,” *Physical Review D*, vol. 98, no. 7, p. 75017, 2018, ISSN: 24700029. DOI: 10.1103/PhysRevD.98.075017. arXiv: 1807.05022.
- [85] T. Hambye and L. Vanderheyden, “Minimal self-interacting dark matter models with light mediator,” *Journal of Cosmology and Astroparticle Physics*, vol. 2020, no. 05, pp. 001–001, 2020. DOI: 10.1088/1475-7516/2020/05/001. [Online]. Available: <https://doi.org/10.1088/1475-7516/2020/05/001>.
- [86] K. G. Begeman, A. H. Broeils, and R. H. Sanders, “Extended rotation curves of spiral galaxies : dark haloes and modified dynamics.,” *mnras*, vol. 249, p. 523, Apr. 1991. DOI: 10.1093/mnras/249.3.523.
- [87] V. Trimble, “Existence and Nature of Dark Matter in the Universe,” *Ann. Rev. Astron. Astrophys.*, vol. 25, pp. 425–472, 1987. DOI: 10.1146/annurev.aa.25.090187.002233.
- [88] P. Salucci and M. Persic, “Dark matter halos around galaxies,” *ASP Conf. Ser.*, vol. 117, p. 1, 1997. arXiv: astro-ph/9703027.
- [89] A. Vikhlinin, A. Kravtsov, W. Forman, C. Jones, M. Markevitch, S. Murray, and L. Van Speybroeck, “Chandra sample of nearby relaxed galaxy clusters: Mass, gas fraction, and mass-temperature relation,” *Astrophys. J.*, vol. 640, pp. 691–709, 2006. DOI: 10.1086/500288. arXiv: astro-ph/0507092.
- [90] D. Clowe, M. Bradac, A. H. Gonzalez, M. Markevitch, S. W. Randall, C. Jones, and D. Zaritsky, “A direct empirical proof of the existence of dark matter,” *Astrophys. J. Lett.*, vol. 648, pp. L109–L113, 2006. DOI: 10.1086/508162. arXiv: astro-ph/0608407.

- [91] *Esa - planck collaboration*, <https://sci.esa.int/s/WLGmGdw>, Accessed: 2021-01-15.
- [92] S. P. Goldman, "Generalized laguerre representation: Application to relativistic two-photon decay rates," *Phys. Rev. A*, vol. 40, pp. 1185–1193, 3 1989. DOI: 10.1103/PhysRevA.40.1185. [Online]. Available: <https://link.aps.org/doi/10.1103/PhysRevA.40.1185>.
- [93] C. Bennett *et al.*, "First year Wilkinson Microwave Anisotropy Probe (WMAP) observations: Preliminary maps and basic results," *Astrophys. J. Suppl.*, vol. 148, pp. 1–27, 2003. DOI: 10.1086/377253. arXiv: astro-ph/0302207.
- [94] N. Aghanim *et al.*, "Planck 2018 results. VI. Cosmological parameters," 2018. arXiv: 1807.06209 [astro-ph.CO].
- [95] J. Jaeckel and A. Ringwald, "The Low-Energy Frontier of Particle Physics," *Annual Review of Nuclear and Particle Science*, vol. 60, no. 1, pp. 405–437, 2010, ISSN: 0163-8998. DOI: 10.1146/annurev.nucl.012809.104433. arXiv: 1002.0329.
- [96] R. Essig, J. J. A. Jaros, W. Wester, and Others, "Working Group Report: New Light Weakly Coupled Particles," in *Proceedings, 2013 Community Summer Study on the Future of U.S. Particle Physics: Snowmass on the Mississippi (CSS2013): Minneapolis, MN, USA, July 29-August 6, 2013*, 2013. arXiv: 1311.0029. [Online]. Available: <http://www.slac.stanford.edu/econf/C1307292/docs/IntensityFrontier/NewLight-17.pdf>.
- [97] J. Alexander and Others, "Dark Sectors 2016 Workshop: Community Report," 2016. arXiv: 1608.08632 [hep-ph]. [Online]. Available: <http://lss.fnal.gov/archive/2016/conf/fermilab-conf-16-421.pdf>.
- [98] R. Foot and S. Vagnozzi, "Dissipative hidden sector dark matter," *Physical Review D - Particles, Fields, Gravitation and Cosmology*, vol. 91, no. 2, p. 23512, 2015, ISSN: 15502368. DOI: 10.1103/PhysRevD.91.023512. arXiv: 1409.7174.
- [99] J. H. Heo and C. S. Kim, "Light dark matter and dark radiation," *Journal of the Korean Physical Society*, vol. 68, no. 5, pp. 715–721, 2016, ISSN: 19768524. DOI: 10.3938/jkps.68.715. arXiv: 1504.00773.
- [100] J. L. Feng, H. Tu, and H. B. Yu, "Thermal relics in hidden sectors," *Journal of Cosmology and Astroparticle Physics*, vol. 2008, no. 10, p. 43, 2008, ISSN: 14757516. DOI: 10.1088/1475-7516/2008/10/043. arXiv: 0808.2318.
- [101] J. L. Feng, M. Kaplinghat, H. Tu, and H. B. Yu, "Hidden charged dark matter," *Journal of Cosmology and Astroparticle Physics*, vol. 2009, no. 7, p. 4, 2009, ISSN: 14757516. DOI: 10.1088/1475-7516/2009/07/004. arXiv: 0905.3039.

- [102] T. Hambye, "On the stability of particle dark matter," *Proceedings of Science*, vol. IDM2010, p. 98, 2010, ISSN: 18248039. DOI: 10.22323/1.110.0098. arXiv: 1012.4587.
- [103] E. C. G. Stueckelberg, "Interaction forces in electrodynamics and in the field theory of nuclear forces," *Helv.Phys.Acta*, vol. 11, pp. 299–328, 1938. DOI: 10.5169/seals-110852.
- [104] F. Englert and R. Brout, "Broken symmetry and the mass of gauge vector mesons," *Physical Review Letters*, vol. 13, no. 9, pp. 321–323, 1964, ISSN: 00319007. DOI: 10.1103/PhysRevLett.13.321.
- [105] P. W. Higgs, "Broken symmetries and the masses of gauge bosons," *Physical Review Letters*, vol. 13, no. 16, pp. 508–509, 1964, ISSN: 00319007. DOI: 10.1103/PhysRevLett.13.508.
- [106] J. Redondo, "Helioscope bounds on hidden sector photons," *Journal of Cosmology and Astroparticle Physics*, vol. 2008, no. 7, p. 8, 2008, ISSN: 14757516. DOI: 10.1088/1475-7516/2008/07/008. arXiv: 0801.1527.
- [107] J. Jaeckel, J. Redondo, and A. Ringwald, "Signatures of a hidden cosmic microwave background," *Physical Review Letters*, vol. 101, no. 13, p. 131801, 2008, ISSN: 00319007. DOI: 10.1103/PhysRevLett.101.131801. arXiv: 0804.4157.
- [108] J. Redondo and M. Postma, "Massive hidden photons as lukewarm dark matter," *Journal of Cosmology and Astroparticle Physics*, vol. 2009, no. 2, p. 5, 2009, ISSN: 14757516. DOI: 10.1088/1475-7516/2009/02/005. arXiv: 0811.0326.
- [109] H. An, M. Pospelov, and J. Pradler, "New stellar constraints on dark photons," *Physics Letters, Section B: Nuclear, Elementary Particle and High-Energy Physics*, vol. 725, no. 4-5, pp. 190–195, 2013, ISSN: 03702693. DOI: 10.1016/j.physletb.2013.07.008. arXiv: 1302.3884.
- [110] J. Redondo and G. Raffelt, "Solar constraints on hidden photons re-visited," *Journal of Cosmology and Astroparticle Physics*, vol. 2013, no. 8, p. 34, 2013, ISSN: 14757516. DOI: 10.1088/1475-7516/2013/08/034. arXiv: 1305.2920.
- [111] A. Fradette, M. Pospelov, J. Pradler, and A. Ritz, "Cosmological constraints on very dark photons," *Physical Review D - Particles, Fields, Gravitation and Cosmology*, vol. 90, no. 3, p. 35022, 2014, ISSN: 15502368. DOI: 10.1103/PhysRevD.90.035022. arXiv: 1407.0993.
- [112] M. Vogelsberger, J. Zavala, and A. Loeb, "Subhaloes in self-interacting galactic dark matter haloes," *Monthly Notices of the Royal Astronomical Society*, vol. 423, no. 4, pp. 3740–3752, 2012, ISSN: 00358711. DOI: 10.1111/j.1365-2966.2012.21182.x. arXiv: 1201.5892.

- [113] M. Rocha, A. H. Peter, J. S. Bullock, M. Kaplinghat, S. Garrison-kimmel, J. Oñorbe, and L. A. Moustakas, "Cosmological simulations with self-interacting dark matter - I. Constant-density cores and substructure," *Monthly Notices of the Royal Astronomical Society*, vol. 430, no. 1, pp. 81–104, 2013, ISSN: 00358711. DOI: 10.1093/mnras/sts514. arXiv: 1208.3025.
- [114] J. Zavala, M. Vogelsberger, and M. G. Walker, "Constraining self-interacting dark matter with the milky way's dwarf spheroidals," *Monthly Notices of the Royal Astronomical Society: Letters*, vol. 431, no. 1, pp. L20–L24, 2013, ISSN: 17453925. DOI: 10.1093/mnrasl/sls053. arXiv: 1211.6426.
- [115] A. H. Peter, M. Rocha, J. S. Bullock, and M. Kaplinghat, "Cosmological simulations with self-interacting dark matter - II. Halo shapes versus observations," *Monthly Notices of the Royal Astronomical Society*, vol. 430, no. 1, pp. 105–120, 2013, ISSN: 00358711. DOI: 10.1093/mnras/sts535. arXiv: 1208.3026.
- [116] D. Clowe, A. Gonzalez, and M. Markevitch, "Weak lensing mass reconstruction of the interacting cluster 1E0657-558: Direct evidence for the existence of dark matter," *Astrophys. J.*, vol. 604, pp. 596–603, 2004. DOI: 10.1086/381970. arXiv: astro-ph/0312273.
- [117] M. Markevitch, A. H. Gonzalez, D. Clowe, A. Vikhlinin, L. David, W. Forman, C. Jones, S. Murray, and W. Tucker, "Direct constraints on the dark matter self-interaction cross-section from the merging galaxy cluster 1E0657-56," *Astrophys. J.*, vol. 606, pp. 819–824, 2004. DOI: 10.1086/383178. arXiv: astro-ph/0309303 [astro-ph].
- [118] S. W. Randall, M. Markevitch, D. Clowe, A. H. Gonzalez, and M. Bradac, "Constraints on the Self-Interaction Cross-Section of Dark Matter from Numerical Simulations of the Merging Galaxy Cluster 1E 0657-56," *Astrophys. J.*, vol. 679, pp. 1173–1180, 2008. DOI: 10.1086/587859. arXiv: 0704.0261 [astro-ph].
- [119] D. Harvey, R. Massey, T. Kitching, A. Taylor, and E. Tittley, "The nongravitational interactions of dark matter in colliding galaxy clusters," *Science*, vol. 347, no. 6229, pp. 1462–1465, 2015, ISSN: 10959203. DOI: 10.1126/science.1261381. arXiv: 1503.07675.
- [120] K. Bondarenko, A. Boyarsky, T. Bringmann, and A. Sokolenko, "Constraining self-interacting dark matter with scaling laws of observed halo surface densities," *Journal of Cosmology and Astroparticle Physics*, vol. 2018, no. 4, p. 49, 2018, ISSN: 14757516. DOI: 10.1088/1475-7516/2018/04/049. arXiv: 1712.06602. [Online]. Available: <https://doi.org/10.1088/1475-7516/2018/04/049>.

- [121] S. Tulin, H. B. Yu, and K. M. Zurek, "Beyond collisionless dark matter: Particle physics dynamics for dark matter halo structure," *Physical Review D - Particles, Fields, Gravitation and Cosmology*, vol. 87, no. 11, p. 115007, 2013, ISSN: 15507998. DOI: 10.1103/PhysRevD.87.115007. arXiv: 1302.3898.
- [122] T. R. Slatyer, "Indirect dark matter signatures in the cosmic dark ages. I. Generalizing the bound on s-wave dark matter annihilation from Planck results," *Physical Review D*, vol. 93, no. 2, p. 23527, 2016, ISSN: 24700029. DOI: 10.1103/PhysRevD.93.023527. arXiv: 1506.03811.
- [123] T. Bringmann, F. Kahlhoefer, K. Schmidt-Hoberg, and P. Walia, "Strong Constraints on Self-Interacting Dark Matter with Light Mediators," *Physical Review Letters*, vol. 118, no. 14, p. 141802, 2017, ISSN: 10797114. DOI: 10.1103/PhysRevLett.118.141802. arXiv: 1612.00845.
- [124] M. Cirelli, P. Panci, K. Petraki, F. Sala, and M. Taoso, "Dark Matter's secret liaisons: Phenomenology of a dark U(1) sector with bound states," *Journal of Cosmology and Astroparticle Physics*, vol. 2017, no. 5, p. 36, 2017, ISSN: 14757516. DOI: 10.1088/1475-7516/2017/05/036. arXiv: 1612.07295 [hep-ph].
- [125] V. Poulin, J. Lesgourgues, and P. D. Serpico, "Cosmological constraints on exotic injection of electromagnetic energy," *Journal of Cosmology and Astroparticle Physics*, vol. 2017, no. 3, p. 43, 2017, ISSN: 14757516. DOI: 10.1088/1475-7516/2017/03/043. arXiv: 1610.10051.
- [126] T. R. Slatyer, "Energy injection and absorption in the cosmic dark ages," *Physical Review D - Particles, Fields, Gravitation and Cosmology*, vol. 87, no. 12, p. 123513, 2013, ISSN: 15507998. DOI: 10.1103/PhysRevD.87.123513. arXiv: 1211.0283.
- [127] R. Essig, E. Kuflik, S. D. McDermott, T. Volansky, and K. M. Zurek, "Constraining light dark matter with diffuse X-ray and gamma-ray observations," *Journal of High Energy Physics*, vol. 2013, no. 11, p. 193, 2013, ISSN: 10298479. DOI: 10.1007/JHEP11(2013)193. arXiv: 1309.4091.
- [128] K. K. Boddy and J. Kumar, "Indirect detection of dark matter using MeV-range gamma-ray telescopes," *Physical Review D - Particles, Fields, Gravitation and Cosmology*, vol. 92, no. 2, p. 23533, 2015, ISSN: 15502368. DOI: 10.1103/PhysRevD.92.023533. arXiv: 1504.04024 [astro-ph.CO].
- [129] S. Riemer-Sørensen, D. Wik, G. Madejski, *et al.*, "Dark matter line emission constraints from NuSTAR observations of the bullet cluster," *Astrophysical Journal*, vol. 810, no. 1, p. 48, 2015, ISSN: 15384357. DOI: 10.1088/0004-637X/810/1/48. arXiv: 1507.01378 [astro-ph.CO].

- [130] M. Hufnagel, K. Schmidt-Hoberg, and S. Wild, “BBN constraints on MeV-scale dark sectors. Part II: Electromagnetic decays,” *Journal of Cosmology and Astroparticle Physics*, vol. 2018, no. 11, p. 32, 2018, ISSN: 14757516. DOI: 10.1088/1475-7516/2018/11/032. arXiv: 1808.09324.
- [131] M. Pospelov and J. Pradler, “Big Bang Nucleosynthesis as a Probe of New Physics,” *Ann. Rev. Nucl. Part. Sci.*, vol. 60, pp. 539–568, 2010. DOI: 10.1146/annurev.nucl.012809.104521. arXiv: 1011.1054 [hep-ph].
- [132] S. Sarkar, “Big bang nucleosynthesis: Reprise,” in *2nd International Heidelberg Conference on Dark Matter in Astro and Particle Physics*, Jul. 1998, pp. 108–130. arXiv: astro-ph/9903183.
- [133] D. Kirkman, D. Tytler, N. Suzuki, J. M. O’Meara, and D. Lubin, “The Cosmological baryon density from the deuterium to hydrogen ratio towards QSO absorption systems: D/H towards Q1243+3047,” *Astrophys. J. Suppl.*, vol. 149, p. 1, 2003. DOI: 10.1086/378152. arXiv: astro-ph/0302006.
- [134] D. Kazanas, R. N. Mohapatra, S. Nussinov, V. L. Teplitz, and Y. Zhang, “Supernova bounds on the dark photon using its electromagnetic decay,” *Nuclear Physics B*, vol. 890, pp. 17–29, 2015, ISSN: 05503213. DOI: 10.1016/j.nuclphysb.2014.11.009. arXiv: 1410.0221.
- [135] J. H. Chang, R. Essig, and S. D. McDermott, “Revisiting Supernova 1987A constraints on dark photons,” *Journal of High Energy Physics*, vol. 2017, no. 1, p. 107, 2017, ISSN: 10298479. DOI: 10.1007/JHEP01(2017)107. arXiv: 1611.03864.
- [136] C. Mahoney, A. K. Leibovich, and A. R. Zentner, “Updated constraints on self-interacting dark matter from Supernova 1987A,” *Physical Review D*, vol. 96, no. 4, p. 43 018, 2017, ISSN: 24700029. DOI: 10.1103/PhysRevD.96.043018. arXiv: 1706.08871 [hep-ph].
- [137] J. H. Chang, R. Essig, and S. D. McDermott, “Supernova 1987A constraints on sub-GeV dark sectors, millicharged particles, the QCD axion, and an axion-like particle,” *Journal of High Energy Physics*, vol. 2018, no. 9, p. 51, 2018, ISSN: 10298479. DOI: 10.1007/JHEP09(2018)051. arXiv: 1803.00993.
- [138] J. A. Frieman, S. Dimopoulos, and M. S. Turner, “Axions and stars,” *Phys. Rev. D*, vol. 36, pp. 2201–2210, 8 1987. DOI: 10.1103/PhysRevD.36.2201. [Online]. Available: <https://link.aps.org/doi/10.1103/PhysRevD.36.2201>.
- [139] M. S. Turner, “Axions from sn1987a,” *Phys. Rev. Lett.*, vol. 60, pp. 1797–1800, 18 1988. DOI: 10.1103/PhysRevLett.60.1797. [Online]. Available: <https://link.aps.org/doi/10.1103/PhysRevLett.60.1797>.

- [140] A. Burrows, M. S. Turner, and R. P. Brinkmann, "Axions and sn 1987a," *Phys. Rev. D*, vol. 39, pp. 1020–1028, 4 1989. DOI: 10.1103/PhysRevD.39.1020. [Online]. Available: <https://link.aps.org/doi/10.1103/PhysRevD.39.1020>.
- [141] R. Essig, R. Harnik, J. Kaplan, and N. Toro, "Discovering New Light States at Neutrino Experiments," *Phys. Rev. D*, vol. 82, p. 113 008, 2010. DOI: 10.1103/PhysRevD.82.113008. arXiv: 1008.0636 [hep-ph].
- [142] A. Scribano, Y. Chung, P. Renton, *et al.*, "Measurement of the B+ total cross section and B+ differential cross section $d\sigma/dp(T)$ in $p(\bar{p})$ collisions at $\sqrt{s}=1.8$ TeV," *Physical Review D*, vol. 65, no. 5, p. 55 025, 2002, ISSN: 0556-2821. DOI: 10.1103/PhysRevD.65.55025. arXiv: 1306.4710 [hep-ph].
- [143] G. Krnjaic, "Probing light thermal dark matter with a Higgs portal mediator," *Physical Review D*, vol. 94, no. 7, p. 73 009, 2016, ISSN: 24700029. DOI: 10.1103/PhysRevD.94.073009. arXiv: 1512.04119.
- [144] F. Kahlhoefer, S. Kulkarni, and S. Wild, "Exploring light mediators with low-threshold direct detection experiments," *Journal of Cosmology and Astroparticle Physics*, vol. 2017, no. 11, p. 16, 2017, ISSN: 14757516. DOI: 10.1088/1475-7516/2017/11/016. arXiv: 1707.08571.
- [145] E. Aprile, J. Aalbers, F. Agostini, *et al.*, "Dark Matter Search Results from a One Ton-Year Exposure of XENON1T," *Physical Review Letters*, vol. 121, no. 11, p. 111 302, 2018, ISSN: 10797114. DOI: 10.1103/PhysRevLett.121.111302. arXiv: 1805.12562.
- [146] N. Fornengo, P. Panci, and M. Regis, "Long-range forces in direct dark matter searches," *Physical Review D - Particles, Fields, Gravitation and Cosmology*, vol. 84, no. 11, p. 115 002, 2011, ISSN: 15507998. DOI: 10.1103/PhysRevD.84.115002. arXiv: 1108.4661 [hep-ph].
- [147] R. H. Helm, "Inelastic and elastic scattering of 187-mev electrons from selected even-even nuclei," *Phys. Rev.*, vol. 104, pp. 1466–1475, 5 1956. DOI: 10.1103/PhysRev.104.1466. [Online]. Available: <https://link.aps.org/doi/10.1103/PhysRev.104.1466>.
- [148] A. Das and B. Dasgupta, "Selection Rule for Enhanced Dark Matter Annihilation," *Physical Review Letters*, vol. 118, no. 25, 2017, ISSN: 10797114. DOI: 10.1103/PhysRevLett.118.251101. arXiv: 1611.04606 [hep-ph].
- [149] M. Ackermann, M. Ajello, A. Albert, *et al.*, "Fermi LAT search for dark matter in gamma-ray lines and the inclusive photon spectrum," *Physical Review D - Particles, Fields, Gravitation and Cosmology*, vol. 86, no. 2, 2012, ISSN: 15502368. DOI: 10.1103/PhysRevD.86.022002. arXiv: 1205.2739. [Online]. Available: <http://dx.doi.org/10.1103/PhysRevD.86.022002>.

- [150] A. Abramowski, F. Acero, F. Aharonian, *et al.*, “Search for photon-linelike signatures from dark matter annihilations with H.E.S.S.,” *Physical Review Letters*, vol. 110, no. 4, 2013, ISSN: 00319007. DOI: 10.1103/PhysRevLett.110.041301. arXiv: 1301.1173. [Online]. Available: <http://dx.doi.org/10.1103/PhysRevLett.110.041301>.
- [151] M. Ackermann, M. Ajello, A. Albert, *et al.*, “Updated search for spectral lines from Galactic dark matter interactions with pass 8 data from the Fermi Large Area Telescope,” *Physical Review D - Particles, Fields, Gravitation and Cosmology*, vol. 91, no. 12, 2015, ISSN: 15502368. DOI: 10.1103/PhysRevD.91.122002. arXiv: 1506.00013. [Online]. Available: <http://dx.doi.org/10.1103/PhysRevD.91.122002>.
- [152] H. Abdallah, A. Abramowski, F. Aharonian, *et al.*, “Search for Dark Matter Annihilations towards the Inner Galactic Halo from 10 Years of Observations with H.E.S.S.,” *Physical Review Letters*, vol. 117, no. 11, 2016, ISSN: 10797114. DOI: 10.1103/PhysRevLett.117.111301. arXiv: 1607.08142. [Online]. Available: <http://dx.doi.org/10.1103/PhysRevLett.117.111301>.
- [153] A. Albert *et al.*, “Results from the search for dark matter in the Milky Way with 9 years of data of the ANTARES neutrino telescope,” *Phys. Lett. B*, vol. 769, pp. 249–254, 2017, [Erratum: *Phys.Lett.B* 796, 253–255 (2019)]. DOI: 10.1016/j.physletb.2017.03.063. arXiv: 1612.04595 [astro-ph.HE].
- [154] MAGIC Collaboration, M. L. Ahnen, S. Ansoldi, *et al.*, “Limits to dark matter annihilation cross-section from a combined analysis of MAGIC and Fermi-LAT observations of dwarf satellite galaxies,” *Journal of Cosmology and Astroparticle Physics*, vol. 2016, no. 2, pp. 039–039, 2016, ISSN: 14757516. DOI: 10.1088/1475-7516/2016/02/039. arXiv: 1601.06590. [Online]. Available: <http://dx.doi.org/10.1088/1475-7516/2016/02/039>.
- [155] A. M. Sirunyan *et al.*, “Search for invisible decays of a Higgs boson produced through vector boson fusion in proton-proton collisions at $\sqrt{s} = 13$ TeV,” *Phys. Lett. B*, vol. 793, pp. 520–551, 2019. DOI: 10.1016/j.physletb.2019.04.025. arXiv: 1809.05937 [hep-ex].
- [156] G. Aad *et al.*, “Measurements of the Higgs boson production and decay rates and constraints on its couplings from a combined ATLAS and CMS analysis of the LHC pp collision data at $\sqrt{s} = 7$ and 8 TeV,” *JHEP*, vol. 08, p. 045, 2016. DOI: 10.1007/JHEP08(2016)045. arXiv: 1606.02266 [hep-ex].
- [157] K. Bondarenko, A. Boyarsky, T. Bringmann, M. Hufnagel, K. Schmidt-Hoberg, and A. Sokolenko, “Direct detection and complementary constraints for sub-GeV dark matter,” *JHEP*, vol. 03, p. 118, 2020. DOI: 10.1007/JHEP03(2020)118. arXiv: 1909.08632 [hep-ph].

- [158] R. Aaij *et al.*, "Search for $A' \rightarrow \mu^+ \mu^-$ Decays," *Phys. Rev. Lett.*, vol. 124, no. 4, p. 041 801, 2020. DOI: 10.1103/PhysRevLett.124.041801. arXiv: 1910.06926 [hep-ex].
- [159] Z. Berezhiani, D. Comelli, and F. L. Villante, "The early mirror universe: Inflation, baryogenesis, nucleosynthesis and dark matter," *Physics Letters, Section B: Nuclear, Elementary Particle and High-Energy Physics*, vol. 503, no. 3-4, pp. 362–375, 2001, ISSN: 03702693. DOI: 10.1016/S0370-2693(01)00217-9. arXiv: 0008105 [hep-ph].
- [160] M. Goodsell, J. Jaeckel, J. Redondo, and A. Ringwald, "Naturally light hidden photons in LARGE volume string compactifications," *Journal of High Energy Physics*, vol. 2009, no. 11, p. 27, 2009, ISSN: 11266708. DOI: 10.1088/1126-6708/2009/11/027. arXiv: 0909.0515.
- [161] Z. Berezhiani and A. Lepidi, "Cosmological bounds on the "millicharges" of mirror particles," *Physics Letters, Section B: Nuclear, Elementary Particle and High-Energy Physics*, vol. 681, no. 3, pp. 276–281, 2009, ISSN: 03702693. DOI: 10.1016/j.physletb.2009.10.023. arXiv: 0810.1317 [hep-ph].
- [162] S. D. McDermott, H. B. Yu, and K. M. Zurek, "Turning off the lights: How dark is dark matter?" *Physical Review D - Particles, Fields, Gravitation and Cosmology*, vol. 83, no. 6, p. 63 509, 2011, ISSN: 15507998. DOI: 10.1103/PhysRevD.83.063509. arXiv: 1011.2907.
- [163] A. Sommerfeld, "Über die Beugung und Bremsung der Elektronen," *Annalen der Physik*, vol. 403, no. 3, pp. 257–330, 1931, ISSN: 15213889. DOI: 10.1002/andp.19314030302. [Online]. Available: <http://dx.doi.org/10.1002/andp.19314030302>.
- [164] P. S. Krstic and D. R. Schultz, "Consistent definitions for, and relationships among, cross sections for elastic scattering of hydrogen ions, atoms, and molecules," *Phys. Rev. A*, vol. 60, pp. 2118–2130, 3 1999. DOI: 10.1103/PhysRevA.60.2118. [Online]. Available: <https://link.aps.org/doi/10.1103/PhysRevA.60.2118>.
- [165] C Cohen-Tannoudji, B Diu, and F Laloë, *Mecanique Quantique, vol.II*, ser. Collection Enseignement des sciences, 16 vol.~1. Masson, 1995, ISBN: 9782705657338. [Online]. Available: <https://books.google.fr/books?id=RnQfAQAAMAAJ><https://books.google.fr/books?id=dnQfAQAAMAAJ>.
- [166] P. Gondolo and G. Gelmini, "Cosmic abundances of stable particles: Improved analysis," *Nuclear Physics, Section B*, vol. 360, no. 1, pp. 145–179, 1991, ISSN: 05503213. DOI: 10.1016/0550-3213(91)90438-4.
- [167] E. W. Kolb and M. S. Turner, *The early Universe*, 5841. Addison-Wesley, 1981, vol. 294, pp. 521–526. DOI: 10.1038/294521a0.

- [168] J. L. Feng, M. Kaplinghat, and H. B. Yu, "Halo-shape and relic-density exclusions of sommerfeld-enhanced dark matter explanations of cosmic ray excesses," *Physical Review Letters*, vol. 104, no. 15, p. 151 301, 2010, ISSN: 00319007. DOI: 10.1103/PhysRevLett.104.151301. arXiv: 0911.0422.
- [169] M. Ibe and H.-b. Yu, "Distinguishing Dark Matter Annihilation Enhancement Scenarios via Halo Shapes," *Phys. Lett. B*, vol. 692, pp. 70–73, 2010. DOI: 10.1016/j.physletb.2010.07.026. arXiv: 0912.5425 [hep-ph].
- [170] A. Loeb and N. Weiner, "Cores in dwarf galaxies from dark matter with a Yukawa potential," *Physical Review Letters*, vol. 106, no. 17, p. 171 302, 2011, ISSN: 00319007. DOI: 10.1103/PhysRevLett.106.171302. arXiv: 1011.6374 [astro-ph.CO].
- [171] S. Tulin, H. B. Yu, and K. M. Zurek, "Resonant dark forces and small-scale structure," *Physical Review Letters*, vol. 110, no. 11, p. 111 301, 2013, ISSN: 00319007. DOI: 10.1103/PhysRevLett.110.111301. arXiv: 1210.0900.
- [172] S. Cassel, "Sommerfeld factor for arbitrary partial wave processes," *Journal of Physics G: Nuclear and Particle Physics*, vol. 37, no. 10, p. 105 009, 2010. DOI: 10.1088/0954-3899/37/10/105009. [Online]. Available: <https://doi.org/10.1088/0954-3899/37/10/105009>.
- [173] H. An, S.-L. Chen, R. N. Mohapatra, and Y. Zhang, "Leptogenesis as a Common Origin for Matter and Dark Matter," *JHEP*, vol. 03, p. 124, 2010. DOI: 10.1007/JHEP03(2010)124. arXiv: 0911.4463 [hep-ph].
- [174] S. A. Khrapak, A. V. Ivlev, G. E. Morfill, and S. K. Zhdanov, "Scattering in the attractive yukawa potential in the limit of strong interaction," *Phys. Rev. Lett.*, vol. 90, p. 225 002, 22 2003. DOI: 10.1103/PhysRevLett.90.225002. [Online]. Available: <https://link.aps.org/doi/10.1103/PhysRevLett.90.225002>.
- [175] S. A. Khrapak, A. V. Ivlev, and G. E. Morfill, "Momentum transfer in complex plasmas," *Phys. Rev. E*, vol. 70, p. 056 405, 5 2004. DOI: 10.1103/PhysRevE.70.056405. [Online]. Available: <https://link.aps.org/doi/10.1103/PhysRevE.70.056405>.
- [176] T. R. Slatyer, "The sommerfeld enhancement for dark matter with an excited state," *Journal of Cosmology and Astroparticle Physics*, vol. 2010, no. 02, pp. 028–028, 2010. DOI: 10.1088/1475-7516/2010/02/028. [Online]. Available: <https://doi.org/10.1088/1475-7516/2010/02/028>.
- [177] T. Hambye, M. H. G. Tytgat, J. Vandecasteele, and L. Vanderheyden, "Dark matter from dark photons: a taxonomy of dark matter production," *Phys. Rev.*, vol. D100, no. 9, p. 95 018, 2019. DOI: 10.1103/PhysRevD.100.095018. arXiv: 1908.09864. [Online]. Available: <http://arxiv.org/abs/1908.09864>.

- [178] L. Vanderheyden, "Dark matter from dark photons," May 2021. arXiv: 2105.07039 [hep-ph].
- [179] X. Chu, T. Hambye, and M. H. Tytgat, "The four basic ways of creating dark matter through a portal," *Journal of Cosmology and Astroparticle Physics*, vol. 2012, no. 5, p. 34, 2012, ISSN: 14757516. DOI: 10.1088/1475-7516/2012/05/034. arXiv: 1112.0493.
- [180] G. L. Kane, P. Kumar, B. D. Nelson, and B. Zheng, "Dark matter production mechanisms with a nonthermal cosmological history: A classification," *Physical Review D*, vol. 93, no. 6, p. 63527, 2016, ISSN: 24700029. DOI: 10.1103/PhysRevD.93.063527. arXiv: 1502.05406.
- [181] M. Klasen and C. E. Yaguna, "Warm and cold fermionic dark matter via freeze-in," *Journal of Cosmology and Astroparticle Physics*, vol. 2013, no. 11, p. 39, 2013, ISSN: 14757516. DOI: 10.1088/1475-7516/2013/11/039. arXiv: 1309.2777 [hep-ph].
- [182] S. Heeba and F. Kahlhoefer, "Probing the freeze-in mechanism in dark matter models with $U(1)'$ gauge extensions," 2019. arXiv: 1908.09834. [Online]. Available: <http://arxiv.org/abs/1908.09834>.
- [183] H. A. Weldon, "Simple rules for discontinuities in finite-temperature field theory," *Physical Review D*, vol. 28, no. 8, pp. 2007–2015, 1983, ISSN: 05562821. DOI: 10.1103/PhysRevD.28.2007.
- [184] M. Le Bellac, *Thermal Field Theory*, ser. Cambridge Monographs on Mathematical Physics. Cambridge University Press, 1996, ISBN: 9780511885068, 9780521654777. DOI: 10.1017/cbo9780511721700. [Online]. Available: <http://www.cambridge.org/mw/academic/subjects/physics/theoretical-physics-and-mathematical-physics/thermal-field-theory?format=AR>.
- [185] E. Braaten and D. Segel, "Neutrino energy loss from the plasma process at all temperatures and densities," *Physical Review D*, vol. 48, no. 4, pp. 1478–1491, 1993, ISSN: 05562821. DOI: 10.1103/PhysRevD.48.1478. arXiv: 9302213 [hep-ph].
- [186] T. Hambye, M. Lucca, and L. Vanderheyden, "Dark matter as a heavy thermal hot relic," *Phys. Lett. B*, vol. 807, p. 135553, 2020. DOI: 10.1016/j.physletb.2020.135553. arXiv: 2003.04936 [hep-ph].
- [187] R. Coy, T. Hambye, M. H. G. Tytgat, and L. Vanderheyden, "The domain of thermal dark matter candidates," May 2021. arXiv: 2105.01263 [hep-ph].
- [188] R. Cowsik and J. McClelland, "An Upper Limit on the Neutrino Rest Mass," *Phys. Rev. Lett.*, vol. 29, pp. 669–670, 1972. DOI: 10.1103/PhysRevLett.29.669.

- [189] K. Sigurdson, “Hidden Hot Dark Matter as Cold Dark Matter,” 2009. arXiv: 0912.2346 [astro-ph.CO].
- [190] K. Griest and M. Kamionkowski, “Unitarity limits on the mass and radius of dark-matter particles,” *Physical Review Letters*, vol. 64, no. 6, pp. 615–618, 1990, ISSN: 00319007. DOI: 10.1103/PhysRevLett.64.615.
- [191] B. D. Fields, K. A. Olive, T.-H. Yeh, and C. Young, “Big-Bang Nucleosynthesis after Planck,” *JCAP*, vol. 03, p. 010, 2020, [Erratum: JCAP 11, E02 (2020)]. DOI: 10.1088/1475-7516/2020/03/010. arXiv: 1912.01132 [astro-ph.CO].
- [192] J. J. Bennett, G. Buldgen, M. Drewes, and Y. Y. Wong, “Towards a precision calculation of the effective number of neutrinos N_{eff} in the Standard Model I: The QED equation of state,” *JCAP*, vol. 03, p. 003, 2020. DOI: 10.1088/1475-7516/2020/03/003. arXiv: 1911.04504 [hep-ph].
- [193] J. Berger, K. Jedamzik, and D. G. Walker, “Cosmological constraints on decoupled dark photons and dark Higgs,” *Journal of Cosmology and Astroparticle Physics*, vol. 2016, no. 11, p. 32, 2016, ISSN: 14757516. DOI: 10.1088/1475-7516/2016/11/032. arXiv: 1605.07195.
- [194] M. Hufnagel, K. Schmidt-Hoberg, and S. Wild, “BBN constraints on MeV-scale dark sectors. Part I. Sterile decays,” *JCAP*, vol. 02, p. 044, 2018. DOI: 10.1088/1475-7516/2018/02/044. arXiv: 1712.03972 [hep-ph].
- [195] V. Iršič *et al.*, “New Constraints on the free-streaming of warm dark matter from intermediate and small scale Lyman- α forest data,” *Phys. Rev. D*, vol. 96, no. 2, p. 023522, 2017. DOI: 10.1103/PhysRevD.96.023522. arXiv: 1702.01764 [astro-ph.CO].
- [196] X. Chu, C. Garcia-Cely, and T. Hambye, “Can the relic density of self-interacting dark matter be due to annihilations into Standard Model particles?” *Journal of High Energy Physics*, vol. 2016, no. 11, p. 48, 2016, ISSN: 10298479. DOI: 10.1007/JHEP11(2016)048. arXiv: 1609.00399.
- [197] R. Foot and S. Vagnozzi, “Solving the small-scale structure puzzles with dissipative dark matter,” *JCAP*, vol. 07, p. 013, 2016. DOI: 10.1088/1475-7516/2016/07/013. arXiv: 1602.02467 [astro-ph.CO].
- [198] M. Duerr, K. Schmidt-Hoberg, and S. Wild, “Self-interacting dark matter with a stable vector mediator,” *Journal of Cosmology and Astroparticle Physics*, vol. 2018, no. 9, p. 33, 2018, ISSN: 14757516. DOI: 10.1088/1475-7516/2018/09/033. arXiv: 1804.10385.
- [199] E. Ma, “Inception of Self-Interacting Dark Matter with Dark Charge Conjugation Symmetry,” *Phys. Lett. B*, vol. 772, pp. 442–445, 2017. DOI: 10.1016/j.physletb.2017.06.067. arXiv: 1704.04666 [hep-ph].

- [200] X. He, G. C. Joshi, H. Lew, and R. Volkas, "NEW Z-prime PHENOMENOLOGY," *Phys. Rev. D*, vol. 43, pp. 22–24, 1991. DOI: 10.1103/PhysRevD.43.R22.
- [201] R. Foot, "New Physics From Electric Charge Quantization?" *Mod. Phys. Lett. A*, vol. 6, pp. 527–530, 1991. DOI: 10.1142/S0217732391000543.
- [202] X.-G. He, G. C. Joshi, H. Lew, and R. Volkas, "Simplest Z-prime model," *Phys. Rev. D*, vol. 44, pp. 2118–2132, 1991. DOI: 10.1103/PhysRevD.44.2118.
- [203] J. Heeck and W. Rodejohann, "Gauged $L_\mu - L_\tau$ Symmetry at the Electroweak Scale," *Phys. Rev. D*, vol. 84, p. 075007, 2011. DOI: 10.1103/PhysRevD.84.075007. arXiv: 1107.5238 [hep-ph].
- [204] S. Gninenko and N. Krasnikov, "The Muon anomalous magnetic moment and a new light gauge boson," *Phys. Lett. B*, vol. 513, p. 119, 2001. DOI: 10.1016/S0370-2693(01)00693-1. arXiv: hep-ph/0102222.
- [205] S. Baek, N. Deshpande, X. He, and P. Ko, "Muon anomalous g-2 and gauged L(muon) - L(tau) models," *Phys. Rev. D*, vol. 64, p. 055006, 2001. DOI: 10.1103/PhysRevD.64.055006. arXiv: hep-ph/0104141.
- [206] C. D. Carone, "Flavor-Nonuniversal Dark Gauge Bosons and the Muon g-2," *Phys. Lett. B*, vol. 721, pp. 118–122, 2013. DOI: 10.1016/j.physletb.2013.03.011. arXiv: 1301.2027 [hep-ph].
- [207] W. Altmannshofer, S. Gori, M. Pospelov, and I. Yavin, "Neutrino Trident Production: A Powerful Probe of New Physics with Neutrino Beams," *Phys. Rev. Lett.*, vol. 113, p. 091801, 2014. DOI: 10.1103/PhysRevLett.113.091801. arXiv: 1406.2332 [hep-ph].
- [208] M. Cirelli, M. Kadastik, M. Raidal, and A. Strumia, "Model-independent implications of the e⁺-, anti-proton cosmic ray spectra on properties of Dark Matter," *Nucl. Phys. B*, vol. 813, pp. 1–21, 2009, [Addendum: Nucl.Phys.B 873, 530–533 (2013)]. DOI: 10.1016/j.nuclphysb.2008.11.031. arXiv: 0809.2409 [hep-ph].
- [209] S. Baek and P. Ko, "Phenomenology of U(1)(L(mu)-L(tau)) charged dark matter at PAMELA and colliders," *JCAP*, vol. 10, p. 011, 2009. DOI: 10.1088/1475-7516/2009/10/011. arXiv: 0811.1646 [hep-ph].
- [210] R. Garani and J. Heeck, "Dark matter interactions with muons in neutron stars," *Phys. Rev. D*, vol. 100, no. 3, p. 035039, 2019. DOI: 10.1103/PhysRevD.100.035039. arXiv: 1906.10145 [hep-ph].
- [211] A. Kamada, K. Kaneta, K. Yanagi, and H.-B. Yu, "Self-interacting dark matter and muon $g - 2$ in a gauged $U(1)_{L_\mu - L_\tau}$ model," *JHEP*, vol. 06, p. 117, 2018. DOI: 10.1007/JHEP06(2018)117. arXiv: 1805.00651 [hep-ph].

- [212] I. Baldes, M. Cirelli, P. Panci, K. Petraki, F. Sala, and M. Taoso, “Asymmetric dark matter: residual annihilations and self-interactions,” *SciPost Phys.*, vol. 4, no. 6, p. 041, 2018. DOI: 10 . 21468 / SciPostPhys . 4 . 6 . 041. arXiv: 1712.07489 [hep-ph].
- [213] S. Weinberg, “Cosmological production of baryons,” *Physical Review Letters*, vol. 42, no. 13, pp. 850–853, 1979, ISSN: 00319007. DOI: 10 . 1103 / PhysRevLett . 42 . 850.
- [214] E. Rrapaj, A. Sieverding, and Y.-Z. Qian, “Rate of dark photon emission from electron positron annihilation in massive stars,” *Physical Review D*, vol. 100, no. 2, 2019, ISSN: 2470-0010. DOI: 10 . 1103 / physrevd . 100 . 023009. arXiv: 1904.10567 [hep-ph].

